UNIVERSITY OF SOUTHAMPTON

FACULTY OF ENGINEERING AND APPLIED SCIENCE
SCHOOL OF ENGINEERING SCIENCES

NUMERICAL PREDICTIONS AND EXPERIMENTAL ANALYSIS OF SMALL CLEARANCE RATIO TAYLOR-COUETTE FLOWS

by William Michael John Batten

Submitted for the degree of
Doctor of Philosophy

August 2002

UNIVERSITY OF SOUTHAMPTON

ABSTRACT

FACULTY OF ENGINEERING AND APPLIED SCIENCE
SCHOOL OF ENGINEERING SCIENCES
Doctor of Philosophy

NUMERICAL PREDICTIONS AND EXPERIMENTAL ANALYSIS OF SMALL CLEARANCE RATIO TAYLOR-COUETTE FLOWS

by William Michael John Batten

An integrated electrical thruster unit for use with work-class under water vehicles has a gap between two cylinders with the inner one rotating resulting in Taylor-Couette flow. It has a small clearance ratio with low Reynolds number turbulent Taylor vortices. To assess the frictional loss in the gap empirical equations were compared, but these show large discrepancies for the small gaps present in the thruster. From these empirical relations a 2mm gap was chosen for the design of the thruster unit. Published literature indicates that the start-up conditions affect the torque due to different Taylor vortex length and also raises questions about the existence of Görtler-type vortices within the turbulent Taylor vortices.

To analyse the flow an experimental rig was designed and constructed with a dynamically similar clearance ratio with a gap of 10mm and an inner radius of 710mm. The presence of Taylor vortices was clearly demonstrated, using a bubbles to visualise the flow. A novel method of analysing the bubbles as a probability spectrum, to measure Taylor vortex length, has been developed. The friction resistance has been measured, demonstrating the empirical equations are approximately correct, from analysis of the power lost in the motor used to drive the rig and dynamometry attached to the outer cylinder.

The laminar flow has been successfully modelled with ELMORE, an in-house finite volume Naiver-Stokes code with grid independent solutions. Studies were carried out on the effect of Reynolds number and end boundaries conditions on flow properties. These proved that if the vortex size is that of a critical length then the skin friction was the highest, unless adjacent to the end wall. It was also shown that it was possible to model just one vortex between two mirror boundaries.

Turbulent Taylor vortices have been studied using the low Reynolds number k-ω formulation using ELMORE and CFX, a commercial, finite volume CFD code. Grid independent results for three radius ratios tested have explained a turbulent flow transition between turbulent two states. For pre-transition the turbulence production is dominated by the outflowing boundary of the Taylor vortex. As the Reynolds number increases, shear driven turbulence, (due to the rotating cylinder) becomes the dominating factor. The effect of Taylor vortex length on skin friction and vortex strength has been evaluated using ELMORE.

The domain has been extended to that of the full geometry, by implementing ELMORE as a parallel solver, to demonstrate the open end effects. These have allowed a comparison of the pressure with the bubble distributions from the experimental results. The transient start-up problem has been solved using a parallel 2-D DNS approach. Although in 2-D, it clearly shows that Görtler vortices are initially present and evolve into stable turbulent Taylor vortices. Four distinct steps have been identified as this flow develops.

CONTENTS

LIST OF FIGURES

LIST OF TABLES

Acknowledgements

I am profoundly grateful to many people for the help and support during my work in preparation for this Phd thesis. For their valuable support, technical input and guidance during my Phd I firstly thank my supervisors, Stephen Turnock, Neil Bressloff and Suleiman Abu-Shark. I am also grateful to Suleiman and Steven for funding the experimental rig from EPSRC Research grant: GG/L11687. For additional feed back and helpful suggestions I am grateful to Richard Pattenden and Ravi Shetty, Gary Coleman and Adam Hughes. For help with my experimental facility I thank; the members of the Mechanical engineering work shops for the construction, especially David Goldsworthy; Rachman for help during filming and whose camera I borrowed; and Harsha, Whui, Afried, Dominic, Dave, James and Richard for help during several reassemblies. For moral support and needed enjoyable distractions, during the cause of my Phd, thanks additionally goes many of the above as well as Noel, Elizabeth, Signe, Ian, Chris, Charles, Jon, Monica and Elli. As always, I am grateful for continual support and encouragement from both my parents, Rosemary and John, and other family members.

Nomenclature

The notation used in the thesis is given here in the following order: upper-case Roman, lower-case Roman, upper-case Greek, lower-case Greek, other symbols and abbreviations.

Upper case Roman

A	constant
A_g	area of stain gauge
B	constant
B	log-law constant
C	constant
C_1	constant used in Wilcox model
C_2	constant used in Wilcox model
C_F	Yamaha's coefficient of friction, $2C_M$
C_M	coefficient of moment due to friction
C_{M_z}	coefficient of moment in the axial direction for one vortex
C_{M_θ}	coefficient of moment in the azimuthal direction of one vortex
C_μ	coefficient used in defining the turbulent viscosity
$\mathbf{F}$	unit force
F	force
F_f	force on each flexture
F_c	dynamometer calibration force
G	Wendt's coefficient of torque
Go	Görtler number
Go_c	Critical Görtler number
I_g	current through a stain gauge

L	cylinder length
M	torque
M_c	dynamometer calibration moment
P	turbulent kinetic energy production
P_s	frictional power
R	cylinder radius
R_1	inner cylinder radius
R_2	outer cylinder radius
R_c	dynamometer calibration radius
R_{effect}	effective resistance of a bridge circuit
R_g	resistance of a strain gauge
R_m	mean flexture radius
Re	Reynolds number based on gap
Re_r	Reynolds number based on radius
Re_T	local turbulent Reynolds number
Ro	Rosby number
U	speed of a cylinder
U_1	speed of the inner cylinder
U_2	speed of the outer cylinder
V_θ	azimuthal velocity field profile
V_O	bridge output voltage
V_S	bridge supply voltage
Ta	Taylor number
Ta_c	critical Taylor number

Lower case Roman

a	Taylor vortex wave number
d	gap width between cylinders
d_o	overall gap width, distance between the stator and magnets
$\mathbf{e}$	unit vector
e	distance between the axis of two eccentric cylinders
$f()$	a function
f_μ	a damping function
h	height used for refraction calculation
h_o	height of pulley above outer cylinder as used for calibrating the dynamometry
k	turbulent kinetic energy
l_f	flexture length
l_g	strain gauge length
l_t	twine length using in dynamometer calibration

n	perpendicular distance from cylinder wall
n^+	non-dimensional wall length
p	pressure
$\hat{p}$	pressure induced by centrifugal force
$\overline{p}$	ensemble averaged pressure
p'	fluctuating pressure
$\overline{q'^2}$	mean-squared turbulent velocity
r	radial cylindrical polar coordinate
r_{rc}	radius of curvature
t	time
t_f	flexture thickness
t_g	Strain gauge thickness
th	sheet thickness
$\mathbf{u}$	unit velocity vector
u^+	mean velocity normalised by the friction velocity
$u_{i,j}$	velocity component
u_r	radial velocity component
u_θ	azmiuthial velocity component
u_z	axial velocity component
$\overline{u_{i,j}}$	ensemble averaged velocity component
$u'_{i,j}$	fluctuating velocity component
u'_r	radial fluctuating velocity component
u'_θ	radial fluctuating velocity component
u'_z	axial fluctuating velocity component
u^*	friction velocity
w_f	flexture width
w_g	strain gauge width
w_t	stator teeth gap width
x	Cartesian coordinate
y	Cartesian coordinate
z	axial Cartesian or cylidrical polar coordinate

Upper-case Greek

Γ	aspect ratio
Υ	Refractive index
Ψ	non-dimensional vortex strength
Ω	rotation rate
Ω_1	rotation rate of inner cylinder
Ω_2	rotation rate of outer cylinder

Lower-case Greek

α	constant used in defining sublayer thickness
δ	boundary layer thickness
δ_1	laminar sublayer thickness on inner cylinder
δ_2	laminar sublayer thickness on outer cylinder
δ_{ij}	Kronecker delta
ϵ	turbulent energy dissipation
ϵ_{root}	root stress on the flexture
ϵ_g	stress in the middle of a strain gauge
η	radius ratio
θ	azimuthal angle in polar coordinates
κ	Von-Kármán constant
λ	non-dimensional size of a pair of Taylor vortices
λ_G	non-dimensional size of a pair of Görtler vortices
μ	dynamic viscosity
ξ	eccentricity ratio
ϖ	ratio of the speed of the inner and outer cylinders
ρ	density
σ	clearance ratio
σ_b	Bubble spectrum intensity
τ	shear stress
τ_w	shear stress at the wall
τ_{rot}	shear stress due to rotation of the flexture
υ	kinematic viscosity
ω	turbulent frequency

Other

$\triangle Z$	length of a pair Taylor vortices
m ∇	gradient operator
ℓ	lengthsacle
ℓ_m	mixing length

Abbreviations

CFD	computational fluid dynamics
CLAM	curved line advection method (Var Leer's)
CV	control volume
DNS	direct navier stokes
HDS	hybrid differencing scheme
LES	large eddy simulation
LDV	laser doppler velocimetry
LIF	laser induced fluorescence
PISO	pressure implicit splitting of operators
PIV	particle image velocimetry
RANS	Reynolds averaged Navier-Stokes
RNG	renormalisation group (Yakhat & Orszag)
RSM	Reynolds stress model
SIMPLE	semi implicit method for pressure linked equations
SIMPLEC	SIMPLE consistent
SIP	strongly implicit procedure
QUICK	quadratic upwind differencing

CHAPTER

1

Introduction

§1.1 Objectives and Motivation

The fluid flow between a rotating inner cylinder and a fixed outer cylinder is of interest in several engineering applications, such as motors, filters, pumps and journal bearings. The motivation for the work presented in this thesis stems from the development of a novel underwater-integrated electrical thruster unit [1, 2, 3]. A significant source of power loss in the electrical thruster arises from the fluid frictional resistance that occurs between two cylinders.

The principle aim of the research was to develop a detailed understanding of the flow in the annular gap of the electrical thruster unit. The underlying physics of the flow developed is that of turbulent vortices, driven by the rotation of the inner cylinder. These vortices are due the centrifugal instabilities which cause the secondary flow of toroidal vortices, known as Taylor vortices [4]. The nature of the physics of the turbulent Taylor vortices is highly complex and not well understood. The majority of the literature to date, on the topic of Taylor vortices, is concerned with the various bifurcations that occur between the stable laminar vortices and turbulent flow. To the best of the author's knowledge, no studies of turbulent Taylor vortices have ever been performed at values of the clearance ratios (the ratio between the annular gap and the inner cylinder radius) approaching that in the thruster. This means that in order to predict the torque in the thruster unit the skin friction coefficient had to be extrapolated from empirical equations found in the literature for other conditions.

In particular, based upon knowledge found in the literature there can be no satisfactory explanation of: how Taylor vortices form from stationary flow; whether Görtler vortices exist within Taylor vortices; the nature of the physics of a flow transition at $Re = 1 \times 10^4$ (close to the operating conditions of the thruster); how do vortices effect skin friction; the consequence of a small clearance ratio and the impact of end boundaries. All of the above issues have an impact upon the design of the gap in the thruster unit. In order to facilitate these poorly understood problems, a new experimental rig was developed and by applying available computational fluid dynamics (CFD) techniques as an investigative tool, the knowledge of flow has been enhanced. Both the experimental and computational methodologies developed can be applied to similar problems, such as other motor designs and journal bearings.

The aims of the experimental work were to design and construct a test rig that is dynamically* similar to the thruster unit, to take accurate torque measurements and visualise the flow. Typical test rigs found in the literature have considerably larger clearance ratios than most applications, such as that of journal bearings. Thus, for this work to be new and to be able to apply it to real problems, the test rig had to have a large radius, to maintain the small clearance ratio of the thruster. This enables the gap to be large enough to have a clear cross-section of sufficient size for visualisation. This also provided a means of validating the computational method.

The initial objective of the numerical studies was to demonstrate that both laminar and turbulent Taylor vortices can be modelled accurately using the finite volume method [5] to solve the Navier-Stokes equations [6] in a 2-D plane. This enabled the components of the flow to be studied so that the understanding of the physics can be further progressed. The further aims of the laminar modelling of Taylor vortices in a small clearance were to develop an understanding of rotating, stationary and mirror the end boundaries and from this, to recommend a methodology for studying turbulent Taylor vortices in a small domain.

The aims of the turbulent modeling research were to to study the effects of Reynolds number and Taylor vortices by choosing a suitable turbulence model. The goals of the Reynolds number studies were to reveal the physics of the transition between two different states of turbulent flow. The other interest is the effect that Taylor vortices have in increasing or decreasing the skin friction and how their lengths affects the skin friction. Further objectives were to extend the domain to the complete geometry of the thruster unit, in order to validate the numerical method and demonstrate the possibilities of the CFD uses as a design tool for future thruster units and in other similar problems. The final area of research was concerned with the effect of start-up upon the formation of turbulent Taylor vortices from stationary flow as the transient development of Taylor-Couette flow effects the number of Taylor cells and hence vortex length.

§1.2 Design of the thruster

As previously stated, the main part of the motivation for the work stemmed from the development of an underwater integrated electrical thruster for use with work-class underwater vehicles†. This thruster has the stator electrics in the solid duct with a permanent magnet rotor in a ring around the propeller. Photographs of some of the components and the assembled electrical thruster are shown in figure 1.1. Shown in part b of this figure, are the relative positions

---

[*] For this case the radius ratio, the gap aspect ratio and the Reynolds number based of the gap all have to be similar.

[†] This work has been carried out at Southampton University under EPSRC Research grant: GG/L11687 under principle investigators of Dr S. Abu Sharkh and Dr. S. Turnock. This grant has provided the funding for the materials used in construction of experimental facility

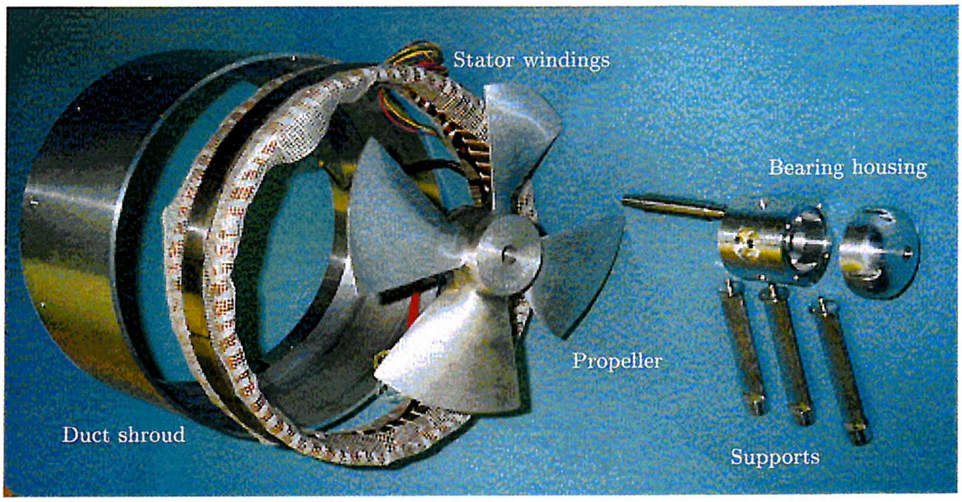

a) Some of the components of the thruster unit

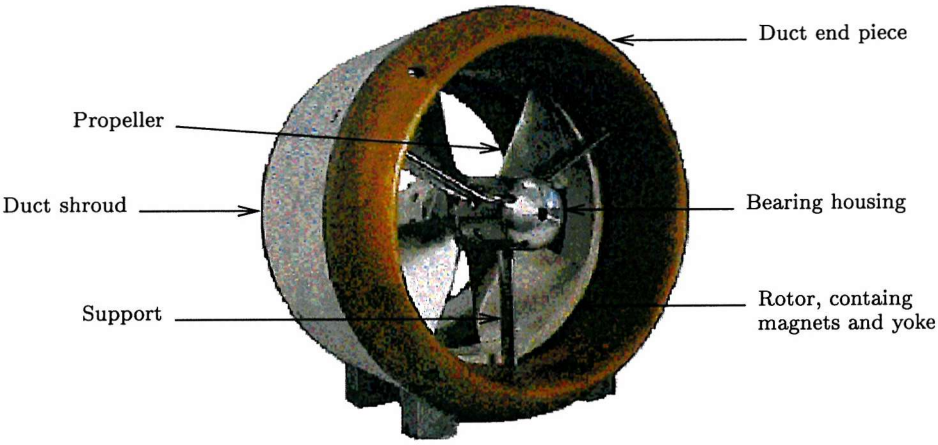

b) The fully assembled thruster unit

Figure 1.1: Photographs of the underwater integrated electrical thruster unit

of the motor stator in the duct casing and the rotor containing the magnets and yoke attached to the rim of the propeller.

The layout of the thruster illustrating this gap between the stator and rotor, is presented in the schematic half section in figure 1.2. The "region of interest" can be split into three parts, two axial gaps at the ends and a radial gap in the middle. The design phases for the first prototype integrated thruster occurred during the start of this research, hence only empirical calculations presented in the next chapter were used to give an estimation of the frictional losses.

It is hoped, that the work presented here can be used for future designs and that it forms the basis of further work towards reducing the frictional resistance of this type of integrated thruster and other similar rotating machines. Most of this thesis concerns the radial gap, as the flow in between two cylinders with the inner cylinder rotating. Different end conditions have

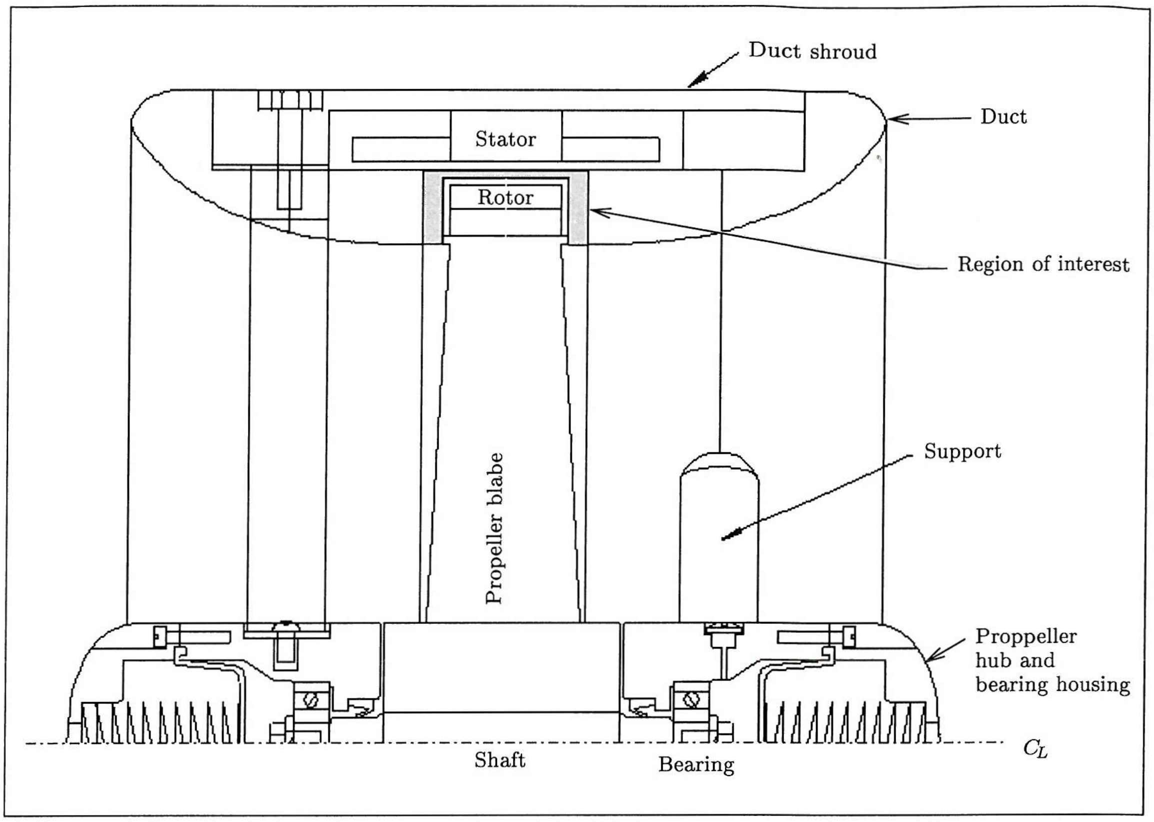

Figure 1.2: Layout of the electrical thruster showing the region of interest

been applied. The radial gap contains the largest region of frictional loss, more compelling flow features and is apparent in the wider range of rotating machinery.

§1.2.1 Electrical Considerations

The gap width in the integrated electric thruster is governed by both the magnetic properties and the frictional resistance between the stators and the magnets. The arrangement is illustrated in schematic section shown in figure 1.3. There are two approaches that can be used when designing such a motor. Firstly, to maintain a constant flux and vary the gap width. As the overall gap width, d_o increases, thicker magnet widths are required to maintain the flux across the gap. This has further problems as with relatively large gap sizes, leakage between the magnets becomes substantial. To overcome this the rotor yoke would have to be made thicker to accommodate the leakage.

The second approach is to keep the magnet size constant and increase the current on the stator core as the gap width increases. So that when the gap width increases the teeth, w_t become smaller and the slots become wider, enlarging the space for the winding therefore allowing a greater current. However, for a given size of motor, the minimum tooth size is governed by manufacturing constraints.

The motor design is also constrained by other factors such as cost and weight limitations. Hence optimising the gap width for a given design specification is a complex problem. Consequently accurate knowledge of the fluid frictional losses for a range of gap widths is required

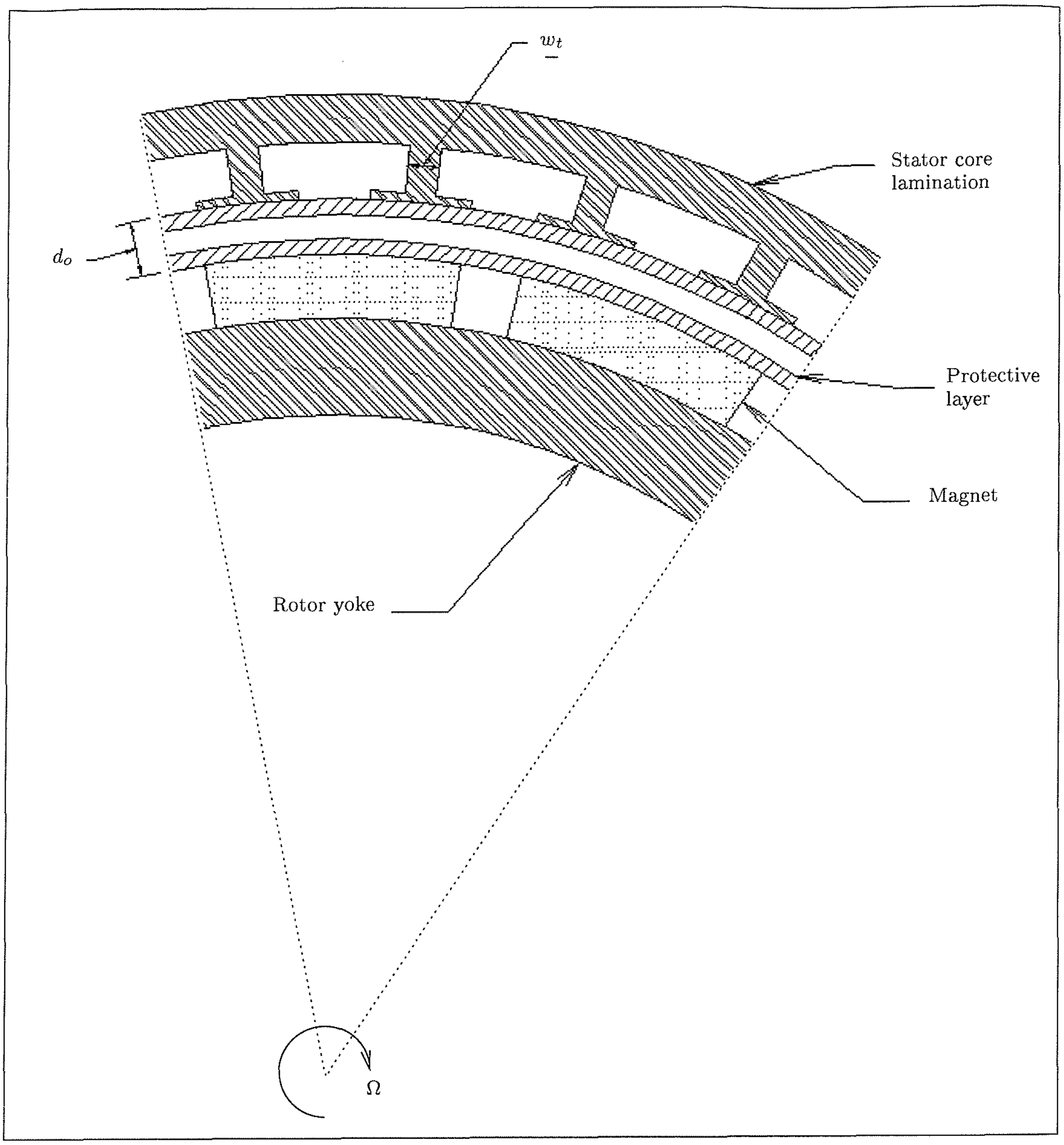

Figure 1.3: Schematic of motor layout

to inform the design process for an optimal motor.

§1.3 General Background

The motion of the fluids between rotating cylinders was first discussed by Isaac Newton in Book II of his Principia. The description of the fluid motion was then elaborated by Stokes who stated:

> ...for if the inner one were made to revolve too fast, the fluid near it would have a tendency to fly outwards in consequence of the centrifugal force, and eddies would be produced. [7]

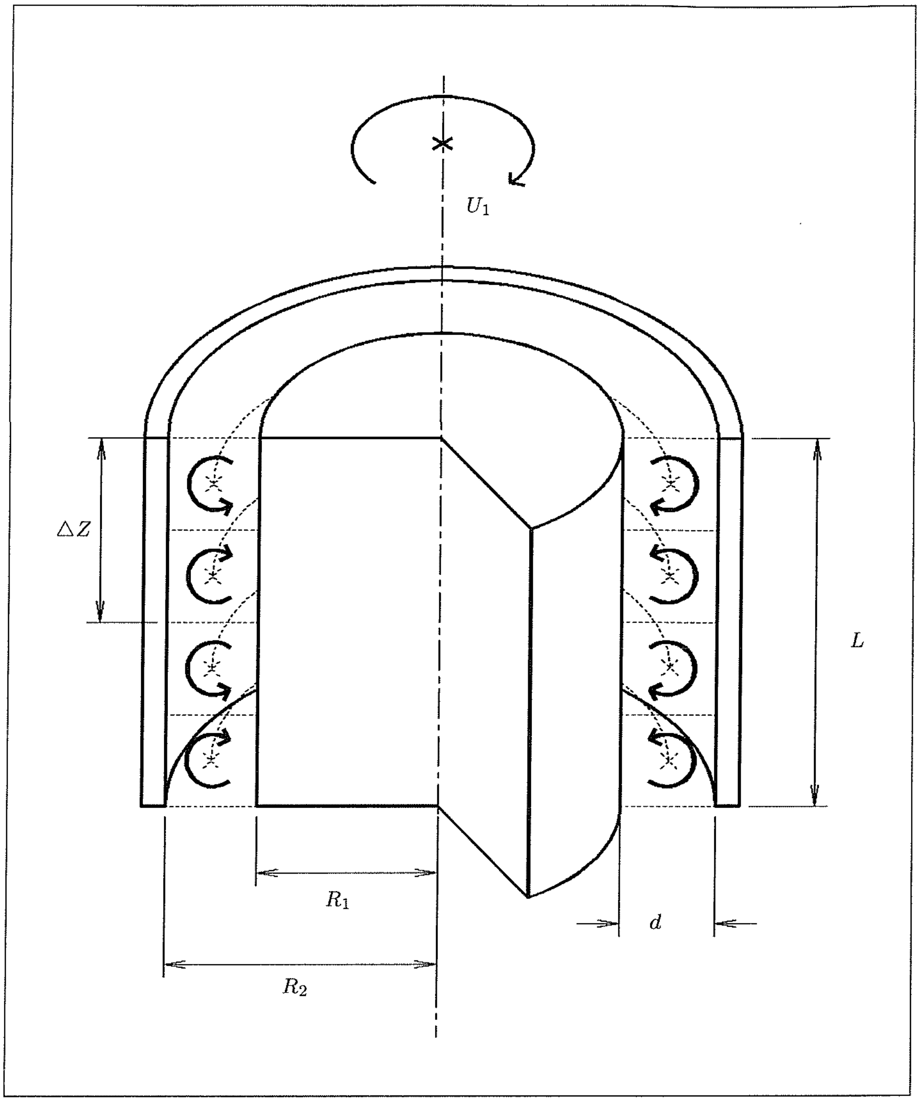

Figure 1.4: Schematic section of the geometry showing the position of Taylor vortices

Max Margules, an Austrian meteorologist proposed using the apparatus to measure viscosity of fluids as cited in [7]. Then seven years later Mallock [8] (Assistant to Lord Rayleigh) actually used the apparatus to measure the viscosity of water. The same year Couette began his investigations in shear flows [9]. Couette used the configuration of two cylinders to create a shear flow. As the rotation can be run indefinitely the shear flow can be studied for long periods of time unlike the shear flow between two moving plates. The laminar shear flow produced is now known as Couette flow. At lower rotation rates Couette found the correct value of the viscosity from torque measurements, but at higher speeds he observed a "second regime" now described as turbulent. Mallock's experiment allowed the rotation of the inner as well as the outer cylinder. The results of these experiments gave the correct value of viscosity for small speeds of the outer cylinder but stated that if the inner cylinder was rotated "the motions seems essentially unstable at all speeds".

Then in 1923 Sir Geoffrey Taylor [4] achieved the first success in the theory of hydrodynamic stability for any system: he observed and calculated by linear stability analysis the critical speed at which the flow between two cylinders with the inner cylinder rotating loses its regularity. He demonstrated both experimentally and theoretically the formation of a toroidal vortex system. He summed up the agreement between the experiments and theory with:

> ...the instability made its appearance at a certain speed in every case it was expected and in no case when it was not.

These laminar vortices, now known as Taylor vortices, occur in pairs and are evenly spaced with a definite periodicity. In each vortex the fluid flows in paths that are spiral around the torus with the direction of the spiral reversing in the other vortex. The boundaries between each vortex are flat and the flow is steady. This is shown schematically in figure 1.4.

The critical speed, for the case of infinite length, at which these vortices form, is dependent upon the radius and gap of the cylinders. The non-dimensional parameter which defines the flow regimes is known as the Taylor number and can be defined for the small gap case as

$$Ta = Re^2 \frac{d}{R_1} \tag{1.1}$$

where Re is the Reynolds number based on gap width,

$$Re = \frac{U_1 d}{\nu} \tag{1.2}$$

where d is the gap width, R_1 is the inner radius, U_1 is the rotational speed at the surface of the inner cylinder and ν is the kinematic viscosity. The Taylor number at which these vortices first appear is known as the critical Taylor number, Ta_c.

As the Taylor number increases further, the flow ceases to be steady and undergoes a sequence of bifurcations into more complex vortical structures. During the first step the vortices are clearly present but the boundary between them produces a wavy shape; this is known as wavy vortex flow. This wavy vortex flow then bifurcates so that the waves slowly revolve around the cylinder. If the Re is further increased the wavy boundary oscillates up and down as well as rotating (like ponies on a merry-go-round) [7] this is known as modulated wavy vortex flow. As the Re is increased further the flow undergoes a rapid sequences of bifurcations to less distinguishable states until the flow becomes turbulent. This final phase of the transition is sometimes described as wavy turbulence. If the Ta is again increased the Taylor vortices reform upon the turbulent flow. This state is known turbulent Taylor vortex flow. This is unusual as the coherent patterns of the stable vortices are coexisting with the chaos of turbulent flow. If both or either the inner and outer cylinder are allowed to rotate in any direction at any speed, then a huge variety of flows can be produced such as twisted, braided and helical vortices. Some of the possible pattern formations are shown in figure 1.5.[‡][§].

To simplify the problem of symmetry breaking in Taylor-Couette flow only mirror symmetry is discussed here; further details using other symmetry transformations are discussed by Stwart & Golubitsky [7]. Considering the case with the inner cylinder rotating, the initial Couette flow

---

[‡] Taken from figure 1, Andereck et al. [10] with permission obtained from J. Fluid Mechanics, Cambridge University Press.

[§] R_0 and R_1 are respectively the Reynolds number of the inner and outer cylinder

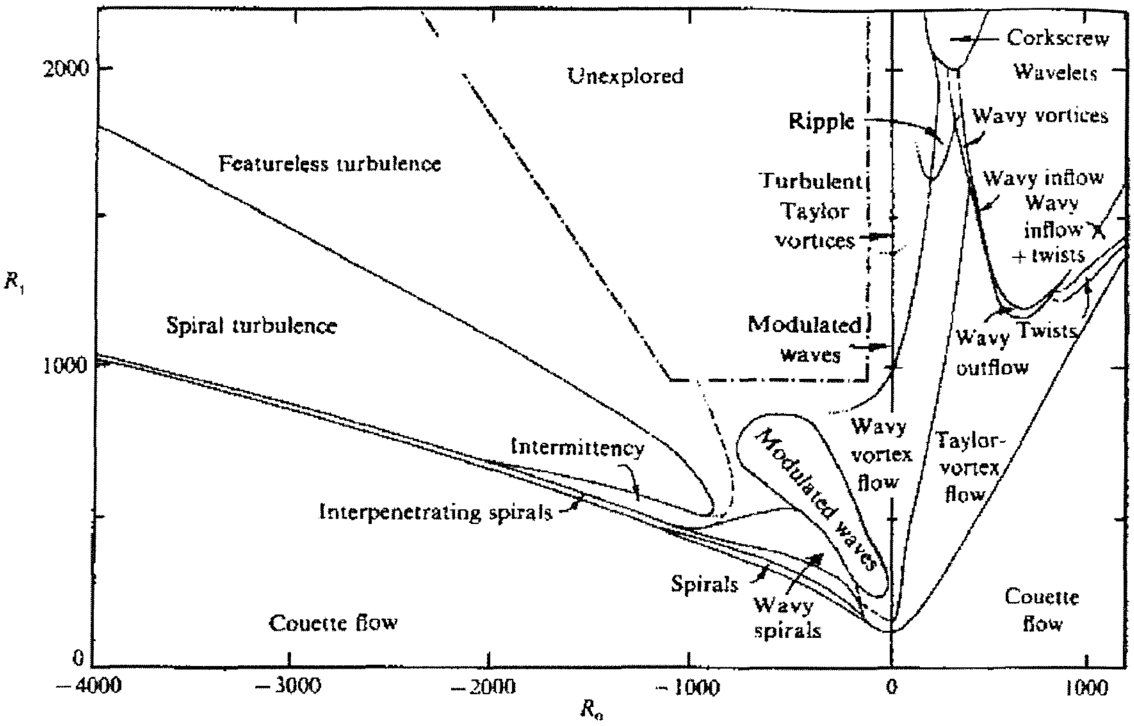

Figure 1.5: Regimes observed in flow between independently rotating concentric cylinders. Dashed lines indicate the transition boundaries that are difficult to establish from visual observation alone since there is no abrupt change in the appearance. Dotted lines indicate the expected, but not yet observed, continuation of several boundaries. (This set of experiments were for a $d/R_1 = 0.18$)

possesses infinite sets of mirror symmetries both in radial planes and lateral planes across the diameter. Upon the formation of Taylor vortices the infinite axial mirror symmetry is broken with a series of static planes of symmetry between each vortex. When wavy vortices are formed there exists no mirror symmetry in radial planes and the circumferential structure is broken by a finite number (dependent upon the number of waves) of lateral planes of symmetry across the diameter. When the flow is further bifurcated, no mirror symmetry exists, complex states are formed, and other types of symmetry are broken to a greater and greater extent until the flow is said to be turbulent. Thus, the Taylor-Couette system of bifurcation and pattern formation towards chaotic flow, can be thought of as a series of symmetry breaking steps.

When turbulent Taylor vortices are formed, symmetry appears to form from chaos but this is not exact. By averaging the turbulence, comparable to taking a Reynolds averaged solution [6], the mean turbulent Couette flow can be thought of possessing the initial mirror symmetry states of the laminar Couette flow. The formation of turbulent Taylor vortices can then be described as the symmetry breaking akin to the formation of the Taylor vortices. This raises the question concerning the existence of wavy turbulent Taylor vortices. Barcilon *et al.* [11] and Smith *et al.* [12] have both suggested that turbulent Taylor vortices break down to featureless turbulence. More recently Parker *et al.* [13] have shown experimentally, using laser doppler velocimetry, LDV, that turbulent Taylor vortices exist at Taylor Numbers around a thousand times higher than that of Smith *et al.*'s work.

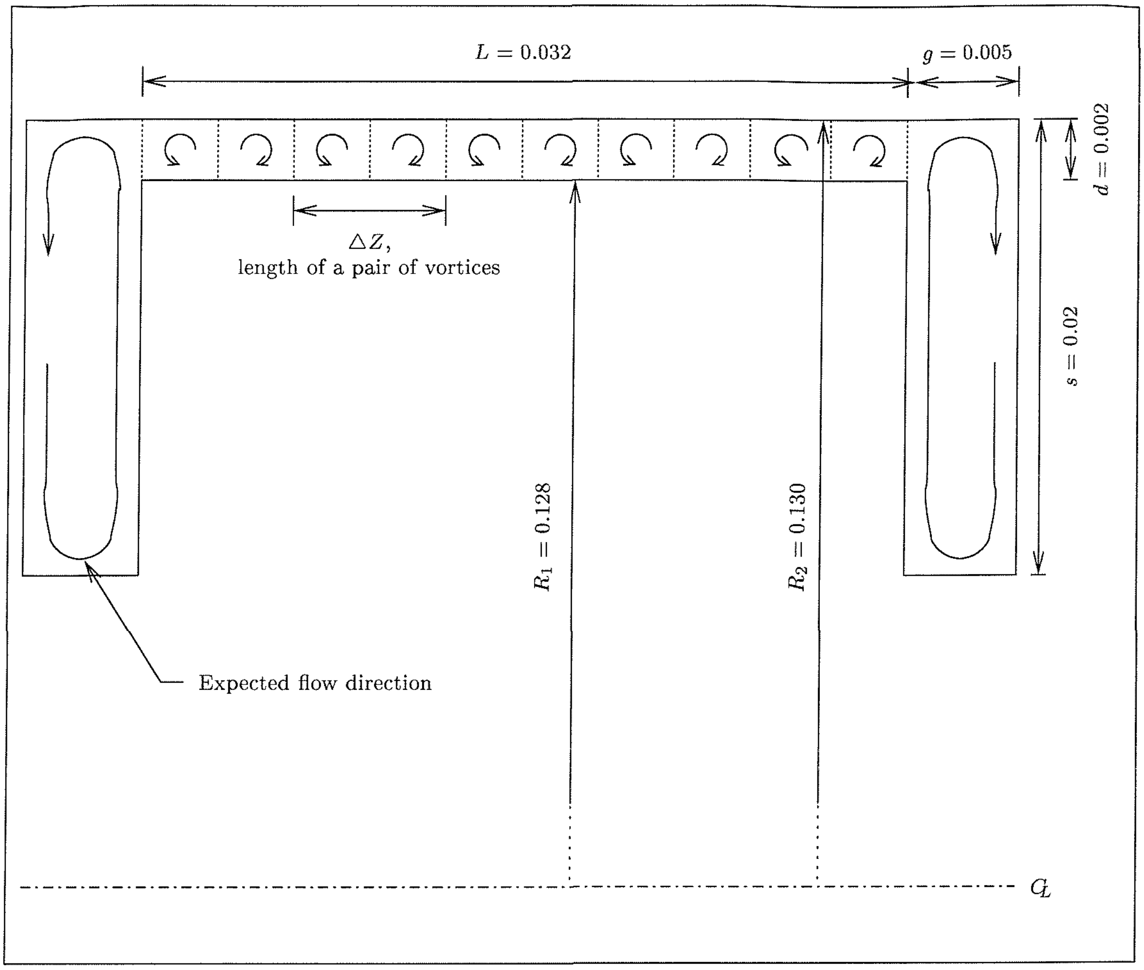

Figure 1.6: Schematic showing the size of the domain under consideration in metres

§1.4 The Domain

Based on this general background information it is reasonable to speculate that in the "region of interest" there will be a number of pairs of turbulent Taylor vortices along the the radial gap and with an end vortex in each of the axial end gaps. The domain as used in the first prototype electrical thruster is presented in figure 1.6. This figure shows the dimensions used throughout the thesis and are only approximately correct for reasons of confidentiality. For the study of the effect of radius ratio, the radial gap, d, was varied between 2mm to 16mm. The maximum operating speed of the thruster unit is about 1500 rpm. Based on a 2mm gap this corresponds to $Re = 5 \times 10^4$.

§1.5 Overview of the Thesis

The chapters of this thesis are structured as follows:

CHAPTER 2: The theoretical consideration of laminar Taylor-Couette flow and the definition of Taylor number is presented. This is followed by considerations of eddy-viscosity approximation to turbulence, the effects of boundary layer, curvature and rotation. The empirical torque equations and a review of the work on Taylor and Görtler vortices is then given. Based upon the literature review predictions are then presented for the thruster unit.

CHAPTER 3: The design of an experimental facility to study Taylor vortices is presented. This is followed by a discussion of the modifications made towards commissioning the experimental rig. The results from a series of torque measurements are then presented. This is followed by a discussion of bubble visualisation study and the development of a novel method of vortex identification.

CHAPTER 4: Presents laminar flow modelling of Taylor vortices including discussion of the effects of the end boundary conditions on the vortex properties. A detailed study of the effect of vortex length on the vortex strength chapter and skin friction is evaluated.

CHAPTER 5: One turbulent Taylor vortex is modelled using the low Reynolds number k-ω model. The effect of Taylor number is demonstrated and the transition to wall driven turbulence is evaluated. The effects of Taylor vortex aspect ratio are also presented.

CHAPTER 6: Further work extending the turbulence modelling to the full thruster geometry is presented with a comparison with the experimental work. The start-up problem is then presented as a 2-D DNS calculation demonstrating the evolution of Taylor vortices from Görtler vortices.

CHAPTER 7. A brief summary of all the work presented and the finding are given. From this recommendations for the electrical thruster and other similar rotating machinery are presented. This is followed by recommendations for the directions for further studies into Turbulent Taylor vortices.

CHAPTER

2

Expected Flow Regimes and Torque Prediction

§2.1 Introduction

The stability of a Couette flow was first studied using linear theory by G.I. Taylor. A summary of his early work and extensions can be found in Chandresekhar's book "Hydrodynamic and Hydromagnetic stability" [14]. Recent reviews of the research conducted on linear and non-linear theory can be found in a review by DiPrima & Swinney [9] and in two books, one by Koshchmieder [15] and the other by Chossat & Ioose [16].

This chapter is concerned firstly with theoretical considerations and the various expressions for Taylor number found in the literature. This is followed by background discussion on turbulence, boundary layers, curvature, rotation effects. A discussion of semi-empirical torque analysis precedes a general review of including in particular turbulent Taylor vortices. The review is concluded in way of predictions for the thruster unit.

§2.2 Theoretical Considerations

§2.2.1 Laminar Taylor-Couette flow

The linear theory of Taylor-Couette flow is based on the Navier-Stokes equations [6]. For incompressible conditions the Navier-Stokes equations can be represented as

$$\frac{\partial u_i}{\partial t} + \underbrace{u_j \frac{\partial u_i}{\partial x_j}}_{\text{convection}} = \underbrace{-\frac{1}{\rho}\frac{\partial p}{\partial x_i}}_{\substack{\text{pressure}\\ \text{gradient}}} + \underbrace{\nu \frac{\partial^2 u_i}{\partial x_j \partial x_j}}_{\text{viscosity}} \tag{2.1}$$

where u is the velocity in the field, x is the spatial coordinate and the subscripts i and j symbolise the direction in the field. Due to incompressibility the continuity equation is,

$$\frac{\partial u_i}{\partial x_i} = 0. \tag{2.2}$$

Expanding equation 2.1 fully in polar co-ordinates, see Appendix A, taking r, θ, z and with u_r, u_θ, u_z for the velocity components, the equation then becomes;

$$\begin{aligned}
\frac{\partial u_r}{\partial t} + u_r\frac{\partial u_r}{\partial r} + \frac{u_\theta}{r}\frac{\partial u_r}{\partial \theta} + u_z\frac{\partial u_r}{\partial z} - \frac{u_\theta^2}{r} &= -\frac{1}{\rho}\frac{\partial p}{\partial r} \\
&\quad + \nu\left\{\frac{\partial^2 u_r}{\partial r^2} + \frac{1}{r}\frac{\partial u_r}{\partial r} + \frac{\partial^2 u_r}{\partial z^2} - \frac{u_r}{r^2} + \frac{2}{r^2}\frac{\partial v_\theta}{\partial \theta}\right\}, \\
\frac{\partial u_\theta}{\partial t} + u_r\frac{\partial u_\theta}{\partial r} + \frac{u_\theta}{r}\frac{\partial u_\theta}{\partial \theta} + u_z\frac{\partial u_\theta}{\partial z} - \frac{u_r u_\theta}{r} &= -\frac{1}{\rho r}\frac{\partial p}{\partial \theta} \\
&\quad + \nu\left\{\frac{\partial^2 u_\theta}{\partial r^2} + \frac{1}{r}\frac{\partial u_\theta}{\partial r} + \frac{\partial^2 u_\theta}{\partial z^2} + \frac{2}{r^2}\frac{\partial u_r}{\partial \theta} - \frac{u_\theta}{r^2}\right\}, \\
\frac{\partial u_z}{\partial t} + u_r\frac{\partial u_z}{\partial r} + \frac{u_\theta}{r}\frac{\partial u_z}{\partial \theta} + u_z\frac{\partial u_z}{\partial z} &= -\frac{1}{\rho}\frac{\partial p}{\partial z} \\
&\quad + \nu\left\{\frac{\partial^2 u_z}{\partial r^2} + \frac{1}{r}\frac{\partial u_z}{\partial r} + \frac{\partial^2 u_z}{\partial z^2}\right\}.
\end{aligned} \tag{2.3}$$

The continuity equation becomes,

$$\frac{\partial u_r}{\partial r} + \frac{u_r}{r} + \frac{1}{r}\frac{\partial u_\theta}{\partial \theta} + \frac{\partial u_z}{\partial z} = 0. \tag{2.4}$$

For steady state flow, $\frac{\partial}{\partial t} = 0$, and assuming that the flow is symmetrical and 2D then, $\frac{\partial}{\partial \theta} = 0$, $u_r = u_z = 0$, $\frac{\partial p}{\partial \theta} = \frac{\partial p}{\partial z} = 0$. Applying $V_\theta = u_\theta = f(r)$ to this symmetrical flow the equations of motion hence reduce to,

$$\frac{V_\theta^2}{r} = \frac{1}{\rho}\frac{\partial p}{\partial r}, \tag{2.5}$$

and

$$\frac{\partial^2 u_\theta}{\partial r^2} + \frac{1}{r}\frac{\partial u_\theta}{\partial r} - \frac{u_\theta}{r^2} = 0. \tag{2.6}$$

Thus the velocity field is

$$V_\theta = Ar + \frac{B}{r}, \tag{2.7}$$

where A and B are constants determined from the boundary conditions; $V(R_1) = \Omega_1 R_1$ and $V(R_2) = \Omega_2 R_2$. Where Ω_1 and Ω_2 denote the rotational speed of the inner and outer cylinder, respectively. R_1 and R_2 are the radius of the inner and outer cylinder, respectively. Hence,

$$A = \frac{R_1^2\Omega_1 - R_2^2\Omega_2}{R_1^2 - R_2^2} = -\Omega_1\frac{\eta^2 - \varpi}{1 - \eta^2} \tag{2.8}$$

and

$$B = \Omega_1\frac{R_1^2(1 - \varpi)}{1 - \eta^2} \tag{2.9}$$

where, $\varpi = \frac{\Omega_2}{\Omega_1}$ and $\eta = \frac{R_1}{R_2}$.

Linearising the Navier-Stokes equations 2.3 and imposing small perturbations in the form $(u'_r, V_\theta + u'_\theta, u'_z)$ and $p = p + p'$ where V_θ is given by equation 2.7 where u'_r, u'_θ and u'_z are small functions of r, z and t. Applying these constraints and assuming that for a symmetrical flow $\frac{\partial}{\partial\theta} = 0$, the equations 2.3 then becomes:

$$\begin{gathered}
\frac{\partial u'_r}{\partial t} - \frac{2Vu'_\theta}{r} = -\frac{1}{\rho}\frac{\partial p'}{\partial r} + \nu\left\{\frac{\partial^2 u'_r}{\partial r^2} + \frac{1}{r}\frac{\partial u'_r}{\partial r} + \frac{\partial^2 u'_r}{\partial z^2} - \frac{u'_r}{r^2}\right\}, \\
\frac{\partial u'_\theta}{\partial t} + \left(\frac{dV}{dr} + \frac{V}{r}\right)u'_r = \nu\left\{\frac{\partial^2 u'_\theta}{\partial r^2} + \frac{1}{r}\frac{\partial u'_\theta}{\partial r} + \frac{\partial^2 u'_\theta}{\partial z^2} - \frac{u'_\theta}{r}\right\}, \\
\frac{\partial u'_z}{\partial t} = -\frac{1}{\rho}\frac{\partial p'}{\partial z} + \nu\left\{\frac{\partial^2 u'_z}{\partial r^2} + \frac{1}{r}\frac{\partial u'_z}{\partial r} + \frac{\partial^2 u'_z}{\partial z^2}\right\}
\end{gathered} \tag{2.10}$$

and the continuity equation is,

$$\frac{\partial u'_r}{\partial r} + \frac{u'}{r} + \frac{1}{r}\frac{\partial u'_\theta}{\partial r} + \frac{\partial u'_z}{\partial z} = 0. \tag{2.11}$$

The boundary conditions for these equations are $u'_r = u'_\theta = u'_z = 0$ at $r = R_1$ and $r = R_2$. Taylor eliminated the pressure from these equations and used the Bessel-Fourier series to solve the problem. To reduce the numerical problem a narrow gap approximation was made, i.e. the gap between the cylinders, $d = R_2 - R_1$ was much smaller than the radius hence, $\eta \to 1$. After several calculation steps see reference [4], Taylor arrived at an equation for the critical condition of vortex instability of Couette flow.

$$Ta_c = 1708\left(1 + \frac{0.652(1-\varpi)(1-\eta)}{1+\varpi}\right) \tag{2.12}$$

where Ta_C is know as the critical Taylor Number. This equation is applicable for $0 \leq \varpi \leq 1$ and $1 - \eta \ll 1$.

In the literature several different Taylor numbers have been presented, dependent upon the problem. Koshmieder [17] and Roberts [18] have defined a Taylor number for both cylinders rotating as,

$$Ta = \frac{2\eta^2}{1-\eta^2}\frac{\Omega^2 d^4}{\varpi^2}, \tag{2.13}$$

The same equation has been represented, for a stationary cylinder for the large gap case as,

$$Ta = \frac{2(1-\eta)}{1+\eta}Re^2. \tag{2.14}$$

which is used by Smith *et al.* [12]. Both equations 2.13 and 2.14 reduce to,

$$Ta = \frac{2d}{2R_1 + d}Re^2. \tag{2.15}$$

This equation reduces to the the small gap case, $\eta \to 1$, given in equation §1.3 where the Taylor number is normally defined as

$$Ta = \frac{R_1\Omega^2 d^3}{\nu^2} = \frac{d}{R_1}Re^2. \tag{2.16}$$

used throughout this thesis.

Chandrasekha [14] reformulated Taylor's work and extended it to all radius ratios. The work showed that by using linear theory the instability between two cylinders with the inner cylinder rotating is governed by

$$Ta = \frac{2}{1+\eta} \cdot \frac{(\pi^2+a^2)^3}{1 - 16a\pi^2 \cosh^2(a/2)\Big((\pi^2+a^2)^2(\sinh a + a)\Big)} \tag{2.17}$$

where, a is the Taylor vortex wave number.

This equation has a minimum, which refers to the critical Taylor Number, Ta_c at which the vortices are formed. At this critical number, there is an associated wave number a_c. This wave number is given by $\lambda = 2\pi/a$, where λ is a non-dimensional size of a pair of Taylor vortices, $\lambda = \triangle Z/d$. $\triangle Z$ signifies the length of a pair of vortices.

Davey [19] has extended the work further and developed a perturbation expansion for the full field velocity profile. This velocity profile is only accurate near the transition from circular Couette flow to Taylor vortex flow.

§2.2.2 Turbulent Flow

The need for turbulence models arises as a result of the application of a statistical averaging to the Navier-Stokes equations, this was first introduced over a century ago by Reynolds in 1894. The simplistic way of considering the averaging process is by studying a single point and single time averages [6]. By doing this the essential information of the flow can be considered. Thus the velocity, u_i and pressure, p of the fluid at any point can be represented by allowing the following statistical splitting,

$$u_i = \overline{u_i} + u_i' \tag{2.18}$$

and

$$p = \overline{p} + p' \tag{2.19}$$

where the mean values $\overline{u_i}$ and $\overline{p}$ are known as point averages. This is equivalent to averaging a series of independent experiments with the same flow conditions. In this case u_i' and p' are the fluctuating velocity and pressure components respectively.

A turbulent flow can therefore be considered as an ensemble of different solutions of the Navier-stokes equation 2.1. As equation 2.2 is linear its average is closed, thus

$$\frac{\partial \overline{u_i}}{\partial x_i} = 0 \tag{2.20}$$

Subtracting equation 2.20 from 2.2 gives

$$\frac{\partial u_i'}{\partial x_i} = 0 \tag{2.21}$$

for the fluctuations. Therefore, both the mean and fluctuating velocities satisfy the incompressible equations.

Averaging the Navier-Stokes equations produces

$$\frac{\partial \overline{u_i}}{\partial t} + \overline{u_j}\frac{\partial \overline{u_i}}{\partial x_j} + \overline{u'_j\frac{\partial u'_i}{\partial x_j}} = -\frac{1}{\rho}\frac{\partial \overline{p}}{\partial x_i} + \nu\frac{\partial^2 \overline{u_i}}{\partial x_j \partial x_j} \tag{2.22}$$

Equation 2.22 can be rewritten by shifting the term

$$\overline{u'_j\frac{\partial u'_i}{\partial x_j}} = \frac{\partial}{\partial x_j}\left(\overline{u'_i u'_j}\right). \tag{2.23}$$

Hence equation 2.22 becomes

$$\frac{\partial \overline{u_i}}{\partial t} + \overline{u_j}\frac{\partial \overline{u_i}}{\partial x_j} = \frac{1}{\rho}\frac{\partial}{\partial x_i}\left[\underbrace{-\overline{p}\delta_{ij}}_{\substack{\text{Mean}\\ \text{pressure}\\ \text{stress}}} + \underbrace{\mu\left(\frac{\partial \overline{u_i}}{\partial x_j} + \frac{\partial \overline{u_j}}{\partial x_i}\right)}_{\substack{\text{Mean viscous}\\ \text{stress}}} \underbrace{-\rho\overline{u'_i u'_j}}_{\substack{\text{Reynolds}\\ \text{stress}}}\right]. \tag{2.24}$$

Equation 2.24 is known as the Reynolds averaged Navier-Stokes equation (RANS). It contains a Reynolds stress term, $-\rho\overline{u'_i u'_j}$, although this is not a real part of the flow it is the only part of the equation that describes the turbulence. This tensor determines how the fluctuating part of the flow interacts with the forces of the mean flow. For fully developed turbulent flow,

$$\rho\left\|\overline{u'_i u'_j}\right\| \gg \mu\left\|\frac{\partial \overline{u_i}}{\partial x_j} + \frac{\partial \overline{u_j}}{\partial x_i}\right\| \tag{2.25}$$

where the Reynolds stresses can easily be as much as 500 times larger than the mean viscous stresses.

Due to the Reynolds stress terms in equation 2.24 it is not possible to solve the turbulent flow without knowing the averages of the fluctuations in the turbulent field. A method of closing the equations is to express the Reynolds stress tensor in terms of the flow itself by introducing a term know as the eddy viscosity, ν_T. This use of an eddy viscosity as known as the Boussinesq assumption [6]. Thus the Reynolds stress tensor can be represented as,

$$-\overline{u'_i u'_j} = -\frac{1}{3}\overline{q'^2}\delta_{ij} + \nu_T\left(\frac{\partial \overline{u_i}}{\partial x_j} + \frac{\partial \overline{u_j}}{\partial x_i}\right) \tag{2.26}$$

where $\overline{q'^2} = 3\overline{u'^2} = \overline{u'_i u'_i}$ is the mean-squared turbulent velocity. This can also be expressed in terms of the turbulent kinetic energy, k per unit mass as

$$k = \frac{1}{2}\left(\overline{u'_i u'_i}\right) = \frac{1}{2}\left(\overline{u'^2_1 + u'^2_2 + u'^2_3}\right). \tag{2.27}$$

The main problem with this type of approximation is that it implies that the three components of turbulent velocity have equal mean-squared values. Combining equation 2.26 and 2.27 Reynolds stress tensor becomes,

$$-\overline{u'_i u'_j} = -\frac{2}{3}k\delta_{ij} + \nu_T\left(\frac{\partial \overline{u_i}}{\partial x_j} + \frac{\partial \overline{u_j}}{\partial x_i}\right) \tag{2.28}$$

§2.2.3 Boundary Layers

In the literature, various wall regions and layers defining properties of boundary layers have been proposed. The most common method is to consider the total shear stress which can be contributed as the sum of the viscous stresses $\mu\frac{du_r}{dy}$ and the Reynolds stresses $-\rho\overline{u_i'u_j'}$. For the case of Taylor Couette flow n is the perpendicular distance from the cylinder wall ($n = r - R_1$) and u_r is the radial velocity. Then at the wall, the shear stress is entirely due to the viscous contribution and hence is defined as

$$\tau_w = \mu\left(\frac{d\overline{u_\theta}}{dn}\right)_{n=0} \tag{2.29}$$

which is the average force per unit area acting in the streamwise azimuthal direction. Using the shear stress equation 2.29 a viscous scale for the friction velocity can be denoted by

$$u^* = \sqrt{\frac{\tau_w}{\rho}}. \tag{2.30}$$

In the region where the flow is dominated by viscous stresses the distance from the wall can be measured in viscous lengths (wall units) and is defined as

$$n^+ = \frac{u^* n}{\nu}. \tag{2.31}$$

In the region dominated by both the viscous and Reynolds stress, a log law is normally defined. This is known as the logarithmic law of the wall due to von Kármán where a normalised velocity, $u^+ = u_\theta/u^*$ is defined as

$$u^+ = \frac{1}{\kappa}\ln n^+ + B, \tag{2.32}$$

where B is a constant. In the literature there are several variations on these constants but generally the constants can be taken to within 5% of

$$\kappa = 0.41, \quad B = 5.2.$$

Using "Prandtl's mixing-length hypothesis." a mixing length, ℓ_m can be expressed in terms of the frictional velocity as,

$$\ell_m = \frac{\mu_T}{u^*}. \tag{2.33}$$

Table 2.1 describes the boundary layer properties for channel flow and from analysis by Pope [6], who compared various direct numerical simulations and experiments. Although this may not be exact for Taylor-Couette flow it gives an indication of what to expect from the numerical simulations. Further details of how the von Kármán boundary layer is applied to RANS solutions is discussed in several books, for example see [6, 5].

§2.2.4 Effects of Curvature

When the mean angular momentum increases, between stationary boundaries, with increasing radius of curvature, the turbulence is suppressed, in this case the curvature is referred to as

Region	Location	Defining property
Inner layer	$n/\delta < 0.1$	U is determined by u_τ and n^+.
Viscous wall region	$n^+ < 50$	The viscous contribution to the shear stress is significant.
Viscous sublayer	$n^+ < 5$	The Reynolds shear stress is negligible compared with the viscous stress.
Outer layer	$n^+ > 50$	The direct effects of viscosity on U is negligible.
Overlap region	$n^+ > 50$, $n/\delta < 0.1$	Region of overlap between the inner and outer layer.
Log-law region	$n^+ > 30$, $n/\delta < 0.3$	The log-law holds.
Buffer layer	$5 < n^+ < 30$	The region between the viscous sublayer and the log-law region.

Table 2.1: Wall regions, layers and their defining properties

stabilising. If the mean angular momentum decreases with increasing radius of curvature, the turbulence would be enhanced and this would be described as destabilising. Thus a convex wall would have a stabilising influence on the turbulent boundary layer while the concave wall would have a destabilising influence.

Wilcken's experimental work in the 1930's, referenced in Mosser & Moins work [20] suggested that changes in the mean flow properties were much larger than predicted by "mixing length" hypothesis. Wilcken also observed that the speed of the development of boundary layers is affected by the curvature. Those on concave surfaces grow faster than flat boundaries and convex are slower to develop.

Sufficiently close to the wall, the mean-velocity profiles have been demonstrated to obey the "law of the wall" hypothesis. At larger distances from the wall, the mean velocity of a convex wall layer exceeds that of the flat-wall profile and vice versa for the concave wall. Changes in turbulent intensities have been shown to be around 10-20% with again increases on the concave wall and decreases on convex walls.

Based on a curvature parameter, δ/R, Hoffmann & Bradshaw cited in [20] stated that for weak curvature deviations in the velocity profile occur beyond the logarithmic region. They defined weak curvature as $\delta/R \approx 0.01$. Where δ is the boundary layer thickness or for closed channel half the channel width. For Taylor-Couette flow R can be defined as R_1 and $\delta = g/2$. This curvature parameter is compared with the radius ratio, η in the table below. It should also be noted that small changes in mean velocity statistics are exacerbated for higher order statistics, such as turbulent production terms.

$\frac{\delta}{R}$	$\eta = \frac{R_1}{R_2}$
0.100	0.833
0.050	0.909
0.010	0.980
0.005	0.990

Mosser & Moin [20] studied low Reynolds number, mildly curved, turbulent channel flow. They used a spectral method to simulate a direct numerical solution, DNS, of the Navier-Stokes equations. Their numerical model was for $\delta/R = 0.0127$ and at $Re = 5980$ based on the gap width. They demonstrated the formation of unsteady Taylor-Görter type vortices in the curved channel. For this case the mean velocities are in excellent agreement for $n^+ < 20$ with plane channel flow. When $n^+ > 20$ the mean velocities for the convex wall lies below and the concave wall lies above. The turbulent intensities were shown to be generally smaller than the computations, again with the convex side being lower. The Taylor-Görter vortices were directly responsible for approximately half of the difference in the Reynolds shear stress between the two sides and half the difference between the wall shear stresses.

More recent studies have been made by Kobayahi & Maekawa on Turbulent flow accompanied by Taylor-Görtler vortices in a 2-D curved channel [21]. The results conclude that the k-ε model was useful for calculating the mean vortex contours, but has no capability for predicting turbulent stress distributions in detail. This result is not surprising as Taylor-Görtler vortices are themselves unsteady and generally such high order statistics are not normally predicted well by RANS solutions. These results do however contradict Mosser & Moin's work that state that RANS solution can not model Taylor-Görtler vortices.

§2.2.5 Effect of Rotation

If sufficient strong rotation is produced the turbulent dynamics can be considerably altered. In particular the anisotropic structure of the turbulent eddies will tend to be elongated in the axis of the rotation. The importance of the rotation for large scales of turbulence is determined by the Rossby number, $Ro = u'/\Omega\ell$, where Ω is the angular velocity of the rotation and ℓ is the eddy length scale.

A large Rossby number corresponds to small effects of rotation and if it is sufficiently high it is reasonably to neglect rotation altogether. The same can be applied if a Rossby number is very small since this would mean that there is strong rotation and hence the large scales of turbulence do not have time to react in the rotation period. The effect of rotation alters the pressure to include the centrifugal force, $\hat{p} = p - \rho\Omega r^2/2$ and adds an extra Coriolis force, $2\Omega u_i$. Rotation also tends to reduce the decay of turbulence by inhibiting the cascade of energy to the small scale eddies and hence time required for the dissipation in the axis of rotation.

For a Taylor Couette flow, assuming that u' is 10% of the speed of the inner cylinder then $Ro = R_1/10\ell$. For the thruster unit where $R_1 = 0.128$ and $d = 0.002$:

ℓ	Ro
d	6.4
$d/5$	32
$d/10$	64
$d/50$	320

This effect of increasing the scale of the eddies in the axial direction, z, for the case of turbulent Taylor-Couette flow, seems fairly improbable as Taylor vortices which would be acting perpendicular to their formation. However the Taylor vortices themselves have a rotational component, hence an associated Rossby number, therefore turbulent eddies travelling in the spiral path inside the Taylor vortex could be affected and thus be elongated in the azimuthal direction.

§2.3 Torque Analysis

Several attempts have been made to fit semi-empirical equations to estimate the frictional torque in the Taylor-Couette system. The two most commonly used are due to Wendt given in [22] and Bilgen & Bilgous [23]. Both of these sets of equations are based on a power law for Reynolds number.

Wendt's empirical equations are

$$G = \begin{cases} 1.45\left(\frac{\eta^{3/2}}{(1-\eta)^{7/4}}\right)Re^{1.5} & \text{for } 4\times 10^{2} < Re < 1\times 10^{4} \\ 0.23\left(\frac{\eta^{3/2}}{(1-\eta)^{7/4}}\right)Re^{1.7} & \text{for } 1\times 10^{4} < Re < 1\times 10^{5} \end{cases} \tag{2.34}$$

$$\text{where, } G = \frac{M}{\rho\nu^{2}L}.$$

and M is the moment acting on the inner cylinder and L is the length of the cylinder.

Bilgen & Bilgous empirical equations are

$$C_M = \begin{cases} 10\left(\frac{d}{R_1}\right)^{0.3}Re & \text{for } Re < 64 \\ 2\left(\frac{d}{R_1}\right)^{0.3}Re^{-0.6} & \text{for } 64 < Re < 5\times 10^{2} \\ 1.03\left(\frac{d}{R_1}\right)^{0.3}Re^{-0.5} & \text{for } 5\times 10^{2} < Re < 1\times 10^{4} \\ 0.065\left(\frac{d}{R_1}\right)^{0.3}Re^{-0.2} & \text{for } Re > 1\times 10^{4} \end{cases} \tag{2.35}$$

$$\text{where, } C_M = \frac{M}{1/2\pi\rho\Omega^{2}R_1^{4}L}.$$

The frictional power, $Ps = M\Omega$, is therefore

$$P_s = 1/2\pi\rho C_M\Omega^{3}R_1^{4}L. \tag{2.36}$$

Wendt's Equations can also be expressed in terms of C_M; where,

$$C_M = \begin{cases} 0.923\left(\frac{dR_2}{R_1^{2}}\right)^{0.25}Re^{-0.5} & \text{for } 5\times 10^{2} < Re < 1\times 10^{4} \\ 0.146\left(\frac{dR_2}{R_1^{2}}\right)^{0.25}Re^{-0.2} & \text{for } Re > 1\times 10^{4} \end{cases} \tag{2.37}$$

Bilgen & Bilgous's equations are based on the authors' own experimental data and other data available in Wendt, Taylor [24] and Donnelly [25]. They collected data in the Reynolds numbers range $10 < Re < 1\times 10^{6}$ and the radius ratios range $0.5 < \eta < 0.988$. From this, they deduced four semi-empirical expressions for the skin friction, C_M. The two equations which are relevant to this paper are given in equation 2.35, these equations are given to an accuracy of ±8.35%. From analysis of figure 4 in Bilgen & Bilgous it is clear that the equations will have a slight tendency to either over estimate C_M for low radius ratios or under estimate C_M for high radius ratios.

Other semi-empirical equations have been used to estimate the frictional losses and are based upon the logarithmic relationships such as Yamaha's [26] equation.

$$\begin{aligned} 1/\sqrt{C_F} &= 7.54 + 11.5 \log Re\sqrt{C_F} \\ C_F &= 2C_M \end{aligned} \tag{2.38}$$

Dorfman's solution of the momentum equations for turbulent flow [27] is similar to Yamaha's work and is based on the assumption that u_r, u_z, $\frac{\partial}{\partial\theta}$, $\frac{\partial}{\partial z}$ are negligible. Hence the momentum equations reduce to

$$\frac{V_\theta{}^2}{r} = \frac{1}{\rho}\frac{\partial p}{\partial r}, \tag{2.39}$$

$$\frac{2}{r}\tau_{r\theta} + \frac{\partial \tau_{r\theta}}{\partial r} = 0. \tag{2.40}$$

For axially symmetric motion,

$$\tau_{r\theta} = \mu\left(\frac{\partial u_\theta}{\partial r} - \frac{v_\theta}{r}\right). \tag{2.41}$$

Dorfman [27] rewrote equation 2.41 by introducing the kinematic turbulent viscosity,

$$\tau_{r\theta} = \mu_T\left(\frac{\partial u_\theta}{\partial r} - \frac{v_\theta}{r}\right), \tag{2.42}$$

and assuming the mixing length theory, ℓ_m satisfies the relationship

$$\ell_m = \frac{\mu_T}{v*} = \kappa\frac{(R_2 - r)(r - R_1)}{R_2 - R_1} \tag{2.43}$$

as a method of modeling the turbulence. On the boundary of the sublayer by taking into account the conservation of the moment of frictional forces,

$$v_{1lam} = U - \alpha v_1^* \tag{2.44}$$

$$v_{2lam} = \alpha v_2^* = \alpha v_1^* \frac{R_1}{R_2} \tag{2.45}$$

$$\delta_1 = \frac{\alpha\nu}{v_1^*} \tag{2.46}$$

$$\delta_2 = \frac{\alpha\nu}{v_2^*} = \frac{\alpha\nu R_2}{v_1^* R_1} \tag{2.47}$$

where α is a constant for both cylinders. Applying equations [2.39, 2.42-2.44] it can be shown that frictional resistance can be represented by

$$\begin{aligned} \frac{2\kappa}{\sqrt{C_M}} = \kappa\alpha(1+\eta^2) - (1-\eta)^2 + \ln\left[\left(1 + \frac{Re_r\sqrt{C_M}}{2\alpha}\right)(1-\eta)\right] \\ + \eta^2 \ln\left[(\eta - 1)\left(\frac{Re_r\sqrt{C_M}}{2\alpha} - 1\right)\right] \end{aligned} \tag{2.48}$$

and the velocity profile represented by

$$\frac{R_1}{r}\frac{v_\theta}{V_1}\frac{2\kappa}{\sqrt{C_M}} = \kappa\left(\frac{2}{\sqrt{C_M}} - \alpha\right) + (1-\eta) - (1-\eta)\frac{R_1}{r} - \ln\left(\frac{r-R_1}{r}\right) \\ - \ln\left(1 + \frac{Re_r\sqrt{C_M}}{2\alpha}\right) - \eta^2 \ln\left(\frac{r}{R_2 - r}\frac{R_2 - R_2}{R_1}\right), \tag{2.49}$$

where Re_r is the Reynolds number based on the radius

$$Re_r = \frac{R_1^2\Omega_1}{\nu}. \tag{2.50}$$

§2.4 Review

Although numerous studies of Taylor-Couette flow at low Reynolds numbers have been carried out, see for example DiPrima & Swinney's review [9], most are concerned with the formation of laminar vortices and the various wavy states formed as the flow becomes chaotic. Recent notable work includes particle image velocimetry, PIV, studies of the spatio-temporal character of waveless and wavy Taylor-Couette flow by Wereley *et al.* [28] and a model of mixing and transport in wavy Taylor-Couette flow by Rudolph *et al.* [29]. Vastano et al. [30] used Lyapunov exponent analysis to simulate the transition to chaos in the Taylor-Couette flow.

The non-uniqueness of the Taylor-Couette system has been observed several times in the literature. For example Coles [31] demonstrated that depending upon the initial conditions, in the same test rig, up to 26 distinct stable wavy vortex flow states could be obtained for the same operating conditions. Benjamin *et al.* [32] presented experimental results for 20 different steady laminar Taylor vortex flows in the same apparatus, $\eta = 0.6$, $\Gamma = 12.61$ and $Re = 359$. All the solutions were of [axes symmetric cellular nature] CHECK! and either had different numbers of vortices and or rotation direction. By considering symmetry and multiplicity it was suggested the likelihood of their being at least a further 19 possibilities. These are unstable and consequently not observed. If Re was gradually increased then the same flow with 12 vortices was always observed. Some of the other flows were produced by either sudden starts and or setting Γ to a different ratio and changing it in all steps to $\Gamma = 12.61$.

§2.4.1 Turbulent Taylor Vortices

The first major studies into the formation of turbulent Taylor vortices were carried out by Koschmeider [17, 33, 15]. Koschmeider's experiments revealed some surprising features of the turbulent vortices. Using a long column and a narrow gap, $\eta = 0.89$ it was demonstrated that there is a steady increase of transient features until, $Ta \approx 100Ta_c$. The main transient features were increases in the number of azimuthal waves and a decrease in the axial wave length. From about $100Ta_c$ onwards the behavior of the flow changed drastically and the azimuthal wavenumber now become independent of Ta and the wavelength became dependent upon the initial conditions. For $Ta > 100Ta_c$ the experiments revealed a range of axial wavelengths between $\lambda_{max} = 3.4$ and $\lambda_{min} = 2.4$ due to the sudden starts. This non-uniqueness is typical of turbulent flow. This occurrence of turbulence from around $100Ta_c$ is in agreement with noise

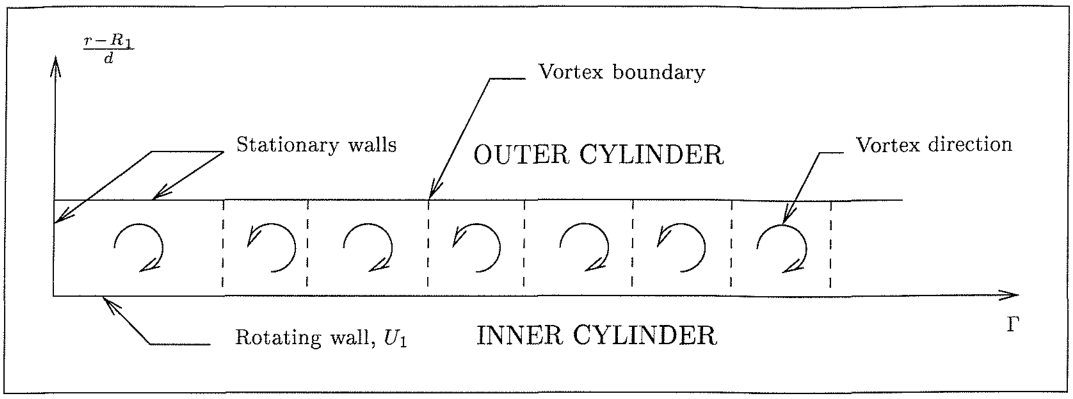

Figure 2.1: Schematic showing the effect of the end wall

in the velocity spectra. This range $100Ta_c < Ta < 1000Ta_c$ is some times known as wavy turbulence.

Another feature of turbulent Taylor vortices is the disappearance of the azimuthal waves. From around $700Ta_c$ it was shown that the vortices are mean and axisymmetrical akin to the initial laminar Taylor vortices. The turbulent vortices have the same independence of wavenumber upon Taylor number and the same dependency upon the startup conditions.

Wereley & Lueptow [34] have measured the azimuthal velocity profile for Taylor vortex, wavy vortex and turbulent Taylor vortex flow between a rotating inner cylinder and a fixed outer cylinder. The test ring had fixed end boundaries and the velocities were measured using Laser Doppler Velocimetry.

More recently turbulent Taylor vortices have been studied at high Reynolds numbers using Laser Doppler Velocimetry [13]. This study used refractive index matching techniques and showed that Taylor Vortices are still present at $Ta = 2.107 \times 10^9$ ($Re = 73440$) for $\eta = 0.672$. They clearly demonstrate that Taylor vortices exist for very high Taylor numbers and that the end wall has a large effect on the vortex sizes, as demonstrated in the illustration, figure 2.1.

From the figures presented but not discussed in the paper, the results establish that the radial and axial intensities have similar ranges but that peaks in azimuthal turbulence intensities were around 2.8 times larger. The peaks for the azimuthal intensities were at the walls of the inner and outer cylinder with a slow decay rate for the vortex outflow at the inner cylinder. These larger intensities could imply that the turbulent eddies are stretched and decay slower in the azimuthal direction. Hence supporting the notion discussed in §2.2.5, that rotational turbulence effects about the centre of the Taylor vortex are more significant than the rotation around the cylinder axis itself.

The maximum radial turbulence intensities are in the middle plane of the vortex outflow from the inner cylinder. The axial turbulence intensities also peak on the outflow, but much closer to the wall and there is also a lower peak at the outer cylinder on the inflow boundary. This clearly demonstrated the importance of modeling the Taylor vortices in order to be able to predict the torque, as the turbulence intensities are strongly influenced by the vortices, whose position is altered by the end walls and as discussed earlier, the startup conditions.

Lathrop *et al.* [22] studied the turbulent flow between concentric cylinders for Reynolds

Taylor-Couette Flow	Rayleigh-Bénard Convection	Characteristics
Taylor Vortices	Bernard Convection	Spatially periodic, symmetric
Wavy Vortices	Oscillation	Temporally oscillating
Modulated or Chaotic Wavy Vortices	Chaos	Quasi-periodic / chaotic
Wavy Turbulence or Fast azimuthal wave mode	Transitional	Still coherent-structural
Soft Turbulence	Soft Turbulence	Non-structural with soft spectrum
Hard Turbulence	Hard Turbulence	Non-structural with hard spectrum

Table 2.2: Transition similarities between Rayleigh-Bénard Convection and Taylor-Couette flow

numbers between $800 < Re < 1.23 \times 10^6$ with a radius ratio of $\eta = 0.7246$. While these experiments reveal no such Reynolds number changes in torque based on a fixed power law akin to that of Bilgen & Bilgous, they did show a hysteretic free transition at a Reynolds number of 1.3×10^4. Above this Reynolds number the experiments suggest that the nature of the flow behaviour is more like that of open-flow systems such as those found in pipes or ducts. Lathrop *et al.*also present the following equations for the laminar sublayer;

$$\frac{\delta_1}{R_1} = 6.32 \left(\eta^{-1} - 1\right)^{2/3} Re^{-2/3} \tag{2.51}$$

and

$$\frac{\delta_2}{R_2} = 8.16 \left(\eta^{-1} - 1\right)^{2/3} Re^{-2/3}, \tag{2.52}$$

where δ_1 is the laminar thickness on the inner cylinder and δ_2 is the corresponding thickness on the outer cylinder.

Takeda [35] performed an experimental study on transitions in rotating Taylor-Couette system by investigating the spatio-temporal velocity field using a ultrasound velocity profile monitor. These experiments provided more evidence for various flow transitions and described the wavy turbulence as the fast azimuthal wave mode. Takaeda decomposed the flow fields using 2-D Fourier transform and this analysis show a clear change in the numer of participating modes classifying the difference between "soft" and "hard" turbulence.

In Rayleigh-Bénard convection there also exists a similar power law transition between the Nusselt and Rayleigh numbers, Ra. [15] At $Ra \sim 4 \times 10^7$ the flow changes from a "soft" turbulence regime to a "hard" turbulence regime, with a corresponding change in scaling exponent. The terms "soft" and "hard" are not commonly used when describing turbulence but come from the context of analysing sepctra, particularly X-rays, where "soft" refers to dominant low energy components and "hard" to dominant high energy components. For these different dominates there will be different associated scaling powers. The similarity in transition states between Taylor-Couette and convection is demonstrated in table 2.2.

The mass transport in turbulent Taylor vortex flow has been studied by Tam *et al.* [36]. They injected a pulse of dye between two cylinders with a rotating inner cylinder. The measurements were for radius ratios $0.494 < \eta < 0.875$ They revealed that transport in the axial direction could be modeled well using a one-dimensional diffusion process. They found a linear dependence of the effective axial diffusion coefficient on the vortex wavelength and Reynolds number.

Turbulent Taylor Vortex flow in a centrifugal rotor* was studied both experimentally and computationally by Wild *et al.* [37]. They studied two radius ratios, $\eta = 0.941$ and 0.974 and Reynolds numbers, $1.5 \times 10^4 < Re < 4 \times 10^4$. For their test cases the experimental results were in relatively good agreement with the semi-empirical expressions of Wendt and Bilgen & Bilgous The computational study employed the standard k-ε model [38] which over predicted their experimental results by an order of 10% or higher. Computations were also performed using other turbulence models with wall functions; the RNG model [39] was within 2% of the standard k-ε model and the Reynolds Stess Model, RSM [40] was 40% higher than the k-ε model. The RNG model without a wall function was also 40% higher than the k-ε model. These results are surprising due to the fact that the RNG and RSM models are generally thought to be more suitable for flows with curvature and rotation than the standard k-ε model [41]. This is possibly due to the fact that the turbulent coefficients are more sensitive and that these models have not been tuned to suit the Taylor-Couette system.

Atkhen *et al.* [42] studied Taylor-Couette flow with an imposed axial flow and a upper free surface in the turbulent Ta regime, $\eta = 0.88$, $Ta \approx 5 \times 10^5$. At high enough Ta bubbles created near the free surface are distributed throughout the test section and this allowed them to study both spatial and temporal properties of the flow with a digital high speed linear camera. These experiments observed bubbles at every pair of Taylor vortices, this result is confirmed by a spectral calculation showing the pressure field at, $Ta = 152$ indicating that the lowest pressure is at the vortex outflow from the inner cylinder. Bubble capture and migration from a free surface has also been studied by Djéridi *et al.* [43] for $\eta = 0.857$. Due to the small size of the rig ventilation occurred for laminar wavy Taylor vortices. These experiments showed that after time bubble grouping between every vortex along the full length of the cylinder.

§2.4.2 Görtler Vortices

Barcilon *et al.* [11] showed the formation of "herring-bone" like streaks in photographs of turbulent Taylor vortices. They suggested that these patterns were due to the existence of Görtler vortices. The analysis was based on the following steps. Görtler vortices are defined by the parameter:

$$Go = \left(\frac{U_m \delta}{\nu}\right)^2 \frac{\delta}{r_{rc}}, \tag{2.53}$$

Where Go is known as the Görtler number, δ is the boundary layer thickness and r_{rc} is the radius of curvature. Assuming that the boundary layer thickness, δ to be the momentum thickness

---

*The authors were interested in the windage losses in a Centrifugal Reverse-Osmosis machine for sea water desalination.

δ_m. Then,

$$\delta_m = \left(\frac{Go\, \nu^2 r_{rc}}{U_m^2} \right)^{\frac{1}{3}}. \tag{2.54}$$

As $U_m \approx \frac{1}{2}\Omega_1 R_1$ is approximately true for the narrow gap case. Thus,

$$Go = \frac{R_1^2 \Omega_1^2 \delta_m^3}{4\nu^2 r_{rc}} = \frac{Ta}{4} \left(\frac{\delta_m}{d} \right)^3 \frac{R_1}{r_{rc}}. \tag{2.55}$$

The minimum critical value of Go is near 0.09 [11]. Then by setting $Go = Go_c = 0.09$ in equation 2.55 becomes

$$\frac{\delta_m}{d} = \left(\frac{0.36}{Ta} \frac{r_{rc}}{R_1} \right)^{1/3}. \tag{2.56}$$

Work from Hammerlin as cited in [11] demonstrated that the critical wavelength $\lambda_G \approx 40\pi\delta_2$ providing $\frac{\delta_2}{r_{rc}} \leq 10^{-4}$. Thus the Görtler wavelength is

$$\lambda_G = 40\pi d \left(\frac{0.36}{Ta} \frac{r_{rc}}{R_1} \right)^{1/3}. \tag{2.57}$$

Assuming that $\frac{r_{rc}}{R_1} \approx 1$ then,

$$\lambda_G \approx \frac{28\pi d}{Ta^{1/3}}. \tag{2.58}$$

The results of Barcilon et al. indicated good agreement with the predicted Görtler vortex spacing. Subsequent visualisation studies at different radius ratio have not shown the formation of similar "herring bone" patterns present in kaleidoscope visualisation by Koschmieder [17, 33] and Lathrop et al. [22] along with others similar experiments cited in [15].

Görtler vortices have however been shown to be present by Wei et al. [44]. This study was based upon a range of Taylor number and thee radius ratios, $\mu = 0.084, 0.5, 0.88$. Görtler vortices were observed using laser-induced fluorescence, LIF for all three radius ratios and the study established that the vortex patterns were not due to the injection of the dye. Visualisation using $\mu = 0.5$ demonstrate the transport of Görtler vortices along the length of the inner cylinder from the vortex inflow boundary. The results with the large gap, $\mu = 0.084$ also show relatively much strong Görtler vortices then Taylor vortices. As the Taylor number was increased the frequency of the formation of Görtler vortices increased more frequently.

For the small radius ratio, $\mu = 0.88$, Görtler vortices were also observed forming at the inner cylinder with strong Görtler vortices during the wavy turbulence transition. No images from the LIF are presented due to reproducing images, at the high speeds. Görler vortices are still present and aluminuma particle photographs are suggestive of "herring-bone" patterns similar to Barcilon et al. but give no explanation. The Görtler wavelengths were also calculated and compared with equation 2.58 in the paper and show good agreement with the large gap over estimating; this is not surprising as the equation is based upon narrow gap approximation.

Ta/Ta_c	Ta	Re	Flow Features
1	1.7×10^3	3.3×10^2	Stable Taylor vortices
1.24	2.1×10^3	3.6×10^2	Stable Wavy Taylor vortices
2.83	4.9×10^3	5.5×10^2	Changes in azimuthal wave numbers
17	2.9×10^4	1.4×10^3	Predominate wave-number variable
73	1.3×10^4	2.8×10^3	Modulated wavy Taylor vortices
≈ 100	1.7×10^5	3.3×10^3	Constant wave number
≈ 420	7.2×10^5	6.9×10^3	Wavy turbulent flow
≈ 1000	1.7×10^6	1.0×10^4	Stable turbulent Taylor vortices
6500	1.2×10^7	2.6×10^4	Design operation speed for the Prototype Thruster
3.0×10^5	5.1×10^8	1.8×10^5	Toroidial eddies begin to lose their regularity
5.0×10^5	8.6×10^8	2.3×10^5	Toroidial eddies cannot be clearly distinguished

Table 2.3: Summary of Critical Taylor Numbers ratios

§2.5 Predictions

As the speed increases in the integrated electrical thruster, the flow in the gap will undergo several bifurcations and transitions, some of which are presented in the table 2.3, which is compiled from [31, 9, 11].

This table is not meant to be definitive, as the exact ratios of critical Taylor numbers at which the flow changes occur, may vary between experimental setups. This is due to the fact that the aspect ratio and start-up conditions can alter the flow. The table demonstrates that for the design operation for the thruster unit the flow is going to be turbulent with axially stable Taylor vortices as the operating Ta/Ta_c is well beyond 1000.

From equation 2.17 the length of laminar Taylor Vortices expected in the thruster will be around 2mm and the turbulent vortex length should be between 20% and 70% larger dependent upon the acceleration rate [15]. From the linear theory described in reference [45] the Görtler vortex wavelength is of the order of 0.25mm. The associated laminar boundary thickness of 0.048mm and 0.063mm on the inner and outer cylinders respectively.

The effect of speed increase on the power consumption is presented in the two parts in figure 2.2, for four semi-empirical equations; Bilgen & Bilgous, Wendt, Yamada and Dorfman, equations 2.35,2.37, 2.38 and 2.48, respectively. For Dorfman's equation a Von-Kármán constant, $\kappa = 0.4$ is taken and three sublayer constants, $\alpha = 3, 6, 9$ are used. This shows a large discrepancy between the four different semi-empirical relationships especially for the 2mm case. The effect of the gap width for the prototype thruster is presented in figure 2.3 using the same equations for the constant operational design speed of 1200 rpm. This graph again demonstrates the large discrepancy between the semi-empirical relationships found in the literature. The results clearly show that the frictional power loss rapidly increases for gaps smaller than about 1mm. The electrical losses rapidly increase, as the gap increases. Hence the optimum

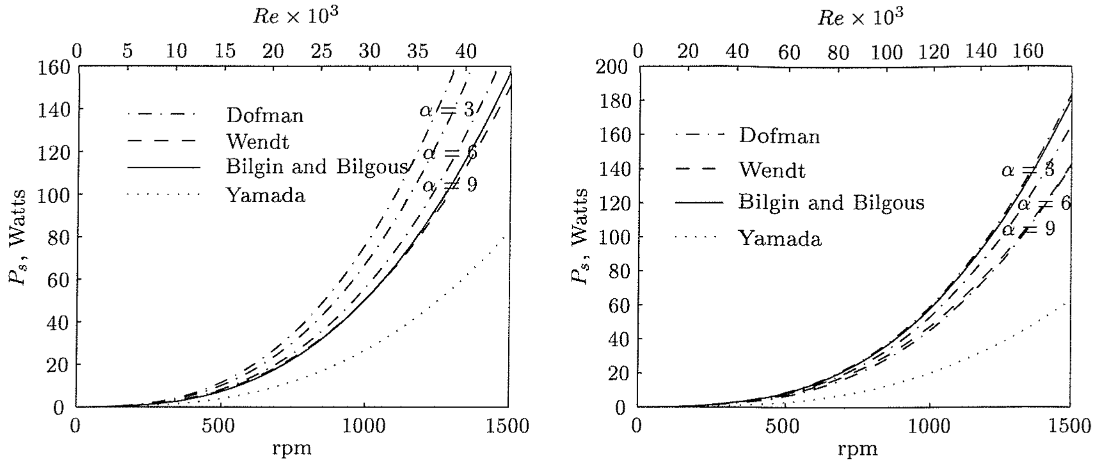

i: $\eta = 0.9861$ (2mm gap)

ii: $\eta = 0.9467$ (8mm gap)

Figure 2.2: Effect of increasing rotation rate on the frictional power loss.

gap width of between 1 and 2mm may seem appropriate.

The discrepancy between the suggested equations seem to be even more apparent as they do not even follow the same trend. Bilgen & Bilgous's equations reaches a minimum value at $Re = 1 \times 10^4$ and then raises as the gap width increases, whereas the other trend-lines decrease as the Reynolds number increases.

The boundary layer positions are presented in 2.4. The positions are based table 2.1 and Bilgen & Bilgous's equations for skin friction. This is not meant to be definite as it is for flat walls and these positions will be altered due to the curvature and rotation effects. This figure does however demonstrate that this is a low Reynolds number problem as the boundary layers make up most of the gap.

From this analysis, it is clearly evident that further work is required to establish the accuracy of these torque predictions for small clearance turbulent Taylor-Couette flow. The effect of vortex length has been shown to alter the skin friction but no understanding of the physics has been presented. The possibilities of Görtler Taylor vortex interactions has been discussed but is not understood. The next chapter describes the development of a experimental rig, with the eventual aim of understanding the physical process and to provide data for validation of numerical calculations presented in the following chapters.

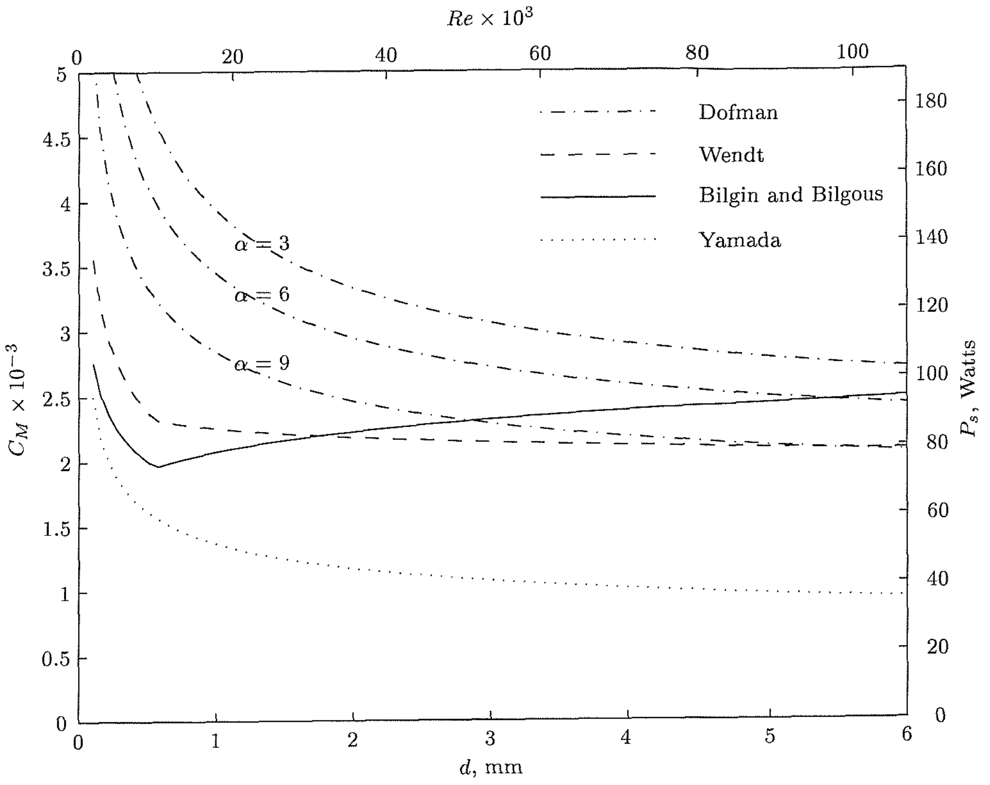

Figure 2.3: Effect gap width on frictional power loss at the design speed of 1200 rpm.

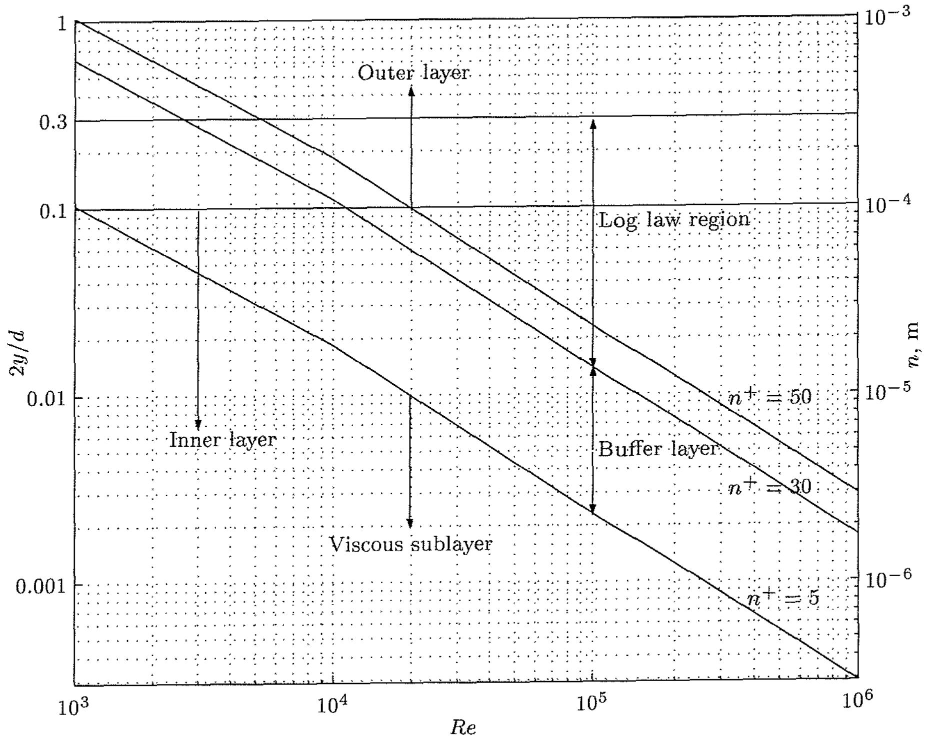

Figure 2.4: Expected boundary layer positions from the inner cylinder for the 2mm case.

CHAPTER

3

Experimental Rig Design and Measurements

§3.1 Introduction

This chapter describes the progress in the design and construction of an experimental rig to study the flow in the thruster unit. The rig is based on two cylinders, an inner cylinder rotating in a clear outer cylinder. These cylinders are placed in a water tank and supported on a framework. The inner cylinder is driven by a series of belts and pulleys from a three phase motor. The outer cylinder is supported on the framework by a dynamometer to measure the torque as a reaction. The dimensions of the rig are based on the first thruster unit and has been scaled such that the gap has been increased from 2mm to 10mm to allow the flow to be visualised.

The majority of experimental facilities, including those referenced within this thesis, are in the region $0.6 < \eta < 0.9$. However, most engineering applications involve much smaller clearance ratios such as motors and the thruster unit, the motivation for this work, the region $0.9 < \eta < 1$ and also large numbers of theories are for $\eta \rightarrow 1$. Hence, the experimental rig for this investigation was designed to be dynamically similar to the thruster unit for which, $\eta = 0.986$.

The initial aim of the experimental work is to investigate the flow in the first prototype thruster unit by measuring the frictional torque and visualising the flow. With the knowledge gained, it was hoped that the computational work can be validated and that methods of reducing the frictional resistance could then be tested. The rig also has the possibility to study the end effects such as open, closed and rotating ends. Experiments could also done on Journal bearings by aligning the cylinders eccentrically. The rig has the potential to study windage loss in other machines such as other electrical motors and with small adaptions the facility could also be used to study the effect of surface roughness on rotating and curved of surfaces by just rotating the inner cylinder.

Due to difficulties with satisfactorily commissioning the experimental facility the initial aims have not been fulfilled to the full potential as of yet. The experimental rig rather than being a commendable tool for testing geometric changes and validating the computational work has become a first prototype. This prototype is hopefully the first step in developing a test facility for experimental studies into rotating fluid problems, in particular that of turbulent Taylor vortices. The prototype, in spite of its limitations, has been used to demonstrate that vortical patterns are present and torque measurements have been taken although with a limited accuracy.

The first part of the chapter is a discussion of the design conception of the initial test facility and the expected properties of the prototype rig. The design of the main components that form the experimental rig are described and illustrated, by means of construction drawings and photographs, in the following section. Next, torque measurements are then presented using the custom-built dynamometer as a reaction on the outer cylinder and using a Voltech "Universal Power Analyzer" to measure the power used by the motor. The following section presents an initial visualisation study of the vortical flow using digitised images of bubbles and a novel method of categorising the size and behaviour of the vortices has been developed.

§3.2 Design Conception and Properties

As the gap in the thruster is only 2mm an exact model would make visualisation of the flow difficult hence it was felt that a scaled experimental rig should be designed to be dynamically similar to the prototype. To be dynamically similar both the Taylor number and Reynolds number have to be identical. From this condition it is necessary that the rig has to have the same radius ratio as the thruster unit and the speed would then be set by the operating Reynolds number range. As the length governs the number of Taylor vortices the aspect ratio (height/width) had to be kept constant as well. Hence the rig was designed to the following constraints.

Radius Ratio, η	0.986
Aspect Ratio, Γ	16
Maximum Operating Re	35000

As the size of the gap increases the inner radius increases and the operational r.p.m decreases for a constant Reynolds number. Five possible sizes are shown in the table 3.1. The required torques are estimated from Bilgen & Bilgous's equations 2.35 and the power using equation 2.36. It is obvious that for visualisation of the flow in the gap, the larger the gap the better but a more sensitive torque measurement device is required. From a manufacturing point of view, the smaller cylinders are easier to produce. It should also be noted that the tolerance on the diameters and the alignment of the cylinders decrease as the radius ratio increases, but it is generally easier machine smaller diameter objects true.

As a compromise between the visualisation, torque measurement and construction a 10mm gap was chosen, this gives the following dimensions for the experimental rig.

Radius, mm	Gap, mm	Length, mm	rpm	Torque, Nm	Power, W
142	2	32	1200	0.72	90.2
355	5	128	192	1.79	36.1
710	10	160	48.0	3.59	18.1
1065	15	240	21.3	5.38	12.0
1420	20	280	12.0	7.18	9.0

Table 3.1: Possible rig dimensions and properties

Inner Cylinder	Outer Radius, R_1	710 mm
	Length, L	160 mm
Outer Cylinder	Inner Radius, R_2	720 mm
	Length	300 mm

These cylinders were placed in a separate tank of water instead of allowing the outer cylinder to form the tank wall as used by other experiments found in the literature. This is beneficial for three main reasons. Firstly, it allows the torque to be measured as a reaction on the outer cylinder. It also means that visualisation of the gap is possible. When looking through a sheet of radius 720 mm from air would only be possible to see a radius of around 530 mm due to the refraction. (Notes on the refraction through a curved sheet are given in Appendix C.) Thirdly, a curved surface stiff enough to hold the water pressure would be difficult to manufacture.

From linear theory discussed in chapter 2, the wavelength of laminar Taylor vortices expected in the experimental rig will be 20 mm (from equation 2.17) and the turbulent vortex length should be between 20% and 70% larger dependent upon the acceleration rate. Also from the linear theory described the Görtler vortex wavelength is of the order of 0.5 mm from equation 2.58. The associated laminar boundary thickness of 0.27 mm from equation 2.51 and 0.35 mm from equation 2.51 on the inner and outer cylinders respectively.

To allow calibration of the frictional losses due to the ends of the cylinder, it was decided that two different lengths of the inner cylinder with the same end clearance for both cases would be required, allowing the end losses to be calibrated.

$$\text{Torque, full length case} = 2 \times (\text{end gap}) + (\text{side gap})$$

$$\text{Torque, half length case} = 2 \times (\text{end gap}) + \frac{1}{2}\ (\text{side gap})$$

This should produce a fairly accurate estimation of the frictional resistance due to the end losses of the cylinder but it may produce slight inaccuracies as the length of the cylinder affects the number of vortices and the length of the vortices can affect the friction. Current computational studies discussed later, have also shown that the vortices towards the edge of the inner cylinders are of varying length and the central vortices are of a more uniform size. Hence, by reducing the inner cylinder the number of central vortices will be reduced but similar vortices will be formed towards the edges. By using the computational knowledge and by altering the acceleration rate, it is hoped that similar vortex distribution can be achieved and therefore producing a more accurate calibration of the end losses.

§3.3 Rig Components

The experimental rig has five main components:

- Inner Cylinder
- Outer Cylinder
- Torque Dynamometer
- Tank and Framework
- Power Transmission System, including the shaft and bearing assemblies

The design of each one of these components has undergone several extensive design cycles some of which are discussed in the three technical notes [46, 45, 47].

§3.3.1 Inner and Outer Cylinder

The inner cylinder is designed to be split into two halves to allow for calibration of the end losses. Both of these cylinders are constructed from two 18mm birch ply disks with a polyurethane foam in the middle. At the edges this foam is coated with filler to enable the cylinders to be trued. The plan views are shown in figure 3.1 and a photograph in figure 3.4. The inner cylinder is attached to the shaft by a pair of stainless steel flanges which are pinned to the shaft and bolted through the cylinder.

The outer cylinder comprises of two spoked disks supporting a clear outer wall as shown in the plan in figure 3.3 and the photograph in figure 3.2. The two supporting disks are constructed from 18mm birch ply. The top disk is attached to the torque measurement device and this disk can be lowered by a set of support brackets when the inner cylinder is split into two, allowing the same end conditions for both test cases. This is demonstrated in figure 3.5 which show the position of either one or two inner cylinders relative to the outer cylinder. Both the inner cylinders and the two spoked disks for the outer cylinder were machined.

§3.3.2 Torque Measurement

Four possible methods of measuring the torque in the experimental rig were considered:

- Measuring the torque on the shaft with a torque metre;
- Measuring the force on the supports between the inner cylinder and the shaft;
- Measuring the reaction of the torque on the outer cylinder;
- Measuring the difference in the power used between air and water tests.

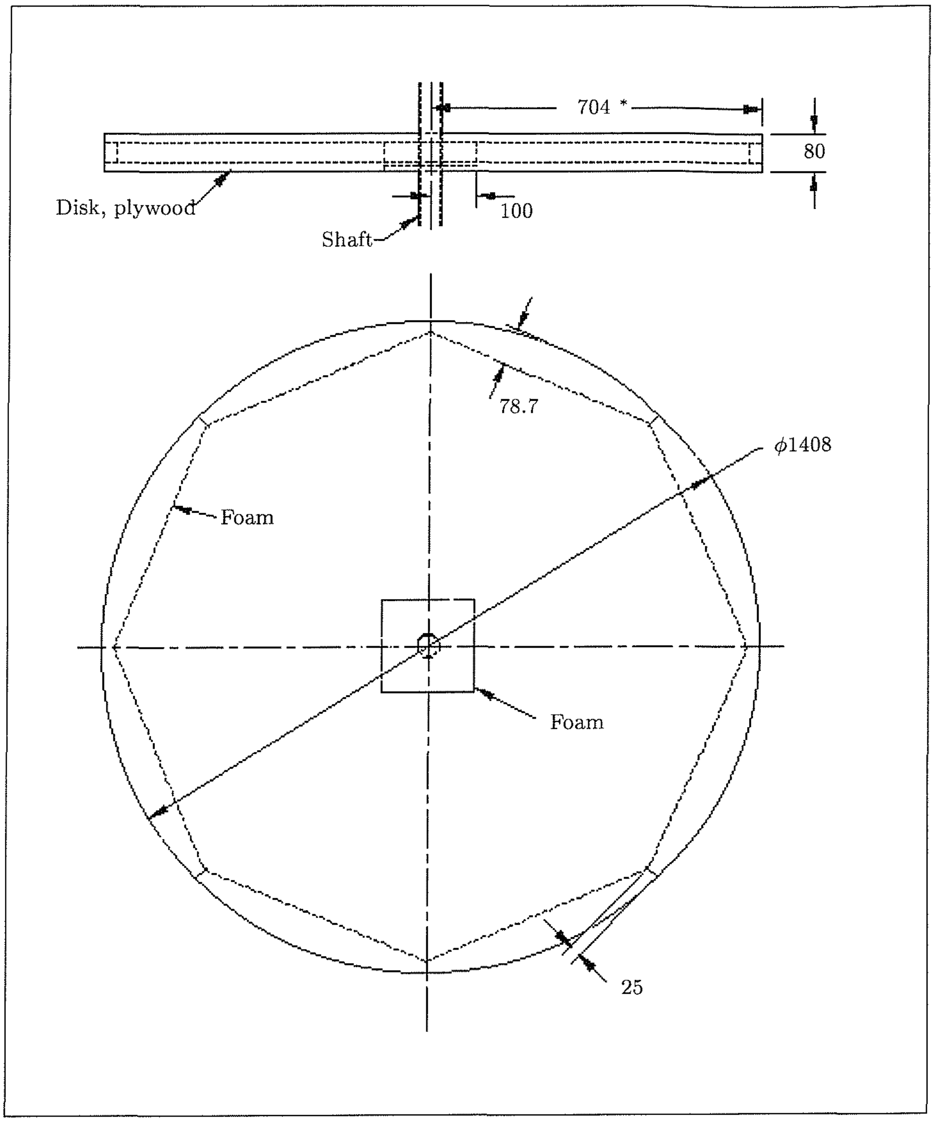

Figure 3.1: Plans of the inner cylinder

The difficulty of measuring the torque on the shaft stems directly from the fact that during the acceleration the inner cylinder produces large inertia forces if the cylinder is to be rotated at dynamically similar rates. As the torque metre on the shaft would have to withstand these high inertial forces as well as being accurate enough at the low static speeds. Therefore, either a torque metre that can measure a large range of torques is required or a method of decoupling the metre from the shaft is needed. Designing or purchasing a torque metre that could accurately measure the range of torques was found to be too expensive for this type of initial investigation. Coupling the torque metre after the acceleration over complicates the problem, as a very smooth operation would be required so as not to disturb the flow between the cylinders. Most torque metres are normally further complicated as they require a set of slip rings to transfer data.

Placing strain gauges on the supports of the inner cylinder also suffer from the problem of high inertial forces. The supports that attach the inner cylinder to the shaft could easily contain a gauged flexure. These flexures could be designed to withstand the inertial forces and still flex enough at the low range but this would place the strain gauges beyond their operating

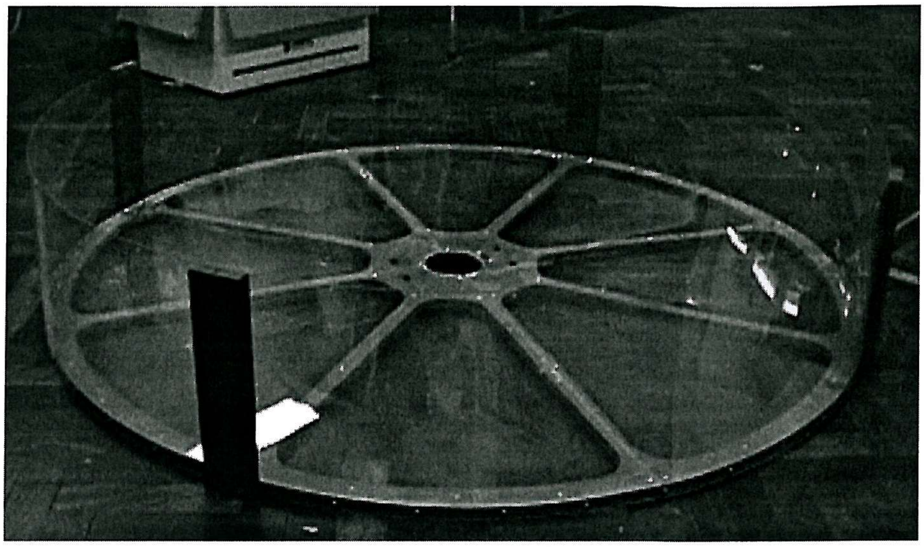

Figure 3.2: Photograph of the outer cylinder excluding the top disk

conditions. Over straining a gauge is not normally considered too much of a problem although repeatedly placing the gauge under too much curvature can easily cause the gauge to become unstuck.

Suspending the outer cylinder and measuring the reaction force was decided to be a simple and cost effective method. As the forces are relatively low and the start-up friction of most bearing arrangements is normally inconsistent, the most sensible option was to mount the outer cylinder on a dynamometer.

To produce an accurate dynamometer, four flexures working in contra-flexure were designed. The outline of the design process along with details of the circuitry for the wiring is presented in appendix §C.1. These flexures are shown in figure 3.6 and are made from aluminum. The flexures are 2mm thick, have a width of 15mm and and a overall length of 50mm. To ensure a reasonable response the flexures are mounted at a radius of 60mm and have two strain gauges on each side of the flexure. The expected strain at the gauge location is around 40 $\mu\varepsilon$ for a 3 Nm torque. The whole assembly is shown in photo 3.7, gauged, wired and firmly attached to a pair of end plates. In order there is no movement between the flexures and the plates, the assembly was glued and bolted tightly together.

The bridge circuit was conditioned using “fylde bridge conditioner”. The bridge supply voltage, V_S and output voltage, V_O were monitored using a digital voltage metre. To allow the voltages to be traced over long periods of time and in some cases days, the voltage was sampled using a computer.

§3.3.3 Tank and Framework

Both the cylinders are immersed in the water tank. The tank is made from 18mm birch plywood with three windows in the side of the tank to allow the flow to be visualised. This tank is supported by a steel framework, a sectional view of the tank and a plan view is shown in figure 3.8. At the top of the tank frame work there is a pair of aluminum channel sections. On

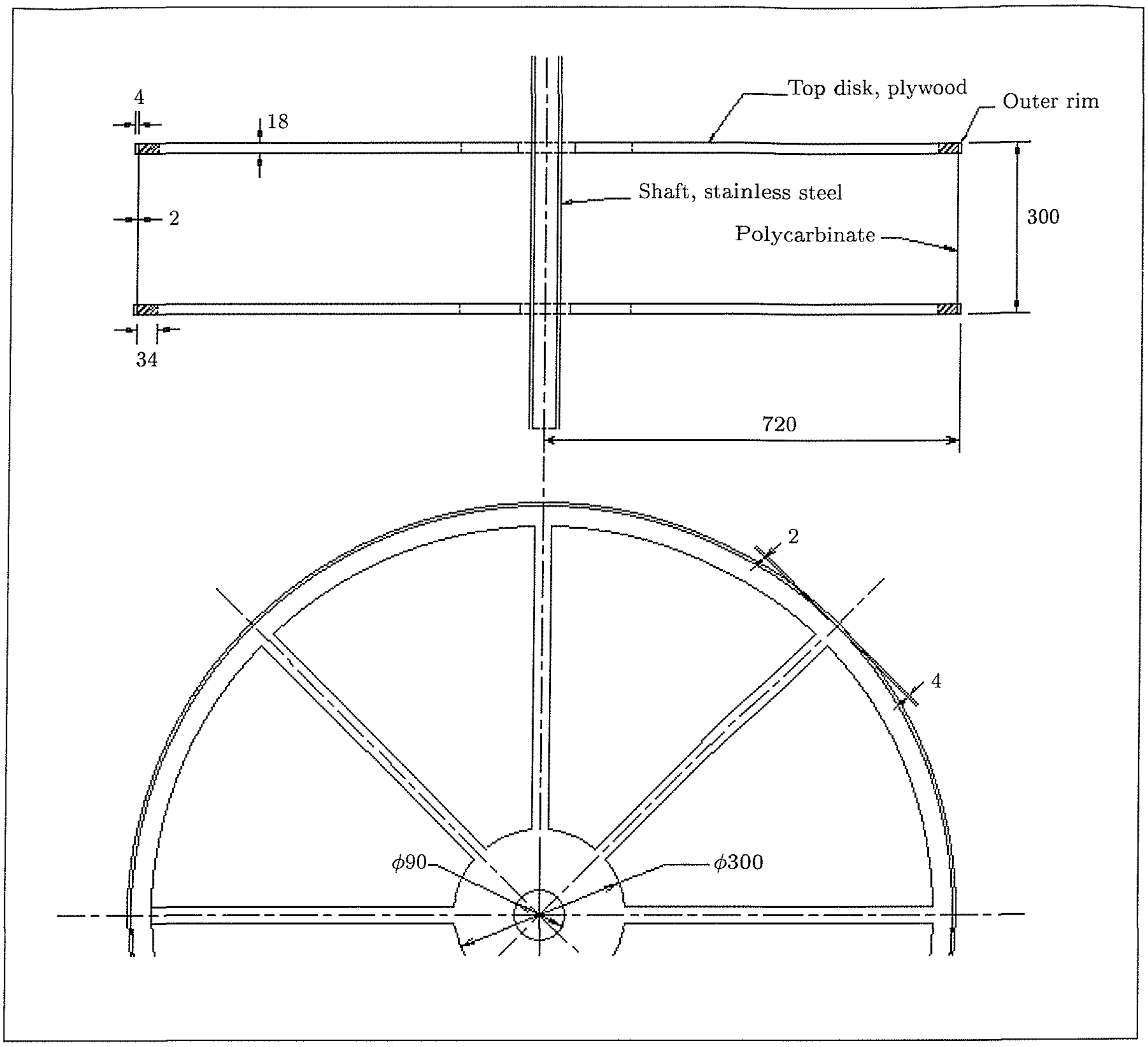

Figure 3.3: Plans of the outer cylinder

the top of the channel sections is the bearings and on the underside is the torque dynamometer. The overall general arrangement is given as a sectional view in figure 3.12.

§3.3.4 Power Transmission System

The general arrangement of the shaft is shown in figure 3.9. The shaft is a stainless steel tube with a plastic bush bearing at the base acting as a guide for the base of the shaft. This base bearing is in a stainless steel housing and is water lubricated. The top of the shaft is supported by a pair of angular contact bearings, so that the weight of inner cylinder can be taken in air as well as for the upward buoyancy force when in water. The inner cylinder is driven by an electric motor and two pairs of pulleys and timing belts.

The inner cylinder is driven by belt drives from a 4kW 3 phase motor. (BS 5000-99 standard, 2890rpm, 50Hz, 415V, 7.2A) and powered by a ABB motor controller. To reduce the rpm to the required rate for the inner cylinder a pair of toothed timing belts were used.

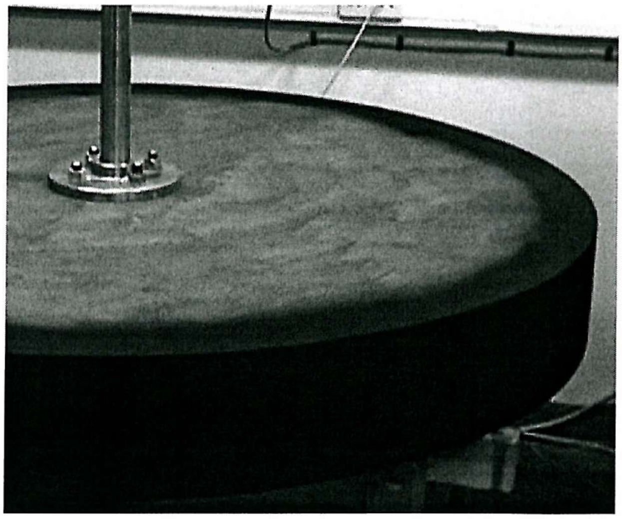

Figure 3.4: Photograph of the inner cylinder attached to the shaft

Motor drive shaft	28 teeth	Middle shaft	90 teeth
Middle shaft	24 teeth	Inner cylinder shaft	90 teeth

This gives a gear ratio drop of approximately 1 : 24. The motor and the mid-shaft are enclosed in a separate framework to reduce vibrations as shown the photograph in figure 3.11. The framework is constructed from mild steel and is both bolted to the wall and supported on padded feet. This is to reduce the effect of vibrations and to make sure that the motor framework does not move towards the main framework due to the belt tension.

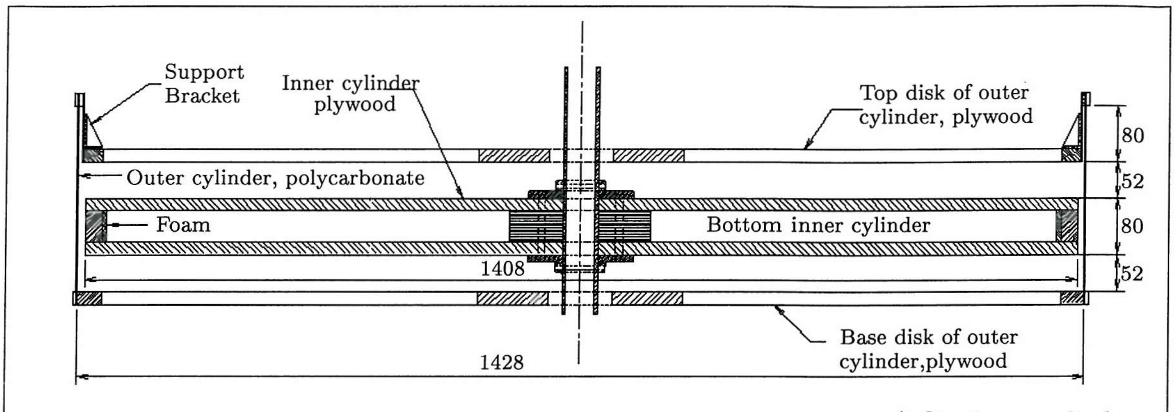

a) One inner cylinder

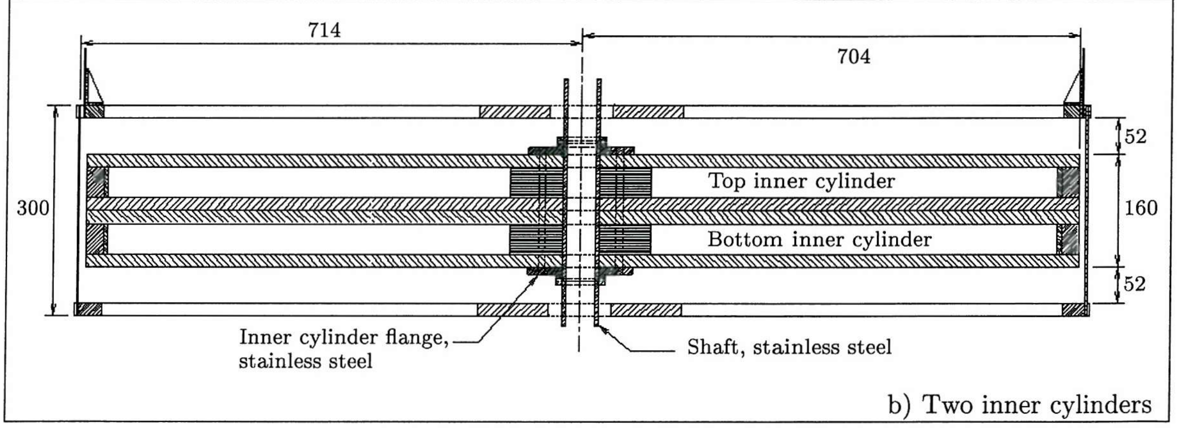

b) Two inner cylinders

Figure 3.5: Both the possible sectional arrangements of the inner and outer cylinder

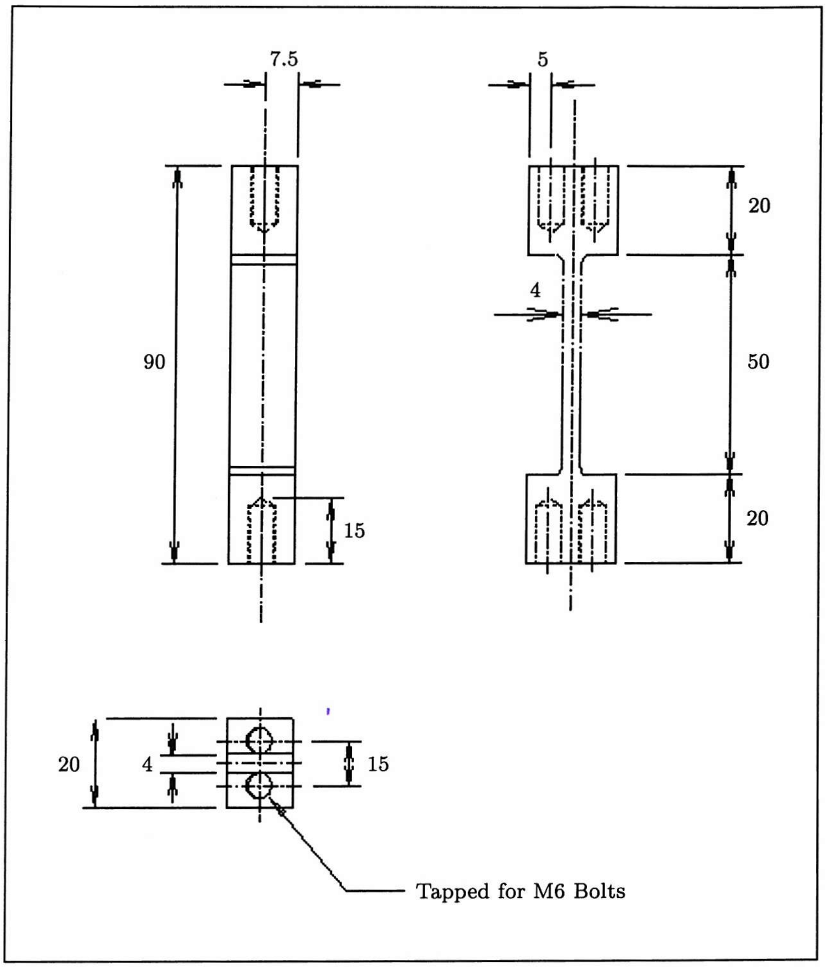

Figure 3.6: Details of the flexure design

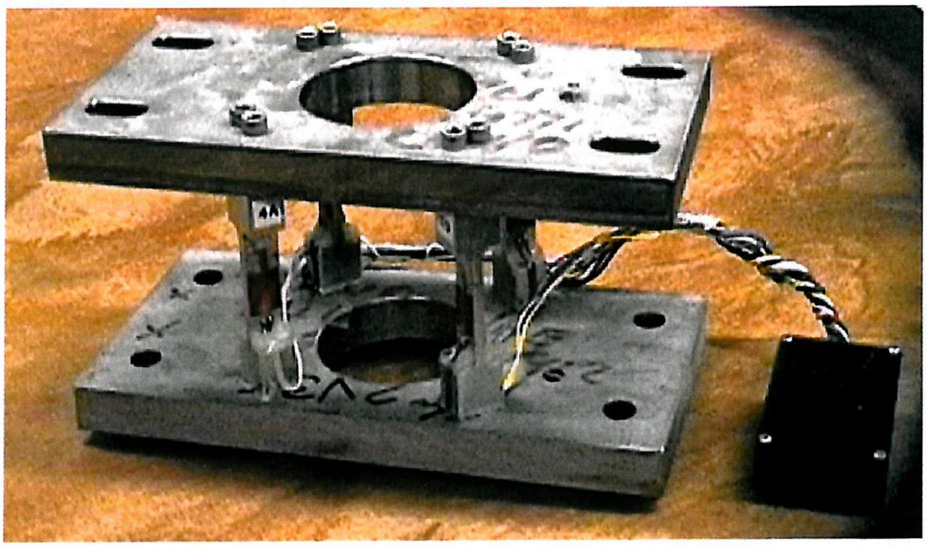

Figure 3.7: Photograph of the dynamometer gauged and wired

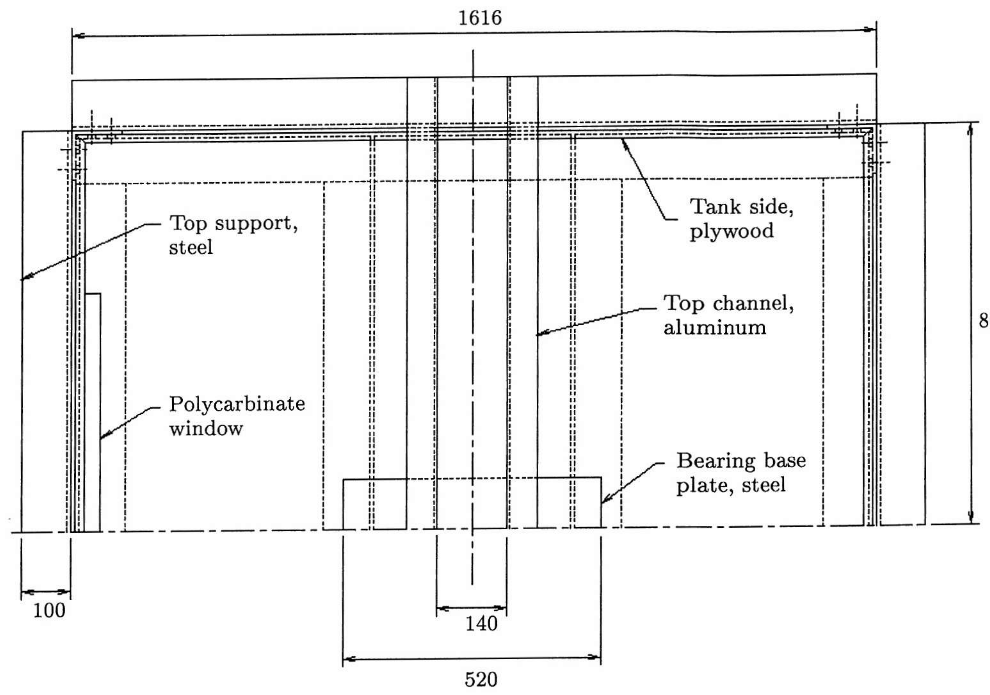

a)Plane view of the tank

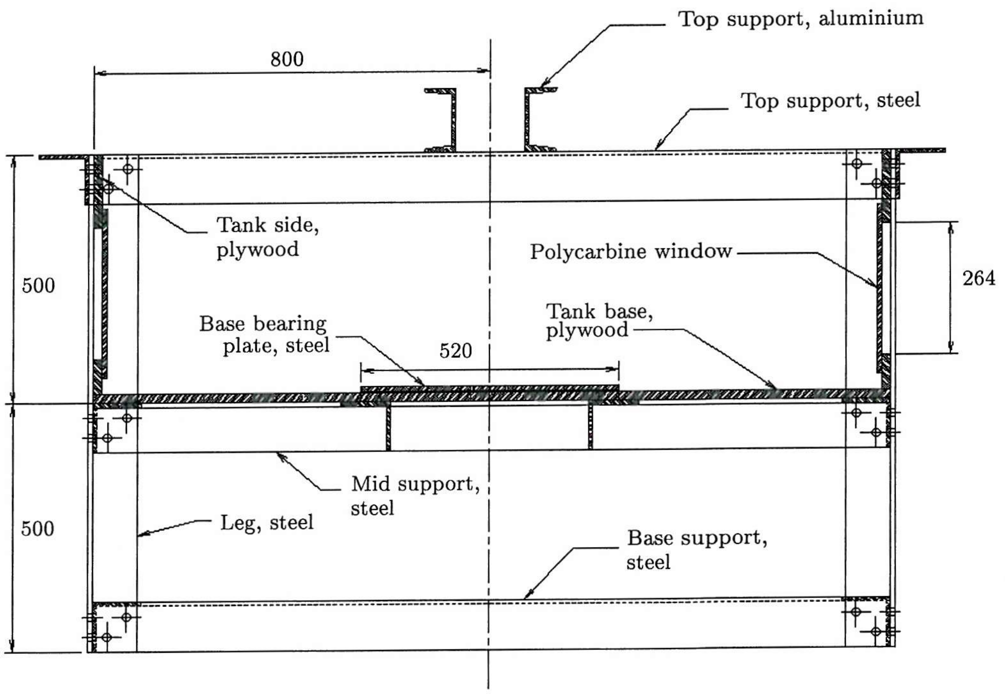

b) Mid Section of the tank

Figure 3.8: Plans of the tank

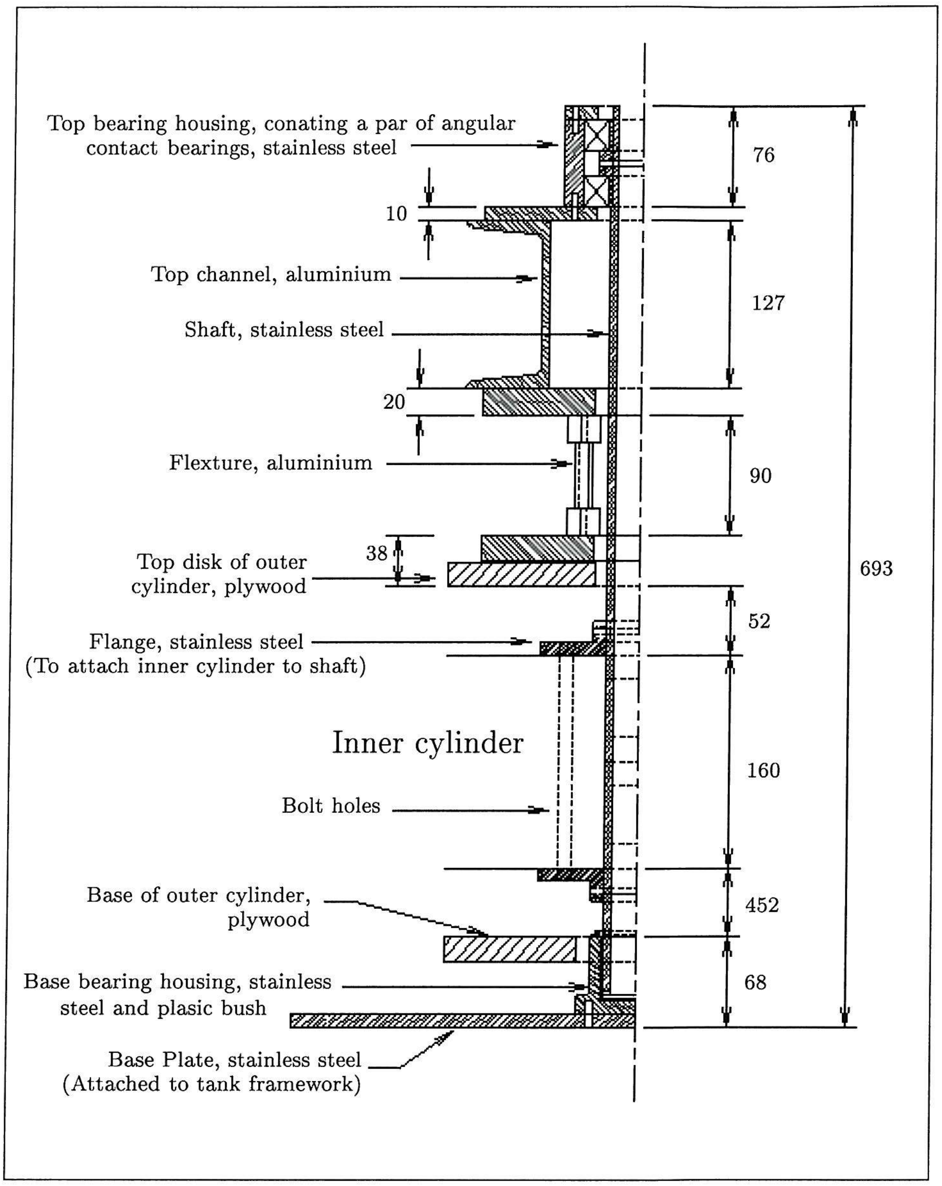

Figure 3.9: Layout of the shaft and attachments

Figure 3.10: Closeup photograph of the top bearing and dynamometer arranged in the rig

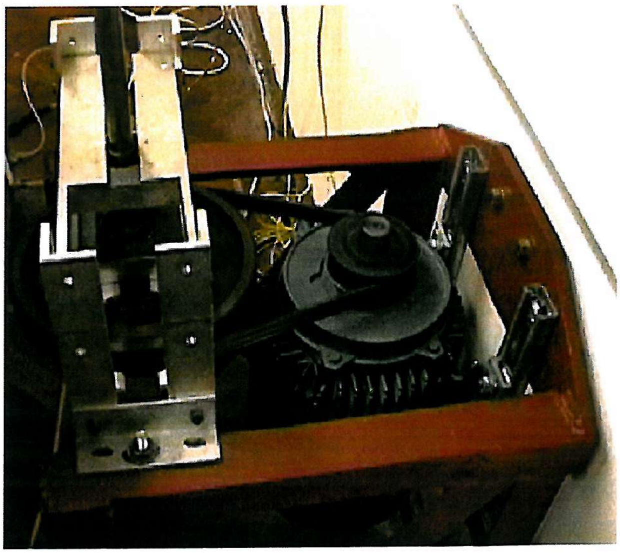

Figure 3.11: Photograph from above of motor framework showing the motor and belt drives

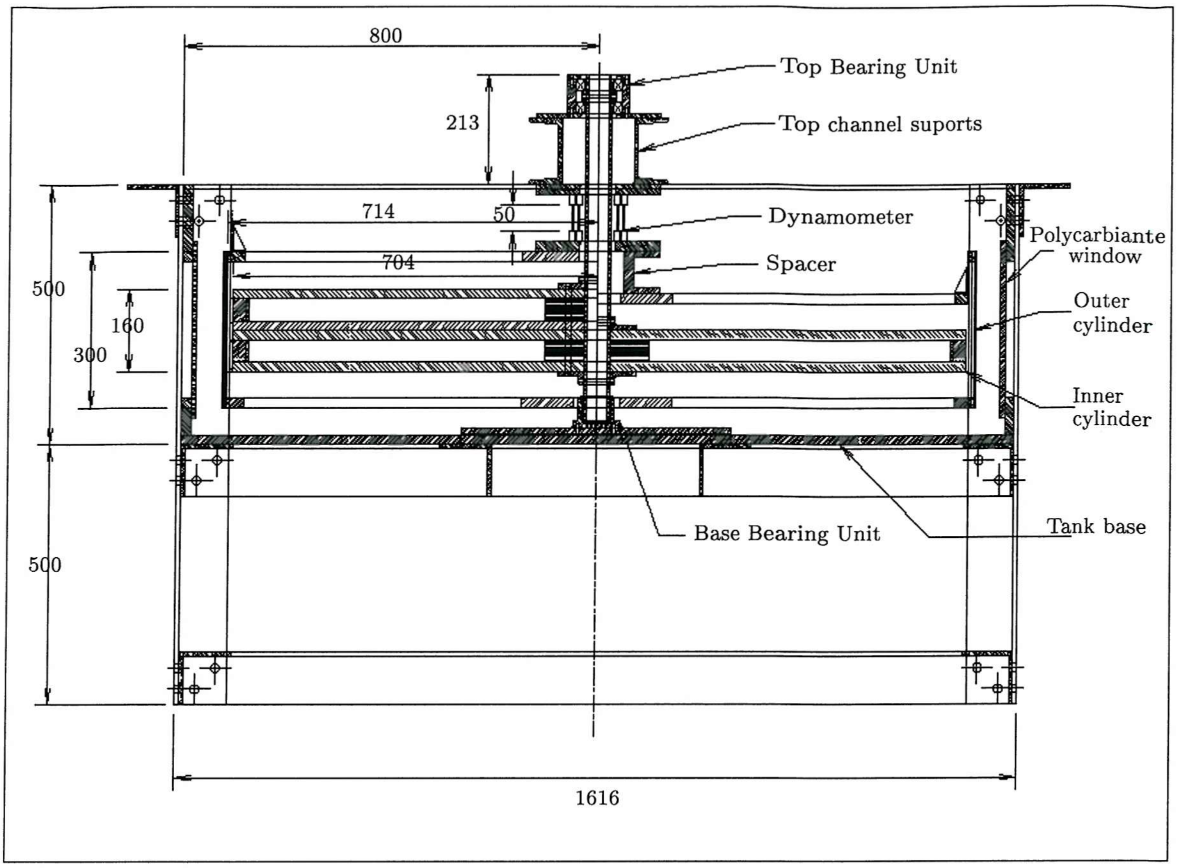

Figure 3.12: Sectional view of the experimental rig

§3.3.5 Complete Rig

All the designs were manufactured in the School of Engineering Sciences workshops, with the exclusion of truing the cylinders. The experimental rig was then constructed and assembled in stages the in the Ship Science laboratory. A full sectional cut of the generally arrangement is given in figure 3.12 and a photograph is shown in figure 3.13 showing the experimental facility operating in the lab.

§3.3.6 Refraction

The refraction due to water and the curved surface of the outer cylinder was calculated as outlined in the appendix §C.2. The refraction paths are presented in the drawing 3.14 and a photograph demonstrating the actual refraction in the tank is given in figure 3.15. This clearly demonstrates that it is possible to visualise in the radial direction between the two cylinders by placing the cylinders in a water tank although for positions close to the to the outer cylinder radius the distortion is increased.

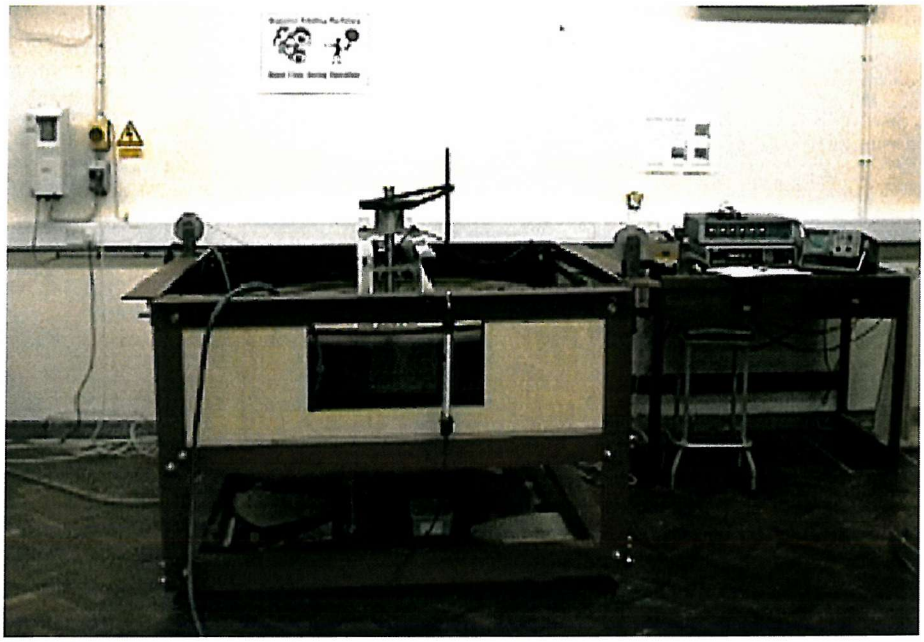

Figure 3.13: Photograph of the whole rig setup in the laboratory

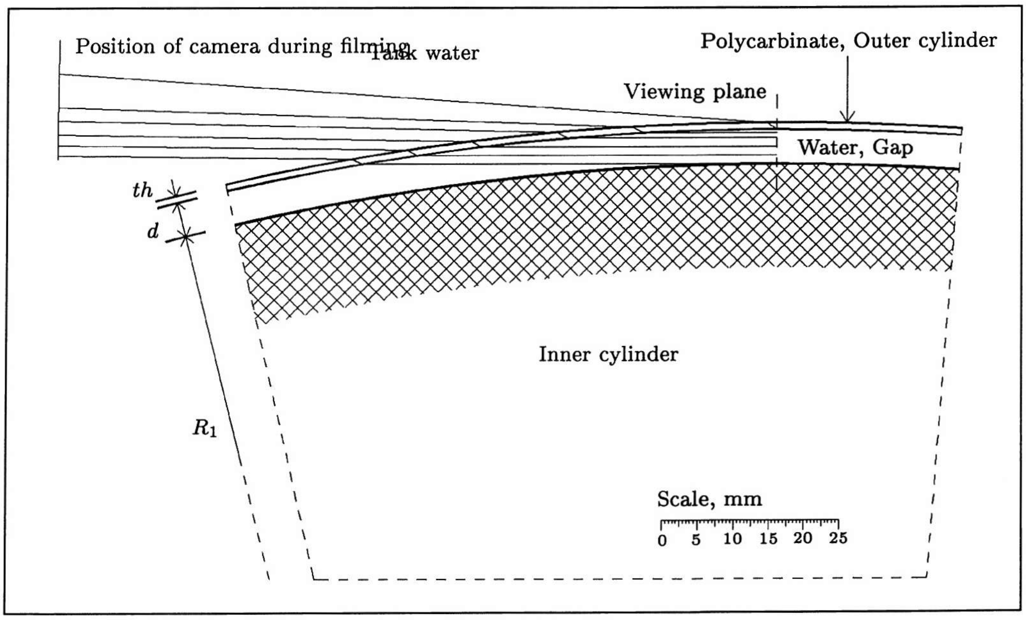

Figure 3.14: Diagram showing the refraction

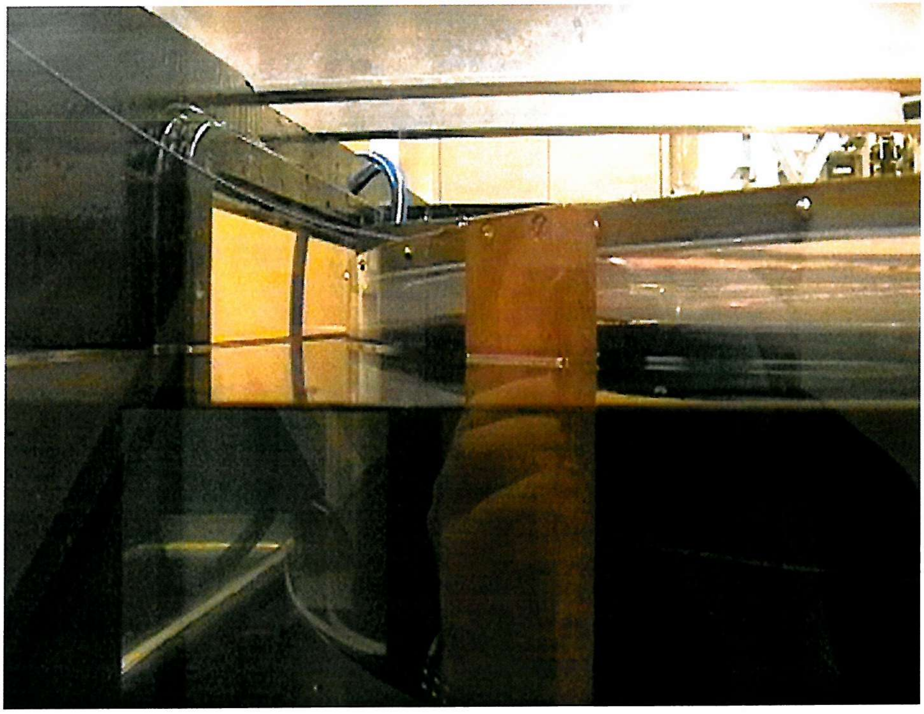

Figure 3.15: Photograph demonstrating the refraction in the tank

§3.4 Modifications to the Cylinders

During the development of the prototype experimental rig several problems occurred and a few developments were required to improve the design of the cylinders. The main alterations included sealing the two halves of the inner cylinder and enclosing the ends of the outer cylinder. The first time the experimental rig was setup, rotating the inner cylinder caused free surface waves due to the spokes on the outer cylinder, in turn causing high torque loading on the dynamometry. Free surface waves were also observed when the tank was only part of the way filled, such that the water level was half way up the inner cylinder.

To combat the formation of free surface waves, it was decided to enclose the inner cylinder by covering the spokes of the outer cylinder with 4mm clear polycarbonate sheeting. Although making the geometry not dynamically similar to the thruster unit, it was designed to combat the high loads caused by the free surface waves. This removed the free surface waves with the full tank and partially with a part full tank.

This caused further problems, as in the now enclosed end gaps between the cylinders, the surface pressure on the top and base of the outer cylinder was greatly increased. On the bottom base of the outer cylinder this was actually advantageous, as the surface pressure acts in the opposite direction of the buoyancy force. On the top surface the extra pressure exacerbated the situation as both forces act in the same direction, producing a much larger increase in the amount of deflection of over 30mm at the rim. To reduce this deflection on the outer cylinder, it was then modified for the third time by adding a small 15mm aluminum "L" section along each of the spokes. This greatly reduced the deflection to just a few millimetres at the cylinder rim.

§3.5 Torque Measurements

Several problems are reported in the following section as regards to making adequate measurements of the torque in the experimental rig. Firstly an investigation into the dynamometry designed for the experimental rig is presented. This includes diagnostics of the problems associated with the design and an attempt to make measurements of the torque.

Secondly, a power analysis method is presented based on analysing the power the motor consumed with a "Voltech PM3000A." These power readings appear to overestimate the expected torque. The ability to be able to make accurate readings of the torque is one of the main reasons that as yet, it has not been possible to fully commission the experimental facility.

§3.5.1 Dynamometry Method

During the initial testing of the experimental rig it was evident that the dynamometer was responding in an unpredictable manner with large amounts of drift. It was initially thought to be caused by either sliding bolts, a flexing of part of the outer cylinder or a part of its associated framework. When the stiffeners were added to the outer cylinder, the dynamometer was firmly glued with "super epoxy" on the bases and bolt holes were firmly packed to minimize any possible slippage.

This unfortunately did not resolve the problem. To further test the dynamometer and to analyse the drift problem, the output was then sampled over much longer periods of time. Figure 3.16 demonstrates a typical response from the bridge circuit (see Appendix figure C.1) where the voltage output, V_O is plotted against time. In this figure the initial zero is recorded followed by one weight, then two weights then one weight, a new zero, then both the weights and finally a new zero is recorded. From this type of response it is obvious that the dynamometry was not working appropriately.

From these and other tests it was clearly evident that the problem was due to the gauges or another electrical fault. This is due to the fact that a decaying V_O with time with a constant supply voltage, V_S, implies that the strain is decaying under constant stress. If this was a problem with the flexures, then under constant load it may be possible to have an increasing strain, provided that the flexures were stressed beyond the elastic limit, but not a decreasing strain.

To further test dynamometry the response was traced over two days as shown in figure 3.17. This figure shows large changes with both a loaded and unloaded condition overnight. It is is evident, as it was a fairly cold night that a part of the circuitry was not temperature compensated. The dynamometry should be temperature compensated as shown in Appendix figure C.1, as each arm of the bridge circuit contains two identical strain gauges. To test that the bridge conditioner was working correctly a simple bridge circuit with four 240Ω resistors was used. Over 24 hrs the deviation in V_S was a few μ volts and V_O deviation was a few μ volts, demonstrating that the bridge conditioner was working adequately.

From this it was clear that the dynamometer had to be taken apart so that each gauge on each flexure could be tested individually. To test each gauge the flexure was held firmly in a bench clamp and a weight was applied perpendicular to the flexure. The strain gauge was then wired in a bridge circuit with 120Ω resistors replacing the other gauges. This circuit although not being temperature compensated produced similar responses to those of figure 3.16 The decay of V_O with time appeared for all of the test cases. The initial peak and the amount of decay varied largely between different strain gauges. This is presumably why the initial circuit was not temperature compensated.

All of the gauges had inconsistent responses, which indicates that it may have been the way the strain gauges were fixed to the flexure, as this would have been different for each case. To test this hypothesis, two of the strain gauges were replaced with similar gauges but with a smaller area. These smaller gauges were thought to make it easier to apply a uniform thickness of glue and would have a smaller stress differential between the ends of the gauge so less unlikely to become unstuck. However it did not resolve the problem and a similar type of response was produced.

Hence, due to time restraints, it was decided to use the dynamometry with these inconsistent strain gauges and try to estimate the torques from the decay response. To estimate the torque three separate bridge circuits were configured. Test case A used the strain gauge that produced the least amount of decay. Test case B used one of the smaller strain gauges and test case C used a pair of strain gauges such that the circuit was temperature compensated. The method of calibrating the dynamometer using weights is discussed in the next subsection, followed by presentation of the results.

Calibration Method

The dynamometer was calibrated in situ, by attaching a prestrained twine from spokes on the outer cylinder to a pulley on the edge of the tank and applying weights, as shown in figure 3.18. As shown in this schematic figure it is possible to calculate the calibration torque, M_c using the following equation,

$$M_c = \frac{\sqrt{l_t^2 + h_o^2}}{l_t} R_c F_c \tag{3.1}$$

where l_t is the length of the twine, h_o is the height of the pulley above the outer cylinder, R_c the radius which the moment is acting and F_c the force due to the mass load. The pieces of plywood were added to the top of the channel support to make the measurement of h_o easier.

Clearly it is not an ideal method of calibrating dynamometer; due to the inaccuracy of alignment between the spokes and the edge of the tank, and the angle of the twine. Although it was felt to be appropriate since when the tank is full of water, there is a buoyancy force due to the outer cylinder compressing the dynamometer and as the outer cylinder is not perfectly uniform, this force is therefore uneven. For these preliminary tests only one pulley was used, as smooth increases in loading were required to produce more uniform decay responses. If the dynamometry were working as designed, then the use of two pulleys to ensure a more uniform torque would be more appropriate.

Results

The results from the three tests are presented in figures 3.19-3.20 where the output voltage, V_O in volts is plotted against time, t in hours. The test consisted of the following steps: a zero reading; set of four calibration loads with fixed weights; a new zero; the four test speeds; finally a new zero reading. The first set of four peaks visible on all traces are for the calibration weights, 2 lb, 12 lb, 22 lb and 32 lb respectively. These calibration weights although producing a larger moment than the torque from the speed tests, are easily within the elastic limit of the flexures. With these higher moments a more accurate calibration slope should be possible. The other group of peaks are data for the four speed tests ranging from 5-8 Hz.

Analysing the data numerically to determine the voltage at a particular gradient or forecasting the asymptote for each particular decay pattern may be possible but is highly problematic due to the fluctuations and unpredictable steps in the data. Hence, due to being able to produce significant amounts of repeatable data, the asymptotes for all data points were carefully interpolated by hand on enlarged figures.

The values for the asymptotes are presented in table 3.2 along with the calibration constant $\frac{V_O}{M_c}$ for all three cases at each weight. The mean and standard deviations from this data is shown below.

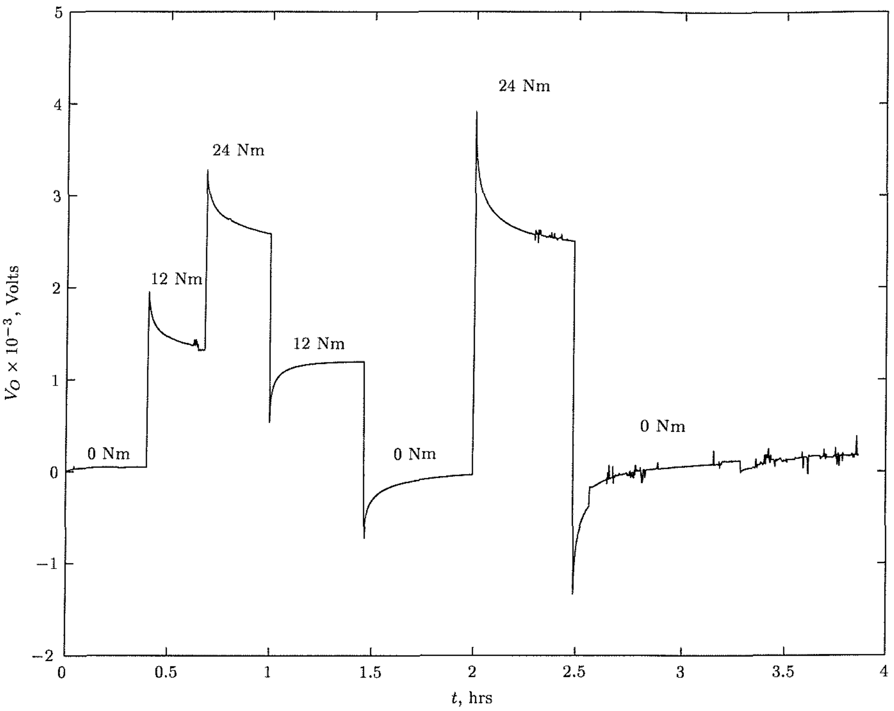

Figure 3.16: Typical decay responses from the dynamometer.

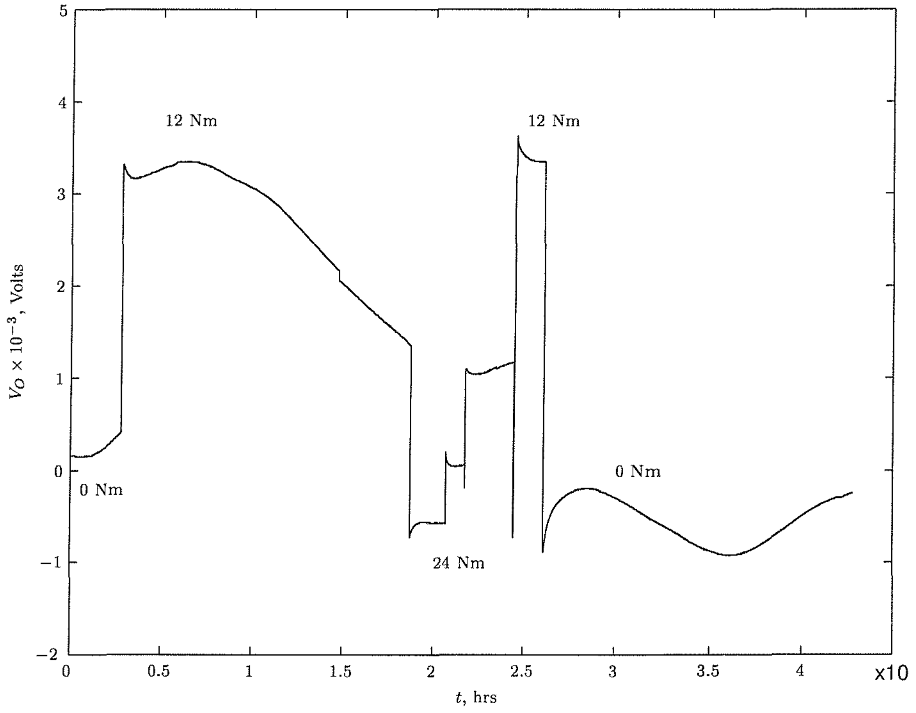

Figure 3.17: Overnight responses from the dynamometer.

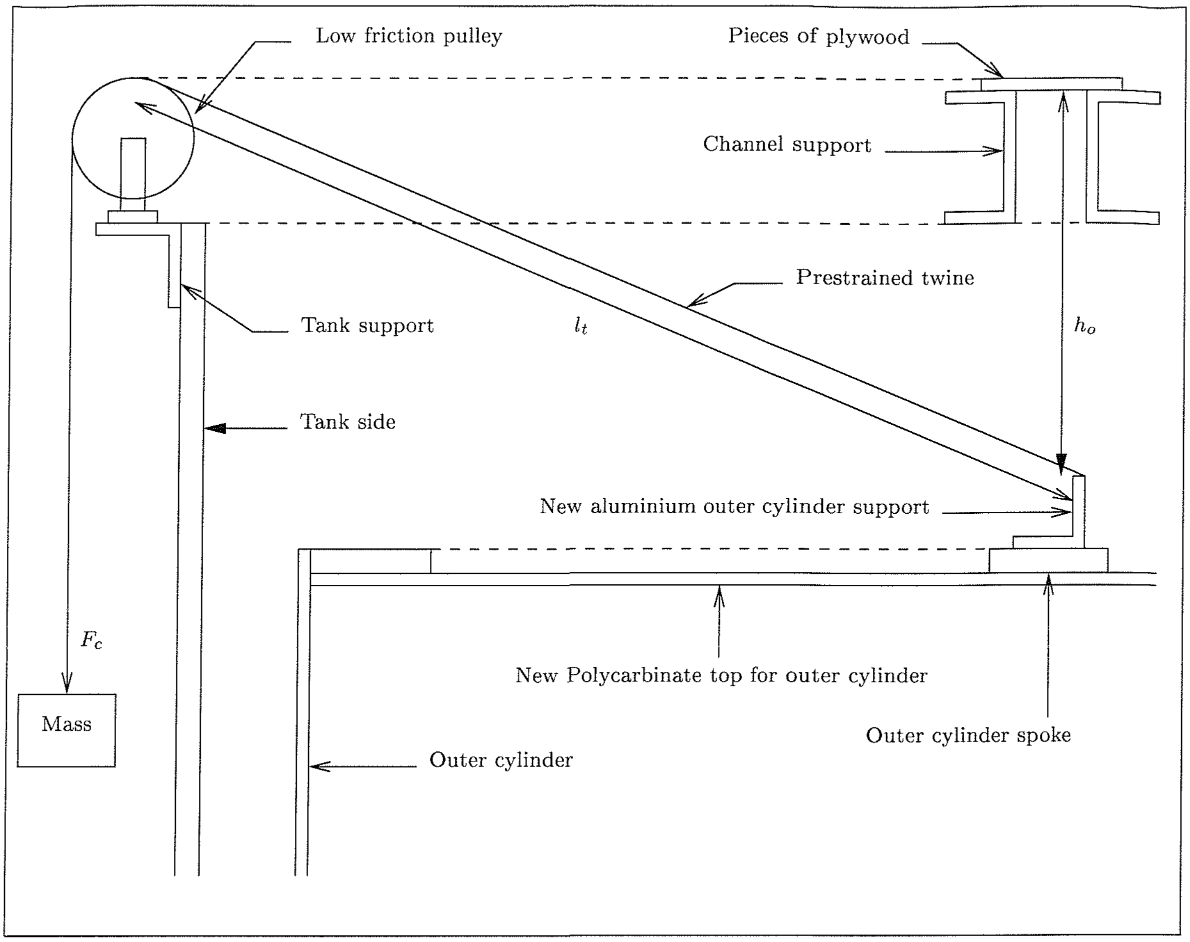

Figure 3.18: Schematic drawing showing the calibration of the dynamometry.

	$(\overline{V_O/M_c}) \times 10^{-6}$	STD $(V_O/M_c) \times 10^{-6}$
Test A	83.7	2.79
Test B	18.0	1.31
Test C	48.8	1.30

This additionally demonstrates the difference in response between the gauges, as both test A and C apparently have the same strain gauges but with the decay asymptotes was almost 50% less.

During all of the tests the bridge supply voltage, V_s close to 5 volts to ensure minimal gauge heating. V_s was continually monitored during the tests and the statistics are presented in the table below. Although V_s was fluctuating about a mean, the relative standard deviation is over 350 times less than calculated for the calibration moments and consequently is insignificant.

	Test A	Test B	Test C
Mean V_S	4.9843	5.0093	5.0009
Min. V_S	4.9808	5.0055	4.9973
Max. V_S	4.9871	5.0123	5.0031
STD V_S	0.0008	0.0010	0.0008

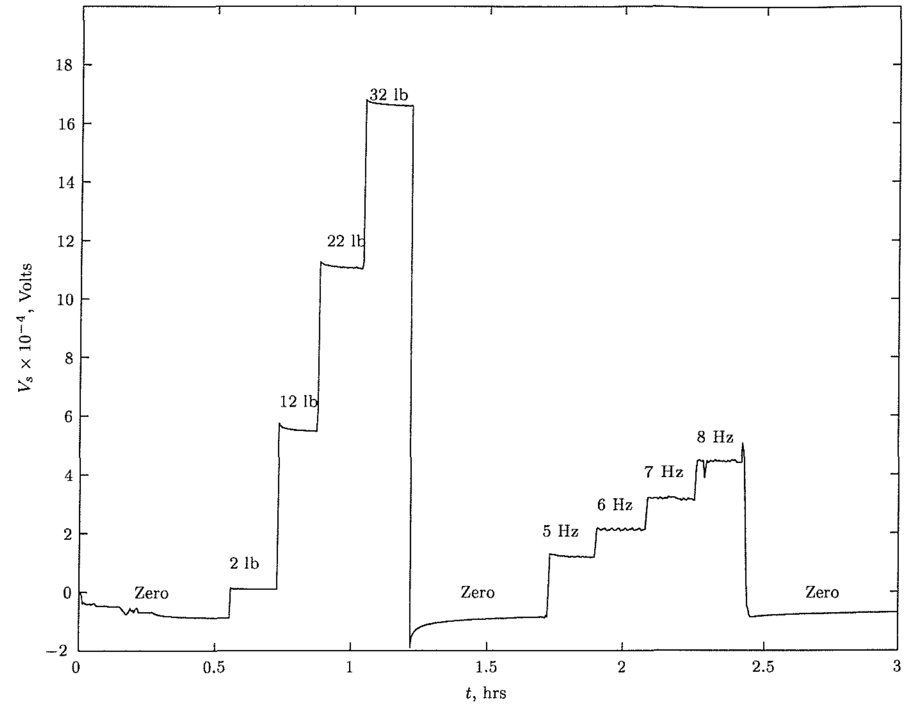

Figure 3.19: Dyno: Test A, Voltage trace from 1st test. (1 Hz is equivalent to $Re = 3640$)

The asymptotes for V_O during the speed tests are presented in table 3.3, using the calibration constant the torque on the outer cylinder is then calculated. These calculated torques using the dynamometry method are discussed later in section §3.5.3 and compared with the power analysis method and empirical equations.

§3.5.2 Power Analysis Method

To analyse the to power the motor, a "Voltech PM3000A, Universal Power Analyzer" was set-up, connecting the motor controller to the motor. This enabled the power consumed by the experimental rig to be analysed. To give an estimate of the power required to overcome the frictional resistance on the inner cylinder, the cylinder was first rotated in air and then in water. The difference between running in air and water would then give an estimation of the power required.

Results

For an initial investigation the Power consumed was analysed on two occasions referred to as, "Power: Test A" and "Power: Test B" for a range of speeds between 4-10 hz corresponding to Reynolds numbers between 14,700 and 36,700. To enable the end disks losses to be calibrated the experiments were carried out at a series different depths. For each speed several measurements of the power consumed and the depth of the water were taken. The averaged data for "Power: Test A" is presented in table 3.4, for this test only one depth was used and speeds ranges from 4-9 hz. For Test B two other depth were used and this is presented in table 3.5. Due to the

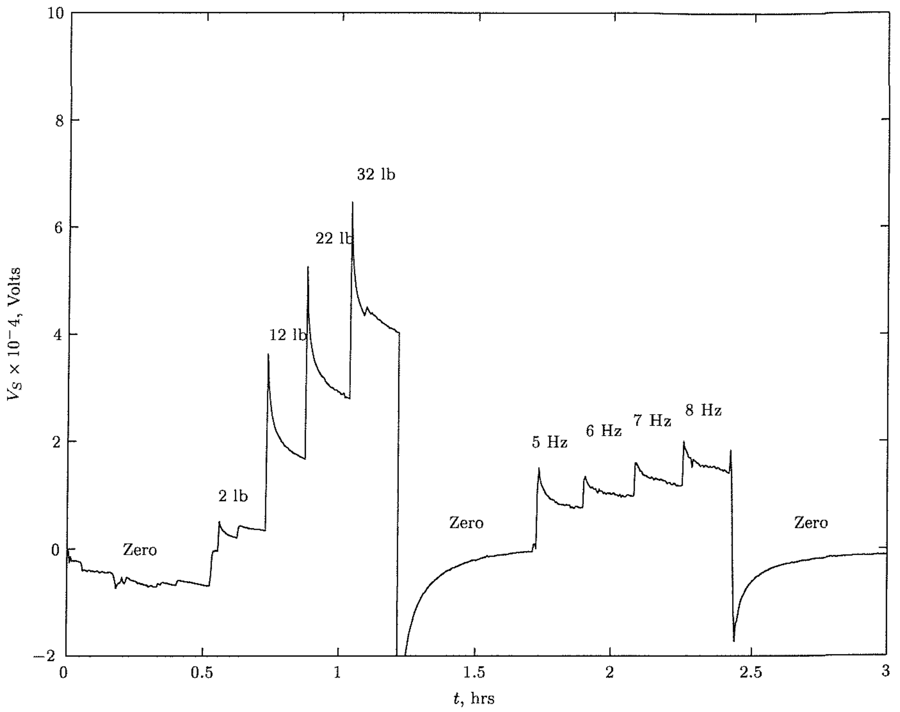

Figure 3.20: Dyno: Test B, Voltage trace from 2^{nd} test. (1 Hz is equivalent to $Re = 3640$)

small changes in power and the accuracy of the power analyser it was felt inappropriate to take depth readings for the speeds of 4 and 5 hz.

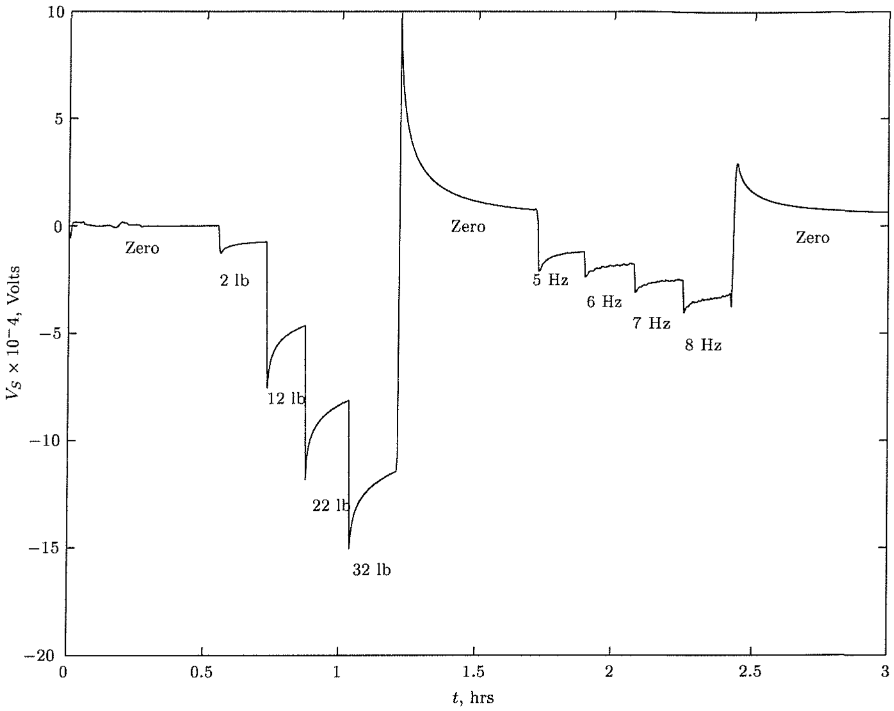

Figure 3.21: Dyno: Test B, Voltage trace from 3rd test. (1 Hz is equivalent to $Re = 3640$)

Test Case	F_c (lb)	M_c	$V_O \times 10^{-3}$	$\frac{V_O}{M_c} \times 10^{-6}$
Dyno: A	2	1.27	0.102	79.7
	12	7.64	0.641	83.4
	22	14.01	1.20	85.3
	32	20.28	1.75	85.9
Dyno: B	2	1.27	0.025	19.8
	12	7.64	0.137	17.9
	22	14.01	0.235	16.8
	32	20.28	0.353	17.3
Dyno: C	2	1.27	0.062	48.7
	12	7.64	0.360	47.0
	22	14.01	0.694	49.6
	32	20.28	1.027	49.9

Table 3.2: Torque Calibration of the three tests

Test Case	Hz	Re	$V_O \times 10^{-3}$	M
Dyno: A	5	18,200	0.125	1.49
	6	22,000	0.297	3.55
	7	25,700	0.398	4.76
	8	29,400	0.531	6.35
Dyno: B	5	18,200	0.0672	3.73
	6	22,000	0.0952	5.29
	7	25,700	0.112	6.22
	8	29,400	0.134	7.47
Dyno: C	5	18,200	0.136	2.79
	6	22,000	0.211	4.32
	7	25,700	0.273	5.59
	8	29,400	0.347	7.11

Table 3.3: Torque Comparison for the three tests

Speed	Re	Empty	Part filled		Full
(Hz)		P_S, watts	P_S, watts	L, mm	P_S, watts
4	14,700	75.7	76.5	45	78.5
5	18,200	78.6	81.5	83	86.0
6	22,000	74.7	83.0	110	92.5
7	25,700	77.3	91.8	126	107.5
8	29,400	79.1	106.5	151	132.5
9	33,000	83.2	125.2	160	163.0

Table 3.4: Averaged results from the first power analysis (Power: Test A)

Speed (Hz)	Re	Empty	Part filled: Case 1		Part filled: Case 2		Full
		P_S, watts	P_S, watts	L, mm	P_S, watts	L, mm	P_S, watts
4	14,700	77.7	-	-	-	-	81.5
5	18,200	78.2	-	-	-	-	86.7
6	22,000	78.7	84	85	84.5	113	91.2
7	25,700	80.85	94	56	95	115	110
8	29,400	83.2	104.2	73	108.6	159	132
9	33,000	86.85	123.5	125	126	160	162.5
10	36,700	91	142	114	143.4	135	197.4

Table 3.5: Averaged results from the second power analysis test (Power: Test B)

§3.5.3 Analysis and Discussion of the Torque Results

To produce an empirical estimation of the friction loss in the complete rig Bilgen & Bilgous's equations were used to calculate the friction in the gap between the cylinders. The estimation for the end gap, which can be represented by an enclosed rotating disk, were calculated using Dorfman's approach [27] as presented in the appendix §B.2. This method also includes a small end gap between the rotating disk and the casing, which is effectively the end condition in the experimental rig. If more accurate readings were possible many more tests would have been carried out. The results from both the dynamometry tests and the power analysis is presented in figure 3.22 for the full geometry and are compared with the empirical estimation. Firstly it is clear that there is a general trend with the power tests over estimating and the dynamometry test under estimating.

The power lost in the 3-phase motor, used in the experiments, is not purely a function of motor speed and the applied load. The power losses in the motor are composed of several components, principally: the I^2R loss in the stator windings; the core loss in the stator; the power loss across the gap; I^2R loss in the rotor windings and the core loss in the rotor. These power losses in the motor are a function of the speed, used mechanical power, to drive the cylinders and other smaller factors such as the ambient room temperature. Therefore, by increasing the applied load for constant speed, it is inevitable that the total power losses in the motor would increase or decrease and be different at other speeds.

The power analysis tests appear to deviate further from the empirical estimation at higher speeds. The applied load differences, between the air and water tests, are significantly larger at the higher speeds. This could be due to the power losses in the motor being considerably greater. The difference between the two sets of data, "Power: Test A" and "Power: Test B" demonstrate the effect of ambient room temperature and the uncertainty in reading from the power analyser.

The dynamometry calculations appear to follow similar trends to the empirical estimations, although always underestimating with significantly different responses between the three bridge circuits. The three tests, all performed at the same time, have a large discrepancy between them, confirming the inaccuracy of the gauges and the problems of estimating the asymptotes for the decay patterns. It is possible that the results from the dynamometry was consistently under estimating, as due to the nature of the decay responses from the dynamometry, it is impossible to tell if enough time has been allowed for the flow to fully develop between the cylinders. The discrepancy between the power analysis and the dynamometry results could also be due to the fact that the cylinders had warped during the periods of analysing the problems with the dynamometry and the visulisation studies. There is also the possibility that the cylinders were not aligned to the same position for all of the tests.

Based upon the power analysis calculations at different depths, it was possible to give an estimate of the side friction between the cylinder by assuming:

$$\begin{aligned} M_{\text{full depth}} &= M_{\text{side gap}}(L) + 2 \times (M_{\text{endgap}}) \,, \\ M_{\text{part filled}} &= M_{\text{side gap}}(L) + (M_{\text{end gap}}) \,. \end{aligned}$$

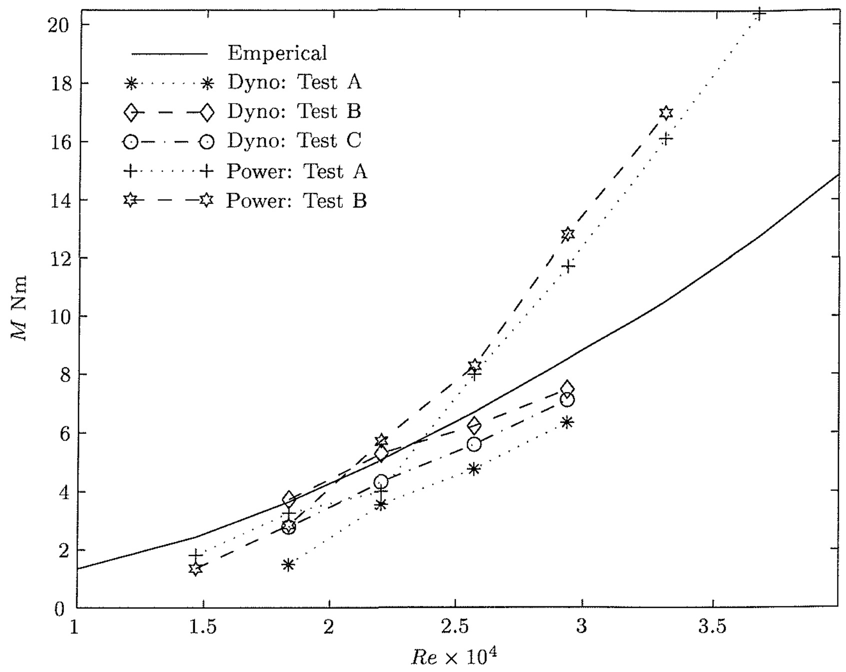

Figure 3.22: Comparison of the torque measurements with the empirical estimations for the complete rig

Using the dynamometry results it was also possible to estimate the friction by subtracting Dorfman's enclosed disk estimations. These calculations are presented in figure 3.23 which again demonstrates the large discrepancy between results. Some of the results from the dynamometry tests, show a negative torque, this not being physically possible. This demonstrates again that these results were underestimating the torque as it is unlikely that Dorfman's estimation is much more that 10% out. This graph also shows a general trend of a minimum in torque at a $Re = 2.5 \times 10^4$, which could be a flow transition. This is very speculative as it is not repeated with all of the results.

From the power analysis at different depths it is also possible to estimate the friction at the ends of the cylinders. The results are compared with Dorfman's estimations for enclosed rotating disk in figure 3.24. This graph again shows the large discrepancy at the higher Reynolds numbers.

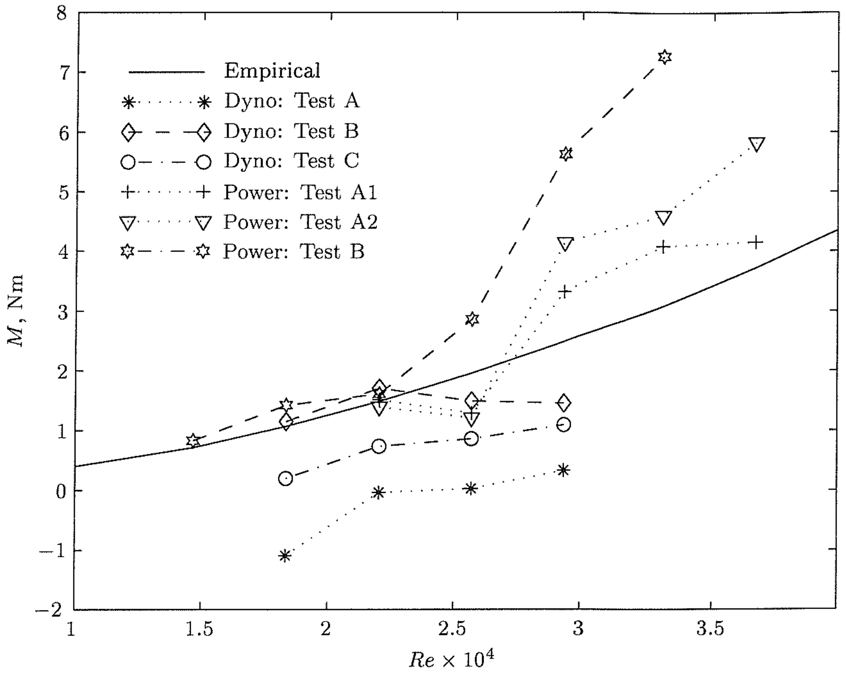

Figure 3.23: Comparison of the torque measurements with the empirical estimations in the gap between the cylinders

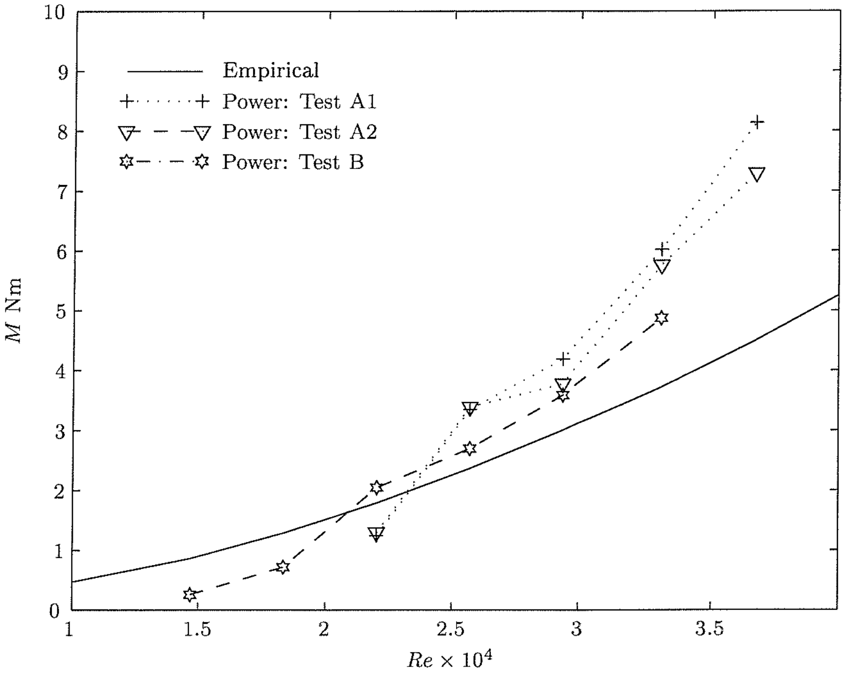

Figure 3.24: Comparison of the torque measurements with the empirical estimations in the gap enclosed disks at the top and bottom of the cylinders

§3.6 Visualisation

The use of air bubbles was considered to be a favorable method for visualization in an experimental rig of this size for a number of reasons. Due to the high speed and turbulence, it would be impractical to demonstrate Taylor vortices using dye injection. The use of fine aluminum particles or Kalliroscope would be very costly due to the total volume of the tank, large numbers of particles are required to identify the positions of Taylor vortices. For turbulent Taylor vortices, identification of sizes has proven difficult, Lathrop *et al.* [22] using Kalliroscope at high Taylor numbers, $Ta \approx 10^5$ for $\eta = 0.667$, although, more recently Parker & Merati [13] have measured turbulent Taylor vortices at $Ta \approx 10^9$ as discussed in section §2.4.

When using bubbles within the experimental rig, they are subjected to the following forces: pressure differences causing them to accumulate in areas of low pressure; forces due to flow momentum; buoyancy drag and gravity. If it is assumed that the pressure forces dominate then for the low bubble flow rates, the bubble grouping will be in the regions of low pressure, corresponding to the region of highest velocity adjacent to the inner cylinder. These regions of low pressure on the surface of the inner cylinder indicate the regions of high velocity and hence low shear stress at the wall. Thus the bubble spectrum resembles the shear stress distribution along the length of the cylinder providing information were to make geometric changes in order to reduce the torque.

The flow momentum will act as a centrifuge within a Taylor vortex either moving any particles towards the centre of the vortex or ejecting to the corners. The bubble buoyancy will cause the bubble to move towards the free surface and the drag forces on the bubble will slow the bubble speed relative to the mean flow causing an associated wake which, in turn, will affect the flow. Therefore to achieve minimal disruption to the flow the smaller the bubbles the less disruptive the visualisation.

§3.6.1 Method

The bubbles are produced by a compressor attached to a thin flexible pipe with approximately 30, 0.5 mm holes near the end. This pipe is inserted at the base of the outer cylinder up-stream of the visualisation window. The flow rate is altered by changing the compressor pressure. For this investigation, the bubbles were recorded by a digital video camera ("Panasonic", type NV-DS15) positioned as depicted in figure 3.14. The video camera image resolution is 800 kbytes, the focal length is 2.9 → 58 mm and frame rate is 50 Hz. Perpendicular to the viewing section a light source was placed in another window and all other windows were blocked to reduce reflections.

From the digital video recordings 40 "bitmap" images were saved at 0.5 ms intervals. A typical image, produced as described above, is shown in figure 3.25. The whole length of the inner cylinder is clearly visible, although the base is slightly obscured due to reflection of the base of the window. All images produced showed bubble grouping as demonstrated in the figure.

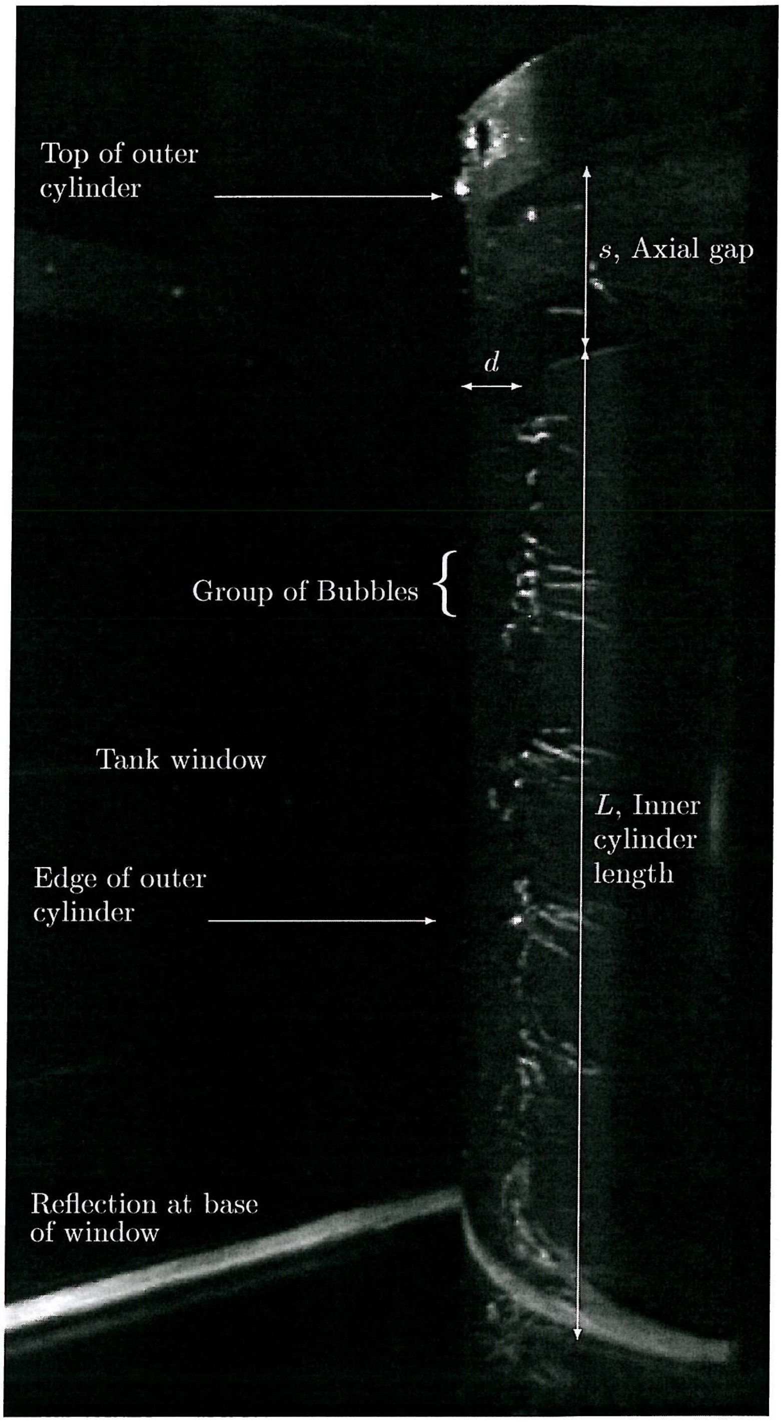

Figure 3.25: Typical image of bubbles captured using the digital video camera

§3.6.2 Bubble Analysis

In order to understand the bubble pattern and produce a spectrum of the bubble intensities along the length of the inner cylinder the images were analysed numerically using "Matlab". The raw bubble images were cropped to the size of the gap yielding an image of 30×4800 pixels. These cropped image were then converted to a gray scale negative. Filtering to a specific gray scale threshold is then performed to remove the background leaving only bubbles. Altering the threshold level had a little effect on the overall pattern but helped by removing noise produced by background light. The bubble spectrums are then computed along the length by summing gray scales across the gap and scaled such that 256 would represent a line of white pixels and 0 a line of black.

This process, is demonstrated in figures 3.26 and 3.27 both at a speed of 8hz, $Re = 29400$. The full set of spectrum images is presented in the appendix §C.3 at intervals of 0.5 ms. These images demonstrate that the number of bubble grouping at $Re = 29400$ oscillated between 5 and 6. As discussed in section §2.4, Djéridi *et al.* [43] observed bubbles between vortices but Atkhen *et al.* [42] observed bubbles between pairs of vortices. Assuming that the bubble grouping was between every pair of vortices this then corresponds to wavelength spacing of between 33% to 60% larger than the critical wavelength expected for laminar Taylor vortices. This is within expected ranges of Koschmieder [48] observations on turbulent Taylor vortices. The regions of low pressure for turbulent Taylor vortices are calculated numerically later in the thesis. A numerical result for the whole domain is compared in Chapter 6, confirming bubble grouping at the vortex outflow from inner cylinder.

Further insight into the nature of the bubble patterns were gained at a higher bubble flow rate, by increasing the compressor pressure, as presented in figure 3.28. These images show vortex formation and indicate that these vortices are large and occupy most of the gap as expected. The bubbles also appear to have a small scale wavy path demonstrating turbulent fluctuations in the flow field. It is not clear what is causing the flow to oscillate between 5 and 6 pairs of vortices, but this is probably due to experimental irregularities, such as warping of the inner and outer cylinders or an oscillation due an axial flow caused by the pressure difference between the inside and outside the outer cylinder.

For the higher bubble flow rates the bubbles tended to move around the Taylor vortex. As the vortex centre is closer to the outflow boundary from the inner cylinder the bubble will take the shortest path around the vortex to return to the region of lowest pressure. Hence, the large gaps between bubble clustering due to the low probability of the bubble at the boundary of the vortex inflow moving towards the inner cylinder.

i: Raw bubble image

ii: Cropped and filtered negative

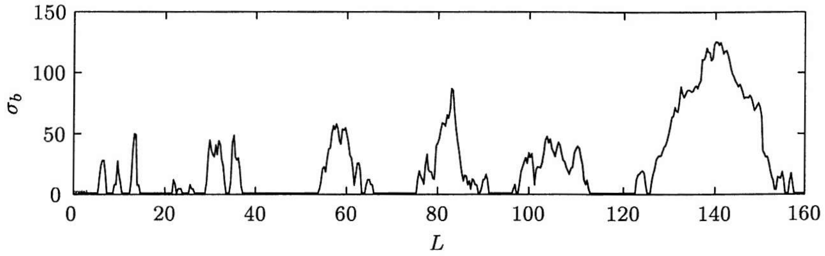

iii: Bubble spectrum along the length

Figure 3.26: Instantaneous bubble spectrum for $Re = 29400$ at 6.5 ms

i: Raw bubble image

ii: Cropped and filtered negative

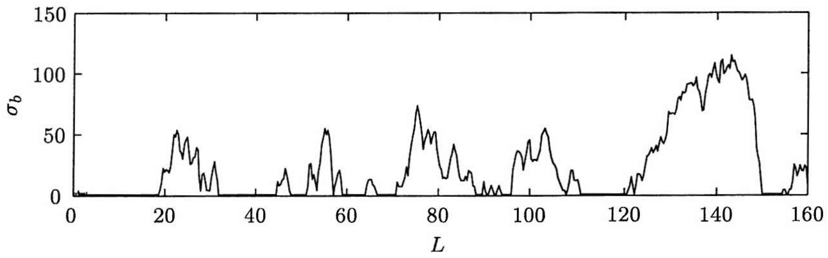

iii: Bubble spectrum along the length

Figure 3.27: Instantaneous bubble spectrum for $Re = 29400$ at 7.5 ms

i: ii: iii:

Figure 3.28: Set of three images of bubbles in the experimental rig at a higher bubble flow rate

§3.7 Recommendations for the Future of the Experimental Facility

As stated in the introduction the initial aims of the experiential facility have not been fulfilled to their full potential in studying turbulent Taylor vortices in the thruster unit. Although any firm conclusions can not be drawn from this first investigation, it is however possible to conclude that the Bilgen & Bilgous equations seem to be approximately correct. Further more accurate torque readings would be required to confirm this using a fully working dynamometry. The visualisation studies have provided evidence of unstable Taylor vortices forming across the gap and Görter type vortical patterns occurring at the inner cylinder. A novel method of vortex identification has also been developed, by using digitised images of bubbles it has shown to be possible to produce a spectrum of vortex intensities along the length of the gap.

From the achievements and shortfalls of the first prototype, it is possible to produce a list of recommendations for future developments of the experiential facility to produce more in-depth research into turbulent Taylor vortices.

I. Due to the problems of warping in the wooden cylinders in the first prototype testing over the short tests periods, it is evident that a stiffer water repellent material would be more appropriate for the future especially as it would be hoped that longer more complex measurements would be carried out. A light high grade plastic would be generally more preferable than using metal as assembling two large and heavy cylinders that are only 10mm apart would be a difficult and cumbersome problem. Using flexible plastic to form the outer cylinder still appears a reasonable choice as it was possible to visualise across the gap using the 2mm polycarbonate. However it may be possible to improve the optics by using a higher grade of plastic that has been heat formed although this would still lead to joints between sections. The only way to overcome this problem is to have the outer cylinder spun as a expensive "one-off" job.

II. During the latter stages of writing the thesis it came apparent that the wrong material constant was used for the design of the flexures. Thus, replacing the flexures with steel ones or placing the existing aluminum flexures further apart would resolve the problems with the dynamometry. To further improve the torque measurements further, it would be more preferable to use as many devices as possible, to produce more accurate results. Hence, the use of an "off the shelf" torque metre on the shaft would make a preferable addition to the facility. If the inner cylinder were to be accelerated at high speeds causing high inertial forces, then it could be decoupled for those tests.

III. To improve the visualisation it may be possible to correct the refraction, by placing a piece of curved material, the same as used for the outer cylinder, in the opposite direction. The use of a specially commissioned lens to magnify the image may also be preferable but these factors could lead to a degradation in the light strength unless high grade material are used. The problem due to refraction can be eliminated by using refractive index matched fluids, although these fluids usually tend to be mildly toxic and large amounts would be required to fill the tank.

IV. The bubble visualisation studies could be advanced by controlling the bubble feed with a flow metre and several bubble feed points. This would enable bubble intensities in the vortices to be characterized with the volume of air contained in the bubbles. To reduce bubble coalescing salt can be added to the water [49], such as Magnesium Sulphate ($MgSO_4$) used in very low concentrations by Zenit *et al.* [50]. Minimizing reflections inside the tank would also be beneficial. Using a digital video camera with a higher resolution would also help improve the accuracy of calculated bubble spectrum.

V. The velocities in the gap between the cylinders could be measured using either Laser Doppler velocimetry, LDV or particle image velocimetry, PIV. Either of these technique could lead to invaluable information on vortex strengths and turbulent intensities. If such techniques were going to be used on the next development this would lead to specific design requirements for the use of lazers.

VI. Controlling the motor with feed back from a tachometer would lead to improved speed control and the possibility of variable ramp acceleration.

CHAPTER

4

Laminar Flow Modelling

§4.1 Introduction

The initial aims of the modelling laminar Taylor vortices, were to demonstrate that the numerical method used in ELMORE, an in-house Navier-Stokes code, could be used to study Taylor vortices. By assuming that the vortices are steady and not travelling in waves around the inner cylinder the domain can then be simplified to a 2-D axial slice. Using this 2-D domain the effect of Reynolds number, aspect ratio and mirror boundaries were studied in order to have an understanding of the effect of topology. From this knowledge a single domain can then be used when analysing the effect of turbulence models without the need for various aspect ratio changes.

The first part of the chapter starts with a brief introduction to Navier-Stokes codes and the finite volume method including pressure correction and interpolation methods used in ELMORE. Secondly the topology is defined for the analysis. The numerical properties including the grid independence is then discussed for these laminar solutions. Next the results from studies in the effects of Reynolds number, aspect ratio and boundary condition are given. Finally conclusions are drawn from this investigation and recommendations for the direction of the turbulence studies are given.

§4.2 Navier-Stokes Method

The most commonly used CFD codes used are based upon the Navier-Stokes equations. The methods solving the equation are beginning to reach a mature stage, and the computer codes are already so many that it is not possible to make a full list. There are a number of research codes widely documented in the technical literature, along with commercial codes, and in-house codes developed at several research institutes, government institutes, industry, etc. The four most used commercial codes to date are STAR-CD, CFX, PHOENICS and FLUENT all having sophisticated user interfaces and are integrated with post-processing facilities. They are designed to perform computations on general configurations and have robust solvers. Research codes generally lack the utilities of the codes available in the market but tend to perform better for specific applications such as wings and internal flows, for which they have been developed for.

During this research both an in-house code, ELMORE, and a commercial code CFX have been used, both of which are based upon the finite volume method. ELMORE has been developed by Dr. N. Bressloff at Southampton University and is also being used for other fundamental research in the School of Engineering. For example, three-dimensional pulsatile flow through asymmetrically and symmetrically constricted vessels. [51]

The finite volume method for Navier-Stokes solvers consists of three basic steps: an integration of the momentum equations over the finite control volume; discretization of the integral equations to a system of algebraic equations; solution of the algebraic equations by an iterative method. The components for all flow variables, ϕ therefore are expressed for each finite cell as an exact conservation. This conservation can be represented by:

$$\left(\begin{array}{c}\text{Rate of change}\\ \text{of } \phi \text{ in the}\\ \text{control volume}\end{array}\right) = \left(\begin{array}{c}\text{Net flux of } \phi \text{ due}\\ \text{to convection into}\\ \text{the control volume}\end{array}\right) + \left(\begin{array}{c}\text{Net flux of } \phi \text{ due}\\ \text{to diffusion into}\\ \text{the control volume}\end{array}\right) + \left(\begin{array}{c}\text{Net rate of creation}\\ \text{of } \phi \text{ inside the}\\ \text{control volume}\end{array}\right)$$

There are a number of different methods for solving the discretized equations. The most common method, used in both CFX and ELMORE, is to solve the equations on two levels: a number of sweeps of a linear equation solver to compute the spatial coupling for each variable and an overall iteration to solve the coupling of the variable.

The underlying topological structure of both CFX and ELMORE are based on the multi-block grid methodology using curvilinear structured grids to define the finite volumes. This method involves the use of a set of blocks, which are glued together, on each of which there is a structured grid. Topological features within the domain are then described using the concept of a patch. Thus mirrors, rotating faces and solid regions, for example, are all described by different types of patch.

To model Taylor-Couette flow it would be preferable to use polar co-ordinates rather than than the curvilinear body-fitted grid to define the geometry, as used in ELMORE and CFX. The use of polar coordinates would cause several changes, the main being that discretization would be much simpler than that of curvilinear system and hence produce a faster convergence. It would be possible to convert ELMORE into a polar co-ordinate code but this would require considerable reworking of the code beyond the time constraint of the research work. This also would have the effect of hindering the development of the code for other problems, used in the School Engineering Sciences, as additions to the code would not be directly transferable.

When solving the Navier-Stokes equations using the finite volume method a pressure correction is required to conserve the mass flow. To produce the pressure correction equation it is derived from the continuity equation on the velocity field and the conservation of momentum. The solution of this equation then produces the corrected pressure field and velocities so that the mass is conserved. In ELMORE the SIMPLEC algorithm is used for steady state problems and PISO for transient problems.

The SIMPLEC (SIMPLE-Consistent) algorithm Van Doormal *et al.* [52] is a variation to the SIMPLE (Semi-Implicit Method for Pressure-Linked Equations) derived by Patankar *et al.* [53] but omits terms that are less significant. Hence the SIMPLEC algorithm is used in ELMORE as instead of the more commonly used SIMPLE algorithm. For transient calculations in ELMORE the non-iterative PISO (Pressure Implicit Splitting of Operators) algorithm developed by Issa [54] was used for the transient startup problem discussed in the latter parts of the thesis. This algorithm relies on the temporal accuracy gained by the discretization as the procedure solves the momentum equations using the pressure from the previous time-step. As the PISO method does not require iterations within a time level it is considered to be less expensive that transient approaches using the SIMPLE type algorithms. The PISO algorithm has yielded accurate results with sufficiently small time steps [55]. It can also be used to simulate flow at all speeds in ELMORE [56], from laminar to compressible turbulent flow.

§4.3 Topology

The problem considered is that of steady state Taylor vortices between a rotating inner cylinder and a stationary outer cylinder, as shown schematically in figure 1.4. The flow is solely induced by the relative motion of the inner cylinder. Assuming that the vortices are uniform and not travelling in waves around the cylinders, the domain can then be simplified as a 2-D axial slice with a pair of periodic boundaries. A typical mesh for the domain is shown in figure 4.1.

To test the periodic boundaries and to assess the effects of the end boundaries, the domain was set up with a uniform grid distribution, with different patches for the stationary, rotating and mirror conditions. The following investigation was carried out using a 2mm gap and an inner radius of 0.128 at speeds around the critical Taylor number, calculated using equation 2.17. A uniform grid distribution was not used as positions of high gradients in the variables were not known. This information would be required for the specification of expanding and contracting grids.

A typical solution is represented in schematic figure 4.1. This figure shows the relative position of a pair of vortices and indicates the position of the inflow and outflow boundaries and vortex centres. For these laminar tests several lengths were chosen to study the effect of aspect ratio for each of the three boundary conditions. For these tests 1-8 Taylor vortices were produced.

§4.4 Solution Procedure

For the laminar simulations in this chapter only results using the in-house code ELMORE are presented. Prior to this research, ELMORE had been tested extensively for several laminar problems and has been bench-marked for standard test cases, such as lid-driven cavities and back-step flows. Therefore a formal comparison between CFX and ELMORE was not considered to be required. All of these calculations were steady state and hence the SIMPLEC algorithm

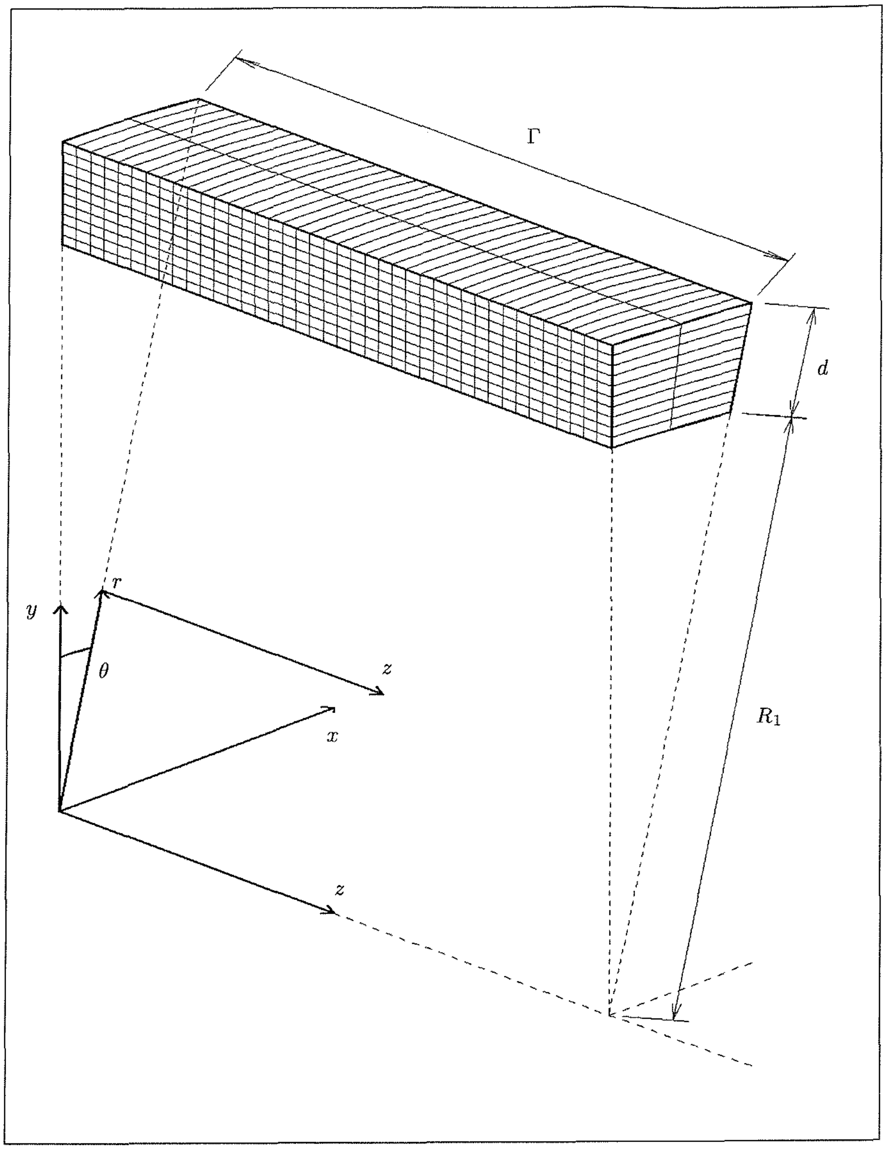

Figure 4.1: Schematic illustration of a typical grid

was used.

The Van Leer's curved line advection method (CLAM) [57] was used for interpolation of the momentum equations in ELMORE for these laminar simulation. It has the advantage that it is a second order scheme and does not suffer as much from 'under-shoots' and 'over-shoots' compared to the more commonly used quadratic upstream interpolation for kinetic (QUICK) variables scheme due to Leonard [5]. For the pressure the hybrid differencing scheme has been used, which is a combination of central and upwind differencing dependent upon a Peclet number [5]. For a low Peclet number it is equivalent to central differencing and for a high Peclet number it is equivalent to upwind differencing. To solve these discretised equations the strongly implicit procedure (SIP) has been used, as it is generally known to work well with curvilinear coordinate systems.

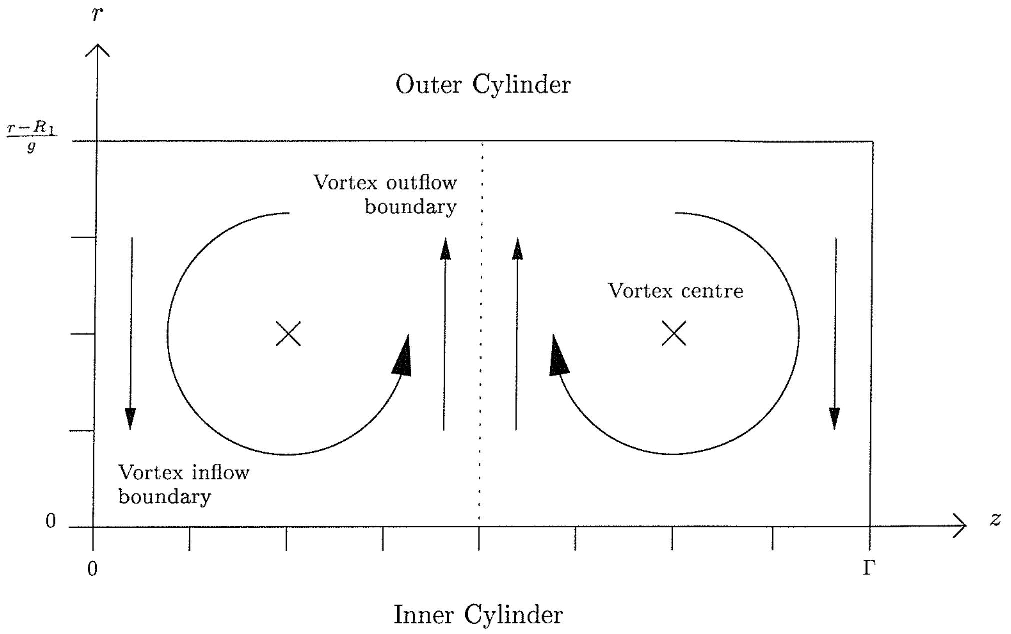

Figure 4.2: Schematic illustration demonstrating the position of a pair of vortices in the domain

§4.5 Numerical Properties

For a steady state flow, the iterative convergence indicates that as the discrete equations are iterated, the computed simulation results approach a fixed value. The iterative convergence of the simulations presented in this thesis were assessed by investigating the residuals. In ELMORE the residual error was calculated from the difference of the sum of the variable throughout the flow field per iteration. Any oscillatory motions in the residuals should be relatively small and dampen during the course of the solution if a steady state of Taylor vortices is sort. This level of residual must reduce by several orders of magnitude to ensure an accurate solution has been produced. The normal convergence criteria is known as the mass source residual, which is the error in the mass conservation. Simply checking the solution for constant mass source residual did not prove adequate as the secondary flow of Taylor vortices were found not to have converged. With no or small changes in mass source residual, the size and even the number of vortices were changing. Hence, to ensure a iterative converged solution had been reached the residuals for each of the variables were checked. For the laminar results presented in this chapter all residual errors reduced by six orders of magnitude.

The iterative convergence of the simulations was affected by the under-relaxation parameters and time step size for transient calculations. It was found that small changes in the under-relaxation parameters strongly influenced the convergence of the solution. From experience suitable under-relaxation parameters were chosen to produce fast stable solutions. By setting all the relaxation factors to around 0.5 the solution was found to converge for all cases. It was possible to reduce the iterative convergence time by increasing the relaxation for the momentum variables by small amounts after the Taylor vortices had formed and begin to stabilise.

When controlling the iteration process the number of sweeps of the linear equation solvers required to solve the simultaneous equations needs to be specified. To ensure that the velocity field satisfies the continuity equation, more iterations are required for the pressure correction than the momentum equations. It was found that 3 sweeps of the momentum equations and 5 sweeps for the pressure equations were sufficient.

For the SIMPLEC algorithm initial conditions are required to initiate the solution. A good initial guess can considerably reduce the convergence time. By overestimating the initial conditions or setting the azimuthal velocity to zero the solution was found to diverge. For all test cases low azimuthal velocities were specified of around 5% the speed of the inner cylinder, unless data at a lower speed was available for the initial guess.

A numerical method can be stated to have grid convergence, if the solution of the discretised equations tends to the exact solution as the grid spacing tends to zero. For purely linear problems this is possible with appropriate discretisation. For these laminar simulations the convergence was checked on a series of successively refined grids. This is dealt with in the following section §4.6 as a series of grid independence tests for each of the boundary conditions. Convergence of a grid independent solution is only possible providing that the discretisation process is consistent and the solution is stable.

All numerical solutions should also lie within proper bounds and hence all solutions have been checked for boundedness. For the tests presented in this thesis, the velocity components must be between zero and the speed of the inner cylinder, or near the speed of the inner cylinder for turbulent flow, and the turbulent kinetic energy must always be positive. There must also be conservation of mass flow through the domain. Finite volume with the SIMPLEC pressure correction and second order discretization is generally considered to produce a satisfactory realisability of the flow features for laminar problems.

In summary main causes for a diverging solutions were found to be:

- insufficient mesh density or poor quality;
- insufficient number of sweeps for the inner iteration;
- incorrect relaxation factors;
- poor initial conditions.

§4.6 Grid Independence Tests

As stated three different boundary conditions were considered, therefore three sets of grid independence data are presented for the stationary walls, rotating walls and mirror ends respectively. For each of the conditions the grid density was doubled five times to demonstrate grid independence. All of the grids are based on a uniform distribution in both the radial and axial direction. The lowest grid density in all cases was defined by placing just 4 cells across the gap and defining the axial number such that square cells were produced. Simply by comparing the skin friction between grid densities it was not possible to prove a grid independence solution. Therefore, the details of the solution had to be analysed further. For all three conditions the azimuthal velocity profiles in the axial and radial directions, Taylor vortex strengths and the axial and azimuthal coefficients of friction are all compared.

The coefficient of friction, C_M is normally considered as the component of the shear stress. For the case of stationary and rotating walls the mean C_M will be only be a function of u_θ for the whole domain. When considering a particular vortices there is an a frictional component due to u_z at the wall. When calculating the shear stress at the wall due to one Taylor vortex then the skin friction will be a function of both u_θ and u_z. By way of example C_{M_θ}, the azimuthal component of friction, was calculated from,

$$\tau_{w_\theta} = \mu \left(\frac{U_1 - u_\theta}{\Delta n} \right), \tag{4.1}$$

where Δn is the distance of the first cell from the wall and u_θ is the associated velocity. Thus the moment acting on the inner cylinder is,

$$M_\theta = 2\pi R_1^2 L \ \tau_{w_\theta}. \tag{4.2}$$

Applying equation §4.6 to the definition of C_M given in equation 2.35,

$$C_{M_\theta} = \frac{4}{\nu U_1^2} \left(\frac{U_1 - u_\theta}{\Delta n} \right). \tag{4.3}$$

The strength of the Taylor vortices has been described using a non-dimensional parameter, Ψ. Where Ψ is a 2D representation, in the $r-z$ plane, of the vortex strength as the integral of vorticity over the area of the vortex. This is defined by the equation below:

$$\Psi = \int_0^R \int_0^\Gamma \frac{1}{U_1} \underbrace{\left(\frac{\partial u_r}{\partial z_n} - \frac{\partial u_z}{\partial r_n} \right)}_{\text{vorticity}} dz_n \, dr_n. \tag{4.4}$$

Where, z_n and r_n are the non-dimensional positions in a particular the vortex, z/d and $(r - R_1)/d$ respectively.

To identify the vortex boundaries the radial velocity was summed across the gap. This distribution was then interpolated using a cubic spline fit onto a much finer spacing to improve accuracy. The vortex outflow can then be found from the maximums in this distribution. The vortex inflow are similarly identified by the minimums in this distribution.

Grid Dimensions	CV	Approx. No. of Iterations	Approx. CPU Time	$\overline{C_M}$
16×4	64	500	0h02	0.0219
32×8	256	2500	0h10	0.0229
64×16	1024	4000	0h30	0.0254
128×32	4096	11000	2h10	0.0267
256×64	16384	34000	27h30	0.0294

Table 4.1: Comparison of grid densities, CPU time stationary and C_M end walls, $Re = 384$ and $\Gamma = 4$

An aspect ratio, $\Gamma = 4$, was used to test for grid independence at a $Re = 384$, which is $1\frac{1}{2}Ta_c$. This means that Taylor vortices were present but at a low enough Ta that they were not wavy. The grid was defined with uniform grid distribution in both the axial and radial direction with the same size spacing. Five grid sizes were tested and the results are presented in table 4.1 and in figure 4.3. The CPU times are based for a single CPU at 500Mz. As some of the calculations were carried out in parallel hence only approximate CPU times are presented.

All results except the 16×4 show good alignment with the mean velocity profile, and at the vortex inflow and outflow interpolated at the boundaries of the second vortex. The azimuthal velocities also align well in the mid plane with small increases in length for the first and last vortex. The length of the first vortex increase by 9% between 64×16 and 128×32 grid densities and then by a further 4.5% between 128×32 and 256×64.

The shear stress values in table 4.1 show a gradual increase in shear stress. This is explained in figure 4.3.iii as towards the stationary end wall there is an increase in shear stress. As the boundary layer velocity at the end wall approaches zero but at the rotating cylinder it approaches the speed of the inner cylinder. This causes a singularity at the corner between the stationary end wall and the rotating cylinder. Taking this into account the shear stress at the inner cylinder will not demonstrate grid independence.

To analyse the data further the vortex strength, axial and radial components of skin friction were calculated for each of the four vortices and these vortex properties were interpolated for $\lambda/2 = 1$. These results are shown in the logarithmic plot 4.3.iv. Both the vortex strength and axial shear stress tend towards a single value with increasing grid density. While the axial shear stress shows a gradual increase with grid density due to the singularity.

The rotating end boundary was also tested at $Re = 384$ and $\Gamma = 4$ for five grid densities. The CPU times and shear stress at the inner cylinder are presented in table 4.2. The data is plotted as before in figure 4.4. These results again show good convergence for the velocity profiles except for 16×4.

The skin friction distribution in figure 4.4.iii demonstrates a much improved convergence along the inner cylinder. There is no singularity as both boundaries are rotating, therefore the boundary layer is tending to the same value. This is reflected in the logarithmic plot 4.4.iv, as

Grid Dimensions	CV	Approx. No. of Iterations	Approx. CPU Time	$\overline{C_M}$
16×4	64	500	0h02	0.0183
32×8	256	2400	0h10	0.0170
64×16	1024	2500	0h30	0.0165
128×32	4096	10000	2h00	0.0165
256×64	16384	33000	22h30	0.0165

Table 4.2: Comparison of grid densities, for rotating end walls, $Re = 384$ and $\Gamma = 4$

all properties for the interpolated vortex length are tending to a single value.

Grid Dimensions	CV	Approx. No. of Iterations	Approx. CPU Time	$\overline{C_M}$
4×4	16	650	$0h02$	0.0193
8×8	64	2700	$0h8$	0.0180
16×16	256	5000	$0h24$	0.0174
32×32	1024	16000	$1h10$	0.0172
64×64	4096	36000	$9h00$	0.0172

Table 4.3: Comparison of grid densities with the mirror end condition, $Re = 384$ and $\Gamma = 1$

To test the mirror boundaries the length was reduced such that $\Gamma = 1$. This meant that only one Taylor vortex formed and therefore the effect of grid density on just a vortex can be demonstrated. The results are analyzed in the same way and are presented in table 4.3 and figure 4.5. For the velocity profiles and the skin friction at the inner cylinder convergence good convergence is achieved apart from the 4×4 problem.

The logarithmic plot 4.5.iv demonstrates convergence to a single value for both the vortex strength and the azimuthal skin friction, with increasing grid density but the axial skin friction decreases. This is expected but not apparent for the other two boundary conditions. As the Taylor vortex itself has associated boundary layers, therefore velocity at the wall of the inner cylinder the axial velocity should be approaching zero. Hence, the skin friction should tend to zero.

To be able to resolve the Taylor vortex boundary layers clearly, a very high grid density or an expanding and contracting grid is required. To be able to resolve in detail the boundary layer between the inflow and outflow boundaries an adaptive grid procedure would be preferable. These measures however would be problematic due to the singularities that exist between the rotating and stationary boundaries and the need for high parallelisation for the large grid densities.

Therefore, for the following tests into the effects of boundary conditions, aspect ratio and

Reynolds numbers on the properties of Taylor vortices, a uniform grid with 32 nodes across the gap was chosen. This is a compromise due to the steep increase in CPU time required, if 64 nodes are used across the gap. Such fine details do not need to be resolved, in order to make comparisons between the much larger physical changes and grid independence was proved.

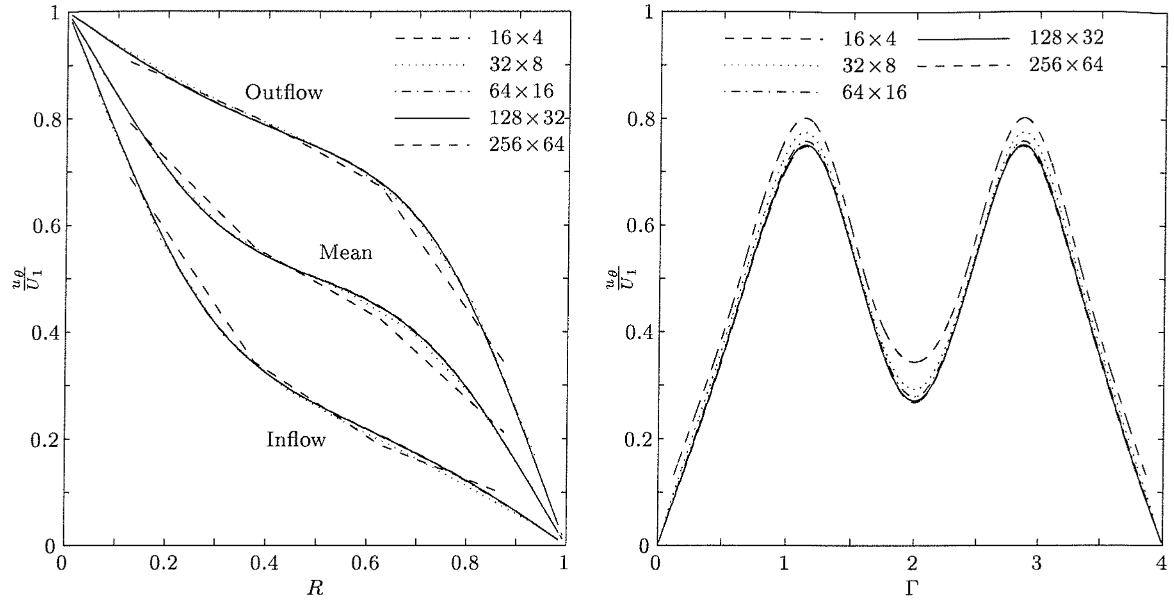

i: Azimuthal velocity profile across the gap for the 2nd vortex.

ii: Azimuthal velocity along the length in the middle of the gap.

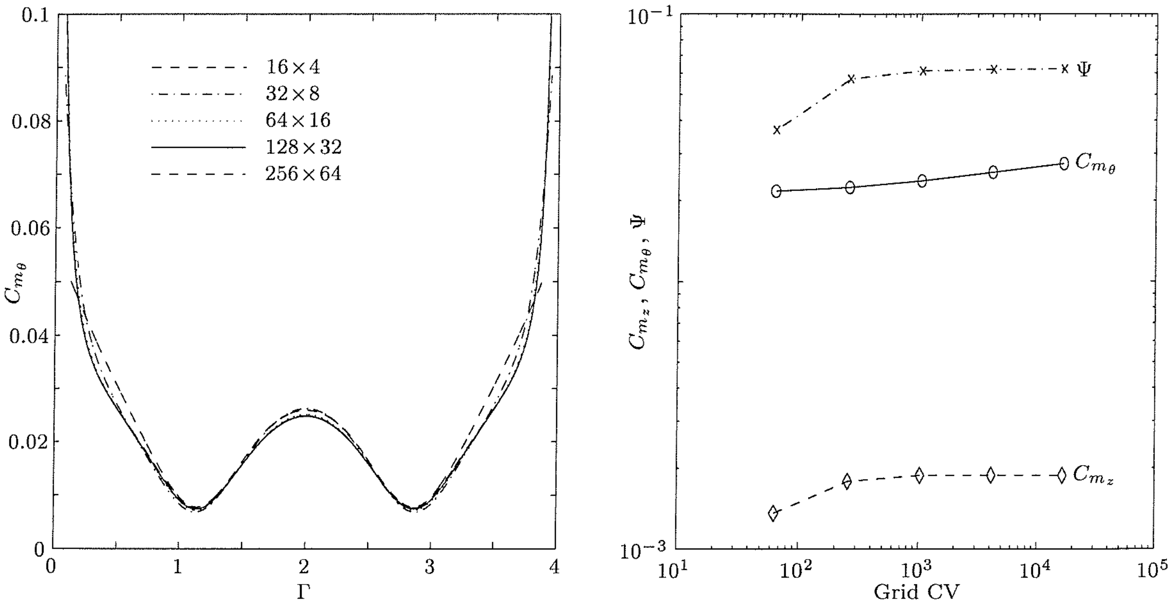

iii: Shear stress along the length of the inner cylinder.

iv: Logarithmic comparison of vortex properties interpolated for $\lambda/2 = 1$.

Figure 4.3: Effect of grid density with stationary end boundaries, $Re = 384$ and $\Gamma = 4$.

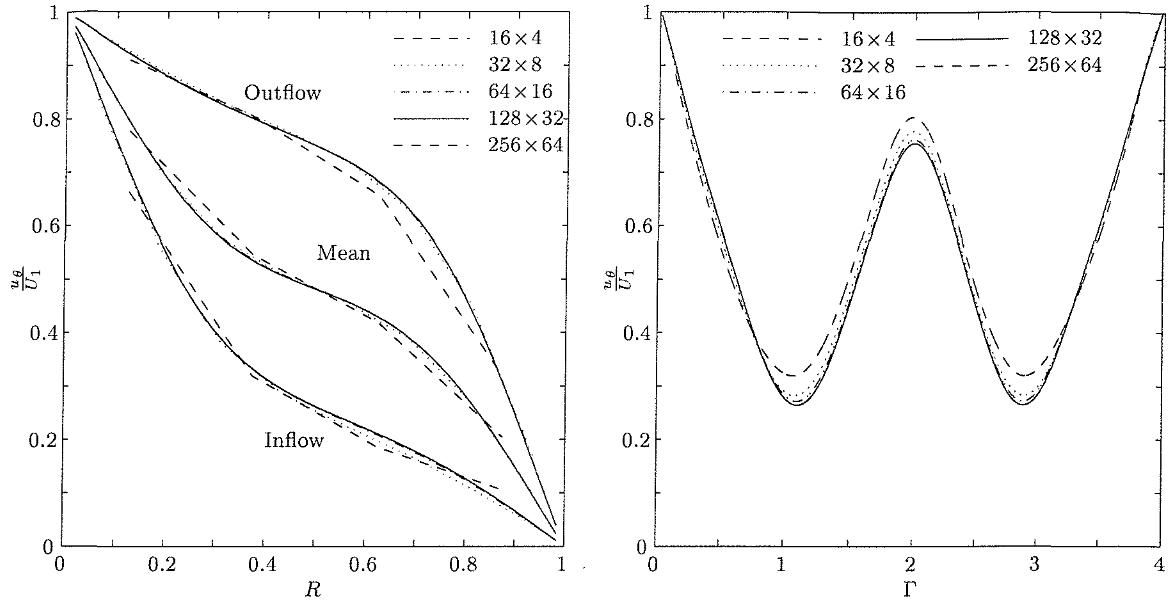

i: Azimuthal velocity profile across the gap for the 2^{nd} vortex.

ii: Azimuthal velocity along the length in the middle of the gap.

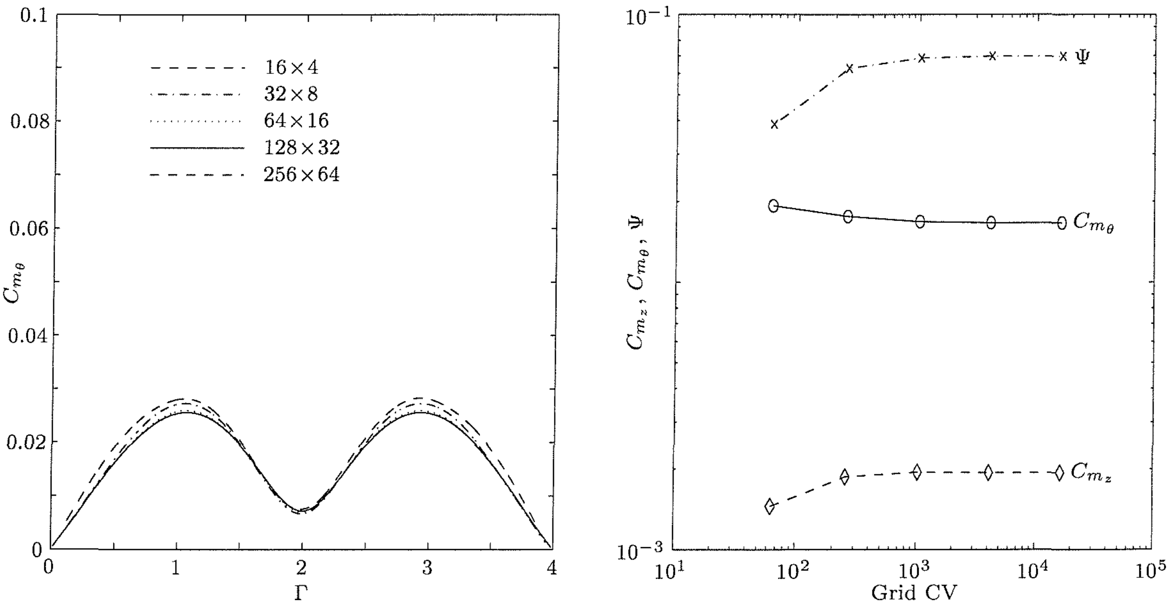

iii: Shear stress along the length of the inner cylinder.

iv: Logarithmic comparison of vortex properties interpolated for $\lambda/2 = 1$.

Figure 4.4: Effect of grid density with rotating end boundaries, $Re = 384$ and $\Gamma = 4$.

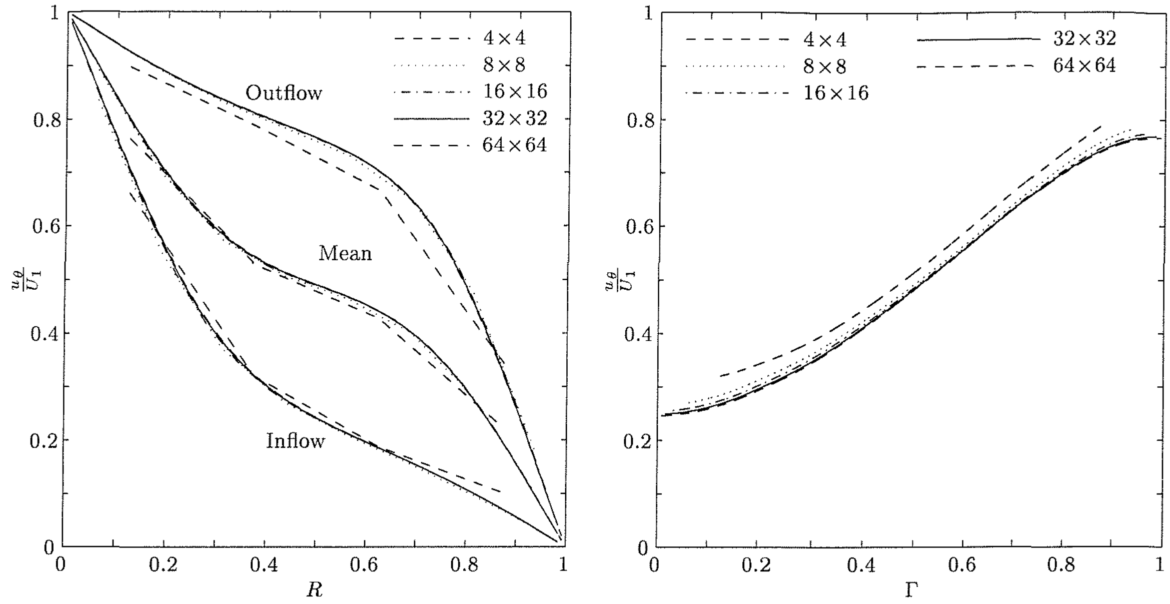

i: Azimuthal velocity profile across the gap.

ii: Azimuthal velocity along the length in the middle of the gap.

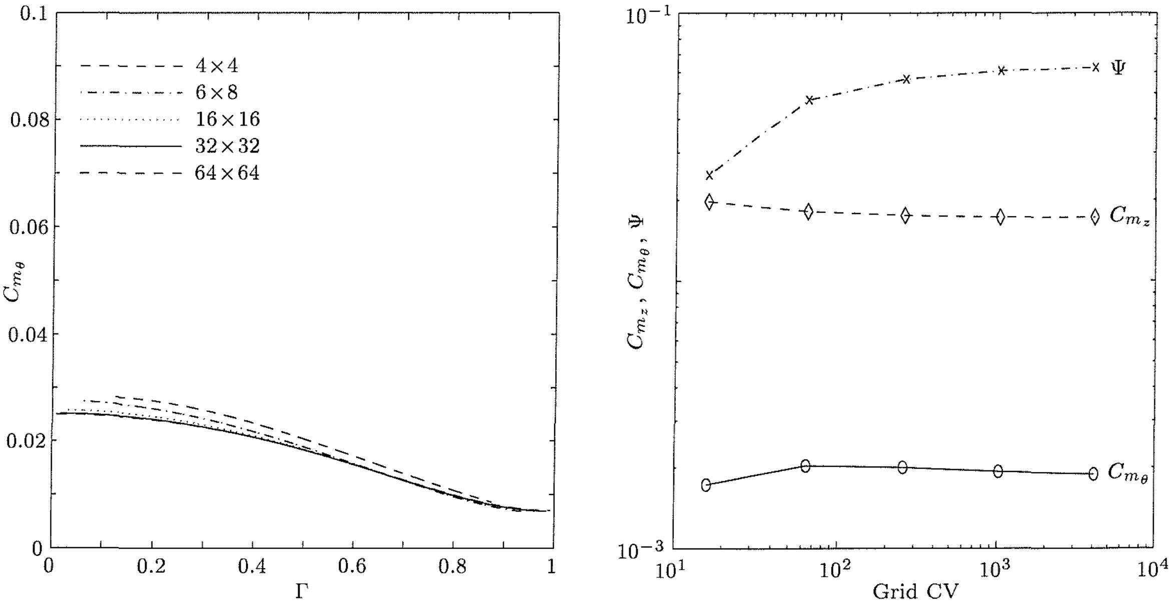

iii: Shear stress along the length of the inner cylinder.

iv: Logarithmic comparison of vortex properties.

Figure 4.5: Effect of grid density with mirror end boundaries, $Re = 384$ and $\Gamma = 1$.

§4.7 Results and Discussion

A typical result is presented in figure 4.6. This figure is for $Re = 348$ and $\Gamma = 6$ with stationary end walls. Six vortices were produced as expected based on 2.17 which give an estimate of length of a pair of vortices, $\Delta Z = 3.98$mm. The maximum axial velocities are along the sides of the inner and outer cylinders with peaks at around $\frac{1}{4}$ of the gap width. The radial velocity profile demonstrates peaks at the vortex inflow and outflow boundaries from the inner cylinder. The vortex centres are off-centre and closer to the outflow from the inner cylinder as shown in the vector plot and with the stream line plot. This causes higher radial velocities at the vortex outflow regions from the inner cylinder. As the torque on the outer cylinder and inner cylinder are the same the forces on the inner cylinder have to be larger. This means that the vortex outflow boundary from the inner cylinder is going to be dominant over the vortex outflow from the outer cylinder and therefore the vortex centre is pulled towards the outflow from the inner cylinder.

The azimuthal velocity is strongly distorted due to the Taylor vortices with low gradients with vortex outflows and high gradients were there are vortex inflows. This can described in terms of energy transfer from the wall. Due to the presence of an vortex outflow from the wall there is a higher energy transfer, therefore there is less energy is transfer in the azimuthal velocity component. This causes a lower gradient in the region of the outflow. This occurs on the outflows for both the inner and outer cylinders. Where as, at the inflow the opposite will be true. This therefore produces a variation of the skin friction along the length of the inner cylinder as demonstrated in the grid independence solutions (figures 4.3.iii, 4.4.iii and 4.5.iii).

The pressure is lower at the inner cylinder than the outer cylinder as the velocities at the inner cylinder are higher. The region of the highest pressure is at a vortex outflow from the inner cylinder. Similarly the lowest pressure is at the the inflow to the outer cylinder. The vorticity plot shows peaks at the four corners of the vortices, again larger at the vortex outflows from the inner cylinder.

To demonstrate the effects of Reynolds number on the flow five different speeds were tested as presented in the table below 4.4 with an constant aspect ratio, $\Gamma = 6$ and stationary end walls. The results are presented as a vector plot in 4.8 and azimuthal velocity profiles in 4.9.

Test case	Speed	Re	C_M
a	0.5	128	0.0586
b	1.0	256	0.0295
c	1.5	384	0.0253
d	2.0	512	0.0226
e	2.5	640	0.0200

Table 4.4: Comparisons of Shear Stress with Reynolds number for, $\Gamma = 6$

The results show the formation of Taylor vortices for cases (c-d) with increasing vortex strengths. For the highest Reynolds number tested an extra pair of vortices are present. As the speed increases azimuthal gradient at the wall increases producing a higher skin friction but this equates to a reduction in the skin friction coefficient, C_M. Due to the fact that $C_M = f(U_1^2)$. The skin friction is compared with Bilgen & Bilgous trend-line in figure 4.7 for various components of the domain.

This figure shows that the effect of the end vortex on the coefficient of friction as calculated along the full length at the inner cylinder at R_1. The coefficient of friction is also presented for the mid-section on the inner cylinder, ignoring the end vortices and also for the full length along the outer cylinder wall at R_2. The results along the full length are significantly higher than that predicted of Bilgen & Bilgous but by considering just the mid section then a much closer agreement is achieved. The difference between the skin friction at the outer cylinder and mid section is due to the frictional resistance on the end walls.

To test the effect of aspect ratio with stationary end wall 7 tests were carried out. For $\Gamma = 1-3$ only one pair of vortices and for $\Gamma = 4$ and $\Gamma = 6$, 4 and 6 vortices formed respectively. The variation of C_M with aspect ratio is presented in table 4.5. This shows that as the aspect ratio of the domain increased the skin friction decreased. The solutions for these stationary end wall tests are presented as a series of vector plots in 4.10 and as a series of azimuthal velocity profiles in figure 4.11.

Test case	Γ	Re	C_M
a	1.00	384	0.0621
b	1.50	384	0.0482
c	2.00	384	0.0417
d	2.50	384	0.0365
e	3.00	384	0.0324
f	4.00	384	0.0293
g	6.00	384	0.0253

Table 4.5: Comparisons of Shear Stress with wall end boundaries.

The domain was tested again for 7 aspect ratios as before but with rotating end walls. The same numbers of vortices were present but rotating in the opposite direction. The variation of C_M with aspect ratio is presented in table 4.6. This again shows, that as the aspect ratio of the domain increased the skin friction decreased. The solutions for these tests with rotating end walls are presented as a series of vector plots in 4.12 and as a series of azimuthal velocity profiles in figure 4.13.

The domain was tested again for 7 aspect ratios as before but with mirror end boundaries. For these cases a much smaller aspect ratios were chosen to demonstrate the effect of vortex length with just on Taylor vortex and determine the maximum vortex length that could be produced. The variation of C_M with aspect ratio is presented in table 4.7 for these cases. The solutions for these test with rotating end wall tests are presented as a series of vector plots in 4.14 and as a series of azimuthal velocity profiles in figure 4.15.

Test case	Γ	Re	C_M
a	1.00	384	0.0684
b	1.50	384	0.0543
c	2.00	384	0.0459
d	2.50	384	0.0395
e	3.00	384	0.0341
f	4.00	384	0.0299
g	6.00	384	0.0264

Table 4.6: Comparisons of Shear Stress with rotating wall end boundaries.

Test case	Γ	Re	C_M
a	0.75	384	0.0162
b	0.9	384	0.0172
c	1.0	384	0.0172
d	1.1	384	0.0169
e	1.25	384	0.0161
f	1.5	384	0.0161
g	2.0	384	0.0171

Table 4.7: Comparisons of Shear Stress with wall end boundaries.

The results from figure 4.10 to 4.15 are presented, in summary, in figure 4.16 as a comparison of vortex strengths and in 4.17 of vortex length on skin friction. The vortex strength graph show a general trend of increasing vortex strength with vortex length. For the case of vortices next to a rotating boundary stronger vortices were produced. For the case of rotating boundaries weaker vortices were produced.

All internal vortices lay in between this range with higher strengths for the vortices next to rotating end boundaries. This is due to the fact that adjacent vortex strength is larger for the rotating vortices and therefore help drive the middle vortices. The vortex strength for the mirror boundaries are similar to that of the internal vortices but the growth with aspect length is not as great.

Increasing the length of the vortex next to the wall decreases the skin friction as the effect of the end wall decreases the further away. For the internal vortices and the mirror test produced similar skin friction coefficients. The mirror boundary tests indicate a peak around the critical vortex length.

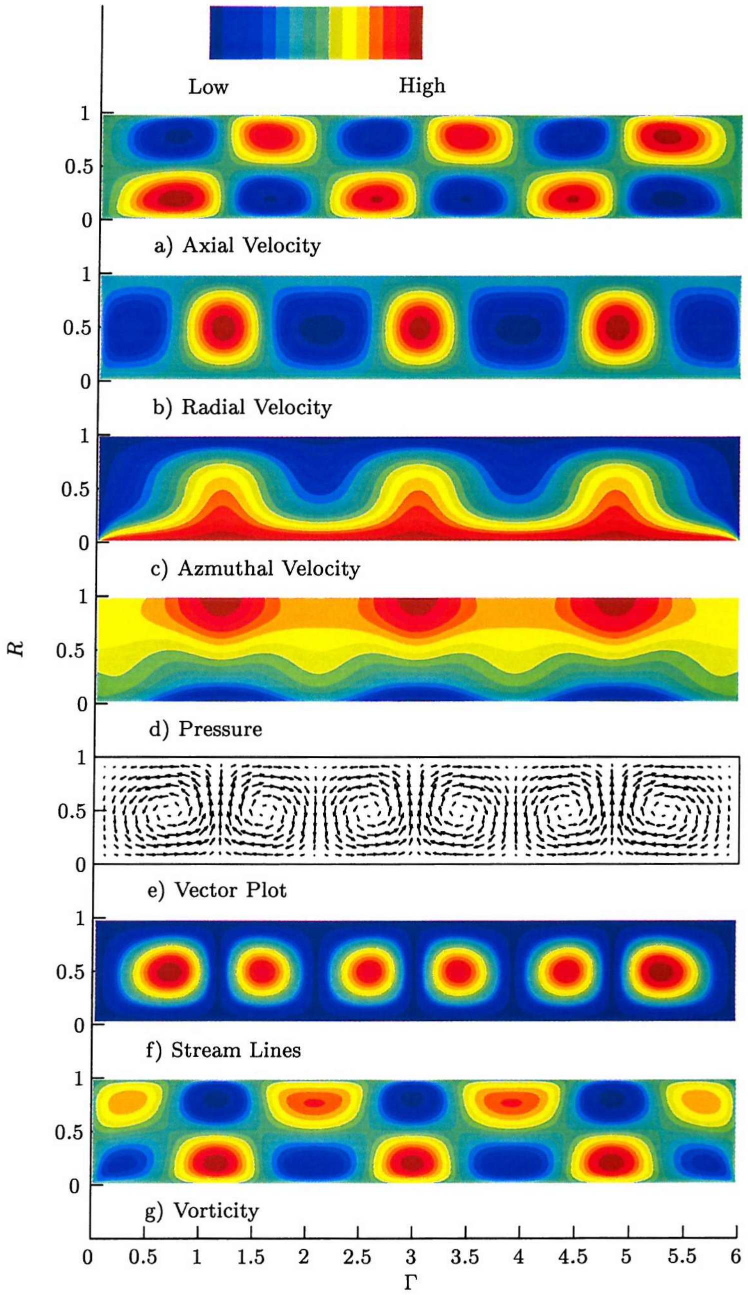

Figure 4.6: Comparison of fluid properties for $Re = 348$, $\Gamma = 6$

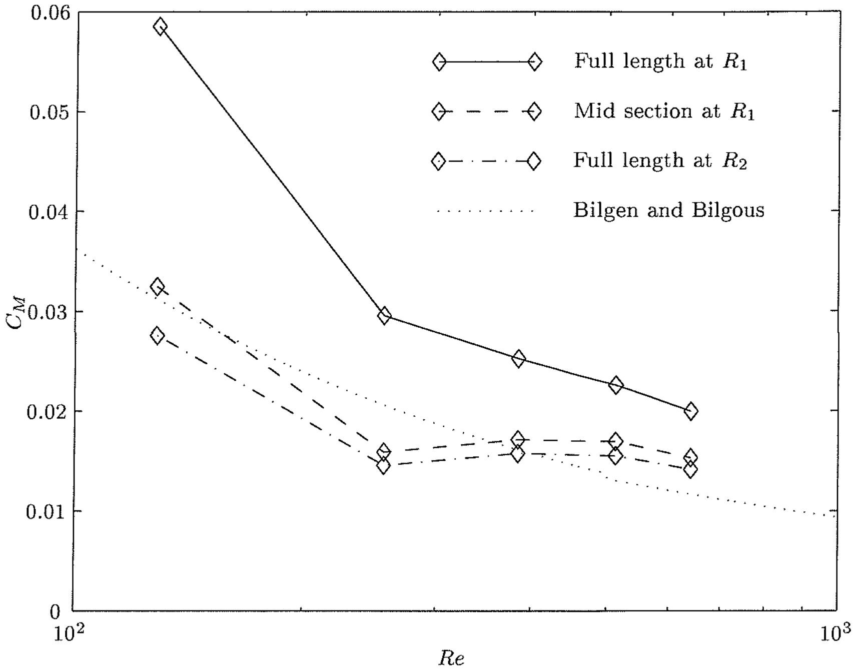

Figure 4.7: Comparison of skin friction within the domain and with the trend-lines of Bilgen & Bilgous

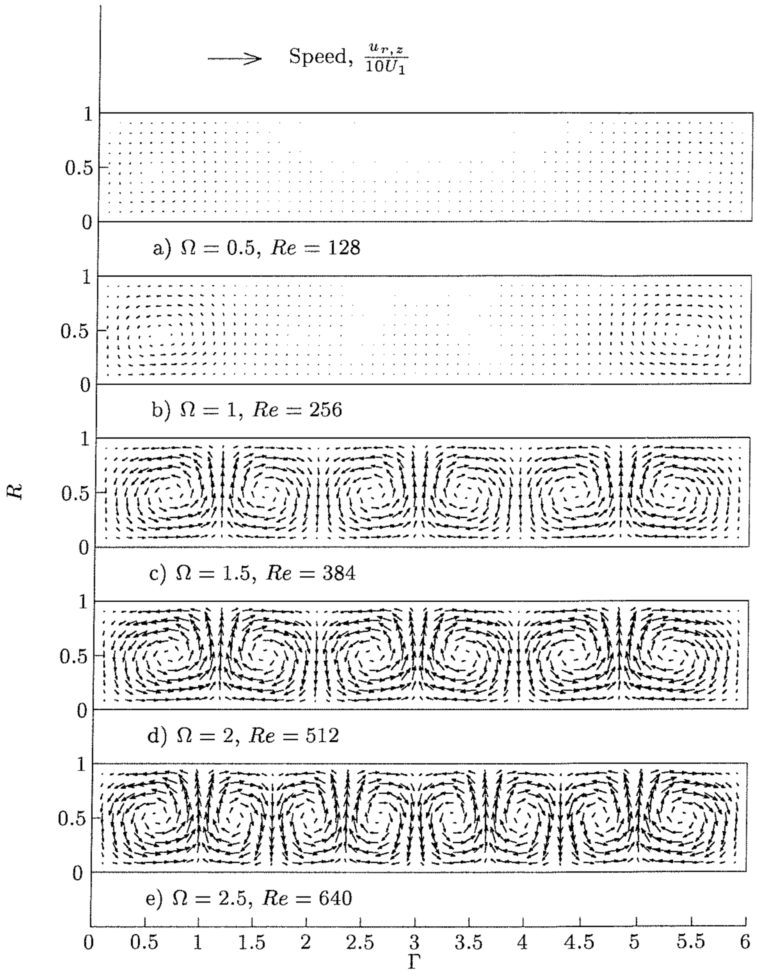

Figure 4.8: The effect of Re on the relative strength of Taylor vortices for $\Gamma = 6$

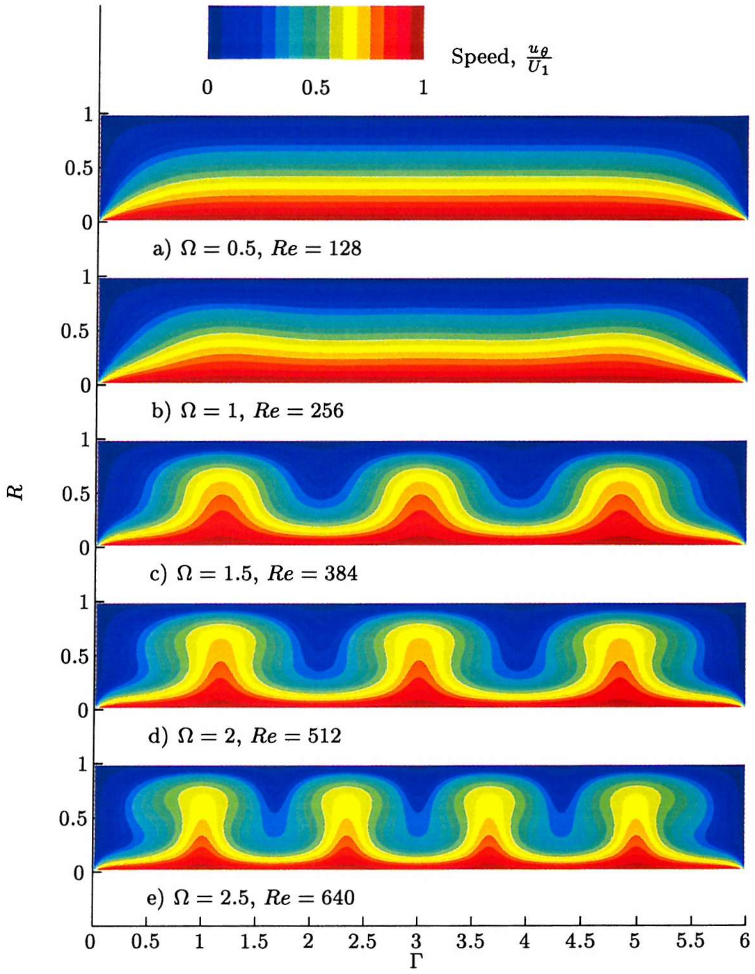

Figure 4.9: The effect of *Re* on the relative azimuthal velocities for $\Gamma = 6$

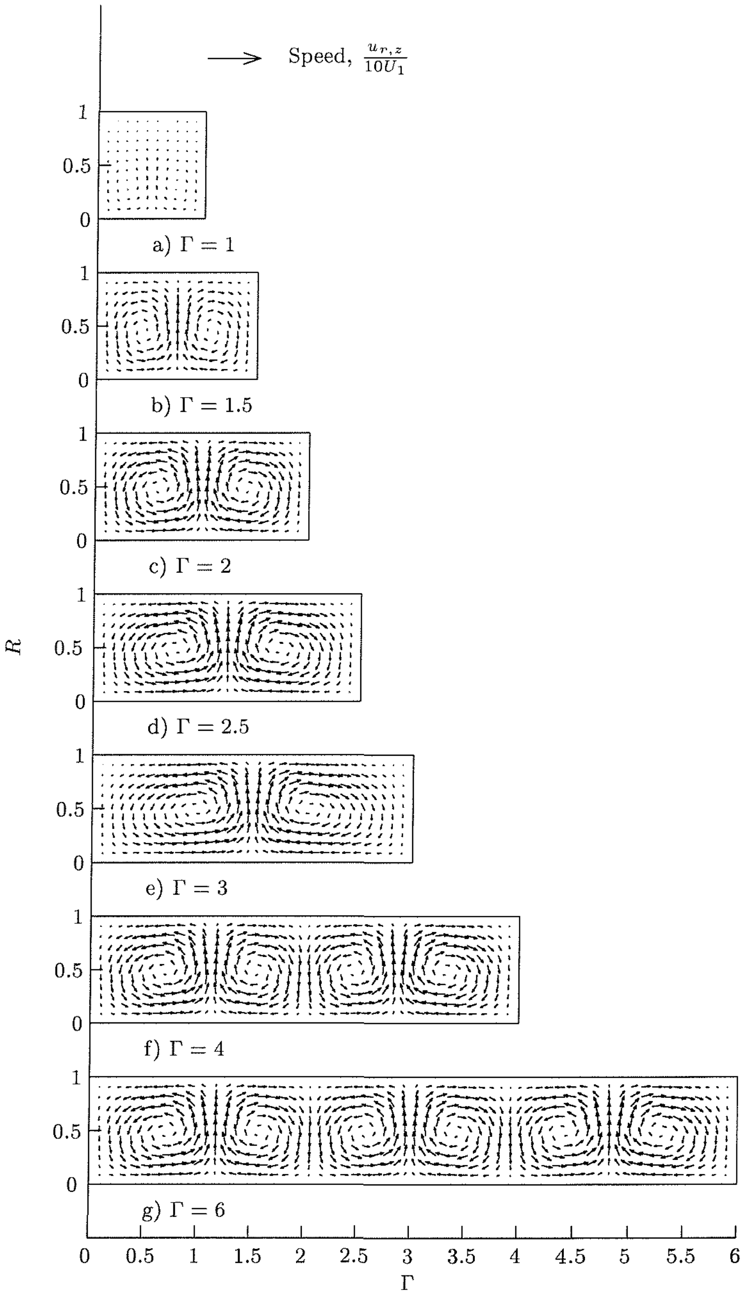

Figure 4.10: The effect of different aspect ratios with stationary end wall on the Taylor vortex velocities

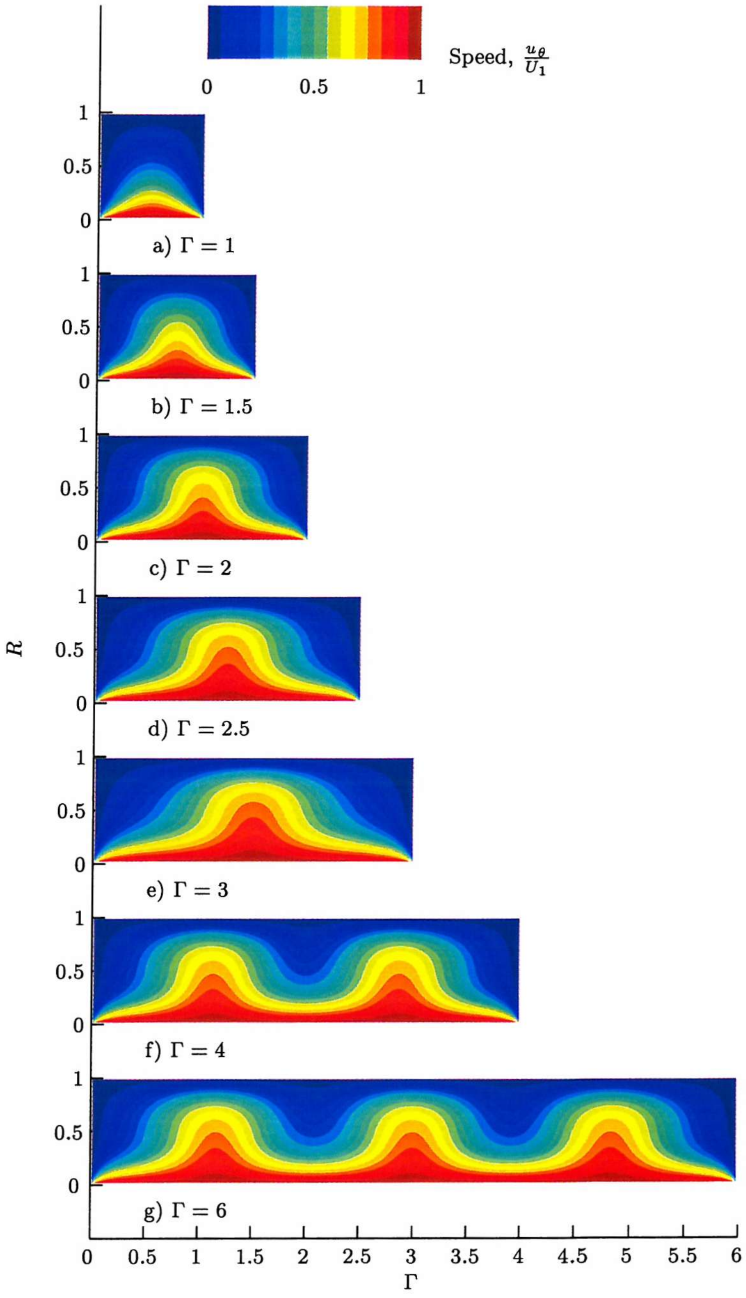

Figure 4.11: The effect of different aspect ratios with stationary end walls on the azimuthal velocity

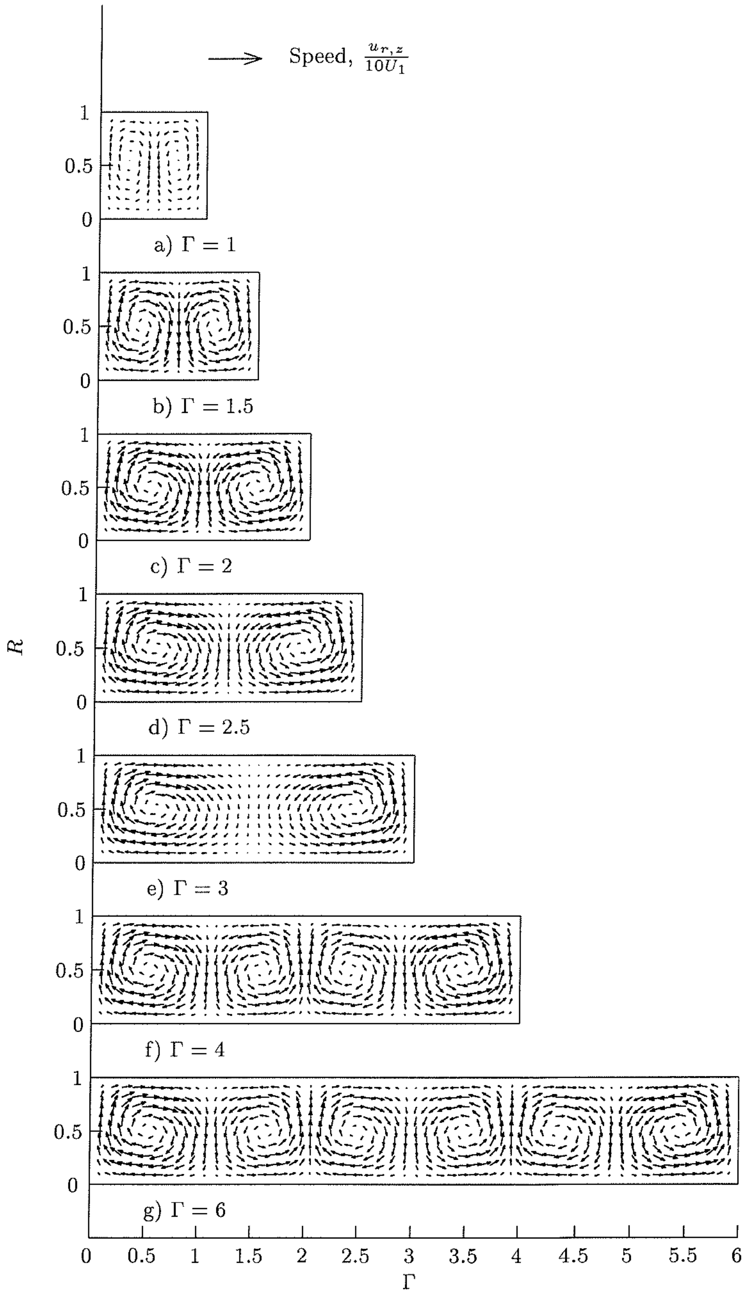

Figure 4.12: The effect of different aspect ratios with rotating on the Taylor vortex velocities

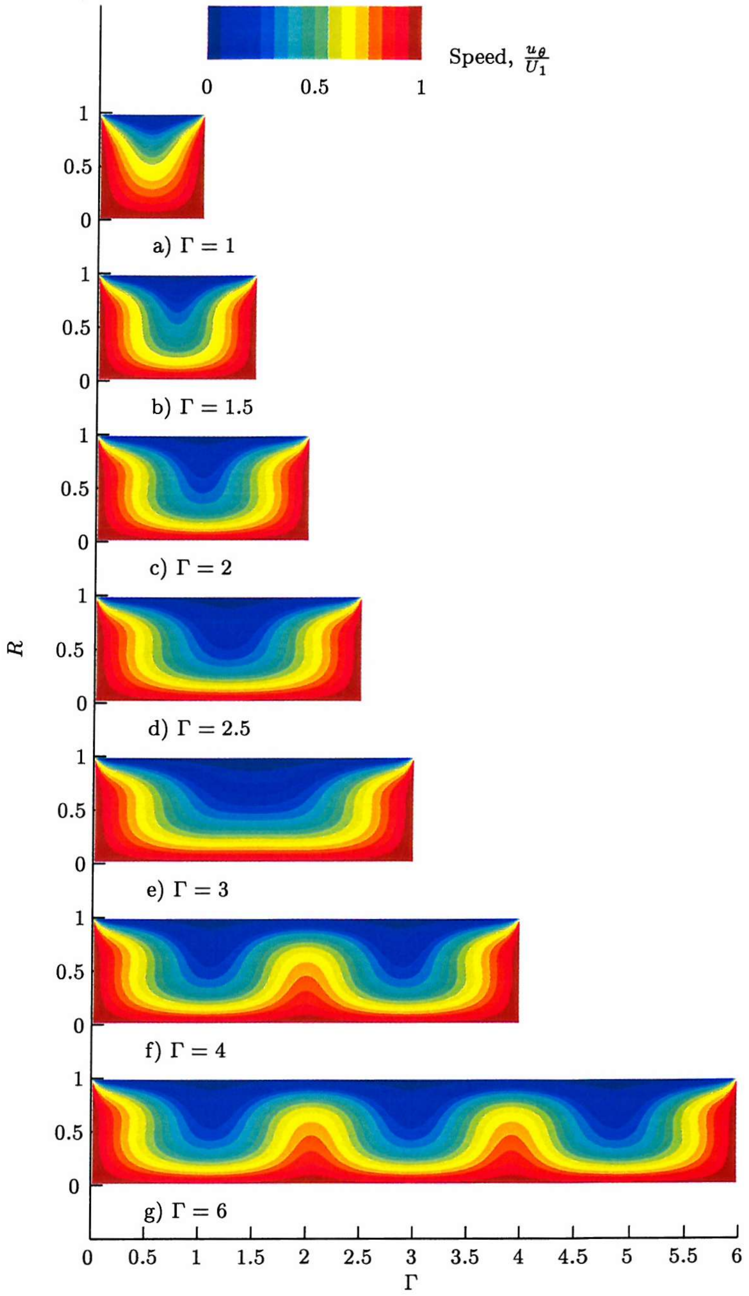

Figure 4.13: The effect of different aspect ratios with rotating on the azimuthal velocity

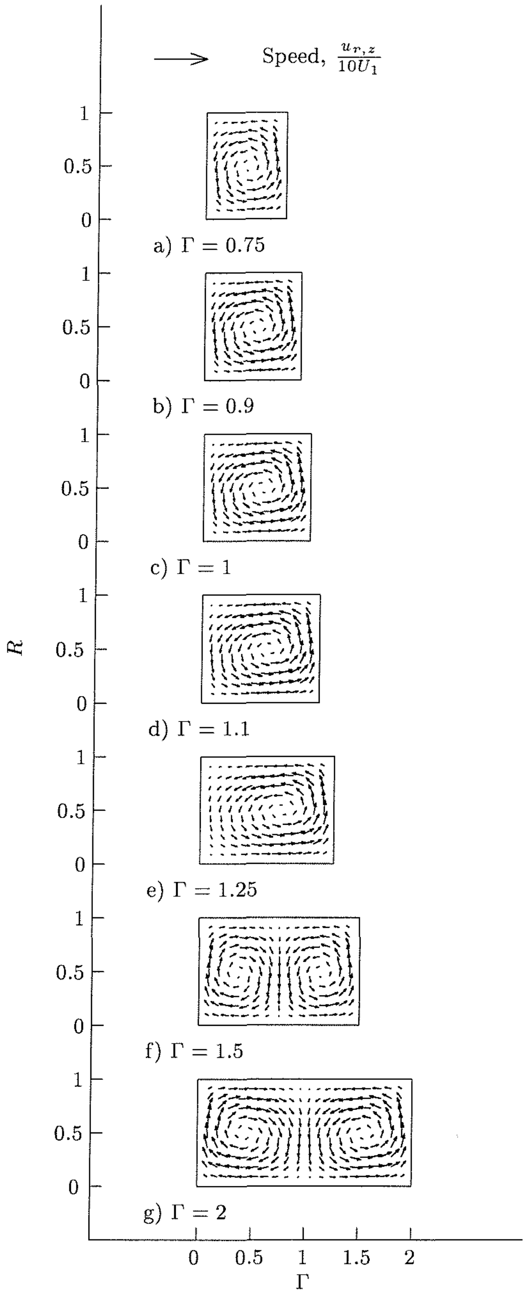

Figure 4.14: The effect of different aspect ratios with end mirrors on the Taylor vortex velocities

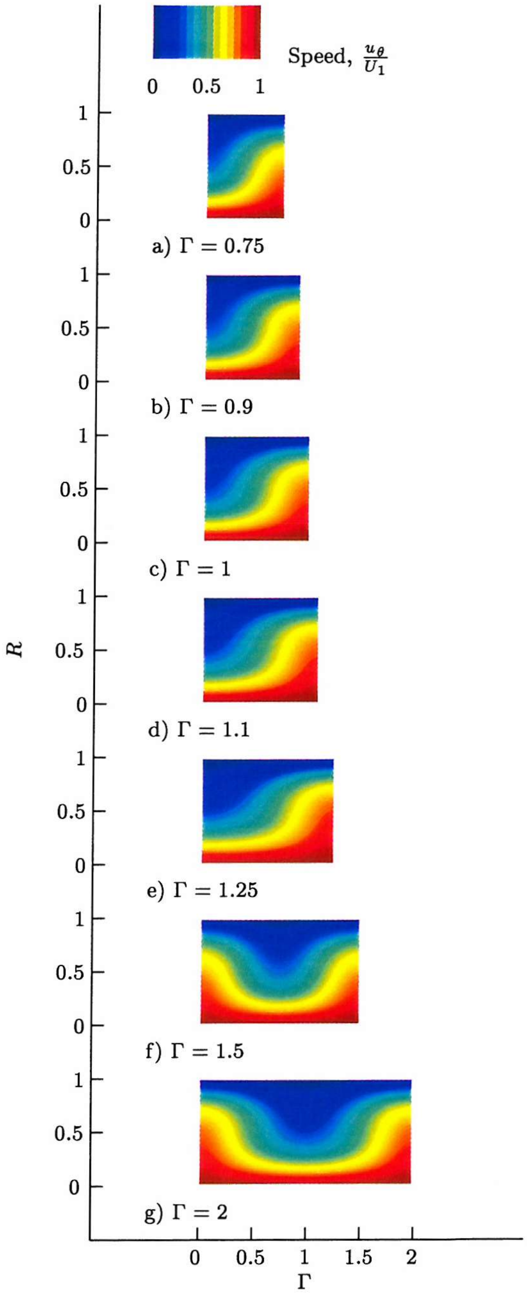

a) $\Gamma = 0.75$

b) $\Gamma = 0.9$

c) $\Gamma = 1$

d) $\Gamma = 1.1$

e) $\Gamma = 1.25$

f) $\Gamma = 1.5$

g) $\Gamma = 2$

Figure 4.15: The effect of different aspect ratios with end mirrors on the azimuthal velocity

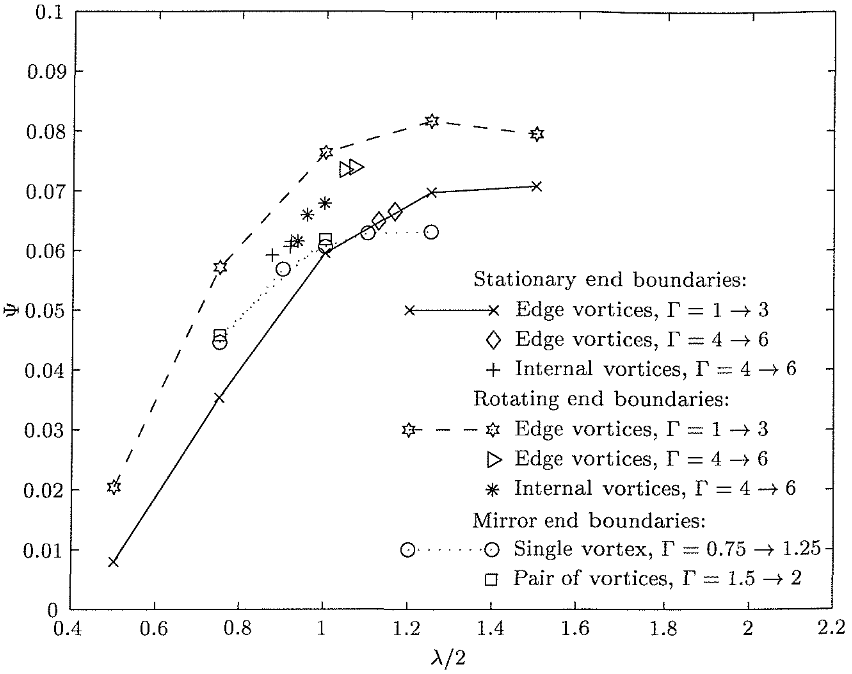

Figure 4.16: Comparison of the effect boundary condition on the variation of vortex strength with vortex cell size at *Re* = 384

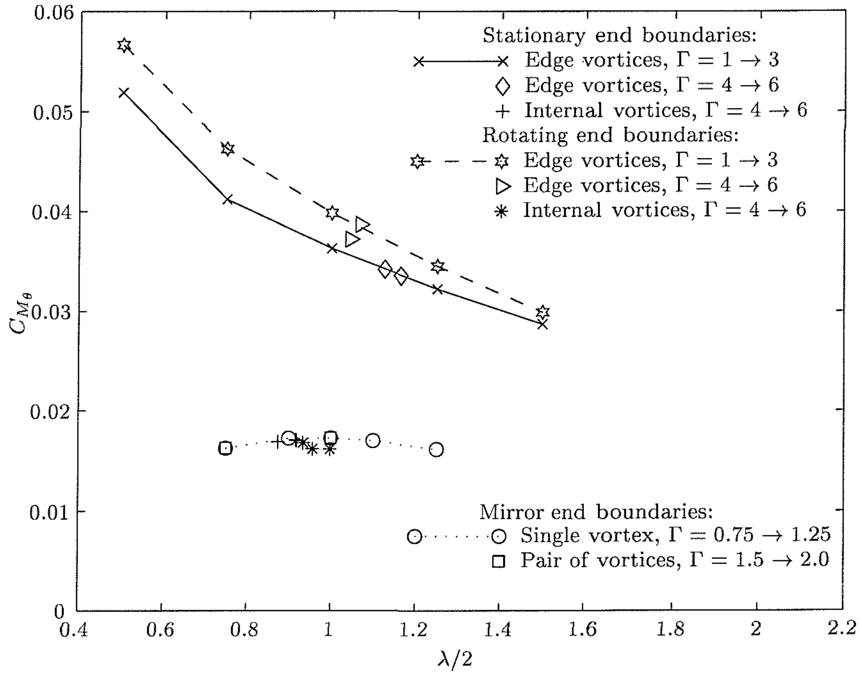

Figure 4.17: Comparison of the effect boundary conditions on the variation of azimuthal shear with vortex cell size at *Re* = 384

§4.8 Conclusions and Recommendations

From these results the following conclusions can be drawn.

I. ELMORE can successfully be used to model laminar Taylor vortices and grid independent results have been produced using the SIMPLEC pressure correction with 2^{nd} order discretization and the CLAM solver.

II. A singularity between the rotating and stationary boundaries has been established and the effect of skin friction has been demonstrated.

III. Just one Taylor vortex can be accurately modelled by using mirror boundaries.

IV. The inner cylinder dominates the effects of the Taylor vortices and the outflow from the Taylor vortex is much stronger than the in flow and hence the vortex centre is offset towards the outflow boundary.

V. The effect of vortex length on skin friction has been illustrated. For the vortex next to a stationary or rotating boundary the shear stress are much higher and the longer the vortex is the less the skin friction.

VI. The skin friction for the middle vortices were similar to that of the mirror boundary and for the majority of theses test over half that of the vortices adjacent to the end walls. For these middle and mirror boundaries there is a peak in the skin friction at the critical vortex length.

VII. The results show that increasing the vortex length increases the vortex strength.

These results demonstrate that to reduce the skin friction the length of the vortices needs to be controlled. By placing small walls at equal distance along the inner cylinder to cause the vortices to be produced in certain positions would not be effective as the end walls have been demonstrated to cause large increases in skin friction.

As it has been shown to be possible to model just a single Taylor vortex with mirror boundaries in 2-D. This domain is therefore an ideal geometry for testing the effects of turbulence models due to the small size. During the following chapter, this new methodology of modelling one Taylor vortex is pursued in order to test turbulence model and determine the influence of Taylor vortices upon the turbulent flow. For turbulence modelling an expanding and contracting grid in the radial direction would be much more appropriate due to the nature of the boundary layer.

CHAPTER

5

Modelling One Turbulent Taylor Vortex

§5.1 Introduction

As discussed in the background review, section §2.4, there is a flow transition at $Re \simeq 1 \times 10^4$ in which there is a significant change in the skin friction, this Re is close to the maximum operating Reynolds number of the thruster unit. Thus the purpose of modelling one vortex was to investigate the effects of turbulence models and then attempt to use this to help explain the flow properties of turbulent Taylor vortices. Particular attention has been given to the effect of Reynolds number and Taylor vortex cell aspect ratio.

Initial attempts are first discussed using the k-ε model, which highlight the need for a low Reynolds number formulation. This lead to the use of Wilcox's Low Reynolds number k-ω model. The numerical procedure and issues of convergence for both modelling with CFX, a commercial CFD code, and ELMORE are then discussed. Results of a series of Reynolds number tests are then presented, with a discussion of vortex to wall driven flow transition. Results for the variation of Vortex length are then presented.

§5.2 Turbulence Model Choice

There are several different types of approximations that can applied to close the equation system 2.24 discussed in the section of turbulent flow §2.2.2.

Algebraic models An algebraic equation is used to solve for the turbulent viscosity. The Reynolds stress tensor,$-\rho\overline{u_i'u_j'}$ is then solved by applying an assumption that related the Reynolds stresses to the velocity gradients and the turbulent viscosity. This assumption is called the Boussinesq assumption 2.26.

One-equation models This type of model a transport equation is solved for a turbulent quantity (usually the turbulent kinetic energy) and a second turbulent quantity (usually a turbulent length scale) from an algebraic expression. The turbulent viscosity is calculated from the Boussinesq assumption.

Two-equation models This type of model uses two transport equations to solve for two scalars. The two scalars are usually the turbulent kinetic energy, k and its dissipation, ϵ. The Reynolds stress tensor is then solved by an assumption which relates the Reynolds stress to the velocity gradients and the turbulent viscosity. The turbulent viscosity is obtained from the two solved transport scalers.

Reynolds stress models For this type of model a transport equation is derived for the Reynolds stress tensor. One extra transport equation has to be added for determining the length scale of the turbulence and usually an equation for the turbulent dissipation is used.

The above turbulence models are listed in increasing order of complexity and hence the extra cost in terms of computational time. All the above models are depend upon coefficients and hence certain models may be more appropriate for different flow conditions. The work based in this thesis is based upon two-equation models as they widely used for a variety of flow dependent upon solution method and where considered to be a good compromise between accuracy and computational cost.

In order to choose a two equation turbulent model which enables the turbulent Taylor vortices to be studied initial investigations were carried out using the standard k-ε model by Launder *et al.* [38] as implemented in ELMORE. This tested the feasibility of using eddy viscosity models to simulate turbulent Taylor vortices. This was not withstanding their known weakness but provided a good starting point for the investigation.

Details of the k-ε model along with the constants used are presented below. The transport equations for the turbulent kinetic energy, k and the turbulent dissipation, ϵ are given by [58],

$$\rho\frac{\partial k}{\partial t}+\rho\frac{\partial u_i k}{\partial x_i}=\frac{\partial}{\partial x_i}\left[\left(\mu+\frac{\mu_T}{\sigma_k}\right)\frac{\partial k}{\partial x_i}\right]+P-\rho\epsilon \tag{5.1}$$

and

$$\rho\frac{\partial \epsilon}{\partial t}+\rho\frac{\partial u_i \epsilon}{\partial x_i}=\frac{\partial}{\partial x_i}\left[\left(\mu+\frac{\mu_T}{\sigma_\epsilon}\right)\frac{\partial \epsilon}{\partial x_i}\right]+C_1\frac{\epsilon}{k}P-C_2\rho\frac{\epsilon^2}{k}. \tag{5.2}$$

The turbulent production term, P is expressed as

$$P=\mu_T\left(\frac{\partial u_i}{\partial x_j}+\frac{\partial u_j}{\partial x_i}\right)\frac{\partial u_i}{\partial u_j}. \tag{5.3}$$

For this k-ε formulation constants were taken as $C_1 = 1.44$, $C_2 = 1.92$, $\sigma_k = 1.0$, $\sigma_\epsilon = \frac{\kappa^2}{C_1 - C_2\sqrt{C_\mu}}$, $\kappa = 0.4187$ and $C_\mu = 0.09$. The turbulent viscosity for the k-ε model is defined by,

$$\nu_T = C_\mu \rho\frac{k^2}{\epsilon}. \tag{5.4}$$

To solve the momentum and turbulent equations the SIMPLEC algorithm was used with CLAM discretisation and the SIP solver, details are discussed later in §5.3. The domain was

Grid density	$\overline{u_\theta}/U_1$	$C_M \times 10^{-3}$	n_1^+	n_2^+
16 × 16	0.716	0.18	20.9	42.8
32 × 32	0.689	3.06	13.7	27.8
40 × 40	0.442	1.34	22.9	19.3
48 × 48	0.438	1.60	20.8	17.2
64 × 64	0.416	2.07	17.8	13.3

Table 5.1: Comparison of flow properties with grid density

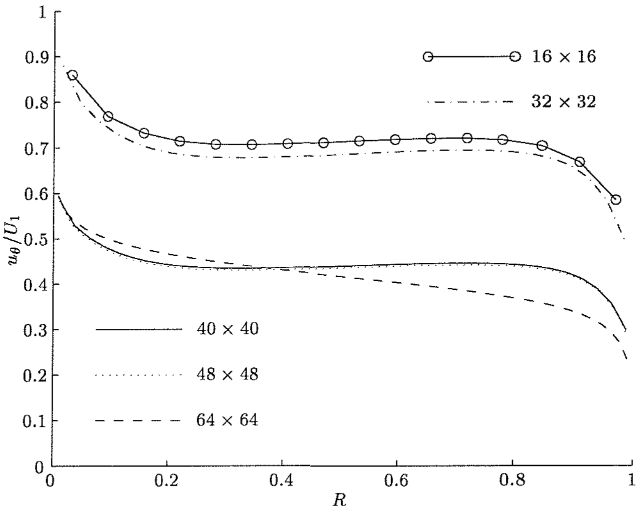

Figure 5.1: The effect of grid density on mean velocity profile

defined to resolve one turbulent Taylor vortex between two mirror boundaries for the 2mm case of the thruster unit, at $Re = 1 \times 10^5$. The cell aspect ratio was taken to be $\Gamma = 1.25$, 25% larger than the critical laminar vortex cell length, as an estimation of the extra wave length of turbulent Taylor vortices [48]. A uniform grid was used and increased in a series of steps as presented in table 5.1. Where $\overline{u_\theta}/U_1$ repents the mean azimuthal velocity, C_M is the azimuthal shear stress, n_1^+ and n_2^+ are respectively the viscous wall lengths on the inner and outer cylinder.

Increasing the grid density had the effect of shifting the first node point towards the wall. This in turn had a profound effect on the solution as demonstrated in figure 5.1 as between grid densities of 32 × 32 and 40 × 40 there is an over 20% reduction in the momentum. This is due to the fact that if an inefficient number of cells are used then the boundary layer cannot be resolved and hence the momentum is over estimated. All solutions produced a single Taylor vortex with the exception of 64 × 64 grid density, where the effects of placing the 1st node too close to the wall, was so dominant that a Taylor vortex did not form.

If the grid density was too high then the 1st node point on the inner and outer cylinder was too close to the viscous sublayer and hence the momentum was under estimated. The 1st node for the 64 × 64 and higher grid densities could be placed outside the sublayer by using a expanding and contracting grid. This would then produce irregularities as the 1st node length

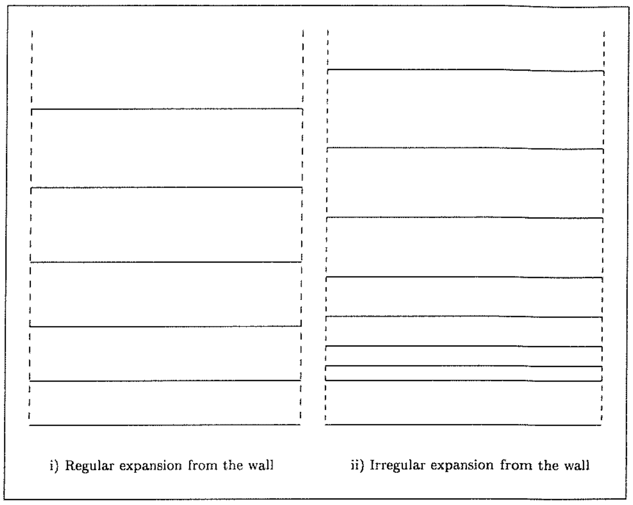

Figure 5.2: Regular and irregular grid expansion from a cylinder wall

would have to be larger than 2^{nd} , 3^{rd} and subsequent node lengths, shown in figure 5.2. These effects would be further exacerbated at the much lower Reynolds numbers of the flow transition, $Re = 1 \times 10^4$.

These problems of producing an accurate model of a turbulent Taylor vortex led the research towards the use of a commercial CFD package, CFX, in order to compare alternative turbulence models. It is important to resolve the laminar sublayer, as it composes of a significant proportion of the gap, and so low Reynolds numbers adaptations are required for the eddy viscosity model. Initially several attempts at modelling turbulent Taylor vortices were made using the low Reynolds number k-ε model [59], as implemented CFX, but produced no sensible converged solution for all cases tested.

It should also be mentioned that Reynolds stress model [40], as implemented in CFX, was investigated at much higher Reynolds number. These tests confirmed what was reported by Wild *et al.* [37] and discussed in Chapter 2 that the torque produced was overestimated by around 50%. These initial results are also not presented as no formal grid independent tests were carried but since the torques were overestimated, as demonstrated before, the Reynolds stress models were not further investigated. The overestimation due to modelling using the Reynolds stress model is presumably due to the more sensitive nature of the effects of rotation. As in the Reynolds stress equations individual components of the stress are modelled as opposed to the more global averaging approach of eddy-viscosity models.

Stated earlier in §2.2.5, the effects of rotation in the actual Taylor vortices could have a significant effect upon the turbulence production in the flow. Therefore, using a Reynolds stress model which includes rotational effects would be inappropriate. These would only include the effects of rotation about the axis of the cylinder and not about the individual vortices. Without any experimental measurements, Direct Numerical Simulation (DNS) or Large eddy simulation (LES) results configuring a Reynolds stress model to include the effects of rotation it would be impossible to derive the appropriate constants. Therefore, without efficient computer resources to perform LES computations or sufficient experimental data the low Reynolds number k-ω model was used in order to capture the sublayer and other low Reynolds number turbulence effects present in Taylor vortices.

Turbulence has been modelled using the low Reynolds number Wilcox Model implemented in both CFX and ELMORE [41]. Since this model avoids the use of wall functions, it allows modelling close to the wall, smooth grid size variation and provides more accurate modelling of turbulent production due to the Taylor vortex formation. The transport equations for the turbulent kinetic energy, k, and the turbulent frequency, ω are given by [58] as,

$$\rho\frac{\partial k}{\partial t}+\rho\frac{\partial u_i k}{\partial x_i}=\frac{\partial}{\partial x_i}\left[\left(\mu+\frac{\mu_T}{\sigma_k}\right)\frac{\partial k}{\partial x_i}\right]+P-\rho\omega k \tag{5.5}$$

and

$$\rho\frac{\partial \omega}{\partial t}+\rho\frac{\partial u_i \omega}{\partial x_i}=\frac{\partial}{\partial x_i}\left[\left(\mu+\frac{\mu_T}{\sigma_\omega}\right)\frac{\partial \omega}{\partial x_i}\right]+C_1\frac{\omega}{k}P-C_2\rho\omega^2, \tag{5.6}$$

where the constants $C_1 = 0.5111$, $C_2 = 0.8333$, $\sigma_k = 2.0$ and $\sigma_\omega = 1.0$. The turbulent viscosity for the low Reynolds number k-ω model is defined by,

$$\mu_T = C_\mu f_\mu \rho\frac{k}{\omega}. \tag{5.7}$$

Taking $C_\mu = 0.09$ and the damping function f_μ given by,

$$f_\mu = exp\left[\frac{-3.4}{(1+Re_T/50)^2}\right], \tag{5.8}$$

with a local turbulent Reynolds number

$$Re_T = \frac{\rho k}{\mu\omega}. \tag{5.9}$$

When analyzing the turbulent energy in the Taylor-Couette system the turbulent production derivatives in polar coordinates are: $(\partial u_r/\partial z)^2$, $(\partial u_\theta/\partial z)^2$, $(\partial u_z/\partial r)^2$, $(\partial u_\theta/\partial r)^2$, $2(\partial u_z/\partial z)^2$, $2(\partial u_r/\partial r)^2$, $(\partial u_z/\partial r)(\partial u_r/\partial z)$, $(\partial u_r/\partial z)(\partial u_z/\partial r)$ and the turbulent dissipation term is $\rho\omega k$. where the components u_r, u_θ, u_z, r and x are the radial, azimuthal and axial velocities and the radial and axial distances, respectively.

The low Reynolds number effects at the wall are accounted for by applying the exact solution to the ω equation in the viscous sublayer,

$$\omega \sim \frac{6\mu}{\rho C_2 n^2} \quad \text{for} \quad n^+ < 2.5. \tag{5.10}$$

To minimize the numerical error of the integration through the sublayer and to ensure n^+ independent results, the first 7 to 10 grid points from the walls were positioned between $0 < n^+ < 2.5$ as advised in [41].

§5.3 Solution Procedure and Numerical Issues

Three radius ratios have been simulated in CFX based upon the radius of the thruster unit, $R_1 = 0.128$ mm, and gaps of 2, 8 and 48 mm. For the simulations using ELMORE, 2 and 8 mm

Case	η	Ta_c	$\triangle Z_T$
2 mm	0.9846	1721	5.01 mm
8 mm	0.9412	1760	20.1 mm
48 mm	0.7246	1981	117.25 mm

Table 5.2: Critical Laminar Taylor Numbers and Wavelengths

Re	2 mm	8 mm	48 mm
5×10^3	80	87	92
1×10^4	87	92	95
5×10^4	96	97	98

Table 5.3: Comparison of the Percentage of Turbulent Core

gaps have been tested, with more extensive tests with the 2 mm gap as it is what is used in the thruster unit. By applying Chandrasekha's equation 2.17 and taking the turbulent wave length, $\triangle Z_T$, to be 25% larger as with the initial k-ε tests, the critical Taylor numbers and domain sizes have been estimated in table 5.2. The length of the domain was $\triangle Z_T/2$, to simulate just one Taylor vortex, for the Reynolds number tests. For the Aspect ratio tests simulations were carried out using ELMORE for just the 2mm case to demonstrate the trends. The length of the domain was varied for aspect ratios from, $\Gamma = 0.5 \rightarrow 2$.

A uniform cell distribution in the axial direction was used as the axial and axial velocity tended to vary uniformly along the length of one cell. However, a non-uniform expanding and then contracting grid was used in the radial direction to place sufficient cells to resolve the azimuthal laminar sublayer on both the inner and outer cylinder walls. The sublayer region comprises a significant proportion of the gap especially for the 2mm case. 2.4. The percentages of turbulent core have been based on based upon equations 2.51 and 2.52 and are presented in table 5.3 and were used for estimating the grid distribution.

Details of pressure correction, discretisation schemes and solver methods can be found in the CFX user manual [58]. For clarity, coherence and to allow direct comparisons between CFX and ELMORE the results from the SIMPLEC algorithm are only presented. The QUICK scheme was used for interpolation for both the momentum and turbulent variables. The momentum equations were solved using the SIP procedure due to Stone and the turbulent equations were solved using line relaxation method. Both of which are the default settings. For the number of sweeps in CFX is controlled by an algorithm such that a minimum and maximum can be set. $1 \rightarrow 5$ sweeps for the momentum and turbulent equations with $1 \rightarrow 30$ sweeps for the pressure equation to ensure convergence.

For calculations using ELMORE, the Van Leer's CLAM scheme was chosen, as this was used for the laminar calculations in Chapter 4. This proved much more effective than the HDS for the momentum equations. The turbulent equations have been solved using the HDS as the

Grid Dimensions	CV	C_M, $Re = 8 \times 10^3$	C_M, $Re = 1.6 \times 10^3$
16x16	256	5.30e-03	4.26e-03
32x32	1024	4.79e-03	3.87e-03
64x64	4096	4.82e-03	3.70e-03
128x128	16384	4.83e-03	3.73e-03

Table 5.4: C_M values for the 8 mm case.

CLAM scheme had only a very small effect on the flow. For example the skin friction was reduced by 0.25%. This is due to the fact that the turbulent variables, k and ω, are strongly dominated by production and dissipation so the accuracy of the convection is less of an issue. In ELMORE, the SIP was used to solve the differencing as used in CFX and7 the laminar work in Chapter 4. In ELMORE, 5 sweeps of the momentum and turbulent equations, with 10 sweeps of the pressure equation were found to be sufficient.

To ensure that the solution had converged, residuals were analysed to confirm that all components had reduced to the steady state of one Taylor vortex. The residuals were normalised with respect to the absolute mean value. For the CFX calculations the normalised axial and radial velocities residuals were less than 10^{-3} and all other residuals converged to less than 10^{-6}. For ELMORE all normalised residuals were less than 10^{-6}.

The 8mm case was used to test for a grid independent solution at $Re = 8 \times 10^3$ and $Re = 1.6 \times 10^4$. The inflow and outflow profiles were aligned with the vortex end cells in the 32×32 case. The velocity profile plots are shown in figures 5.3, 5.4 and the shear stress values are presented in table 5.4. The results show good alignment of the mean profiles, with small changes in the inflow and outflow profiles with the shear stress coefficient, C_M. Therefore, the 64×64 grid was used for the remainder of the test cases to save computation cost as increasing the grid density had little improvement upon the accuracy.

The initial studies were carried out using CFX. For the later calculations using ELMORE the node positions within the sub-layer were much more critical. In CFX less node points were required in the region $n^+ < 2.5$ to produce sensible converged solutions. Whereas in ELMORE the solution was much more sensitive and hence for all the solutions 10 nodes were placed within $n^+ < 2.5$ for all solutions. If more or less nodes were placed within the region then it was possible to achieve the under and over shoots akin to figure 5.1 found during the initial k-ε tests.

If the end mirror boundaries are replaced with periodic boundaries an axial flow is developed instead of the Taylor vortices. Also, unsteady disturbances were produced on the surface of the inner cylinder, which may be akin to Görtler vortices but which did not have distinguishable flow features. The SimpleC pressure correction algorithm was also compared with the iterative PISO approach in CFX. In the latter case the laminar boundary layer produced was larger than expected (approx 40% of the gap width) and consequently, the torques produced were 20% less than predicted by Bilgen & Bilgous.

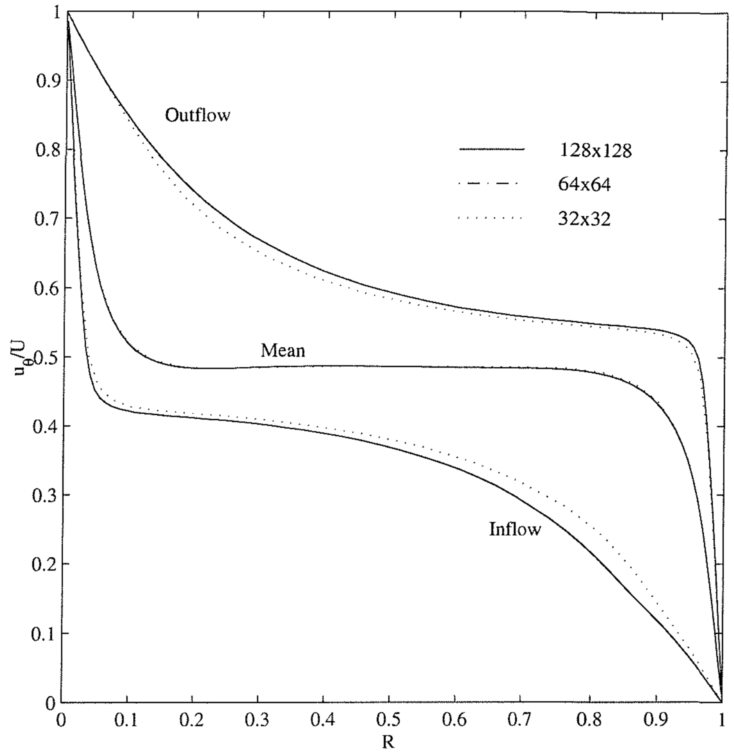

Figure 5.3: Profile Plot for the 8 mm case, $Re = 8 \times 10^3$

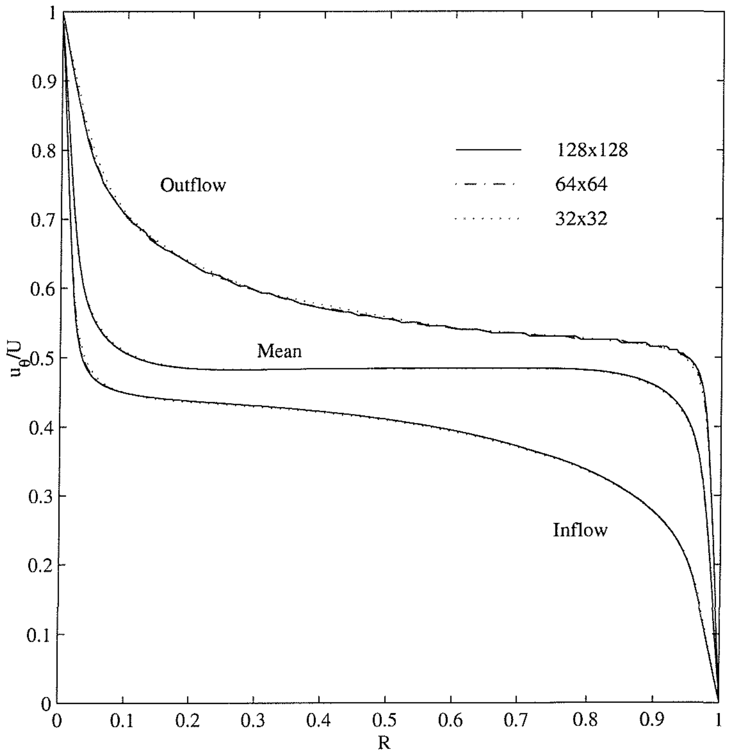

Figure 5.4: Profile Plot for the 8 mm case, $Re = 1.6 \times 10^4$

d	Test Case	Re	Γ	Bilgen & Bilgous	CFX	ELMORE
2mm	a	5×10^3	1.25	0.0042	0.0044	0.0054
2mm	b	8×10^3	1.25	0.0033	0.0039	0.0044
2mm	c	1×10^4	1.25	0.0030	0.0036	0.0037
2mm	d	2×10^4	1.25	0.0026	0.0030	0.0027
2mm	e	5×10^4	1.25	0.0021	-	0.0028
2mm	f	1×10^5	1.25	0.0019	-	0.0025
8mm	a	5×10^3	1.25	0.0064	0.0130	0.0075
8mm	b	8×10^3	1.25	0.0050	0.0061	0.0048
8mm	c	1.6×10^4	1.25	0.0041	0.0037	-
8mm	d	2×10^4	1.25	0.0039	0.0042	-

Table 5.5: List of test cases and a comparison of C_M values for the Reynolds number tests

§5.4 Results and Discussion

Two types of tests were performed: with a constant Taylor vortex length and variable Re; and with a constant Re number and variable Taylor vortex length. Firstly, the results of the effect of Reynolds number with constant aspect ratio is presented. These results compare the simulation with both CFX and ELMORE for a range of speeds for the 2mm case and briefly for the 8mm case. These results also illustrate the sensitivity of the low k-ω formulation to coding approach. The results are analysed further, in the second part, explaining the reasons for the flow transition from "soft" to "hard" turbulence. The effect of radius ratio is also discussed with regards to a flow transition using CFX results. The results of variation of aspect ratio for a constant Reynolds number is then presented for the 2mm case in the third part and discussed.

§5.4.1 Reynolds Number Tests

The test conditions for all converged 2mm and 8mm simulations tested are presented in table 5.5 and to compare against the empirical equations given by Bilgen & Bilgous, the skin frictions are compared. The skin friction for the 2mm test case is also plotted in figure 5.5.i to demonstrate the trends. For the 2mm test case all the numerical simulations over-predict the empirical relationship. The CFX results consistently over-estimates C_M by around 20%. The ELMORE results initially over-estimated by almost 30% but the error reduces with a minimum at $Re = 2 \times 10^4$ and then over-estimates by up to 20%.

For the 8 mm case the CFX predictions of skin friction are almost within Bilgen & Bilgous's margin of error, with the exception of the low speed case, $Re = 5 \times 10^3$, where the CFX analysis over-estimated by around 50%. This is presumably due to the very low turbulent production. The ELMORE results for $Re = 5 \times 10^3$ and $Re = 8 \times 10^3$ appear more consistent with the trendline of Bilgen & Bilgous.

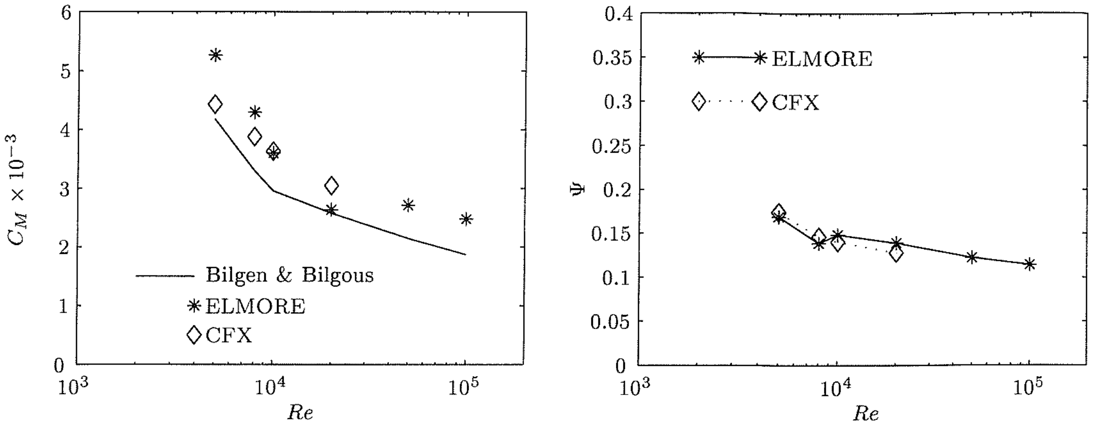

i: Azimuthal shear stress for one vortex

ii: Non-dimensional vortex strength for one vortex

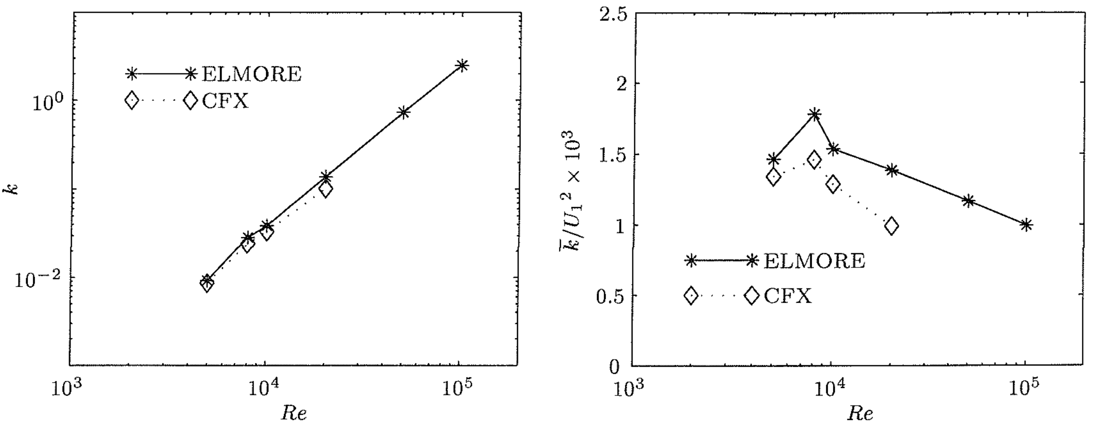

iii: Mean turbulent kinetic energy for one vortex

iv: Non-dimensional mean turbulent kinetic energy for one vortex

Figure 5.5: Comparison of Taylor vortex properties for the 2 mm case, $\Gamma = 1.25$, for both CFX and ELMORE

These discrepancies between CFX, ELMORE and the Bilgen & Bilgous are highlighted for the 2 mm gap in figure 5.5.i. This demonstrates the effect of coding approach and the node distribution because as stated earlier ELMORE proved more sensitive to node position and hence different grid distributions were used. If the sublayer is thinner then the nodes spaced in the centre are going to spread out be spread out more and hence the velocity profile may be less defined. Further studies on the effect of node placement and grid density would be required to demonstrate this sensitivity. Due to unavailability of validation data specific to this domain, either from the experimental facility developed in chapter 3 or from another source, it was not felt appropriate to perform a more in depth study.

The 2mm results from the CFX simulations are presented in figure 5.6 and for ELMORE in figure 5.7 as a series of vector plots, azimuthal velocity and turbulent kinetic energy profiles. All results produced an anti-clockwise Taylor vortex apart from case f in figure 5.7.i where

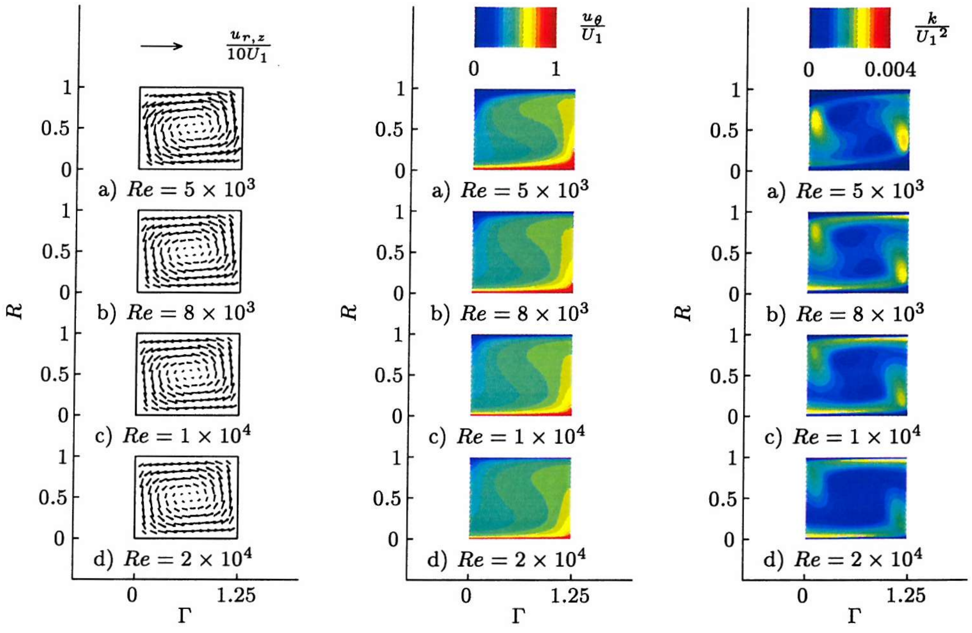

i: Vector plots

ii: Azimuthal velocity profiles

iii: Turbulent kinetic energies

Figure 5.6: The effect of *Re* on vortex properties for the CFX simulations, 2mm test case, $\Gamma = 1.25$

a clockwise vortex was formed. This clockwise sense of rotation is also inconsistent with the laminar results presented in figure 4.14. This change in vortex direction is presumably due to a different initial source of perturbation within the numerics as it is for the highest *Re*.

The results are further analysed in figure 5.5.ii-iv, a comparison between ELMORE and CFX of vortex strength, ψ defined as equation 4.4, the mean turbulent kinetic energy, $\bar{k}$ and the non-dimensional mean turbulent kinetic energy, $\frac{\bar{k}}{U_1^2}$ for one Taylor vortex. The mean turbulent kinetic energy was defined as,

$$\bar{k} = \int_0^L \int_{R_1}^{R_2} \frac{k}{L(R_2 - R_1)}\, dr\, dz \tag{5.11}$$

Both ELMORE and CFX show consistent reduction in ψ and a steady growth in $\bar{k}$ with increasing *Re*. Figure 5.5.iv shows a peak in $\frac{\bar{k}}{U_1^2}$ for the ELMORE and CFX solution at $Re = 8 \times 10^3$ which is associated with the flow transition discussed in the next section. The fall in $\frac{\bar{k}}{U_1^2}$ with *Re* is linked to the reduction in ψ as with lower $\frac{u_r}{U_1}$ and $\frac{u_z}{U_1}$ the gradients due to the distortion of the flow field (in particular $\frac{u_\theta}{U_1}$ as shown in figures 5.6.ii and 5.7.ii) by the vortex are less. Hence, there is less turbulent production due to the vortex and therefore a fall in the non-dimensional turbulent kinetic energy, as in figures 5.6.iii and 5.7.iii.

A comparison of the logarithmic mean wall profiles for both CFX and ELMORE is presented in figure 5.8. Figures 5.8.i and 5.8.ii are at $Re = 8 \times 10^3$, they illustrate the difference in wall profile between ELMORE and CFX. The results using CFX tended to 'over-shoot' Von Kármán

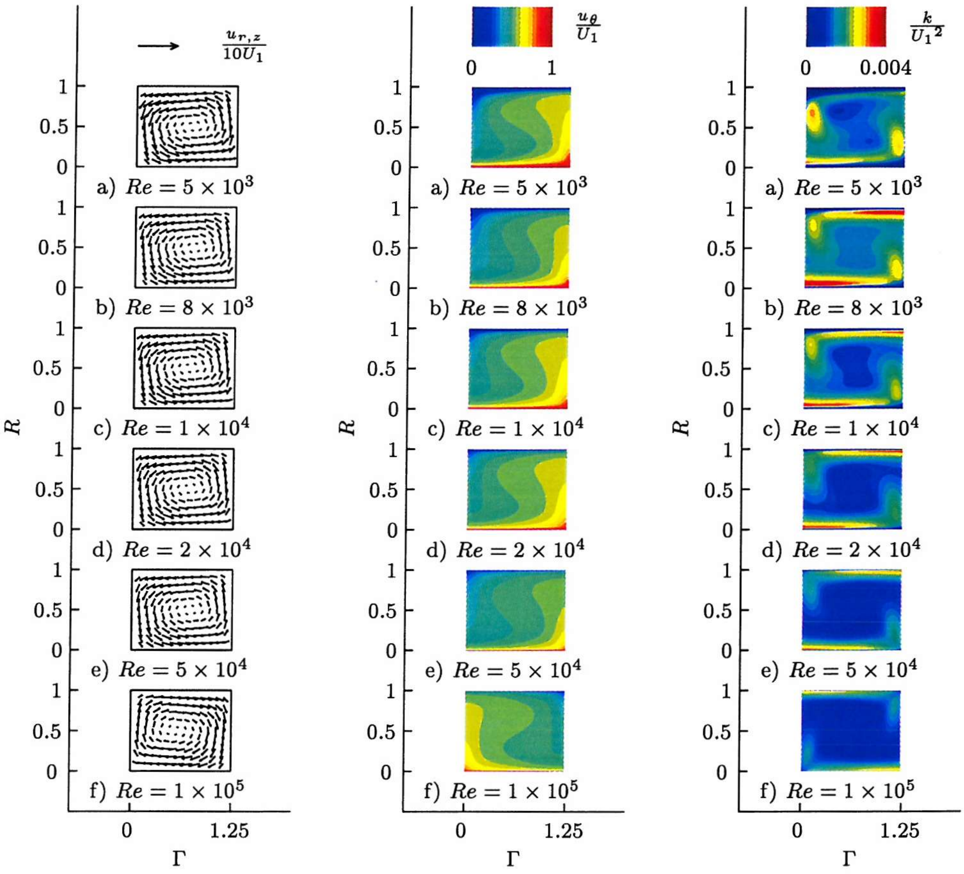

i: Vector plots

ii: Azimuthal velocity profiles

iii: Turbulent kinetic energies

Figure 5.7: Effect of *Re* on vortex properties for the ELMORE simulations, 2mm test case, $\Gamma = 1.25$

law of the wall, equation 2.32 by larger amounts than ELMORE. Although the QUICK scheme, as used in CFX, has a tendency to suffer as much from ‘under-shoots’ and ‘over-shoots’ [5] it is presumably more linked to the less sensitive nature the of node positions associated to the coding approach. As CFX is a well developed code, it may have extra smoothing functions or other ‘tweaks’ to improve robustness and hence commercial viability. For higher *Re* tended to follow Von Kármán law of the wall as shown figure 5.8.iii for ELMORE at $Re = 1 \times 10^5$. The flattening of the wall profile at high $n+$ is due to flattening of the azimuthal profile due to the vortex. This is further discussed last section §5.4.3.

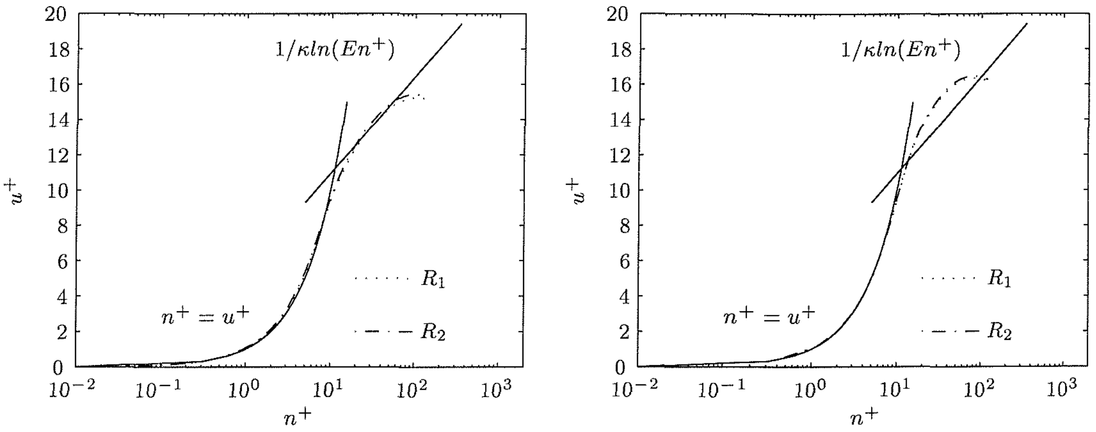

i: Mean wall profile, $Re = 8 \times 10^3$, ELMORE

ii: Mean wall profile, $Re = 8 \times 10^3$, CFX

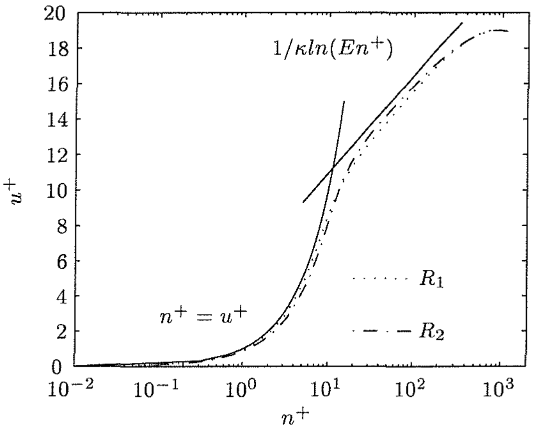

iii: Mean wall profile, $Re = 1 \times 10^5$, ELMORE

Figure 5.8: Comparison of mean wall profiles for the 2mm case, $\Gamma = 1.25$, for both CFX and ELMORE

Test Case	Before Transition	After Transition
2 mm, ELMORE	$Re = 5.0 \times 10^3$ $Ta/Ta_c = 224$ see figure 5.9	$Re = 8.0 \times 10^3$ $Ta/Ta_c = 573$ see figure 5.10
2 mm, CFX	$Re = 5.0 \times 10^3$ $Ta/Ta_c = 224$ see figure D.5	$Re = 8.0 \times 10^3$ $Ta/Ta_c = 573$ see figure D.6
8 mm, ELMORE	$Re = 5.0 \times 10^3$ $Ta/Ta_c = 653$ see figure 5.11	$Re = 8.0 \times 10^4$ $Ta/Ta_c = 2140$ see figure 5.12
8 mm, CFX	$Re = 8.0 \times 10^3$ $Ta/Ta_c = 2140$ see figure D.7	$Re = 1.6 \times 10^4$ $Ta/Ta_c = 8550$ see figure D.8
48 mm, CFX	$Re = 8.0 \times 10^3$ $Ta/Ta_c = 8900$ see figure D.9 and figure D.10	$Re = 2.0 \times 10^4$ $Ta/Ta_c = 55600$ see figure D.11

Table 5.6: List of Re, Ta/Ta_c and figure numbers for the test cases before and after transition, for both ELMORE and CFX.

§5.4.2 Flow Transition Analysis

As discussed in section §2.4 a transition from "soft" to "hard" turbulence was identified at $Re \approx 10^4$. In order to analyse this transition, the components of the turbulent Taylor vortex are compared in a series of non-dimensional profile plots either side of the transition for all three test cases. The velocity components, kinetic energy and the dissipation and production terms have been non-dimensionalised by the speed of the inner cylinder, U_1, the square of the shear stress velocity, $u_\tau = \sqrt{\tau_w/\rho}$ and a parameter $\frac{\nu}{\rho u_\tau{}^4}$, respectively. These terms are plotted against a non-dimensional radius, $R = \frac{r-R_1}{d}$ and the length $L = \frac{l}{d}$.

The associated Reynolds numbers and figure numbers describing conditions before and after transition for all ELMORE and CFX test cases calculated are presented in appendix D table 5.6. For the 8 mm case the transition occurred earlier for ELMORE then CFX, this presumably linked to the lower C_M in table 5.5. At $Re = 2 \times 10^4$, $\Gamma = 1.25$ for the 48 mm case the numeric model was unsteady. Several attempts to force a converged solution were tried by altering the grid distribution, grid densities and initial conditions. The only method of achieving a converged solution was by altering the aspect ratio of the vortex cell size. When the cell aspect ratio was reduced to unity, $\Gamma = 1$, the solution converged either side of the transition but with two vortices. This is shown in figures D.10 and D.11. The converged single cell case with an

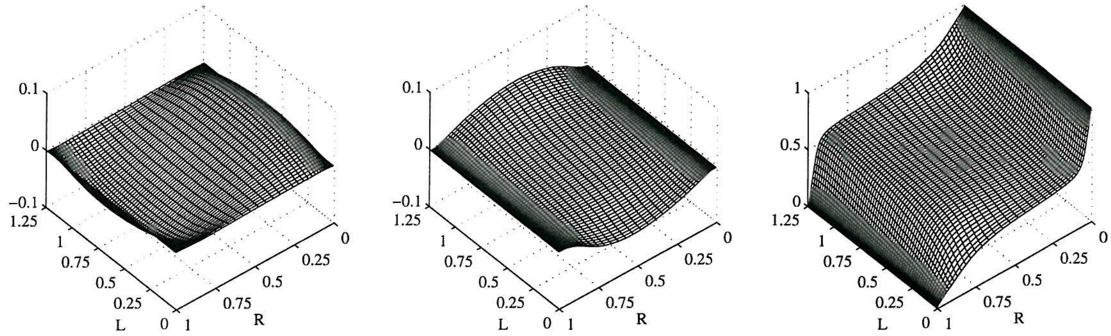

i: Axial Velocity, $\frac{u_z}{U_1}$

ii: Radial Velocity, $\frac{u_r}{U_1}$

iii: Azimuthal Velocity, $\frac{u_\theta}{U_1}$

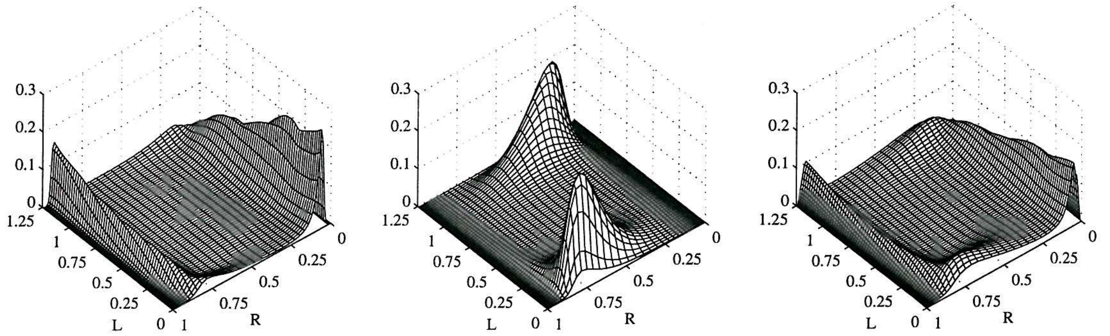

iv: Axial Turbulence Production, $\frac{\nu\mu_T(du_\theta/du_z)^2}{\rho {u_\tau}^4}$

v: Radial Turbulence Production, $\frac{\nu\mu_T(du_\theta/du_r)^2}{\rho {u_\tau}^4}$

vi: Turbulent Dissipation, $\rho\omega k \cdot \frac{\nu}{\rho u_\tau}$

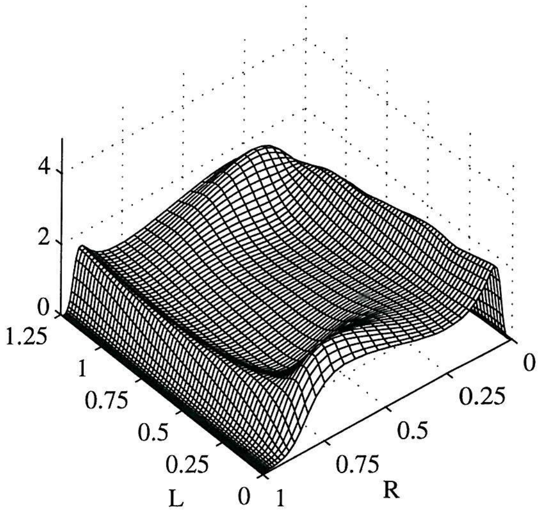

vii: Turbulent Energy, $\frac{k}{{u_\tau}^2}$

Figure 5.9: Components for 2mm case $Re = 5 \times 10^3$

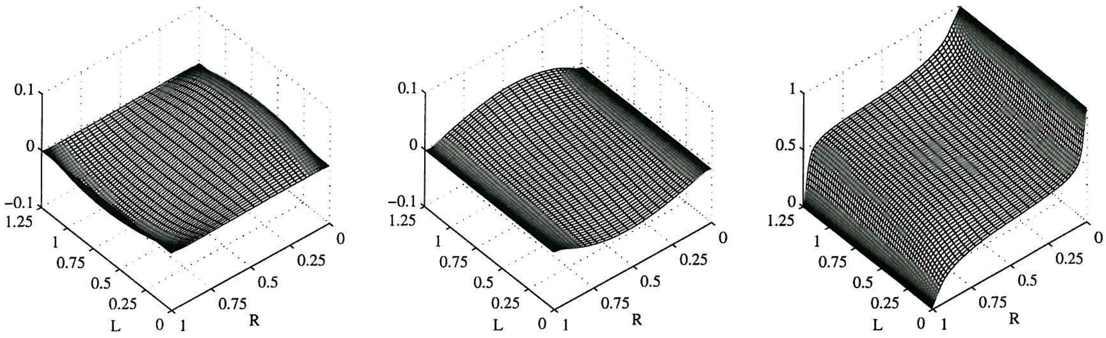

i: Axial Velocity, $\frac{u_z}{U_1}$

ii: Radial Velocity, $\frac{u_r}{U_1}$

iii: Azimuthal Velocity, $\frac{u_\theta}{U_1}$

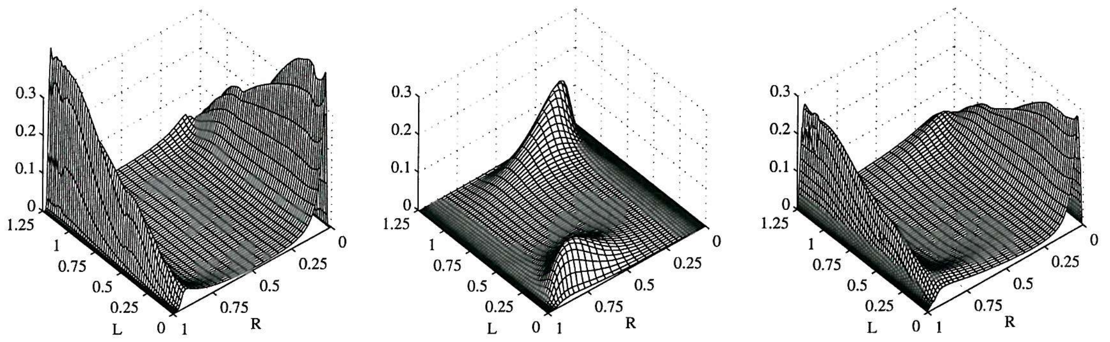

iv: Axial Turbulence Production, $\frac{\nu\mu_T(du_\theta/du_z)^2}{\rho u_\tau^4}$

v: Radial Turbulence Production, $\frac{\nu\mu_T(du_\theta/du_r)^2}{\rho u_\tau^4}$

vi: Turbulent Dissipation, $\rho\omega k \cdot \frac{\nu}{\rho u_\tau}$

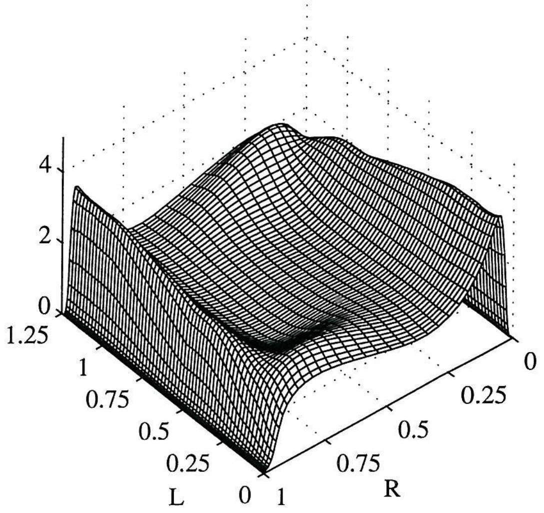

vii: Turbulent Energy, $\frac{k}{u_\tau^2}$

Figure 5.10: Components for 2mm case $Re = 8 \times 10^3$

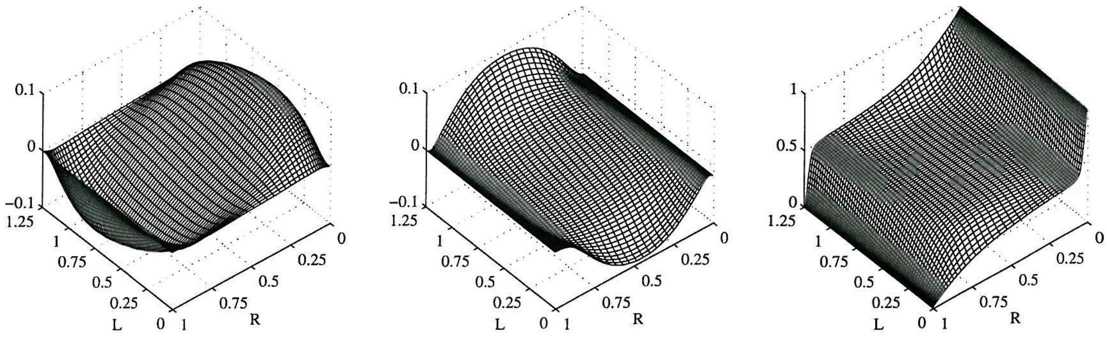

i: Axial Velocity, $\frac{u_z}{U_1}$

ii: Radial Velocity, $\frac{u_r}{U_1}$

iii: Azimuthal Velocity, $\frac{u_\theta}{U_1}$

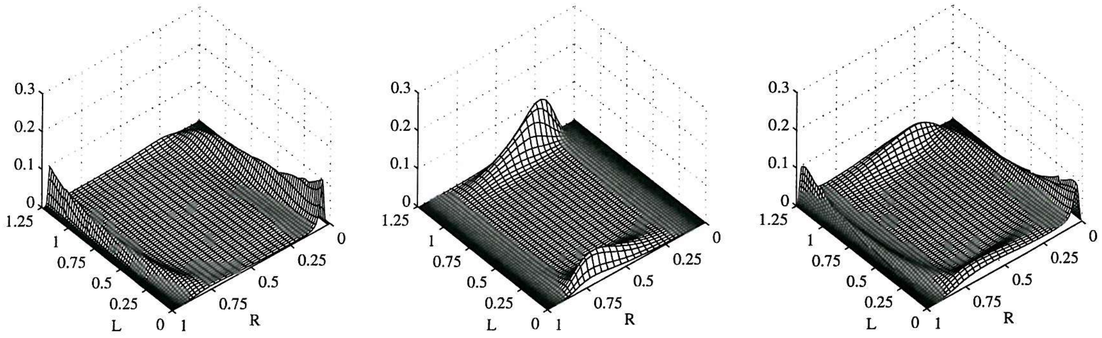

iv: Axial Turbulence Production, $\frac{\nu\mu_T(du_\theta/du_z)^2}{\rho u_\tau{}^4}$

v: Radial Turbulence Production, $\frac{\nu\mu_T(du_\theta/du_r)^2}{\rho u_\tau{}^4}$

vi: Turbulent Dissipation, $\rho\omega k \cdot \frac{\nu}{\rho u_\tau}$

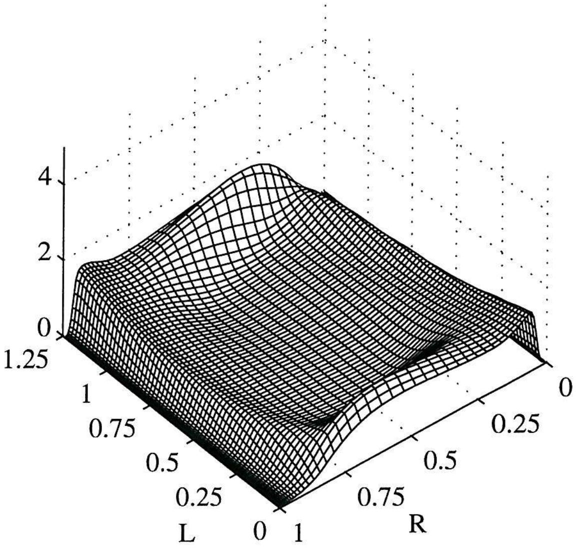

vii: Turbulent Energy, $\frac{k}{u_\tau{}^2}$

Figure 5.11: Components for 8mm case $Re = 5 \times 10^3$

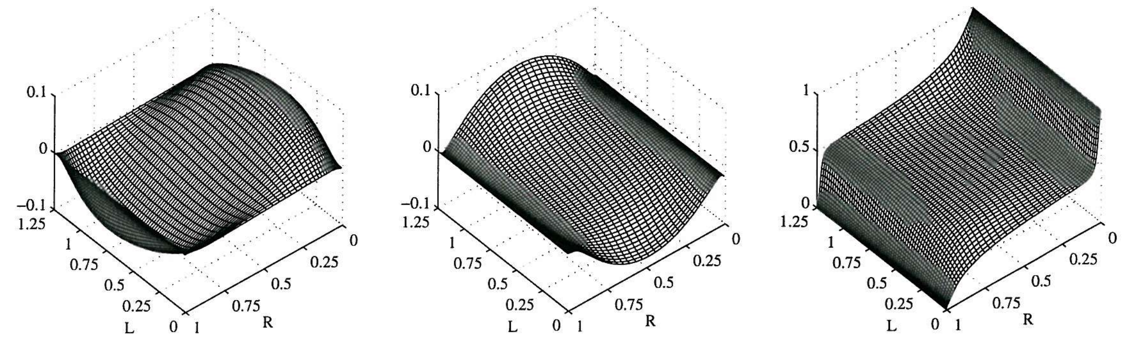

i: Axial Velocity, $\frac{u_z}{U_1}$

ii: Radial Velocity, $\frac{u_r}{U_1}$

iii: Azimuthal Velocity, $\frac{u_\theta}{U_1}$

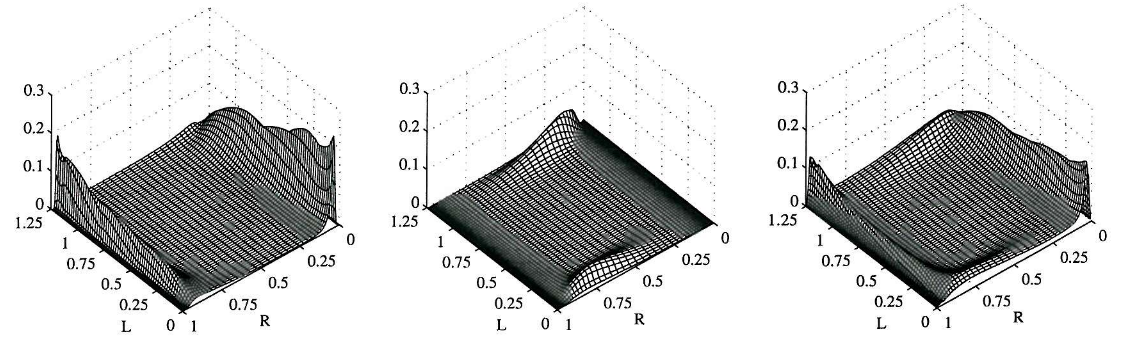

iv: Axial Turbulence Production, $\frac{\nu\mu_T(du_\theta/du_z)^2}{\rho {u_\tau}^4}$

v: Radial Turbulence Production, $\frac{\nu\mu_T(du_\theta/du_r)^2}{\rho {u_\tau}^4}$

vi: Turbulent Dissipation, $\rho\omega k \cdot \frac{\nu}{\rho u_\tau}$

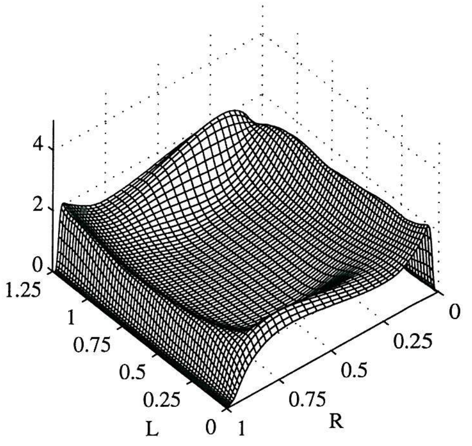

vii: Turbulent Energy, $\frac{k}{{u_\tau}^2}$

Figure 5.12: Components for 8mm case $Re = 8 \times 10^3$

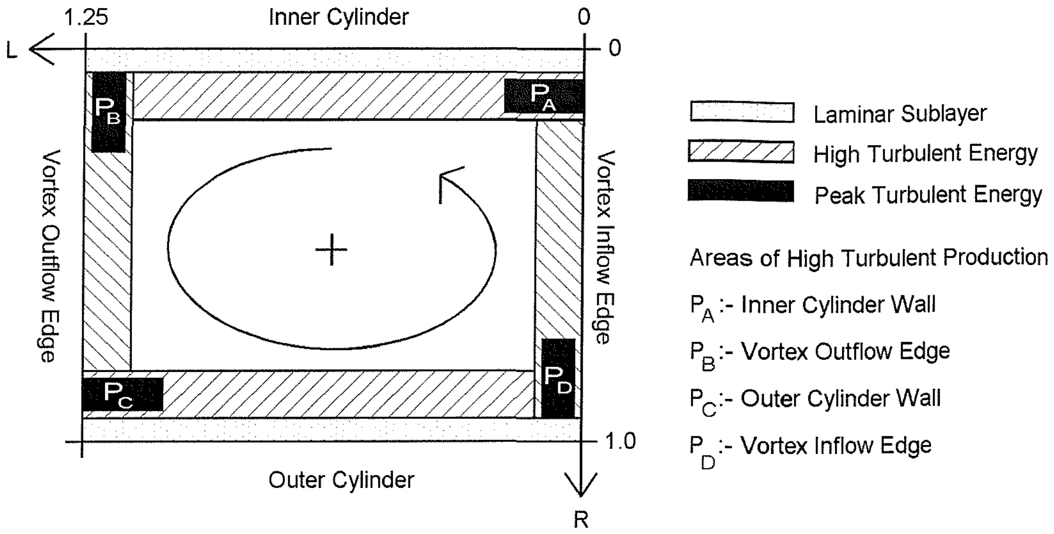

Figure 5.13: Schematic Drawing of a Taylor Vortex indicating areas of high turbulent energy.

aspect ratio of 1.25 is also presented in figure D.9 for comparison.

The axial and radial velocity components, u_z* and u_r, for both the 2 mm and 8 mm case are similar as in figures 5.9-5.12.i-ii and D.5-D.8.i-ii. The velocity components are larger for the 8 mm case than 2 mm, this is further demonstrated in figures D.9.i-ii for the 48 mm case where the maximum non-dimensionalised velocity has doubled. The azimuthal velocity components, u_θ, are also consistent across figures 5.9-5.12.iii and D.5-D.11.iii with higher axial gradients than radial gradients before the transition.

The turbulent kinetic energy plots, k (figures 5.9.vii, 5.11.vii, D.5.vii and D.7.vii) have maximum peaks in the radial plane, at the outflow edge of the vortex. After the transition, (figures 5.10.vii, 5.12.vii, D.6.vii and D.8.vii) have maximum peaks in the axial direction, along the edge of the inner cylinder. This is also demonstrated in figures D.10.vii and D.11.vii with two vortices for the 48 mm case .

The two most significant contributions, by a factor of approximately 1000, to the production of turbulent kinetic energy are due to the azimuthal velocity gradients in the radial direction $\mu_T(\frac{du_\theta}{dr})^2$ (figures 5.9-5.11.iv and D.5-D.11.iv) and in the axial direction $\mu_T(\frac{du_\theta}{dz})^2$ (figures 5.9-5.11.v and D.5-D.11.v). The test cases show relatively larger peaks in the radial production, vortex boundaries, than the axial production, wall boundaries, before the transition. The turbulent dissipation, $\rho\omega k$, also show similar trends (figures 5.9-5.12.vi and D.5-D.11.vi) following the pattern of the turbulent kinetic energy.

All these presented computations clearly show that as Reynolds number increases there is a transition to a flow dominated by the wall shear stress, as discussed by Lathrop *et al.* [22] At lower Reynolds numbers turbulence production is dominated by the outflow of the Taylor vortex. This is represented schematically in figure 5.13 where regions P_A and P_C are associated with the turbulent wall shear stress production and P_B and P_C are associated with the vortex

---

*In the appendix D, u_x is used to donate the axial velocity

d	Test Case	Re	Γ	Bilgen & Bilgous	ELMORE
2mm	a	8×10^3	0.50	0.00331	0.00325
2mm	b	8×10^3	0.75	0.00331	0.00354
2mm	c	8×10^3	1.00	0.00331	0.00415
2mm	d	8×10^3	1.25	0.00331	0.00413
2mm	e	8×10^3	1.50	0.00331	0.00410
2mm	f	8×10^3	1.75	0.00331	0.00409
2mm	g	8×10^3	2.00	0.00331	0.00415

Table 5.7: List of test cases and a comparison of C_M values for the aspect ratio tests

inflow and outflow shear stresses, where,

$$P_A < P_B \quad \text{and} \quad P_C < P_D \quad \text{before transition}$$
$$P_A > P_B \quad \text{and} \quad P_C > P_D \quad \text{after transition}$$

For the higher Reynolds number cases turbulence production is dominated by the wall shear stress derivative $\frac{\partial u_\theta}{\partial r}^2$ signified by P_A.

The results suggest that the transition to wall dominated turbulent production occurs at a lower Reynolds number for higher radius ratios. This can be demonstrated by comparing figures D.6 and D.7. Both these test cases are at the same Reynolds number but the transition has occurred for the 2 mm case but not the 8 mm case. This is due to the fact that Ta/Ta_c is around 75% lower for the 2 mm case. Hence the vortex strength is less, see figures D.6-D.7(i-ii). This in turn leads to relatively less turbulent production at the vortex outflow and inflow edges, hence the transition occurs at a lower Reynolds number. It is also of interest to note that the non-dimensionalised radial and axial velocity components are higher before the transition.

§5.4.3 Aspect Ratio Tests

The conditions of the test cases carried out in order to illustrate the effect of Taylor vortex aspect ratio, Γ are presented in table 5.7. All tests were carried out for the 2 mm case at $Re = 8 \times 10^3$. The results are presented in figure 5.14 as a vector plot, azimuthal velocity and turbulent kinetic energy profiles. For all cases one Taylor vortex formed apart from; case a, $\Gamma = 0.5$, where no vortex formed and case g, $\Gamma = 2.0$, where two vortices formed. In order to interpret the results a comparison of vortex properties is presented in figure 5.15.

Increasing the vortex strength improves the energy transfer from the inner and out cylinder. So for higher vortex strength the azimuthal gradient at the cylinder wall will be higher. Thus, if no Taylor vortex is present the skin friction will be lower. This is shown in figure 5.15.i. The vortex also has the effect of flattening the azimuthal profile across the main flow 5.14.ii, as more energy is dissipated within the sublayer. The middle azimuthal and axial velocities without a Taylor vortex is presented in figure 5.16 , $\Gamma = 0.5$ and with a Taylor vortex in fig

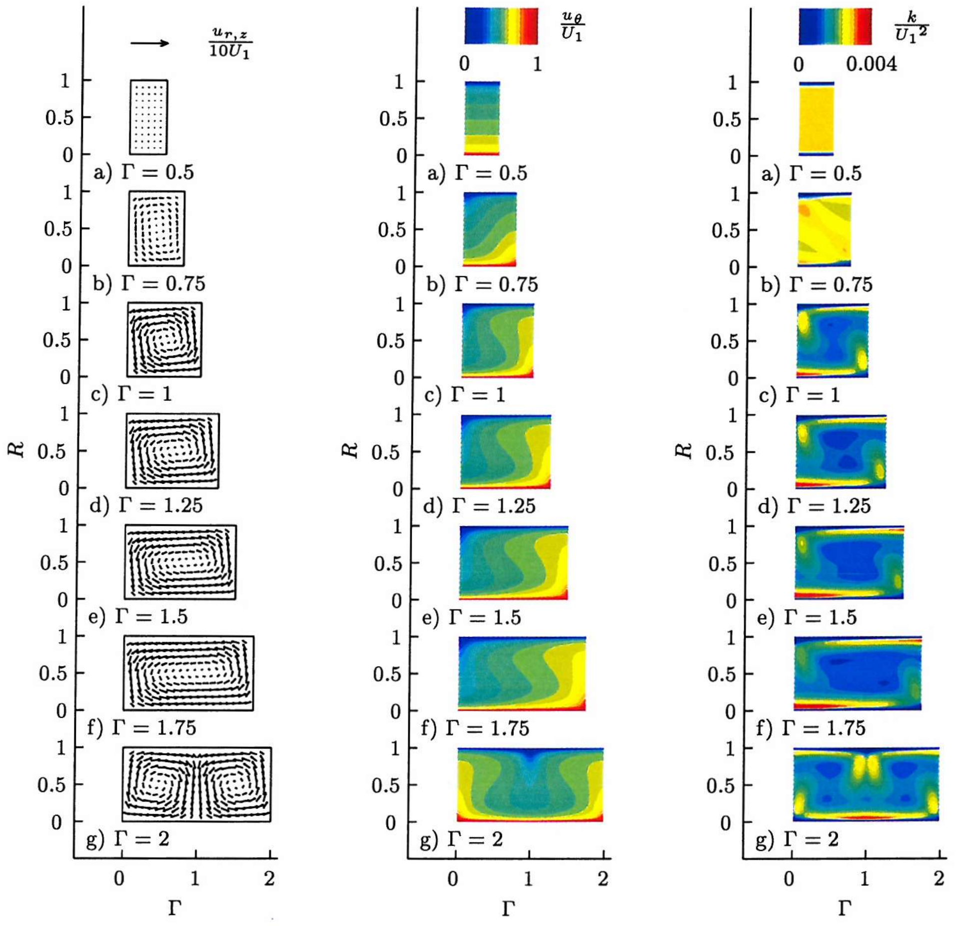

i: Vector Plot

ii: Azimuthal velocity profile

iii: Turbulent kinetic energy

Figure 5.14: Effect of Γ on vortex properties for the, 2mm test case, $Re = 8 \times 10^3$, using ELMORE

ure 5.17 , $\Gamma = 1.5$. The improved energy transfer from the wall is so strong that across the gap at the middle of the vortex u_θ in the main flow is higher at the outer cylinder than at the inner cylinder. Figure 5.17.i show that both azimuthal and axial sublayers overlap and that axial velocities are greatest at the interface between the sublayer and the main flow.

The effect of the flattening of the azimuthal profile is further demonstrated in figure 5.15.iv as without a Taylor vortex the wall profile follow Von Kármán law of the wall, for $n^+ > 10$. Whereas with a Taylor vortex the wall profile reaches the law of the wall but then drops off. This effect of the flow not obeying the law of the wall is akin to what happens with curved channel flow discussed in section §2.2.4. The flattening of the azimuthal profile across the main flow causes a reduction in the overall $\overline{k}$ figure 5.15.iii as the gradients in the main flow are substantially less. The amount of reduction of $\overline{k}$ decreases as the peak intensities are further spread out as Γ increases, shown in figure 5.14.iii.

Figure 5.15.i shows a peak in C_M at $\Gamma = 1.0$, at the critical laminar wave length for the 2 mm case, after rising 25% from no vortex case. The sear stress then decrease by only 2%

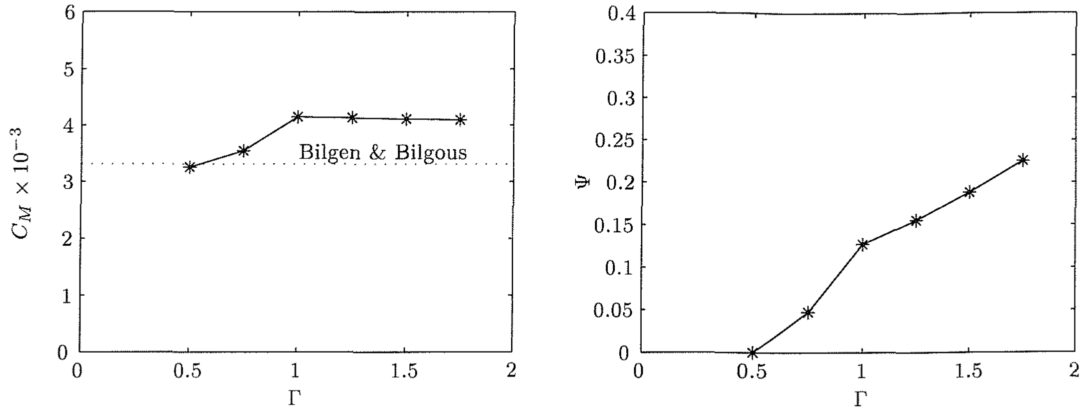

i: Azimuthal shear stress

ii: Non-dimensional Taylor vortex strength

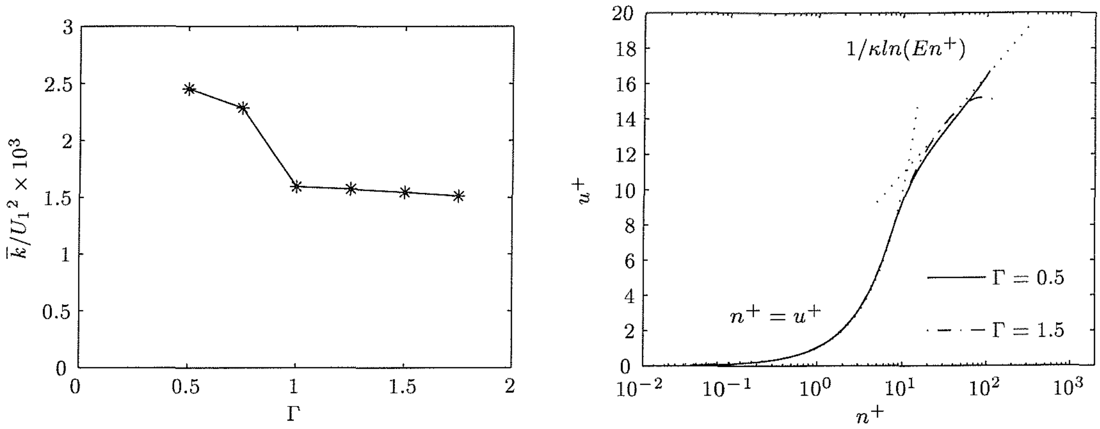

iii: Non-dimensional mean turbulent kinetic energy

iv: Mean Wall profile

Figure 5.15: Comparison of Taylor vortex properties with Γ for the 2mm case, $Re = 8 \times 10^3$, using ELMORE.

and not a large as the expected 10% in section §2.4 for vortex lengths larger than critical laminar wave length. This slight fall in Taylor vortex skin friction strength after Γ1.0 presumably linked to flattening of $\overline{k}$. As although the vortex strength is increasing the mean azimuthal velocity profile is not getting any flatter.

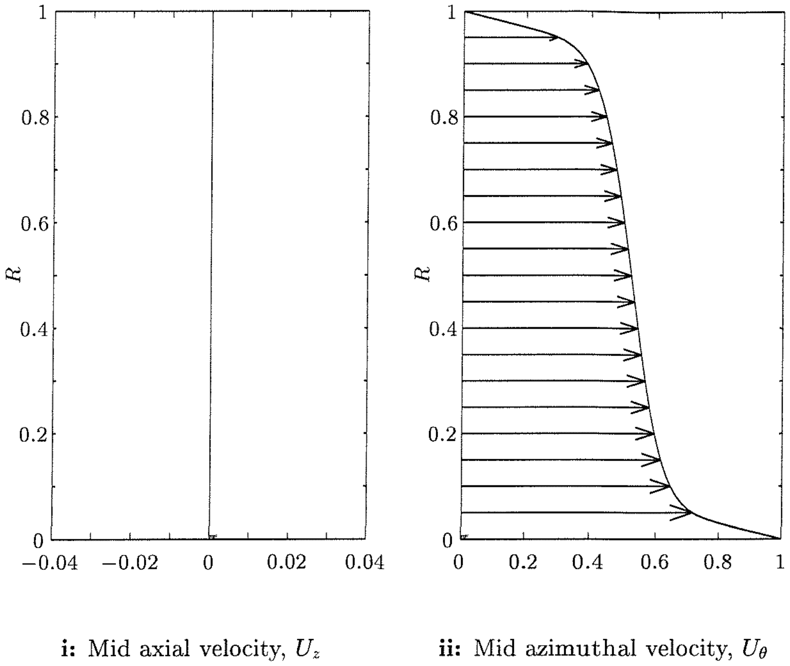

i: Mid axial velocity, U_z **ii:** Mid azimuthal velocity, U_θ

Figure 5.16: Boundary layer profiles for $\Gamma = 0.5$ at the centre plane of a Turbulent Taylor vortex, $Re = 8 \times 10^3$

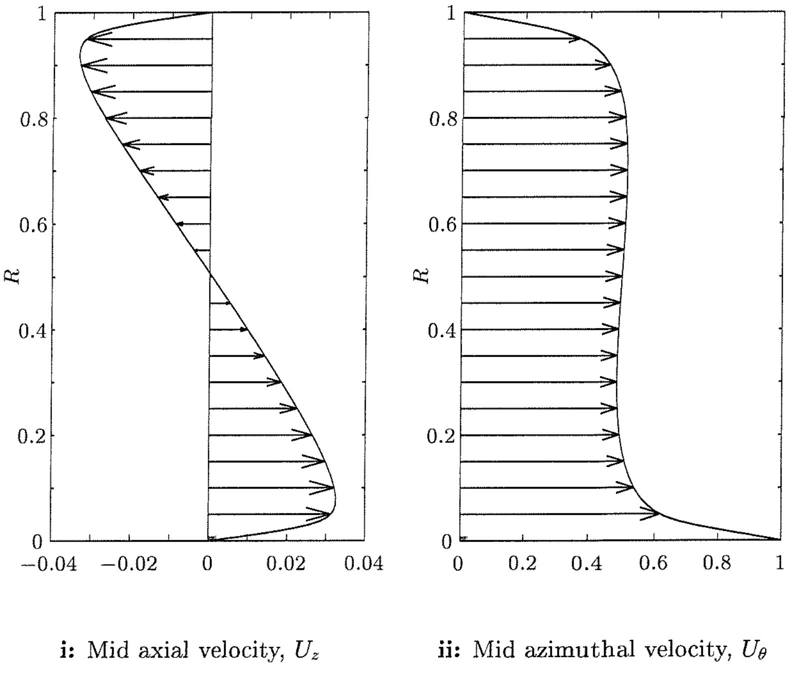

i: Mid axial velocity, U_z **ii:** Mid azimuthal velocity, U_θ

Figure 5.17: Boundary layer profiles for $\Gamma = 1.5$ at the centre plane of a Turbulent Taylor vortex, $Re = 8 \times 10^3$

§5.5 Conclusions

Based on these results for one turbulent Taylor vortex the following conclusions can be drawn.

I. For the range of Reynolds number tested and high radius ratios a low Reynolds number turbulence model is required to produce meaningful results. The low Reynolds number k-ω has proved effective and solutions have been presented using both CFX and ELMORE with the SIMPLEC pressure correction.

II. Discrepancies between CFX and ELMORE for the 2mm gap case of the thruster unit have demonstrated the effect of coding approach and the sensitivity of the low Reynolds number k-ω model to node placement within the sublayer.

III. The transition from "soft" to "hard" turbulent flow in the Taylor-Couette system with an inner cylinder rotating and a fixed outer cylinder has been identified for a wide range of radius ratios using both CFX and ELMORE. At relatively low Reynolds numbers turbulent production is dominated by the flow between two adjacent Taylor Vortices. A transition occurs as the Reynolds number is increased to a condition where the shear stress of the rotating cylinder becomes the dominant source of turbulent kinetic energy production.

IV. It has also been shown that developed turbulent flow can occur for $Ta/Ta_c < 1000$ for small gaps and that the transition occurs earlier for these flows.

V. Taylor vortices have also proved to have a flattening of the azimuthal velocity profile causing an increase in the skin friction of 25%, for the 2 mm case at $Re = 8 \times 10^3$. This is due to improved energy transfer at the wall due to the Taylor vortex.

VI. The Aspect ratio tests show a maximum torque when the Taylor vortex length is that of the critical laminar length, for the 2 mm case at $Re = 8 \times 10^3$.

In order to resolve the node placement problem adaptive grid refinement would be preferable when modelling the sublayer, as during the solution procedure adaptations could be made to the grid to ensure a constant number of cells in the sub-layer. Although full confidence in the ability of the k-ω model to predict turbulent Taylor vortices cannot be demonstrated due to the limited experimental data available and lack of LES/DNS data. The results where however are good enough to provide an explanation for the flow transition from "soft" to "hard" turbulence. In the next chapter the domain is extended to the full geometry of the thruster unit to allow the effects of the open ends to be studied. The next chapter also presents the first steps for a full DNS solution for both validation of turbulence models and to provide insight into evidence for Görtler vortices. In order to do this a parallel solution was pursued due to the size of the problem. The available license for CFX did not provide parallel support and therefore just ELMORE was used in the next chapter.

CHAPTER

6

Modelling the Complete Thruster and its Start-up

§6.1 Introduction

Moore's law predicted in 1965 that every 18 months there will be a doubling of the number of components in intergrated electronics [60]. This forecast was presented for the increase in performance through to 1975 but still holds true today.* Hence over the course of a 3 → 4 year Phd, this equates to more than quadrupling in computer clock speed alone. Increases in performance have also been caused, due to recent advances in parallel computational configurations, in particular at the School of Engineering Sciences at the University of Southampton, with the introduction of fast, readily available parallel linux clusters [61]. Both these factors, have enabled much larger computational problems to be solved. This means that the basis of the computational efforts previously discussed, in the chapters on laminar flow and single turbulent Taylor vortex modelling, can be extended to computational domains, approaching that of real world problems at PhD level research.

The first part of this chapter is concerned with modelling the full gap problem in the thruster unit in 2-D. These results are then compared with the bubble experiments. The pressure profile is used to explain the distribution spectrum produced. The effects of acceleration on the formation of Taylor vortices are then solved using a 2-D, DNS method. This demonstrated the evolution of turbulent Taylor vortices form Görtler vortices and the development of boundary layers are examined. Both these sets of simulations were carried out on linux clusters and provide initial investigations required for further research.

---

*As stated in Intel's research web pages, http://www.intel.com/research, Oct 2001. "Through Intel's technology, Moore's Law has been maintained for far longer, and still holds true as we enter the new century. The mission of Intel's technology development team is to continue to break down barriers to Moore's Law."

§6.2 Fuller Thruster Modelling

The one turbulent Taylor vortex geometry has been extended to a full 2D model of the thruster unit to include the open ends of the thruster. The grid distribution is shown in figure 6.1 using 8 blocks and 35,000 cells. This demonstrates the problem of having to pack the cells close to the walls as this distribution is then extruded into the domain. This geometry has been solved using the SIMPLEC algorithm and the k-ω model in ELMORE at $Re = 2 \times 10^4$. Over 100,000 iterations were required which took just over 40 CPU days, on a lunix cluster with 500Mz CPU's. The solution was found to be unsteady with the numbers of vortices altering and never fully converged.

As shown in figure 6.2 the end Taylor vortex is rotating in the same direction as the vortex in the end gap. Between these two vortices an extra vortex was temporarily formed, which also occurred at the other end. The other internal vortices tended to move and reduce in size producing a wavy turbulent Taylor vortex pattern. As the SIMPLEC algorithm was used this reasoning is hypothetical. Hence the domain needs to be extended into a further 3-D domain and the use of a transient algorithm, such as the PISO scheme.

The velocity profiles presented in figure 6.3 represented similar trends as for the one Taylor vortex solutions in chapter 4. Figure 6.3.i and 6.3.ii indicate that both end Taylor vortices (the vortex adjacent to the open gaps) are rotating in the same direction as the flow in the end gap. Figure 6.3.iii with high azimuthal velocity gradients at vortex inflows and shallow velocity gradients at the vortex outflows, resemble that of the one vortex tests.

The turbulent Taylor vortex properties are presented in figure 6.4, again with similar trends for the middle vortices presented for the one Taylor vortex cases. Figure 6.4.i compares the vortex strength with the vortex wavelength and shows a much smaller increase than reported for the one vortex test presented in figure 5.15.ii. The overall vortex strengths, in figure 6.4.ii are slightly larger than expected from the one vortex results. This is similar to the results for the laminar internal vortices presented in figure 6.4.i.

For the end Taylor vortex cases smaller vortex strengths were produced and it has higher skin friction coefficients. This is similar to what occurred for the laminar results as the internal vortices had slightly higher vortex strengths, (figure 6.4.i) and the skin friction was lower (figure 6.4.ii). The lower Taylor vortex strength is due to the vortex in the end gap rotating in the same direction, hence at the boundaries between the two vortices the velocities are in opposing directions. The fact that these two vortices do not merge to form one vortex, demonstrates the strength and stability of turbulent Taylor vortices.

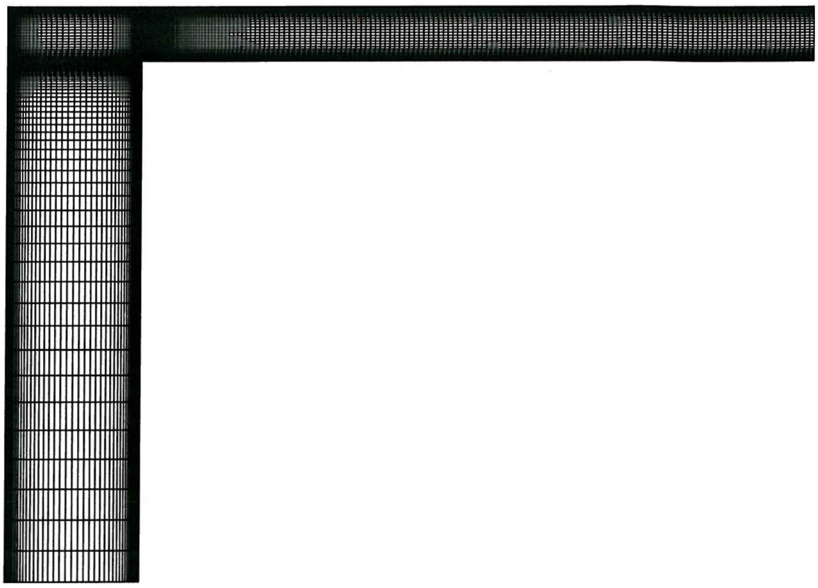

Figure 6.1: 2-D slice showing half the mesh.

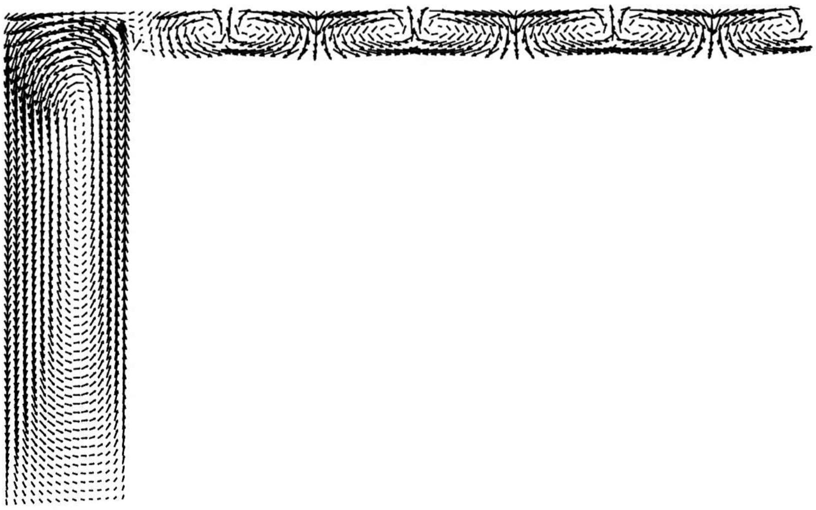

Figure 6.2: Interpolated vector plot, $u_z \times u_r$, for half the domain.

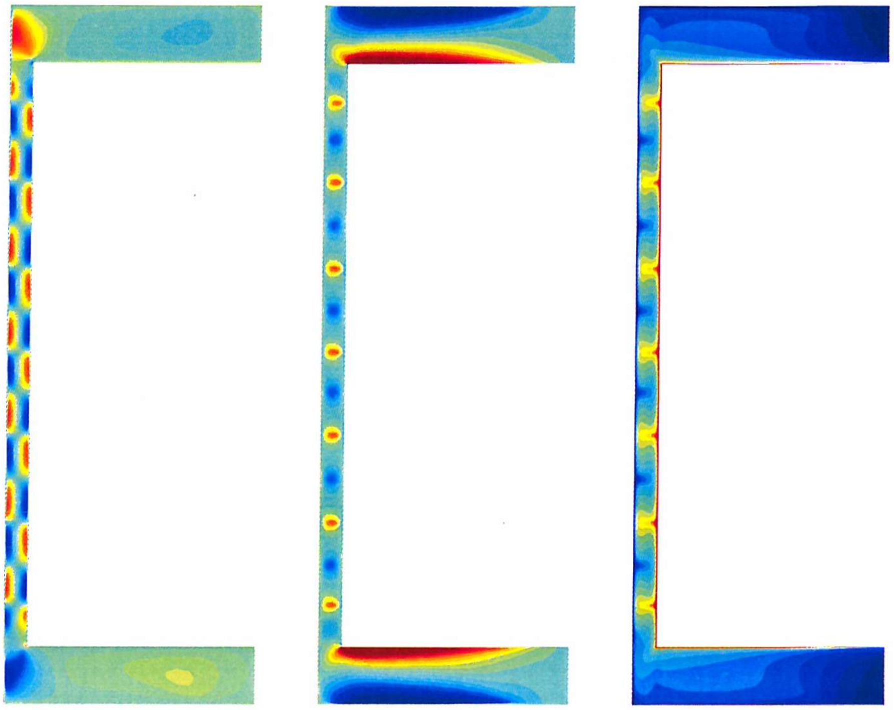

i: Axial velocity profile, u_z

ii: Radial velocity profile, u_r

iii: Azimuthal velocity profile, u_θ

Figure 6.3: Comparison of solved variables for the full geometry, red to blue corresponds high to low values respectively.

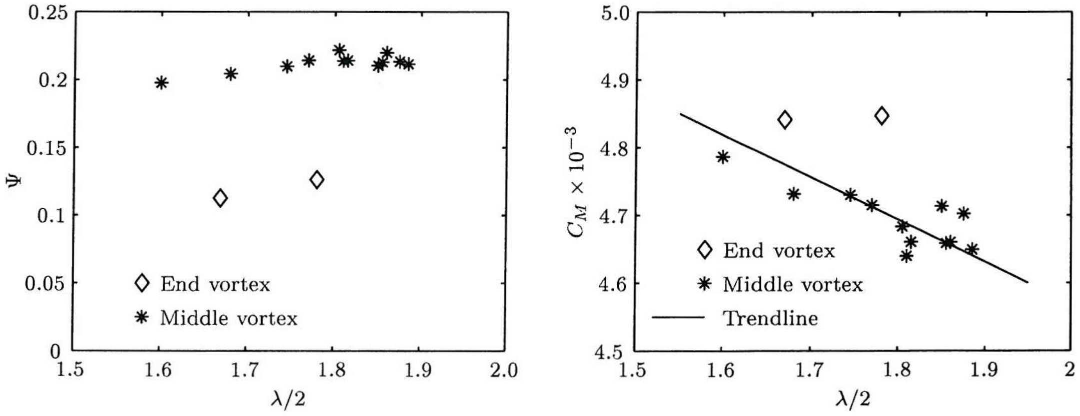

i: Vortex strength

ii: Skin friction

Figure 6.4: Comparison of vortex properties with vortex length inside the full geometry.

§6.2.1 Pressure and Bubble Measurement Comparison

The results have been compared to the bubble spectrum produced during the experimental analysis as discussed in §3.6. The bubbles are subjected to two main forces the pressure, causing them to accumulate in areas of low pressure and the forces due to flow momentum. The regions of low pressure occur close to the inner cylinder peaking at the vortex outflow boundary. This is demonstrated in figure 6.5 where the minimum regions of pressure are shown in the profile plot. The pressure has been summed and inverted for the inner half of the gap to produce a pressure spectrum, indicating regions of high bubble probability. This spectrum, shows the alignment of the pressure spectrum with the vortex outflows.

To compare the bubble spectrum the mean spectrum was plotted as shown in the figure 6.5. Thus, each of the peaks will represent an outflow boundary. There are three main peaks in the middle demonstrating at least three pairs of vortices. Another two pairs have been added but are speculative as the bubble results, as discussed in chapter 3, stated that the flow appeared to be unstable.

The effect of a higher bubble flow rate was presented in figure 3.28. This figure shows bubbles across the whole width of the gap. This larger number of bubbles will cause them to move around the Taylor vortex. As the vortex centre is closer to the outflow boundary from the inner cylinder the bubble will take the shortest path around the vortex to return to the region of lowest pressure. Hence the large gaps between bubble clustering due to the low probability of the bubble at the boundary of the vortex inflow towards the inner cylinder.

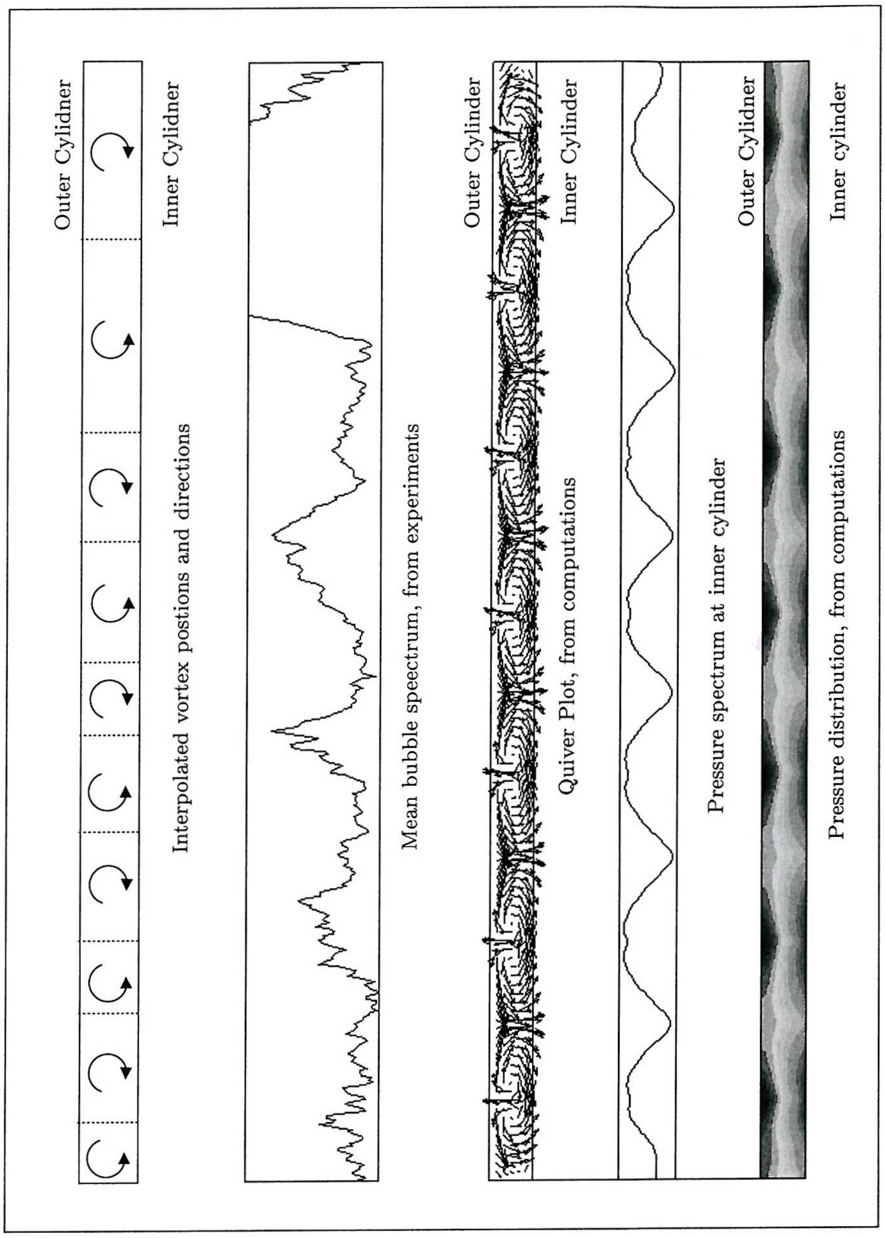

Figure 6.5: Comparison between the thruster computations and the bubble spectrum from the experiments

§6.3 The 2D Start-up Problem

The following computations form the basis for studies into the effects of start-up on the formation of turbulent Taylor vortices. As stated in the background information, in Chapter 2, the number of Taylor vortices formed is a function of the acceleration of the inner cylinder. As demonstrated in the previous chapter the size of vortices affect the shear stress and the strength of the vortices. Thus, it is possible that by applying knowledge of the acceleration effects the number of vortices can be controlled and hence the skin friction reduced.

To solve this problem a full 3-D DNS solution is required to allow transitional phases to be modelled. This is important as during the initial phases of the acceleration processes the flow is laminar as the turbulent production lags behind the growth of momentum. Therefore, modelling the development of turbulence which effects the formation of Taylor vortices is required. To perform a full 3-D simulation to resolve all the eddies is well beyond the available resources at the time. So to carry out this initial phase of research the gap was modelled as a 2-D slice, as used in all calculations, and flow was solved from a stationary flow field without use of any turbulent models.

Vortex stretching is the process by which the largest turbulent eddies interact with and extract energy from the mean flow. The velocity gradients in the mean flow shears and distorts these turbulent eddies. Thus one end of the vortex is forced to move faster than the other causing the eddies to become stretched. In two-dimensional turbulence the energy cascade goes the other way. This is because there is no vortex stretching which occurs in the third dimension. Thus instead of the energy transfer from larger to small eddies, the vortices tend to coalesce to form larger vortices as the energy is transferred.

However, for this solution the 2-D plane is not in the direction of the flow and hence eddy coalescing due to the rotation of the inner cylinder in the azimuthal direction is not resolved. This type of solution is thus akin to a 1-D DNS solution of plane Couette flow. The author realises that this is an artificial approach to DNS modelling and it should be done in 3-D to resolve the turbulent eddies. As even in flows where the mean velocities and pressures vary in one or two dimensions the turbulent fluctuations always have a three-dimensional spatial character. Thus the method used here, is referred to as a Pseudo Direct Numerical Simulation, P-DNS. Since, there are no turbulent eddies are present in the final solution it can not be considered as a spatially filtered LES.

To solve this transient flow the domain was split into six uniform blocks to allow parallel simulation. The PISO algorithm was used for the pressure correction. The solution is discretised with a three-time level method [62]. This is second order in both time and space for the small time steps required for the PISO algorithm. The SIP solver was used as before for the momentum equations. All initial variables were set to zero to simulate the formation from rest. Initially the P-DNS were carried out on a much smaller domain but it was discovered that at the block interfaces, vortices were forming at the inner cylinder. To demonstrate that the effect of the block interface was not the sole cause of vortices, the domain was extended to half the length of that in the thruster with a single block interface in the middle. To establish the effect of end boundaries, one boundary was rotating while the other was stationary. To demonstrate the effect of speed, tests were carried out at two Reynolds number of 5×10^3 and 8×10^3.

To ensure that sufficient cells were placed across the gap to accurately model the flow 150 cells were used. This is more than twice that used for the turbulence modelling. The grid was uniformly expanding and then contracting across the gap. The first node was placed well inside the laminar sublayer. For $Re = 5 \times 10^3$, the first node was at $n+ = 0.3$, this is well below the $n+ = 1$ criteria commonly used for spectral DNS calculations. For finite volume calculations, using 2^{nd} order discretisation a higher grid density is required to capture the flow and this position is similar to that used for the turbulence modelling. 1000 cells were used across the length and to define the periodic boundary 4 cells are required in the azimuthal direction. Thus, a total of 600,000 cells were used to define the domain. A time step of 10^{-5} sec. was used. For $Re = 5 \times 10^3$, 150,000 time steps were solved using 6, 500Mz, CPUs. This required just over 12 whole days and a constant skin friction was asymptotically approached.

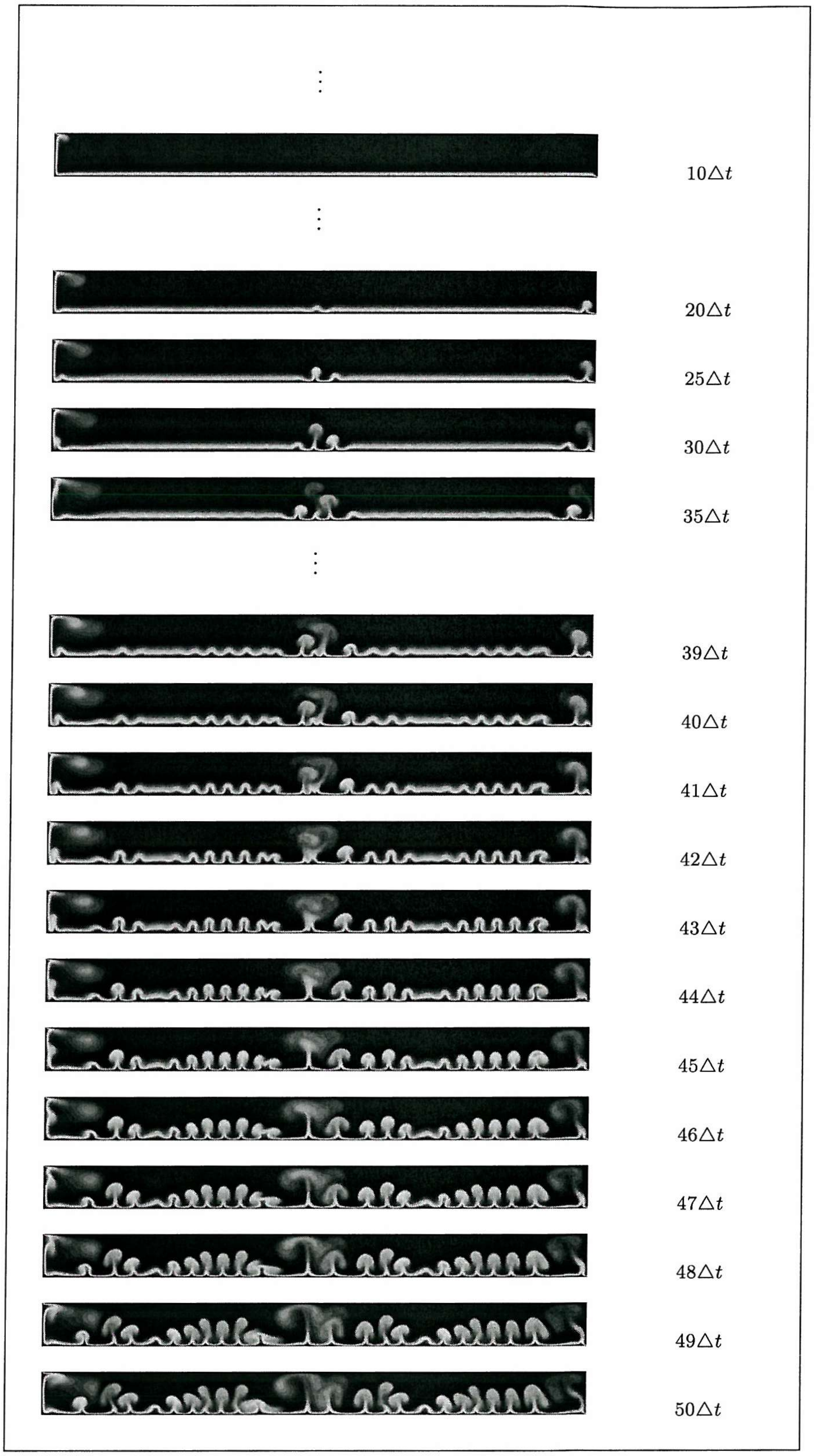

Figure 6.6: Part I: Initial formation of Görtler vortices, $Re = 5 \times 10^3$, $\triangle t = 0.0025\,\mathrm{s}$

Figure 6.7: Part II: Mixing of Görtler vortices phase, $Re = 5 \times 10^3$, $\triangle t = 0.0025\,\text{s}$

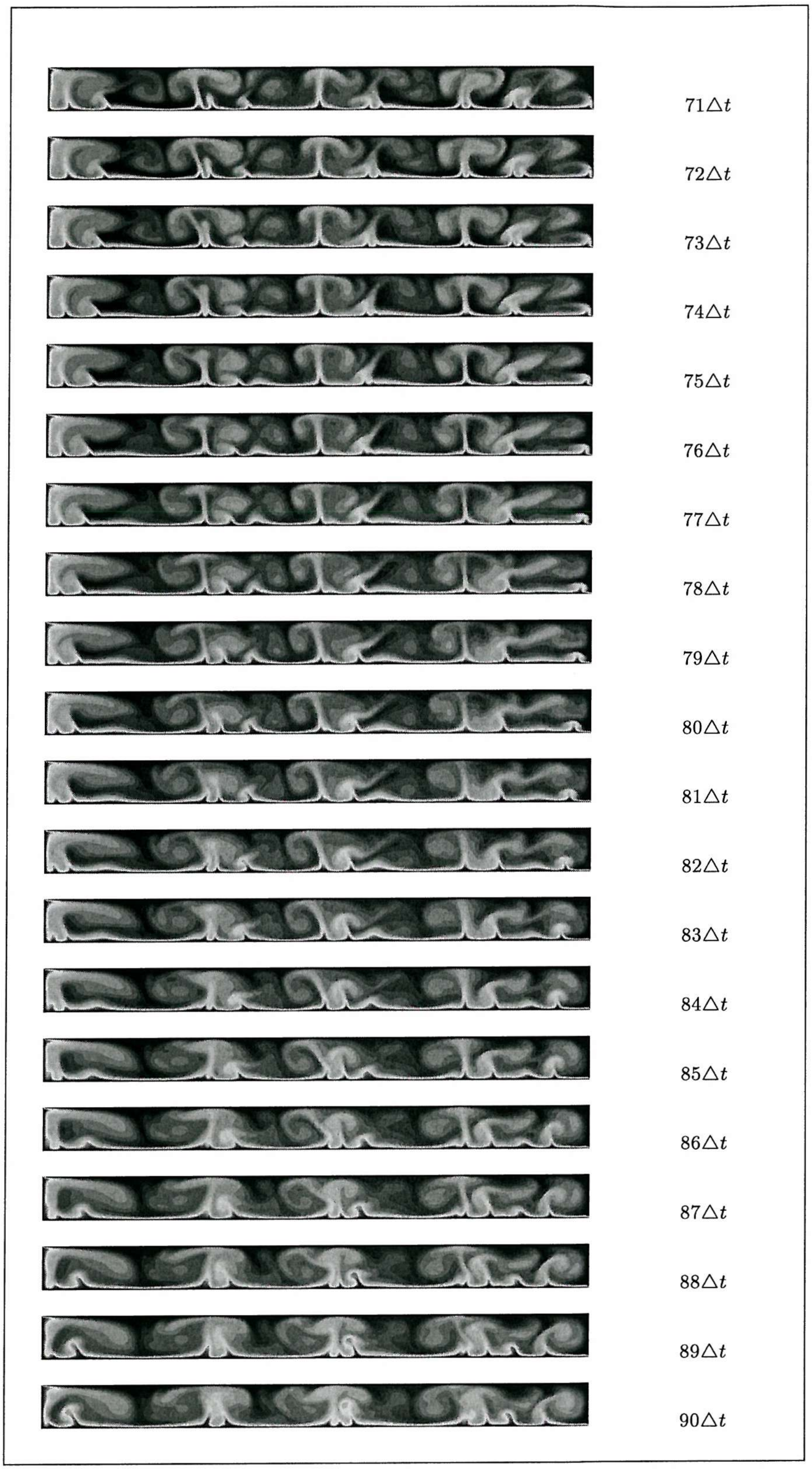

Figure 6.8: PART III: Chaotic Görtler/Taylor vortex mixing phase, $Re = 5 \times 10^3$, $\triangle t = 0.0025\,\mathrm{s}$

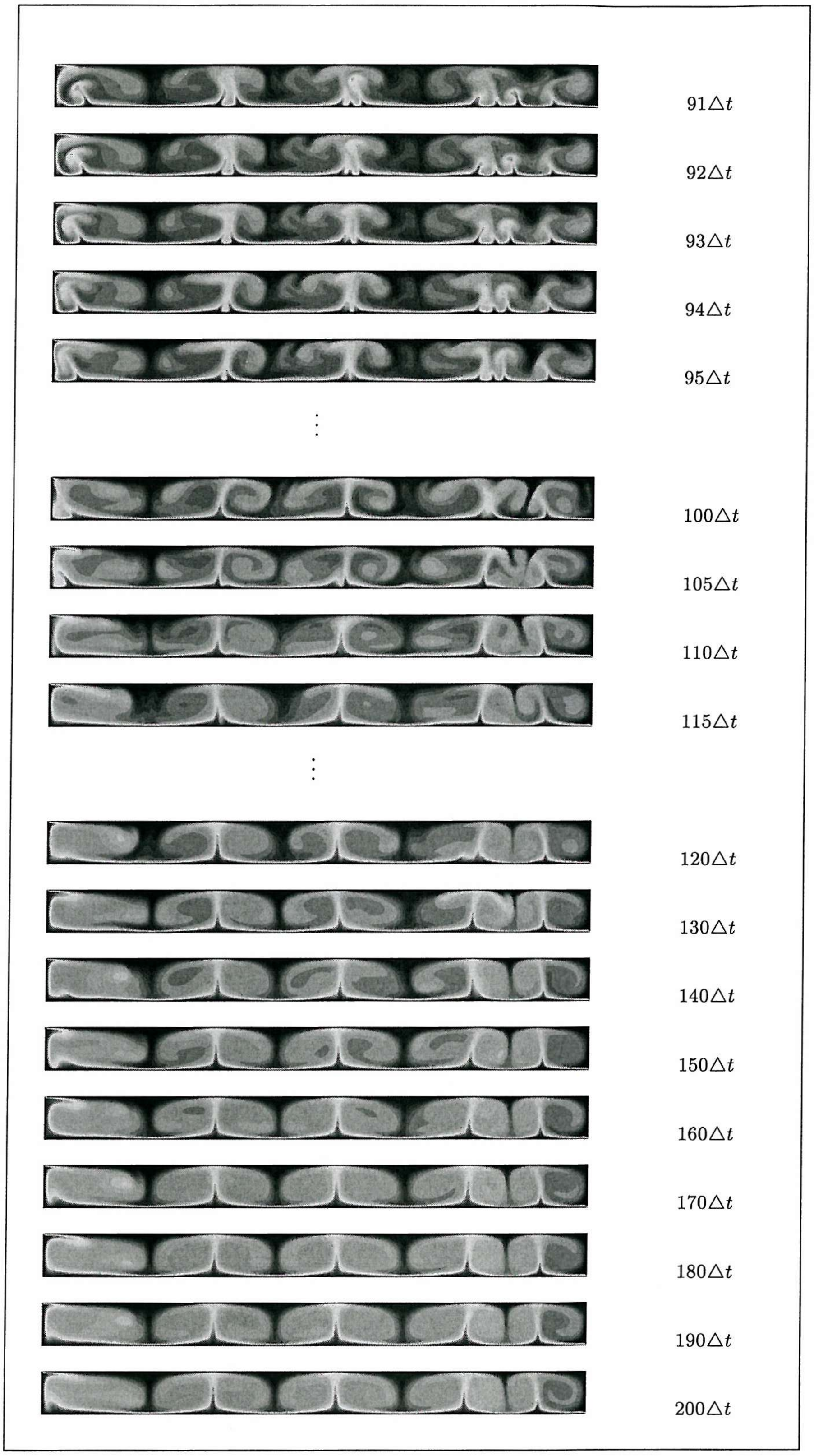

Figure 6.9: Part IV: Stabilization of the Taylor vortices, $Re = 5 \times 10^3$, $\triangle t = 0.0025\,\text{s}$

§6.3.1 Results and Discussion

Figures 6.6 to 6.9 represent the development of Taylor vortices as a series of azimuthal velocity plots. For coherence in the text the results for $Re = 8 \times 10^3$ are presented in the appendix E.1 to E.4. These results are instead presented as a series of close-up images, again demonstrating the formation of Taylor vortices in the series as a series of four steps, in figure 6.10. To improve clarity for the quiver plots the data was interpolated to a much coarser grid. $\triangle t$, corresponds to the time between transient dumps of data. As the time step was 10^{-5} and data was dumped from the solver every 250 time steps, $\triangle t = 0.0025$ sec.

All the figures demonstrate the formation of stable Taylor vortices from Görtler-type vortices forming at the inner cylinder. The following series of steps have been identified for $Re = 5 \times 10^3$:

I. formation of Görtler-type vortices ($35\triangle t \rightarrow 50\triangle t$);

II. mixing of Görtler-type vortices ($35\triangle t \rightarrow 50\triangle t$);

III. mixing of Görtler-type and Taylor vortices ($75\triangle t \rightarrow 100\triangle t$);

IV. stabilization of Taylor vortices ($100\triangle t \rightarrow$).

Initially a series of well ordered pairs of Görtler-type vortices at the inner cylinder is clearly demonstrated in the first quiver plot in figure 6.10. This is in contrast to the usual definition of Görtler vortices which form on concave surfaces. Next is a phase of Görtler-type vortices mixing, this is due to the initial vortices dissipating across the gap with new vortices forming at the inner cylinder. During, the third phase Taylor vortices begin to form but as the flow has not fully developed Görtler-type vortices are still being produced from the surface of the inner cylinder. Finally as the flow is fully developed, the Taylor vortices stabilise and no further Görtler-type vortices are produced.

An initial pair of Görtler-type vortices are present at the block boundary in figures 6.6 and E.1. This is due to the source of perturbation at the block interface being the most dominant. Two "dummy" cells were used to pass information between the each of the blocks and hence to eliminate this source of perturbation, more cells than the order of the discretisation scheme are required. A premature perturbation like this could also form in an experimental facility due to a large scratch on the surface of the inner cylinder. This perturbation however does not dominate in the final solution as it does not form vortices in the latter parts of the calculation (figures 6.8-6.9 and E.3-E.4).

The numbers of vortices produced are compared with calculations based on equation 2.58 cited in Chapter 2 in the table below.

Re	Expected no. of vortices pairs	Actual no. of vortices pairs
5×10^3	10	23
8×10^3	14	32

This difference is due to the fact that equation 2.58 is based upon the assumption that the mean momentum velocity, $U_m \approx \frac{1}{2}\Omega_1 R_1$. By applying these results is possible to recalculate equation 2.58 for the start-up problem,

$$\lambda_G \approx \frac{12 \pm 0.1\,\pi d}{Ta^{1/3}} \tag{6.1}$$

This would then refer to, $U_m \approx \frac{1}{3}\Omega_1 R_1$, assuming the same critical wavelength and Görtler number.

The variation of skin friction and the development of the azimuthal velocity profile over time are presented in figure 6.11 and 6.12 respectively. These show that an initial drop in skin friction at the wall, as a laminar boundary layer begins to develop. This is illustrated for $30\triangle t$ as the mean azimuthal velocity profile is linear from the outer wall since no Görtler-type vortices have formed. At $30\triangle t$, Görter-type vortices have just started to form and the skin friction at the inner cylinder rises after the initial minimum in figure 6.11 and the velocity profile begins to tend away from the linear laminar profile towards that of a turbulent profile.

At $50\triangle t$, a peak in the skin friction as been reached and the velocity profile has tended towards the logarithmic profile. At this stage the Görtler-type vortices start to mix and the skin friction on the inner cylinder begins to fall as the velocity profile across the gap grows. This is highlighted in figure 6.12.ii with the large increase in the mean azimuthal velocity profile from the outer cylinder for $\triangle t = 50 \rightarrow 70$. This corresponding to the sharp increase skin friction at the outer cylinder in figure 6.11. The small secondary inflection in the growth of the skin friction, occurs around $\triangle t = 100$ due to the stabilisation of the Taylor vortices. For $\triangle t > 200$, the skin friction tends towards a constant value, along with the mean azimuthal velocity profile, on both the inner and outer cylinder, shown in figure 6.12.

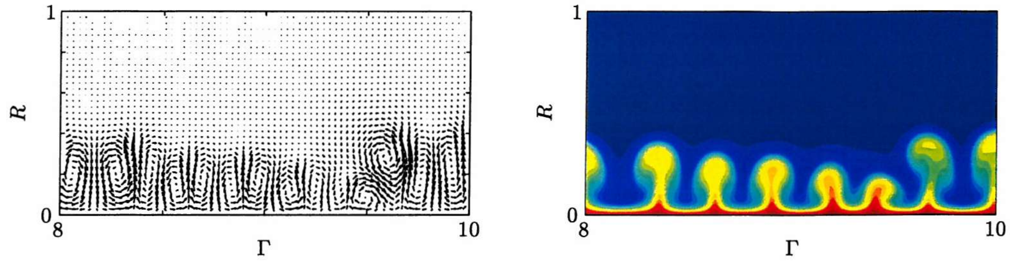

Vector Plot, $u_r \times u_z$ at $26\triangle t$

Azimuthal Velocity, u_θ at $26\triangle t$

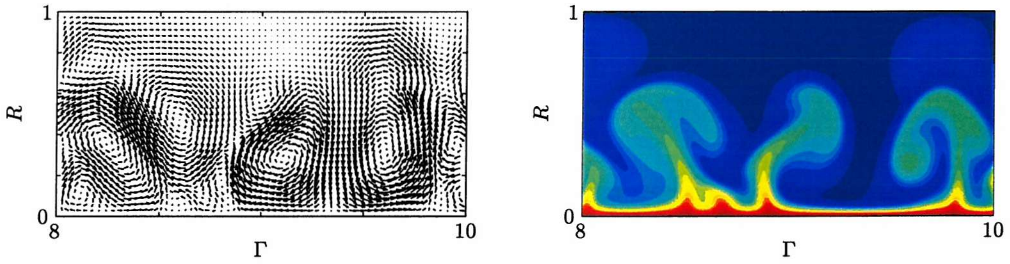

Vector Plot, $u_r \times u_z$ at $36\triangle t$

Azimuthal Velocity, u_θ at $36\triangle t$

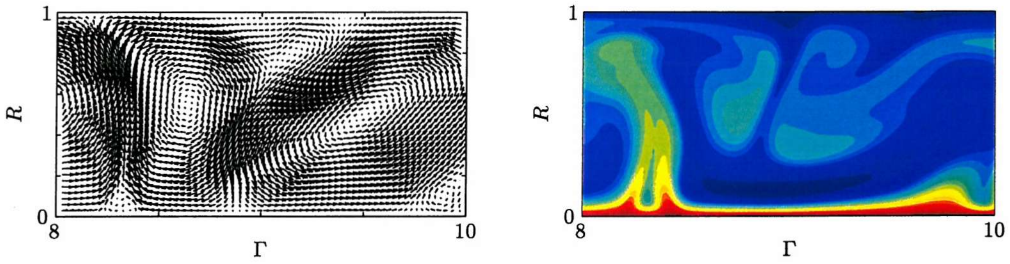

Vector Plot, $u_r \times u_z$ at $46\triangle t$

Azimuthal Velocity, u_θ at $46\triangle t$

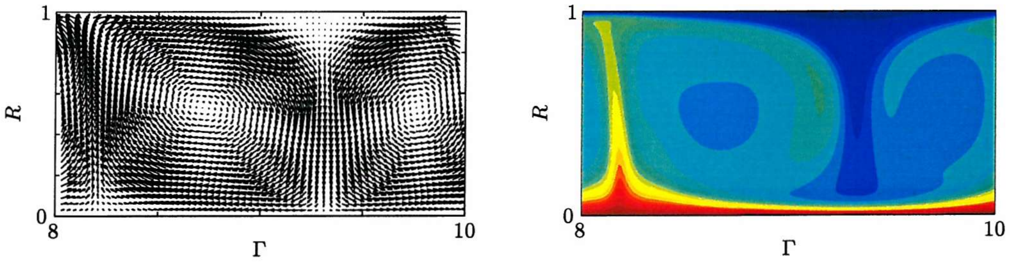

Vector Plot, $u_r \times u_z$ at $96\triangle t$

Azimuthal Velocity, u_θ at $96\triangle t$

Figure 6.10: Series of close-up images, showing the formation of one Taylor vortex from several of Görtler vortices, $Re = 1 \times 10^8$, $\triangle t = 0.0025$ s

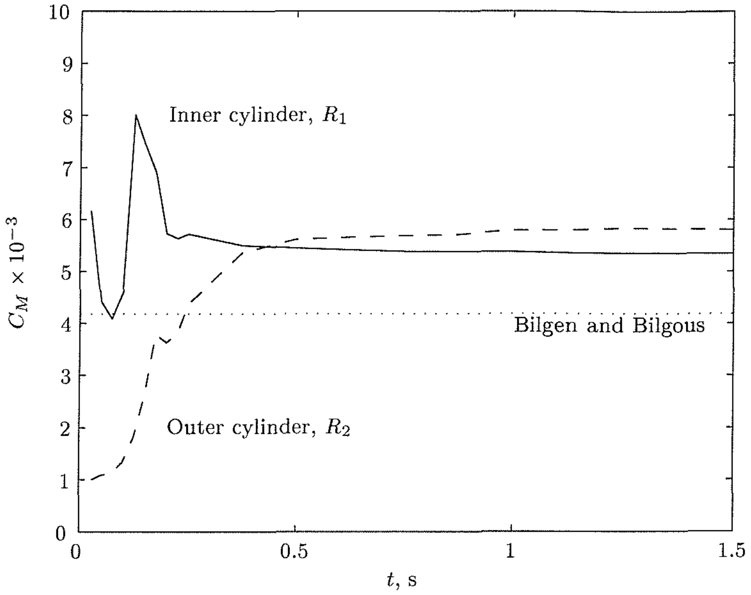

Figure 6.11: Variation of coefficient of friction with time at $Re = 5 \times 10^3$

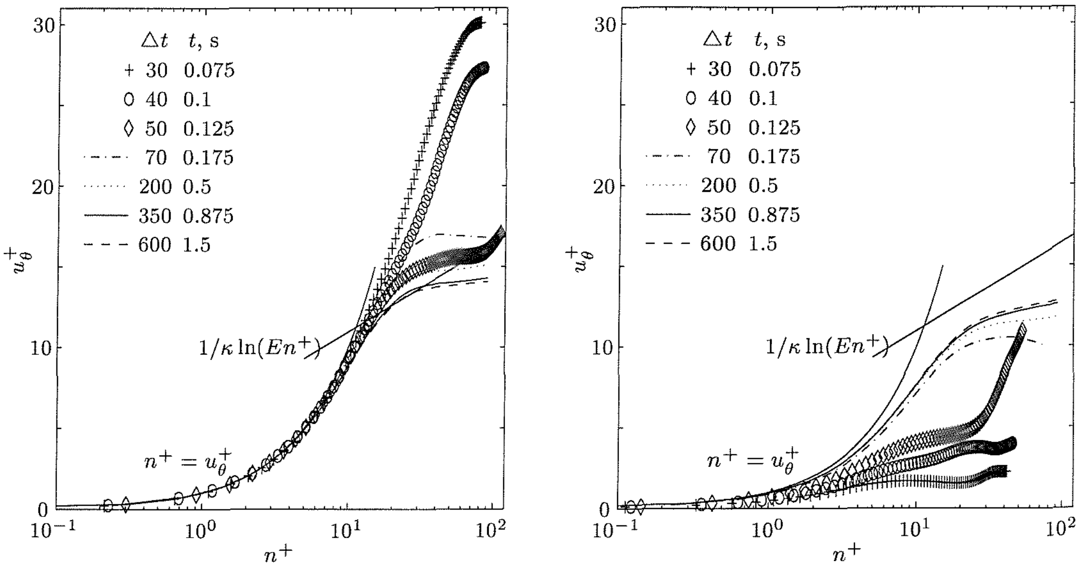

i: Inner cylinder, R_1 **ii:** Outer cylinder, R_2

Figure 6.12: Development of the mean azimuthal velocity profile at $Re = 5 \times 10^3$

§6.4 The "Herring-bone" Conundrum

To determine if any turbulent fluctuations were present and analyse any oscillating vortex boundaries, the azimuthal fluctuation, $\left(\frac{u'_\theta}{\overline{u_\theta}}\right)$ was evaluated for the last 0.4 sec in figure 6.11 for the $Re = 5 \times 10^3$. The results are plotted against time along the length of the domain, at the inner cylinder, $n^+ \simeq 19$, mid-plane, $n^+ \simeq 50$ and the outer cylinder, $n^+ \simeq 19$, in figure 6.13 for fluctuations.

At the end vortex adjacent to the rotating wall, $\Gamma = 0 \rightarrow 2$, larger fluctuations of over 10% are present. The adjacent two Taylor vortices have similar fluctuation patterns but are significantly less. Fluctuations are also present as pulses, visible in the latter steps in figure 6.9. The other main fluctuations are at the mid-plane, figure 6.13.ii, in the region $\Gamma = 8 \rightarrow 11$. This fluctuation is due to oscillation between two vortex boundary layers.

Wei *et al.*'s LIF experiments [44], discussed in §2.4.2, demonstrated the formation of Görtler vortices at the inner cylinder and observed them travelling along the inner cylinder wall towards the vortex outflow. If the Görtler vortex is formed at position "A", figure 6.14 in the 1st , 2nd or 3rd vortex, then as the vortex is dissipated into the main flow it would be transported around the Taylor vortex. Firstly, along the inner cylinder, then across the gap at the vortex outflow, along the outer cylinder, back towards the outer cylinder at the vortex inflow and finally long the inner cylinder towards the origin. The distance a formed Görtler vortex can travel is dependent upon the rate of dissipation of the vortex and the strength of the Taylor vortex. With strong vortex strengths and small gaps then the probability of visualising a Görtler vortex on the surface of the outer cylinder is much higher.

If the Görtler vortex is travelling along the length of the outer cylinder this would then be represented by a diagonal in the plane view, as illustrated by "C-H" in the 1st vortex in figure 6.14. Each Taylor vortex has the opposite sense of rotation, so the direction of the diagonal is a mirror image at vortex inflow and outflows providing identical vortex strengths and sizes. Hence, the formation of the "herring-bone" pattern. Providing the Görtler vortices, are forming periodically then the "herring-bone" pattern formed in figure 6.14 with time would also be reproduced in the azimuthal direction. This distinctive "herring-bone" pattern is what Barcilon *et al.*and Wei *et al.*observed, as is discussed in §2.4.2.

The fluctuations adjacent to the wall, $\Gamma = 0 \rightarrow 2$, in figure 6.13 could be a 2-D representation of these Görtler vortices as they clearly form a "herring bone" pattern and the pulses appear to be tracking around the Taylor vortices. Although further 3-D simulations are required to solve this conundrum and the reason for the oscillating boundary.

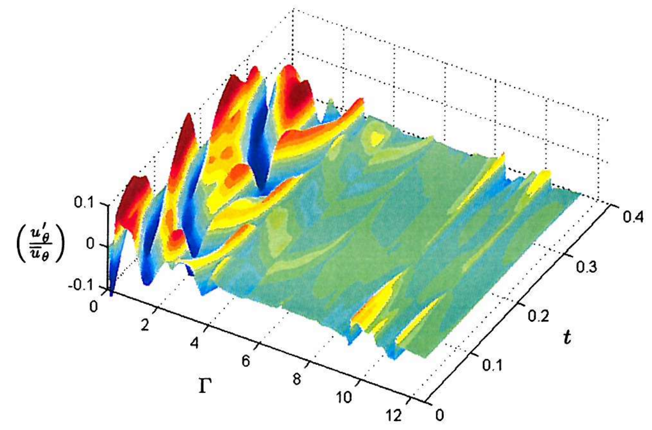

i: Inner cylinder, $n^+ \simeq 19$

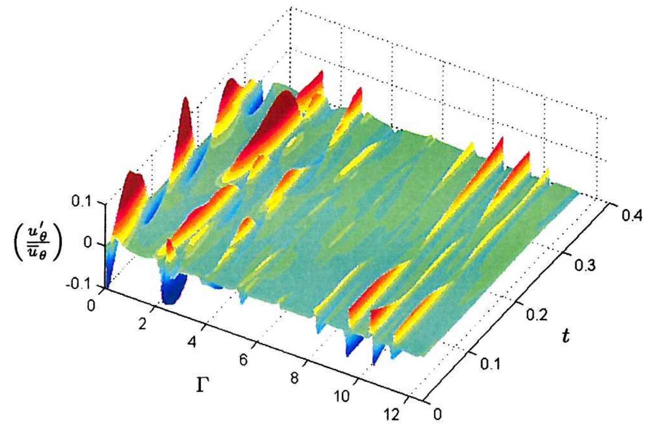

ii: Mid-plane, $n^+ \simeq 90$

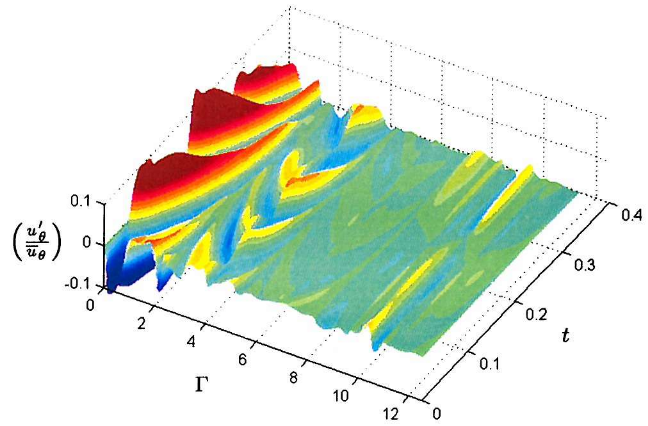

iii: Outer cylinder, $n^+ \simeq 19$

Figure 6.13: Development of the mean azimuthal velocity profile at $Re = 5 \times 10^3$

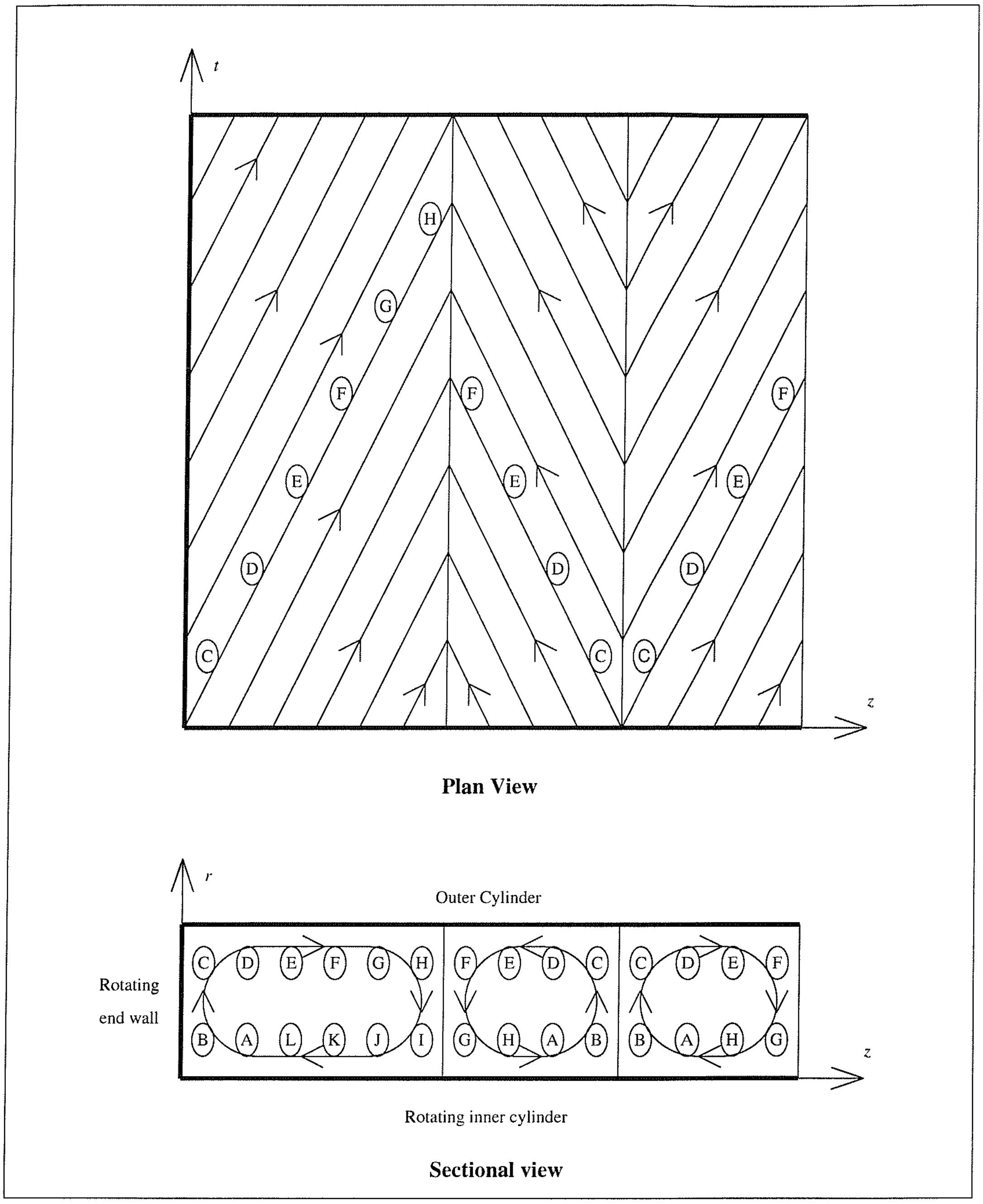

Figure 6.14: Schematic drawing of Görtler vortex paths inside Taylor vortices

§6.5 Further Work

In order to develop the understanding of the effect of: the end gaps, the start-up problem and the 'herring-bone" structure 3-D simulations would be required. For the low-Reynolds number simulations with a 2mm gap it would be appropriate to solve the problem as a DNS solution. To resolve all the turbulent eddies at the operating speeds of the thruster unit would be very computationally costly and hence an LES model is still probably more appropriate.

A review of strategies for turbulence modelling and simulations has been discussed by Spalart [63]. Spalart suggests that for high Reynolds number cacluations RANS/LES hybrids, may be appropriate as a way of reducing the size of grid resolution. Davidson [64] have developed such an hybrid LES/RANS model for predicting recirculating flows. The model couples the two-equation k-ω model in the near-wall region (RANS part) with a one-equation k_{sgs} model [6] (LES part) in the core region.

The accuracy of the simulation is also effected by the discretisation method used. This problem is commonly over come by the use of spectral methods [65] The goal of the work is to reduce the skin friction which may involve complex geometries with steps which are very difficult to model using spectral methods. So the use of finite difference and volume methods with LES and DNS is preferable.

An evaluation of a finite difference fourth order code for DNS calculations has been carried out by Gullbrad [66]. These results show a slight under estimation of the mean velocity profile and velocity fluctuations between the finite difference code and the spectral code. The results however show a negligible difference between 4th and 2nd order codes. The energy spectra however shows a steep drop off at the higher wave numbers with the fourth order scheme dropping off at slightly higher wave numbers than the 2nd order scheme. This is as predicated by Ferziger in [65] where a Taylor series analysis of fourier modes shows the deviation from the spectral method for both the 2nd and 4th order methods. The 4th order method deviated at double the wave number.

These higher wave numbers are associated with the smaller scales of the fluctuations. Thus by using a finite volume or finite difference code the discretization is acting as a filter with the higher order schemes filtering less. As these smaller wave lengths are not being resolved, larger time step sizes should be chosen, as both the spatial and temporal descretization should be balanced.

§6.6 Conclusions

Based on the fuller models the following conclusions can be drawn.

I. ELMORE can be used to study Taylor vortices formed in the thruster. The solution can be unsteady if the end Taylor vortex has the same sense of rotation as the vortex in the end gap. By comparing the pressure distribution with the mean bubble spectrum from the experimental results it is possible to compare the number of vortices present in the solution. For the computation presented 14 vortices were formed and by analysing the bubble spectrum it is evident that 10-12 Taylor vortices formed in the experimental rig.

II. The start-up simulation demonstrates the evolution of ordered Görtler-type vortices to stabilized Taylor vortices through stages of chaotic mixing for $\eta = 0.985$ and $Re = 5 \times 10^3, 8 \times 10^3$. With more Görtler-type vortices forming earlier for the higher *Re*. Upon the formation of Görtler-type vortices there is a large peak in the shear stress on the inner cylinder and then the shear stress decays to around 20% higher than Bilgen & Bilgous equations. This is replicated by dramatic changes in the mean velocity profiles.

III. Fluctuations in the final solution for $Re = 5 \times 10^3$ demonstrate the "herring bone" pattern as observed by Barcilon *et al.* [11]. This pattern is present for some of the vortices formed and presumably is strongly dependent on Taylor vortex sizes and strengths.

From the basis of these fuller modelling issues, further work is required to extend the domain to 3-D to be able to fully resolve the unsteady flow. For the low *Re* test cases DNS simulations should be possible using ELMORE, particularly for shorter domain lengths and higher parallelisation. To improve the accuracy higher order space and time discretisation would be more appropriate. For higher Reynolds numbers of the thruster unit a LES approach would be required. The purpose of this simulation would be to determine the effect of the turbulent eddies on the flow. These fuller 3-D simulations would hopefully solve the "herring bone" conundrum.

CHAPTER

7

Conclusions and Recommendations

§7.1 Summary

This study, of small clearance ratio Taylor-Couette flows, has substantially progressed the understanding of the physics for this type of gap flow. Both laminar and turbulent Taylor vortices have been proved to exist and have been studied for clearance ratios much smaller than that previously reported in the literature. In order to do this, both computational and experimental studies have been performed. This work was motivated by the study of the frictional loses in an underwater integrated-electrical thruster unit.

The experimental work is based upon the development of a new geometry for Taylor-Couette experimental facility, at a very small clearance ratio, and an innovative bubble technique to analyse vortex sizes and positions. The computation studies highlight the value of using the finite volume method with existing numerical schemes and the new methodology of simulating just one Taylor vortex to analyse this small clearance flow. The author has hence been able to improve the knowledge of the flow physics of turbulent Taylor vortices, and demonstrated the effectiveness of the numerical schemes used for the design of thruster units.

This new experimental facility has a clearance ratio much smaller than any found in the literature. The effectiveness of the facility to provide visualisations of Taylor vortices in this small clearance has been clearly demonstrated, as the author was able to develop a novel method of analysing the Taylor vortices as a bubble spectrum. This was possible as the facility affected by refraction to the same extent as in the majority of other work in literature. Normally refraction in this type of experiment allows only the flow near the outer cylinder to be studied. This novel bubble method allows not only the number of vortices to be established but also the oscillations to be tracked with time and the identification of regions of low pressure.

The new methodology of studying just one Taylor vortex was developed during the initial laminar simulations. This set of simulations show that ELMORE could be used to model Taylor vortices; the results in particular have highlighted the effects of end boundaries. This new methodology is based upon solving one vortex between a pair of periodic boundaries in the azimuthal direction and a pair of mirror boundaries in the axial direction. The method of using just one vortex to solve the flow has enabled the value of the k-ω turbulence model to be demonstrated for this problem, and allowed grid independent results to be easily computed due to the size of the domain. The grid independent results can then be extrapolated onto much larger domains, such as the thruster unit.

The literature reviewed, raised several poorly understood problems which have been highlighted. These problems have been addressed mainly by the numerical simulations. Based on this background review the following four points have been raised and discussed in this thesis. The principle enhancements are:

I. the effect of Reynolds number and the flow physics of a transition at $Re \simeq 1 \times 10^4$:
    - Taylor vortices have been shown to form for $Ta/Ta_c < 1000$, earlier than reported by Koschmieder [15] for the small clearance ratio of the thruster;
    - the flow transition from "soft" to "hard" turbulence has been explained;
    - pre-transition the turbulent production between the vortices dominates and post-transition the turbulent production at the wall dominates;

II. the effect of turbulent Taylor vortices on skin friction:
    - the vortices cause an increase in the skin friction;
    - the vortices cause a departure from the von Kármán logarithmic law of the wall;
    - if the vortex length is that of the critical laminar length then the skin friction is the highest;

III. the effects of end conditions on flow properties:
    - rotating boundaries cause an enlargement of the adjacent vortex due to the additional energy of the rotating face;
    - stationary boundaries reduce the size of the adjacent vortex;
    - open end boundaries, such as that in the thruster unit can cause oscillations in the number of Taylor vortices formed;

IV. how do turbulent vortices form and do Görtler vortices exist within turbulent Taylor vortices:
    - turbulent Taylor vortices form from Görtler-type vortices due the unstable growth of boundary layer, these vortices then mix and form stable Taylor vortices;
    - no Görtler vortices were formed during the numerical simulations of steady state Taylor cells due to the 2D nature of the solution, but small instabilities were present in the solution;

- a possible mechanism has been suggested for the convection of Görtler vortices, describing the herring bone pattern found Barcilon *et al.* [11] and Wei *et al.* [44].

From this broadening of the knowledge base and the innovative techniques developed in this thesis, future work would lead to improved thruster units, as the influences of Reynolds number, vortex length and end boundaries upon skin friction have been revealed for this small clearance ratio flow. In particular, by setting the length of the gap in the thruster and hence the number of vortices formed, the skin friction can be reduced by ensuring that the length of the vortices is not that of the critical laminar length. The computational method developed also highlights the effectiveness of CFD as a design tool for this case. This work also forms an improved foundation for further studies in other similar engineering applications such as motors, pumps and journal bearings.

Further details of the conclusions found are presented in the next sections. Firstly, the expected flow in the thruster is presented. The next section details a summary of the development of experimental facility and its key conclusions. Similarly the numerical work is summarised in the next section. This work then draws recommendations for further studies into Taylor-Couette flow.

§7.2 Expected flow

From the background work reported in the thesis, the expected flow found in the annular gap in the electrical thruster to consists of 14 pairs of Taylor vortices for laminar flow. For the turbulent flow of the operating conditions of the thruster the number of vortices will be between 6 and 12. Previously published empirical equations presented showed large discrepancies. Bilgen & Bilgous's [23] empirical equations show an optimum gap width for constant radial Reynolds number. From this a 2mm gap was chosen for the design of the thruster unit. Although this was not the minimum reported in Bilgen & Bilgous's equations it was felt appropriate due to the to the lack of knowledge about the flow transition.

§7.3 Experimental Work

To analyse the flow an experimental rig was designed and constructed with a dynamically similar clearance ratio to that of the thruster with a gap of 10mm to allow visualisation. This meant that the inner radius was 710mm. Some of the goals of the experiments have not be achieved, as accurate torque measurements have not been made. The presence of Taylor vortices was clearly demonstrated, using air bubbles to visualise the flow.

I. The friction resistance has been measured, demonstrating the empirical equations are of the same order of magnitude, from analysis of the power lost in the motor used to dive the rig and dynamometry attached to the outer cylinder.

II. Turbulent Taylor vortices have been visualised by feeding air bubbles through the experimental rig. A novel method of analysing the bubbles as a probability spectrum has been developed. From these bubble spectrum, vortex size, positions of outflow boundaries and regions of low pressure have been identified.

§7.4 Computational Work

The laminar flow has been successfully modelled with ELMORE, an in-house code. Studies were carried out on the effect of Reynolds number and end boundary conditions on flow properties. The vortex next to both rotating and stationary end boundaries produces a significantly larger skin friction. Other vortices formed had properties similar to those formed between mirror boundaries. If the vortex size is that of the critical length then the skin friction was the highest. It was also shown that it was possible to model just one vortex between two mirror boundaries. From the laminar results the following conclusions can be drawn.

I. ELMORE can successfully be used to model laminar Taylor vortices and grid independent results have been produced using the SIMPLEC pressure correction with 2^{nd} order discretization and the CLAM solver. Laminar Taylor vortices have been modelled with both fixed, rotating and mirror end boundaries. Just one Taylor vortex can be accurately modelled by using mirror boundaries.

II. The inner cylinder dominates the effects of the Taylor vortices and the outflow from the Taylor vortex is much stronger than the in flow and hence the vortex centre is offset towards the outflow boundary.

III. The effect of vortex length on skin friction has been illustrated. For the vortex next to a stationary or rotating boundary the shear stress are much higher and the longer the vortex is the less the skin friction due to the singularity between the stationary and rotating boundaries.

IV. The skin friction for the middle vortices were similar to that of the mirror boundary and over half less than that of the vortices adjacent to the end walls. For these middle and mirror boundaries there is a peak in the skin friction at the critical vortex length. The results show that increasing the vortex length increases the vortex strength.

Turbulent Taylor vortices has been studied using the low Reynolds number k-ω formulation. Simulations using CFX, a commercial CFD code and ELMORE have both demonstrated that there is a flow transition between "soft" and "hard" turbulance. The effect of Taylor vortex length and further Reynolds number tests have been carried out using ELMORE illustrating the effects of vortex properties on skin friction. The domain has been extended to that of the full geometry 2D geometry using ELMORE as a parallel solver to demonstrate the open end effects and to allow comparison of the pressure with the bubble distributions from the experimental results. The transient start-up problem has been solved using a P-DNS approach also in parallel. From this work on turbulent simulations the following conclusions can be drawn.

I. One turbulent Taylor vortex can be modelled using the low Reynolds number k-ω between two mirror boundaries using the SIMPLEC pressure correction in both CFX and ELMORE. Taylor vortices have been solved for a wide range of radius ratios and Reynolds numbers. Discrepancies between CFX and ELMORE in predicting the skin friction have demonstrated the sensitivity of both the coding approach and node placement.

II. For the three radius ratios tested and from analysis of the turbulence production the flow transition from "soft" to "hard" turbulence has been explained. Pre-transition, the turbulence production is dominated by the outflowing boundary of the Taylor vortex. As the Reynolds number increases, shear drive turbulence, (due to the rotating cylinder) becomes the dominating factor. Therefore, at relatively low Reynolds numbers turbulent production is dominated by the flow between two adjacent Taylor Vortices. A transition occurs as the Reynolds number is increased to a condition where the shear stress of the rotating cylinder becomes the dominant source of turbulent kinetic energy production.

III. It has also been shown that developed turbulent flow can occur for $Ta/Ta_c < 1000$ for small gaps and that the transition occurs earlier for these flows.

IV. Taylor vortices have shown to flatten the azimuthal velocity profile causing an increase in the skin friction of 25% and a maximum torque when the vortex length is that of the critical laminar length, for the 2 mm case at $Re = 8 \times 10^3$. This is due to improved energy transfer at the wall due to the Taylor vortex.

V. ELMORE can be used to study Taylor vortices formed in the thruster. The solution can be unsteady if the end Taylor vortex has the same sense of rotation as the vortex in the end gap. For the computation presented 14 vortices were formed.

VI. By comparing the pressure distribution with the mean bubble spectrum from the experimental results it is possible to compare the number of vortices present in the solution. By analysing the bubble spectrum it is evident that 10-12 Taylor vortices formed in the experimental rig.

VII. The start-up simulations demonstrates the evolution of ordered Görtler-type vortices to stabilized Taylor vortices in four steps: formation of ordered Görtler-type vortices at the inner cylinder; mixing of Görtler-type vortices as the turbulence starts to develop; a mixing phase Taylor and Görtler-type vortices; stabilisation of the Taylor vortices with no other apparent vortex formation. Upon the initial formation of Görtler-type vortices there is a large peak in the shear stress on the inner cylinder and then the shear stress decays to around 20% above Bilgen & Bilgous's results, similar to the turbulent results for one vortex.

VIII. Fluctuations in the final solution for $Re = 5 \times 10^3$ are suggestive of the "herring bone" pattern as observed by Barcilon *et al.* [11]. This pattern is present for some of the vortices formed and presumably is strongly dependent on Taylor vortex sizes and strengths.

§7.5 Recommendations for Future Work

Based upon the work carried out during this thesis the following recommendations for future work in small clearance ratio Taylor-Couette flow can be made.

I. With improvements in the experimental facility, particularly using stiffer cylinders, working dynamometry and feed back to the motor controller from a tachometer. Then the effect of Taylor vortices on the skin friction and other vortex properties could be studded in further detail. The vortex properties could be studied further with using the bubble spectra technique developed and either LDV or PIV measurements. To improve visulisation across the gap the refraction could be readjusted with either refractive index matched fluids or a lens to readjust the refraction. These measurements would also provide needed test cases at high radius ratios for validation.

II. 3-D DNS/LES simulations for a small domain would hopefully solve the conundrum of the existence of Görtler vortices within turbulent Taylor vortices and provide valuable data in order to tweak RANS and or RANS/LES models. This more accurate turbulence model could be used for further empirical studies, predictions of larger problems such as the whole thruster and applied to other rotating machinery, such as journal bearings.

APPENDIX

A

Cylindrical Polar Coordinates

In cylindrical coordinates (r,θ,z)

$$\begin{aligned} x_1 &= x = r\cos\theta, \\ x_2 &= y = r\sin\theta, \\ x_3 &= z = z. \end{aligned} \tag{A.1}$$

as shown in figure A.1. By defining **e**, as a unit vector then $\delta\mathbf{x}$ can be represented as

$$\delta\boldsymbol{x} = \delta r\boldsymbol{e}_r + r\delta\theta\boldsymbol{e}_\theta + \delta z\boldsymbol{e}_z \tag{A.2}$$

and where,

$$\begin{aligned} \boldsymbol{e}_r &= \cos\theta\boldsymbol{e}_1 + \sin\theta\boldsymbol{e}_2, \\ \boldsymbol{e}_\theta &= -\sin\theta\boldsymbol{e}_1 + \cos\theta\boldsymbol{e}_2, \\ \boldsymbol{e}_z &= \boldsymbol{e}_3. \end{aligned} \tag{A.3}$$

The unit vectors do not change with r or z but change with θ,

$$\begin{aligned} \frac{\partial\boldsymbol{e}_r}{\partial\theta} &= \boldsymbol{e}_\theta, \\ \frac{\partial\boldsymbol{e}_\theta}{\partial\theta} &= -\boldsymbol{e}_r, \\ \frac{\partial\boldsymbol{e}_z}{\partial\theta} &= 0. \end{aligned} \tag{A.4}$$

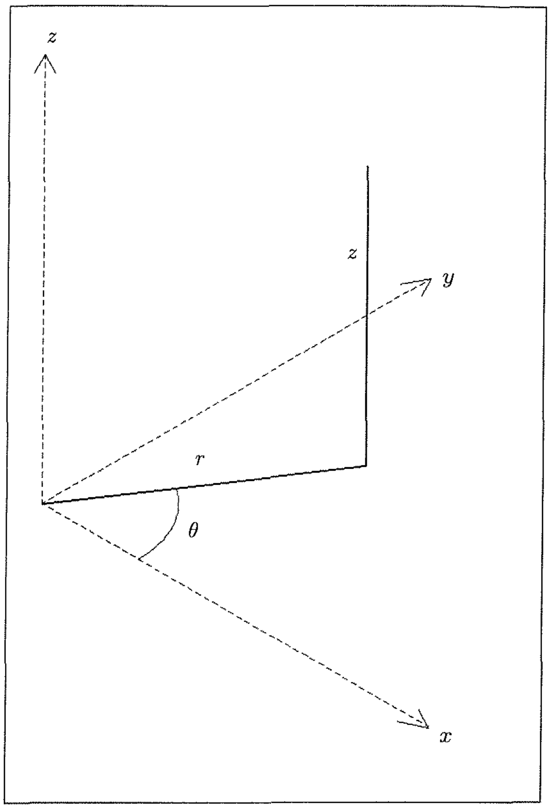

Figure A.1: Polar Coordinates

By defining **F** as a unit force it is hence possible to define the following equations

$$\nabla\phi = \frac{\partial\phi}{\partial r}\boldsymbol{e}_r + \frac{1}{r}\frac{\partial\phi}{\partial\theta}\boldsymbol{e}_\theta + \frac{\partial\phi}{\partial z}\boldsymbol{e}_z, \tag{A.5}$$

$$\nabla\boldsymbol{F} = \frac{1}{r}\frac{\partial r\boldsymbol{F}_r}{\partial r} + \frac{1}{r}\frac{\partial\boldsymbol{F}_\theta}{\partial\theta} + \frac{\partial\boldsymbol{F}_z}{\partial z}, \tag{A.6}$$

$$\nabla\cdot\boldsymbol{F} = \frac{1}{r}\begin{vmatrix} \boldsymbol{e}_r & r\boldsymbol{e}_\theta & \boldsymbol{e}_z \\ \frac{\partial}{\partial r} & \frac{\partial}{\partial\theta} & \frac{\partial}{\partial z} \\ \boldsymbol{F}_r & r\boldsymbol{F}_\theta & \boldsymbol{F}_z \end{vmatrix}, \tag{A.7}$$

$$\nabla^2 = \frac{1}{r}\frac{\partial}{\partial r}\left(r\frac{\partial}{\partial r}\right) + \frac{1}{r^2}\frac{\partial^2}{\partial\theta^2} + \frac{\partial^2}{\partial z^2}, \tag{A.8}$$

and

$$\boldsymbol{u}\cdot\nabla = u_r\frac{\partial}{\partial r} + \frac{u_\theta}{r}\frac{\partial}{\partial\theta} + u_z\frac{\partial}{\partial z}. \tag{A.9}$$

APPENDIX

B

Additional background information

Additional information to complement what is in the background chapter 2 is given here. It is presented as notes on the flow in eccentric cylinders and a brief discussion on Dorfman's prediction of the torque in enclosed disks. The section on eccentric cylinders can be used to give estimated of when separation occurs in the thruster and is a starting point for further work. The section on enclosed disks is given for use as predictions of the end losses in the experimental rig.

§B.1 Eccentric Cylinders

The Taylor vortex system between two eccentric cylinders brings a significant increase in the mathematical difficulty to the problem, as the system is no longer axisymmetric. The flow between eccentric cylinders is defined by the clearance ratio, σ based on the mean gap, d_m and an eccentricity ratio, ξ defined by distance between the axis, e of the cylinders divided by the mean gap.

$$\sigma = \frac{d_m}{R_1} \tag{B.1}$$

$$\xi = \frac{e}{d_m} \tag{B.2}$$

Taylor vortices still appear at eccentricities up to 0.5 and the critical Taylor number increases as a function of the eccentricity [15]. Provided the flow has not separated the critical wavelength is almost independent of ξ. When the flow is separated the wavelength of the vortices increases. This separation occurs if,

$$\xi \geq 0.30278 + 0.03818\sigma. \tag{B.3}$$

If separation has not occurred then there is not any significant increase in the frictional torque. Separation also has only a marginal effect on the formation and stability of the Taylor vortices between the cylinders and has been shown to only give a weak mark on the Taylor vortices. [48]

Eagles et al. [67] assumed slightly supercritical conditions, a small clearance ration, a small eccentricity and fixed Taylor vortex size their calculations. they demonstrated that the critical Taylor number of the flow between eccentric cylinders is,

$$Ta_{ec} = 1694.97(1 + 1.618\sigma)(1 + 2.6185\xi^2) + 0(\sigma^2, \sigma\xi^2, \xi^4), \tag{B.4}$$

using

$$Ta_e = \left(\frac{U_1 R_1}{v}\right)^2 \sigma^3 \tag{B.5}$$

Further theoretical investigation of Taylor vortex flow between eccentric cylinders is examined by Chossat and Iooss [16].

§B.2 Dorfman's Enclosed Disks Estimates

Dorfman's analysis [27] presumes that the gap s between the disk and the casing is small such that the separate boundary layers on the two walls coalesce. The author's assumptions in the analysis shown in the text to be generally within 10% of the experimental data for $s/R = 0.02$ except with a deviation of flow transition. Dorfman demonstrates two transients, firstly from low Reynolds number laminar flow to high Reynolds number laminar flow at $Re_r \approx 10^4$. Then a laminar to turbulent transition at $Re_r \approx 10^5$.

For low Reynolds number laminar flow ($Re_r < 10^4$),

$$C_{DM} = 2\pi \frac{R}{s} \frac{1}{Re_r}, \tag{B.6}$$

where,

$$C_{DM} = \frac{4M}{\rho \Omega^2 R^5}. \tag{B.7}$$

For high Reynolds number flow ($10^4 < Re_r < 10^5$) the results are presented in the form of a table to demonstrate the effect of small changes in the gap between the casing and the rotating disk.

R_2/R_1	$C_{DM}/2\,Re_r^{0.2}$
1.00000	1.3234
1.00019	1.3237
1.00338	1.3299
1.00655	1.3351
1.00970	1.3418
1.01282	1.3477
1.01591	1.3534
1.01899	1.3591
1.02204	1.3646
1.02506	1.3701
1.02807	1.3755
1.03106	1.3808
1.03403	1.3860
1.03697	1.3912
1.03989	1.3962
1.04279	1.4012
1.04568	1.4061
1.04855	1.4109
1.05140	1.4157

Table B.1: Moment coefficients for a enclosed rotating disks for laminar conditions

For turbulent Reynolds number flow ($10^5 < Re_r$) the results are presented in the form of a table, as previously, to demonstrate the effect of small changes in the gap between the casing and the rotating disk.

R_2/R_1	$C_{DM}/2\, Re_r^{0.2}$
1.00000	0.03569
1.00030	0.03571
1.00357	0.03593
1.00681	0.03616
1.01004	0.03638
1.01324	0.03660
1.01643	0.03681
1.01960	0.03703
1.02275	0.03724
1.02588	0.03745
1.02900	0.03766
1.03210	0.03787
1.03518	0.03807
1.03824	0.03827
1.04129	0.03848
1.04432	0.03867
1.04733	0.03887
1.05033	0.03907

Table B.2: Moment coefficients for a enclosed rotating disks for turbulent conditions

APPENDIX

C

Additional Information on the Experimental Rig

Additional information to compliment what is discussed in chapter 3 on the experiments is given here. It is presented in the following order as: notes on the design of the dynamometry; refraction through a curved sheet and series of 40 graphs representing the bubble spectrum as a for $Re = 29400$ at intervals of 0.5 ms.

§C.1 The Dynamometry Design

§C.1.1 Mechanical properties

Taking the maximum design torque, M and assuming four flextures with mean flexture radius, R_m, as shown if figure C.1.a, then the force per flexture,

$$F_f = \frac{M}{4R_m} \,. \tag{C.1}$$

$$I/y = \frac{wt^2}{6} \tag{C.2}$$

where w is the width and t is the thickness of the flexture.

$$I = \frac{wt^3}{12} \,. \tag{C.3}$$

In contraflexture the root strain is,

$$\epsilon_{root} = \frac{F_f l_f}{2E(I/y)} \,. \tag{C.4}$$

Where l_f is the length of the flexture and E is elastic modulus of the material. The strain at the middle of the gauges is determined by,

$$\begin{aligned} \epsilon_g =& \frac{l_f/2 - l_{pos} - l_G/2}{l_f/2}\,\epsilon_{root} \\ =& \frac{l_f - 2l_{pos} - l_G}{l_f}\,\epsilon_{root}\,, \end{aligned} \tag{C.5}$$

where l_{pos} is distance from the gauge form the end of the flexture and l_G is the gauge length. The deflection in the flextures is defined as,

$$\delta = \frac{F_f l_f}{3EI} \,. \tag{C.6}$$

The shear stress due to rotation,

$$\tau_{rot} = \frac{F_f}{w_f t_f} \,. \tag{C.7}$$

§C.1.2 Bridge Circuit Properties

Assuming all strain gauges are of same resistance, R_G and that there are two gauges per arm in the bridge circuit as shown in figure C.1.b. Then the equivalent resistance, R_{equiv} is

$$\frac{1}{R_{equiv}} = \frac{1}{4R_g} + \frac{1}{4R_g}\,,$$

therefore,

$$R_{equiv} = 2R_g \,. \tag{C.8}$$

Defining V_S as the supply voltage then the current at the gauge, I_G is

$$I_g = \frac{1}{2}\frac{V_S}{R_{equiv}} = \frac{V_S}{4R_g} \,. \tag{C.9}$$

The power per gauge, W_g is designated by,

$$W_g = I_g^2 R_g = \frac{V_S^2}{16R_g} \,. \tag{C.10}$$

The gauge area is $A_g = w_g t_g$ hence the power dissipation per gauge is $W_g \;/\; A_g$. The output voltage, V_O is defined by,

$$V_O = V_S k \epsilon_g \tag{C.11}$$

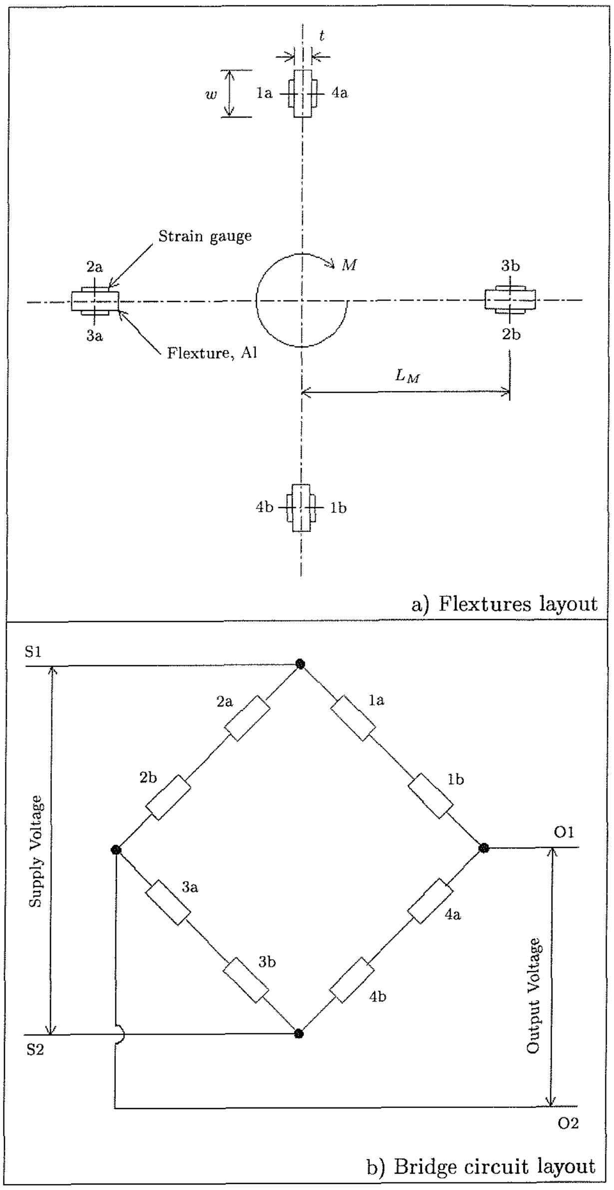

Figure C.1: Arrangement of the flextures and strain gauges

§C.2 Refraction through a Curved Sheet

Defining the refractive index, Υ, as the ratio of the speed of light in a vacuum to the speed in the medium. For example at room temperature water is generally taken as $\Upsilon_{water} = 1.330$ and for standard clear polycarbinate is $\Upsilon_{poly} = 1.586$. Snell's law states that $\Upsilon \sin\theta_n$ is a constant. Where θ_n is the angle normal to the surface. By applying Snell's law to the interfaces in figure C.2

$$\Upsilon_{water}\ \sin\theta_1 = \Upsilon_{poly}\ \sin\theta_2\ , \tag{C.12}$$

$$\Upsilon_{poly}\ \sin\theta_4 = \Upsilon_{water}\ \sin\theta_3\ . \tag{C.13}$$

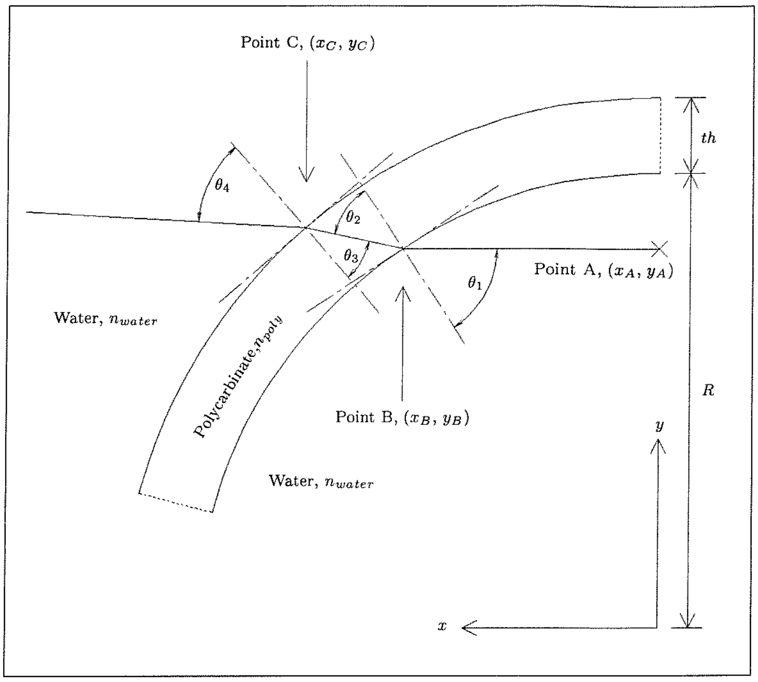

Figure C.2: Refraction through a curved sheet

By taking point A as being a height, h above the origin then

$$x_A = 0\,, \qquad y_A = h\,. \tag{C.14}$$

Point B, the position where the light ray hits the polycarbinate, can then be defined as,

$$x_B = \sqrt{R^2 - h^2}\,, \qquad y_B = h\,. \tag{C.15}$$

where R is the radius of the sheet. The sine of the incidence angle at Point A is defined by $\sin\theta_1 = \frac{h}{R}$. By applying similar triangles $\sin\theta_3 = \frac{R}{R+th}\sin\theta_2$, where th is the thickness of the sheet. To find point C, a length, L, the distance between Points B and C, must first be defined as,

$$L = \left(R^2 + (R+th)^2 - 2R(R+th)\cos(\theta_2 - \theta_3)\right)^{\frac{1}{2}}\,. \tag{C.16}$$

Using equation D.5 point C can be then defined as,

$$x_C = x_B + L\cos(\theta_1 - \theta_2)\,, \qquad y_C = y_B + L\sin(\theta_1 - \theta_2)\,. \tag{C.17}$$

§C.3 Bubble Spectra

From the data produced by the digital video camera, 40 images were decoded at intervals of 0.5 ms as standard "bitmaps" images. The bubble spectrum was then calculated, as outline in the main text, along the length of the inner cylinder. These bubble spectra are presented in figures C3-C5.

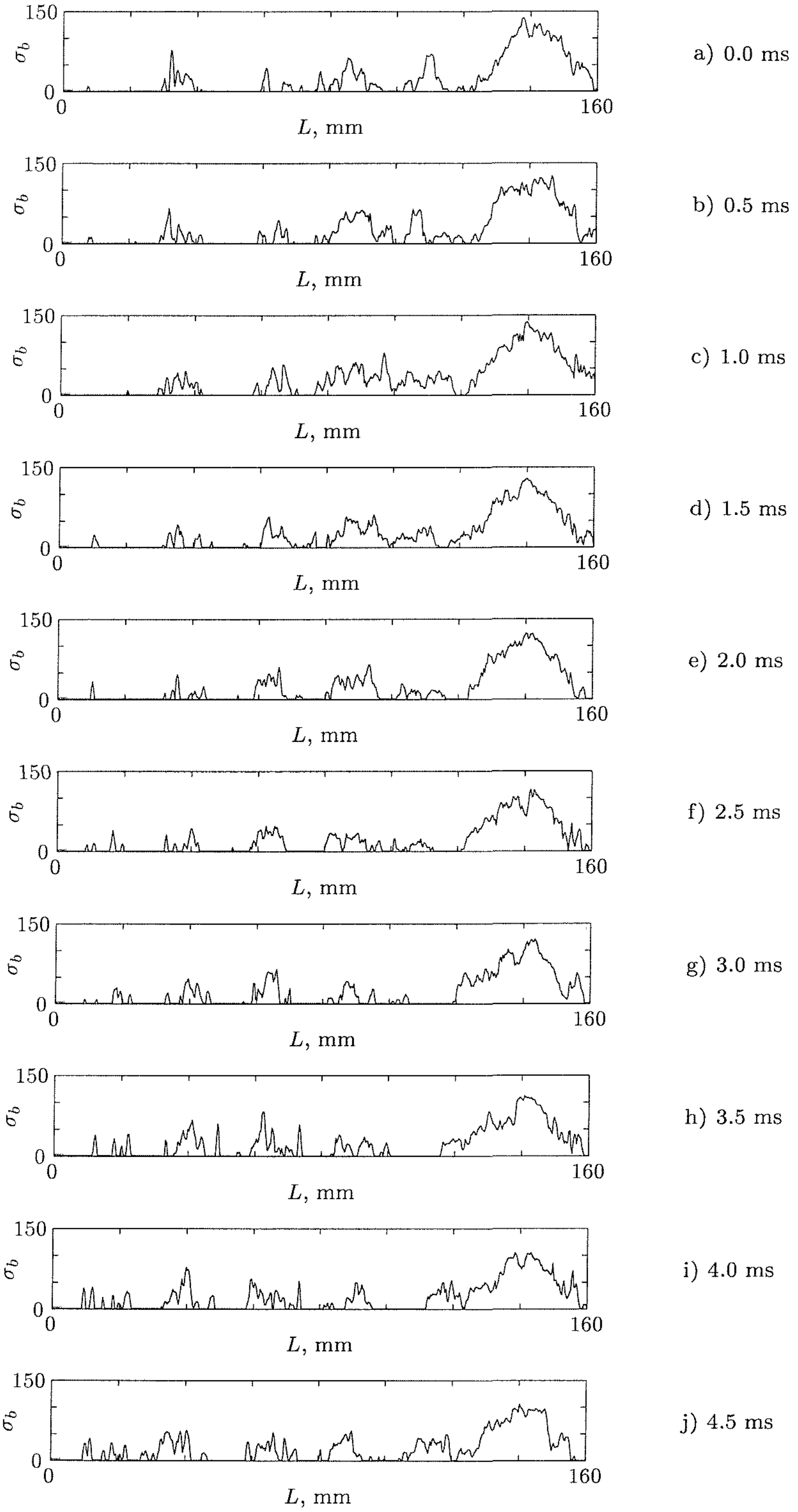

Figure C.3: Instantaneous bubble spectrum for $Re = 29400$ at $0.0, 0.5, \ldots 4.5$ ms represented in graphs a,b, ... j) respectively

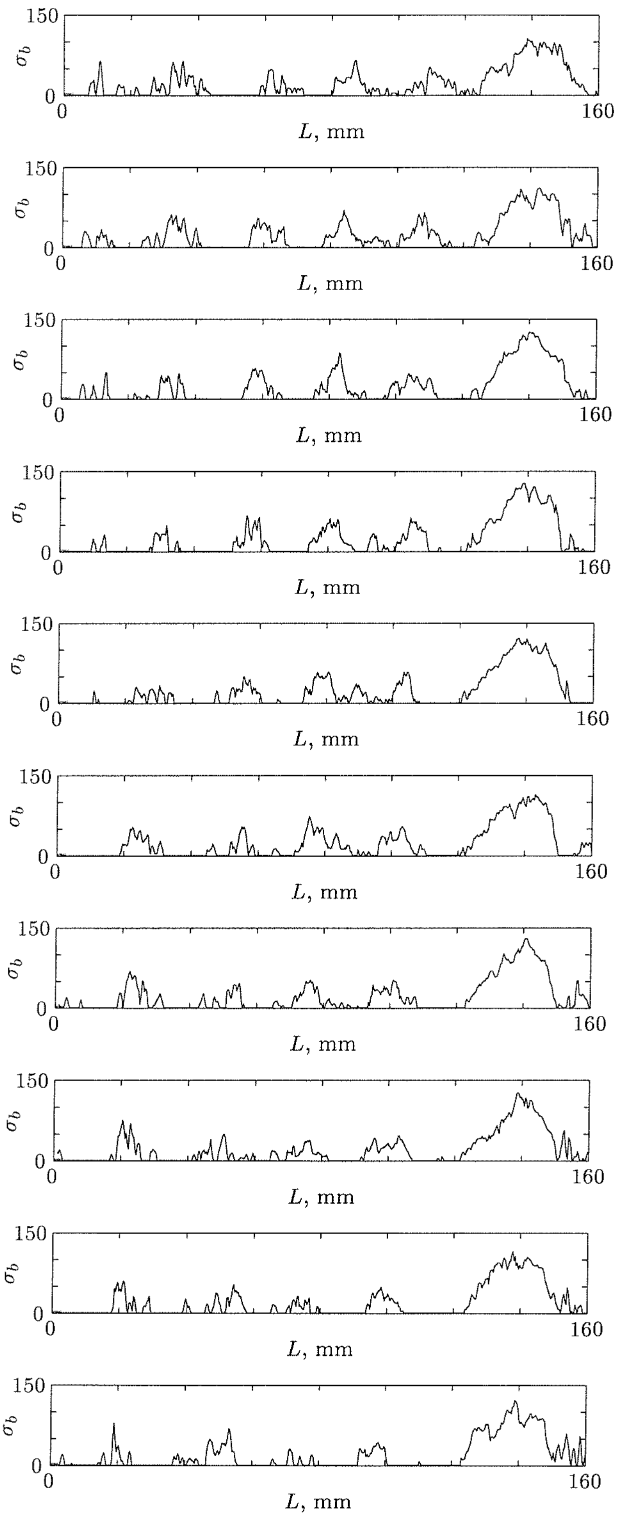

a) 5.0 ms

b) 5.5 ms

c) 6.0 ms

d) 6.5 ms

e) 7.0 ms

f) 7.5 ms

g) 8.0 ms

h) 8.5 ms

i) 9.0 ms

j) 9.5 ms

Figure C.4: Instantaneous bubble spectrum for $Re = 29400$ at $5.0, 4.5, \ldots 9.5$ ms represented in graphs a,b, ... j) respectively

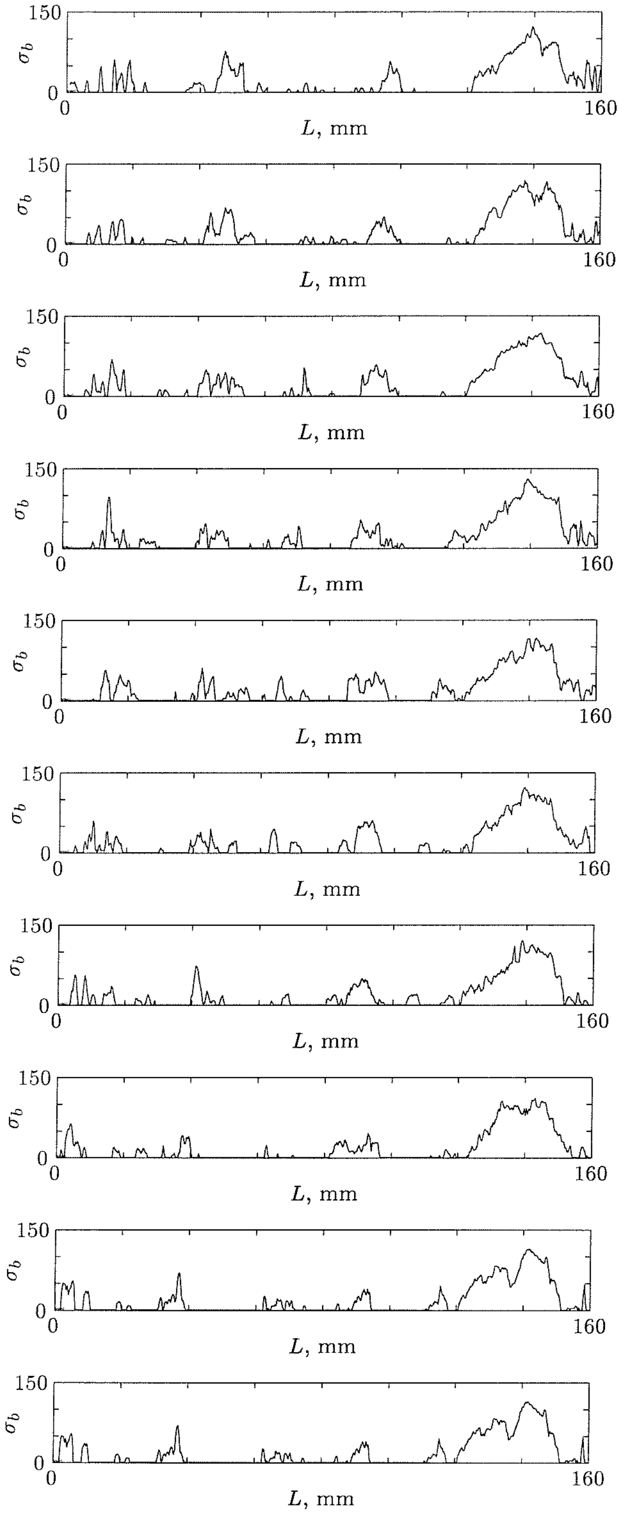

a) 10.0 ms

b) 10.5 ms

c) 11.0 ms

d) 11.5 ms

e) 12.0 ms

f) 12.5 ms

g) 13.0 ms

h) 13.5 ms

i) 14.0 ms

j) 14.5 ms

Figure C.5: Instantaneous bubble spectrum for $Re = 29400$ at $10.0, 10.5, \ldots 14.5$ ms represented in graphs a,b, ...j) respectively

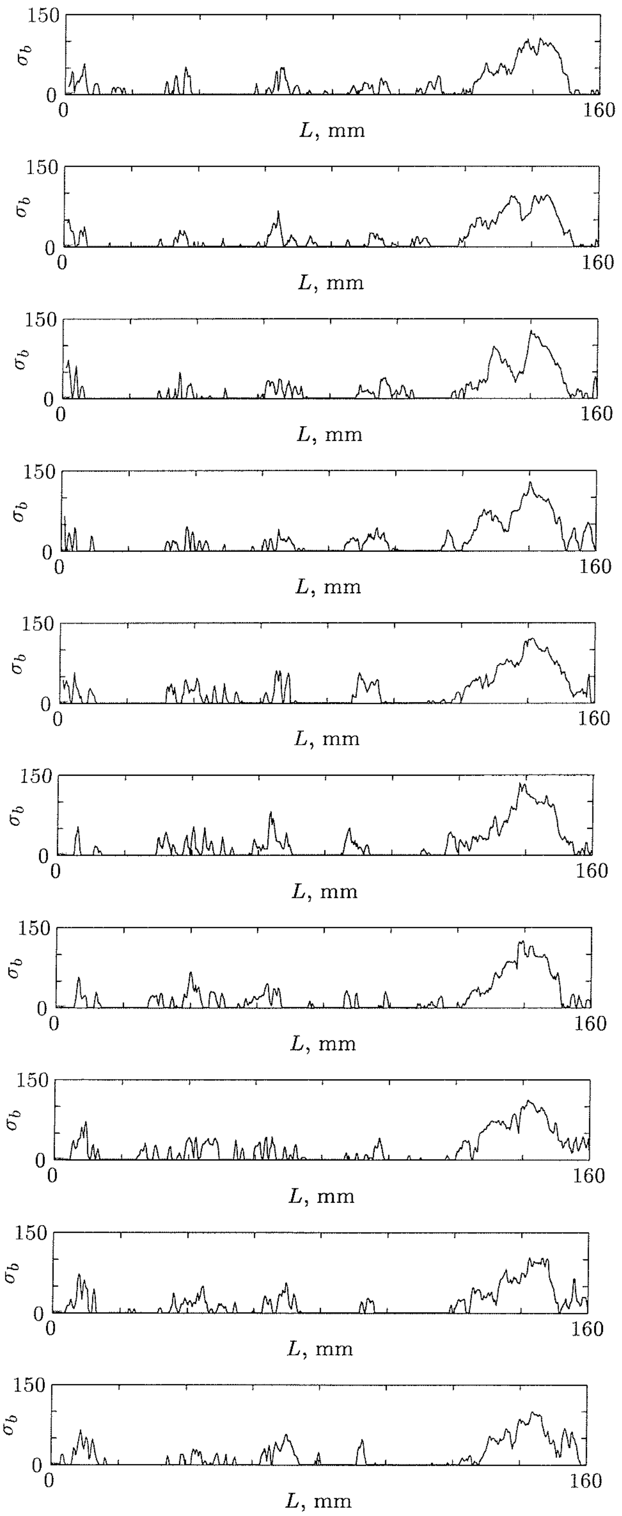

a) 15.0 ms

b) 15.5 ms

c) 16.0 ms

d) 16.5 ms

e) 17.0 ms

f) 17.5 ms

g) 18.0 ms

h) 18.5 ms

i) 19.0 ms

j) 19.5 ms

Figure C.6: Instantaneous bubble spectrum for $Re = 29400$ at $15.0, 15.5, \ldots 19.5$ ms represented in graphs a,b, …j) respectively

APPENDIX

D

Journal Paper: Vortex to wall driven turbulence production

Journal of Numerical Methods in Fluids 2002 Volume 128, Pages 207-226

Transition from Vortex to Wall Driven Turbulence Production in the Taylor-Couette System with a Rotating Inner Cylinder

W.M.J. Batten, N.W. Bressloff and S.R. Turnock

Abstract

Axisymmetically stable turbulent Taylor vortices between two concentric cylinders are studied with respect to the transition from vortex to wall driven turbulent production. The outer cylinder is stationary and the inner cylinder rotates. A low Reynolds number turbulence model using the k-ω formulation, facilitates an analysis of the velocity gradients in the Taylor-Couette flow. For a fixed inner radius, three radius ratios 0.734, 0.941, 0.985 are employed to identify the Reynolds number range at which this transition occurs. At relatively low Reynolds numbers, turbulent production is shown to be dominated by the outflowing boundary of the Taylor vortex. As the Reynolds number increases, shear driven turbulence, (due to the rotating cylinder) becomes the dominating factor. For relatively small gaps turbulent flow is shown to occur at Taylor Numbers lower than previously reported.

Keywords: Taylor-Couette flow, CFD, Low Reynolds number turbulence, k-ω

§D.1 Introduction

The flow between a rotating inner cylinder and a fixed outer cylinder is of interest in several engineering applications, such as motors, filters, pumps and journal bearings. The motivation for this work stemmed from the development of a novel underwater-integrated electrical thruster unit [2], [3] and [1]. A significant source of power loss in the electrical thruster arises from the frictional resistance that occurs between two such cylinders.

This flow has been studied since G.I. Taylor [4] reported the formation of an array of alternating laminar toroidal vortices at a particular speed dependent upon the geometry of the problem. The Taylor number is defined as

$$Ta = Re^2 \frac{d}{R_1}. \tag{D.1}$$

Where Re is the Reynolds number based on gap width,

$$Re = \frac{Ud}{\nu}, \tag{D.2}$$

d is the gap width, R_1 is the inner radius, U is the speed of the inner cylinder and ν is the kinematic viscosity. The Taylor number at which these vortices first appear is known as the critical Taylor number, Ta_c. As the Taylor number is further increased, the flow changes through various wavy and chaotic states to turbulent flow. Koschmeider [15] stated that when $Ta \approx 1000 Ta_c$ order emerges from chaotic flow and the flow is turbulent with axisymmetric stable uniform vortices. This corresponded to a $Re = 4.16 \times 10^3$ with a radius ratio, $\eta = \frac{R_1}{R_2} = 0.896$, where the outer radius $R_2 = R_1 + d$.

The current paper analyses turbulent Taylor vortices in the Reynolds number range $5 \times 10^3 < Re < 5 \times 10^4$ for three different radius ratios $\eta = 0.7246$ [22], $\eta = 0.9412$ [37] and $\eta = 0.9846$ [2]. Based on an inner radius of 128 mm, which is approximately equal to that in [37] and [2], these values of η correspond to a gap width of 48.64 mm, 8.00 mm, 2.00 mm respectively. Hence forth, the analysis will refer to the 48 mm, 8 mm and 2 mm test cases. This paper demonstrates that stable axisymmetric turbulent Taylor vortices occur for a relatively small gap (the 2 mm case) at Taylor numbers significantly lower than the value of $1000T_C$ suggested by Koschmeider. Also, by analysing components in the turbulent production terms of the k-ω model [41] a transition is indentified at all three radius ratios as the flow becomes more like a wall bounded shear flow.

Experimental evidence for this transition exists in the detailed torque measurements of Taylor-Couette flow from which various semi-empirical equations have been derived. The two most commonly used are due to Wendt given in [22] and Bilgen and Boulos [23]. Both of these sets of equations are based on a power law for Reynolds number, $Re \approx 10^4$.

Wendt's empirical equations are

$$G = \begin{cases} 1.45\left(\frac{\eta^{3/2}}{(1-\eta)^{7/4}}\right) Re^{1.5} & \text{for } 4 \times 10^2 < Re < 1 \times 10^4 \\ 0.23\left(\frac{\eta^{3/2}}{(1-\eta)^{7/4}}\right) Re^{1.7} & \text{for } 1 \times 10^4 < Re < 1 \times 10^5 \end{cases} \tag{D.3}$$

where, $G = \frac{M}{\rho \nu^2 L}$, M is the moment L is the length and ρ is the density.

Bilgen and Boulos's empirical equations are

$$C_M = \begin{cases} 1.03\left(\frac{d}{R_1}\right)^{0.3} Re^{-0.5} & \text{for } 5 \times 10^2 < Re < 1 \times 10^4 \\ 0.065\left(\frac{d}{R_1}\right)^{0.3} Re^{-0.2} & \text{for } Re > 1 \times 10^4 \end{cases} \tag{D.4}$$

$$\text{where, } C_M = \frac{M}{1/2\pi\rho U^2 R_1^2 L}.$$

Wendt's Equations can also be expressed in terms of C_M:

$$C_M = \begin{cases} 0.923\left(\frac{dR_2}{R_1^2}\right)^{0.25} Re^{-0.5} & \text{for } 4 \times 10^2 < Re < 1 \times 10^4 \\ 0.146\left(\frac{dR_2}{R_1^2}\right)^{0.25} Re^{-0.2} & \text{for } 1 \times 10^4 < Re > 1 \times 10^5. \end{cases} \tag{D.5}$$

Bilgen et al.'s equations are based on the authors' own experimental data and other data available in Wendt, Taylor [24] and Donnelly [25]. They collected data in the Reynolds numbers range $10 < Re < 1 \times 10^6$ and radius ratios, $\eta = \frac{R_1}{R_2}$, ranging from $0.5 < \eta < 0.988$. From this, they deduced four semi-empirical expressions for the skin friction, C_M. The two equations which are relevant to this paper are given in equation D.4, stated to an accuracy of ±8.35%.

Although numerous studies of Taylor-Couette flow at low Reynolds numbers have been carried out (see, for example [9] and [16]), most are concerned with the formation of laminar vortices and the various wavy states formed as the flow becomes chaotic. There have been a few experimental studies at higher Reynolds numbers; notably visualisation work by Burkhalter et al. [17], who made detailed vortex wavelength measurements for several cylinder combinations and Townsend [68], who conducted a series of turbulent hot-wire probe experiments.

More recently, turbulent Taylor vortices have been studied at high Reynolds numbers using Laser Doppler Velocimetry [13]. This study used refractive index matching techniques and showed that Taylor Vortices are still present at $Ta = 2.107 \times 10^9$ ($Re = 73440$). Lathrop et al. [22] studied the turbulent flow between concentric cylinders for Reynolds numbers between $800 < Re < 1.23 \times 10^6$ with a radius ratio of $\eta = 0.7246$. While these experiments reveal no such Reynolds number change in torque based on a fixed power law akin to that of Bilgen et al, they did show a hysteretic free transition at a Reynolds number of 1.3×10^4. Above this Reynolds number the experiments suggest that the nature of the flow behaviour is more like that of open-flow systems such as those found in pipes or ducts.

Turbulent Taylor vortex flow in a centrifugal rotor was studied both experimentally and computationally by Wild et al. [37]. Two radius ratios were considered, $\eta = 0.941$ and 0.974 at Reynolds numbers in the range, $1.5 \times 10^4 < Re < 4 \times 10^4$. For their test cases the experimental results were in relatively good agreement with the semi-empirical expressions of Wendt and Bilgen et al. The computational study employed the standard k-ε model [38] which over predicted their experimental results by 10% or higher. Computations were also performed using other turbulence models with wall functions; the Renormalization Group (RNG) model [39] was within 2% of the standard k-ε model and the Reynolds Stress Equation model (RSM) [40] was 40% higher than the k-ε model. The RNG model without a wall function was also 40% higher than the k-ε model.

These results are surprising as the RNG and RSM models are generally thought to be more suitable for flows with curvature and rotation than the standard k-ε model [41]. This may be due to the fact that the turbulence models are more sensitive to the chosen coefficients and that these models have not been tuned for this problem. In the present work, as the gaps are small and the Reynolds number range is relatively low, adjacent grid points to the walls lie within the sublayer leading to large inaccuracies with the standard k-ε model. To overcome this problem the Wilcox low Reynolds number k-ω model [41] is used.

§D.2 Computational Method

The problem considered is that of steady state turbulent Taylor vortices between a rotating inner cylinder and a stationary outer cylinder, as shown schematically in figure D.1. The flow is solely induced by the relative motion of the inner cylinder. Assuming that the flow can be modelled using the Reynolds-averaged Navier-Stokes equations and that the vortices are uniform and not travelling in waves around the cylinders, the domain can then be simplified as a 2-D axial slice with a pair of periodic boundaries. Presuming the Taylor vortices are symmetrical, a mirror boundary is placed at either end of the vortex. The vortex sizes are constrained by the length of the domain, which is defined as follows.

Chandrasekha showed in [14] by using linear theory that instability between two cylinders with the inner cylinder rotating is governed by

$$Ta = \frac{2}{1+\eta} \cdot \frac{(\pi^2 + a^2)^3}{1 - 16a\pi^2 \cosh^2(a/2)\Big((\pi^2 + a^2)^2(\sinh a + a)\Big)} \tag{D.6}$$

where, a is the Taylor vortex wave number.

This equation has a minimum, which refers to the critical Taylor Number, Ta_c at which the vortices are formed. At this critical number, there is an associated wave number a_c. This wave number is given by $\lambda = 2\pi/a$, where λ is a non-dimensional size of a pair of Taylor vortices, $\lambda = \triangle Z/d$. $\triangle Z$ signifies the length of a pair of vortices and d is the gap width.

The turbulent Taylor vortex cell length is highly dependent upon the start-up conditions. As Koschmieder reported in [17] the wavelength varied from 20% larger than the critical value, during rapid accelerations to 70% larger during quasi-steady accelerations (accelerations much less than the relaxation time, d^2/ν). Many engineering applications employ rapid accelerations so a wavelength for the Taylor vortices was taken to be $1.25 \times \lambda$. Using equation D.6 and taking the turbulent vortex length to be $\triangle Z_T = 1.25 \times \triangle Z$, the critical Taylor numbers and turbulent wave lengths for the three test cases examined are given in table D.1.

A uniform cell distribution in the axial direction was used as the axial velocity tended to vary uniformly along the length of one cell. However, a non-uniform expanding and then contracting grid was used in the radial direction. This was setup to place sufficient cells in the laminar sublayer, defined by, [22]

$$\frac{\delta_1}{R_1} = 6.32 \cdot (\eta^{-1} - 1)^{2/3} \cdot Re^{-2/3} \tag{D.7}$$

$$\frac{\delta_2}{R_2} = 8.16 \cdot (\eta^{-1} - 1)^{2/3} \cdot Re^{-2/3} \tag{D.8}$$

where δ_1 is the laminar sublayer thickness on the inner cylinder and δ_2 is the corresponding thickness on the outer cylinder. Applying equations D.7 and D.8 to the present cases the widths of the turbulent cores are presented in table D.2. The sublayer region comprises a significant proportion of the gap especially for the 2mm case.

The Taylor-Couette problem was simulated using a commercial RANS flow solver [58]. This is a structured multi-block finite volume code. Turbulence was modelled using the low Reynolds number Wilcox Model as described in the following section. The QUICK differencing scheme was used in the SimpleC pressure correction algorithm and Algebraic Multi-grid was used to accelerate convergence.

To ensure that the solution had converged, residuals were analysed to confirm that all components had reduced to a steady state and that there were no oscillatory motions in the final solution. The residuals were normalised with respect to the absolute mean value. The normalised axial and radial velocities residuals were less than 10^{-3}. All other residuals converged to less than 10^{-6}.

The 8mm case was used to test for a grid independent solution at $Re = 8 \times 10^3$ and $Re = 1.6 \times 10^4$. The inflow and outflow profiles were aligned with the vortex end cells in the 32x32 case. The velocity profile plots are shown in figures D.2, D.3 and the shear stress is presented in tables D.3, D.4. The results show good alignment of the mean profiles, with small changes in the inflow and outflow profiles with the shear stress coefficient, C_M. Therefore, the 64x64 grid was used for the remainder of the test cases to save computation cost as increasing the grid density had little improvement upon the accuracy.

§D.2.1 Low Reynolds Number Turbulent Wilcox Model

Turbulence has been modelled using the low Reynolds number Wilcox Model [41]. Since this model avoids the use of wall functions, it allows modelling close to the wall and provides more accurate modelling of turbulent production due to the Taylor vortex formation. The transport equations for the turbulent kinetic energy, k, and the turbulent frequency, ω are given by [58]

$$\frac{\partial}{\partial t}\rho k + \nabla \bullet (\rho k \mathbf{U}) = \nabla \bullet \left[\left(\mu + \frac{\mu_T}{\sigma_k}\right)\nabla k\right] + P - \rho\omega k \tag{D.9}$$

and

$$\frac{\partial}{\partial t}\rho\omega + \nabla \bullet (\rho\omega \mathbf{U}) = \nabla \bullet \left[\left(\mu + \frac{\mu_T}{\sigma_k}\right)\nabla k\right] + C_1\frac{\omega}{k}P - C_2\rho\omega^2 \tag{D.10}$$

where μ is the dynamic viscosity and the constants $C_1 = 0.5111$, $C_2 = 0.8333$ and $\sigma_k = 2$ (Prandtl number). The turbulent production term, P is expressed as

$$P = \mu_T \nabla \mathbf{U} \bullet \left(\nabla \mathbf{U} + (\nabla \mathbf{U})^T\right). \tag{D.11}$$

The turbulent viscosity is defined by

$$\mu_T = C_\mu f_\mu \rho \frac{k}{\omega} \tag{D.12}$$

taking $C_\mu = 0.09$ and the damping function f_μ given by

$$f_\mu = exp\left[\frac{-3.4}{(1+R_T/50)^2}\right] \tag{D.13}$$

with a local turbulent Reynolds number

$$R_T = \frac{\rho k}{\mu\omega}. \tag{D.14}$$

When analyzing the turbulent energy in the Taylor-Couette system the turbulent production derivatives in polar coordinates are: $(\partial u_r/\partial x)^2$, $(\partial u_\theta/\partial x)^2$, $(\partial u_x/\partial r)^2$, $(\partial u_\theta/\partial r)^2$, $2(\partial u_x/\partial x)^2$, $2(\partial u_r/\partial r)^2$, $(\partial u_x/\partial r)(\partial u_r/\partial x)$, $(\partial u_r/\partial x)(\partial u_x/\partial r)$ and the turbulent dissipation term is $\rho\omega k$, where the components u_r, u_θ, u_x, r and x are the radial, azimuthal and axial velocities and the radial and axial distances, respectively.

The low Reynolds number effects at the wall are accounted for by applying the exact solution to the ω equation in the viscous sublayer,

$$\omega \sim \frac{6\mu}{\rho C_2 y^2} \quad \text{for} \quad y^+ < 2.5. \tag{D.15}$$

where y is the distance from the wall, $y^+ = \frac{y\sqrt{\rho\tau_w}}{\mu}$ and τ_w is the shear stress at the wall. To minimize the numerical error of the integration through the sublayer and to ensure y^+ independent results, the first 7 to 10 grid points from the walls were positioned between $0 < y^+ < 2.5$ as advised in [41].

§D.3 Results

The results are validated against the empirical equations given by Bilgen et al. and are given in table D.5. For the 2mm test case the numerical simulations over predict the empirical relationship by around 20%. The 8mm case predicted the skin friction almost within Bilgen et al's margin of error, with the exception of the low speed case, $Re = 5000$, where the CFD analysis over estimated by around 50%. This was possibly due to the very low turbulent production. The results for the 48mm test case were inconsistent due to numerical problems, hence three results are presented for the 48mm case.

The components of the turbulent Taylor vortex are compared in a series of non-dimensional profile plots either side of the transition for all three test cases. The velocity components, kinetic energy and the dissipation and production terms have been non-dimesionalised by the speed of the inner cylinder, U, the square of the shear stress velocity, $u_\tau = \sqrt{\tau_w/\rho}$ and a parameter $\frac{\nu}{\rho {u_\tau}^4}$, respectively. These terms are plotted against a non-dimensional radius, $R = \frac{r-R_1}{d}$ and the length $L = \frac{l}{d}$.

The associated Reynolds numbers and figure numbers describing conditions before and after transition for all three test cases are presented in table D.6.

At $Re = 2 \times 10^4$ for the 48 mm case the numeric model was unsteady. Several attempts to force a converged solution were tried by altering the grid distribution, grid densities and initial conditions. The only method of achieving a converged solution was by altering the aspect ratio of the vortex cell size. When the cell aspect ratio was reduced to unity, $\triangle Z_T = 96$ mm, the solution converged either side of the transition but with two vortices. This is shown in figures D.10 and D.11. The converged single cell case with an aspect ratio of 1.25 is also presented in figure D.9 for comparison.

The axial and radial velocity components, u_x and u_r, for both the 2 mm and 8 mm case are similar, figures D.5-D.8.i-ii. The velocity components are larger for the 8 mm case than 2 mm, this is further demonstrated in figures D.9.i-ii for the 48 mm case where the maximum non-dimensionalised velocity has doubled. The azimuthal velocity components, u_θ, are also consistent across figure D.5-D.11.iii with higher axial gradients than radial gradients before the transition.

The turbulent kinetic energy plots, k, figures D.5.vii and D.7.vii have maximum peaks in the radial plane, at the outflow edge of the vortex. After the transition, figures D.6.vii and D.8.vii have maximum peaks in the axial direction, along the edge of the inner cylinder. This is also demonstrated in figures D.10.vii and D.11.vii with two vortices.

The two most significant contributions, by a factor of approximately 1000, to the production of turbulent kinetic energy are due to the azimuthal velocity gradients in the radial direction $\mu_T\left(\frac{du_\theta}{du_r}\right)^2$, figures D.5-D.11.iv and in the axial direction $\mu_T\left(\frac{du_\theta}{du_x}\right)^2$, figures D.5-D.11.v. The test cases show relatively larger peaks in the radial production, vortex boundaries, than the axial production, wall boundaries, before the transition. The turbulent dissipation, $\rho\omega k$, also show similar trends as shown in figures D.5-D.11.vi following the pattern of the turbulent kinetic energy.

§D.4 Discussion

The present computations clearly show that as Reynolds number increases there is a transition to a flow dominated by the wall shear stress, as discussed by Lathrop et al. At lower Reynolds numbers turbulence production is dominated by the outflow of the Taylor vortex.

This is represented schematically in figure D.4 where regions P_A and P_C are associated with the turbulent wall shear stress production and P_B and P_C are associated with the vortex inflow and– outflow shear stresses, where,

$$\begin{array}{llll} P_A < P_B & \text{and} & P_C < P_D & \text{before transition} \\ P_A > P_B & \text{and} & P_C > P_D & \text{after transition} \end{array}$$

For the higher Reynolds number cases turbulence production is dominated by the wall shear stress derivative $(\partial u_\omega/\partial r)^2$ signified by P_A.

The results suggest that the transition to wall dominated turbulent production occurs at a lower Reynolds number for higher radius ratios. This can be demonstrated by comparing figures D.6 and D.7. Both these test cases are at the same Reynolds number but the transition has occurred for the 2 mm case but not the 8 mm case. This is due to the fact that Ta/Ta_c is around 75% lower for the 2 mm case. Hence the vortex strength is less, see figures D.6-D.7.i-ii. This in turn leads to relatively less turbulent production at the vortex outflow and inflow edges, hence the transition occurs at a lower Reynolds number. It is also of interest to note that the non-dimensionalised radial and axial velocity components are higher before the transition.

The problem has also been tested using a low Reynolds number k-ε model [40]. At Reynolds numbers below 10^4 no turbulent energy is produced. For Reynolds numbers between $1 \times 10^4 < Re < 5 \times 10^4$ the solution appears to be unsteady. This is possibly due to the damping function used to implement the low Reynolds number effects as opposed to the adoption of the wall treatment which is applied in the k-ω model.

If the end mirror boundaries are replaced with periodic boundaries an axial flow is developed instead of the Taylor vortices. Also, unsteady disturbances were produced on the surface of the inner cylinder, which may be akin to Görtler vortices but which are not distinguishable in a 2-D flow.

The SimpleC pressure correction algorithm was also compared with the iterative PISO approach. In the latter case the laminar boundary layer produced was larger than expected (approx 40% of the gap width) and consequently, the torques produced were 20% less than predicted by Bilgen et al.

§D.5 Conclusions

A transition in turbulent flow in the Taylor-Couette system with an inner cylinder rotating and a fixed outer cylinder has been identified for a wide range of radius ratios. At relatively low Reynolds numbers turbulent production is dominated by the flow between two adjacent Taylor Vortices. A transition occurs as the Reynolds number is increased to a condition where the shear stress of the rotating cylinder becomes the dominant source of turbulent kinetic energy production. It has also been shown that developed turbulent flow can occur for $Ta/Ta_c < 1000$ for small gaps and that the transition occurs earlier for these flows. The results also demonstrate the applicability of the k-ω model to the 2-D simulation of rotating fluids associated with turbulent Taylor vortices.

Bibliography

For clarity, the bibliography is combined with the main text at the end of the thesis.

Appendix

§D.6 Tables

Case	η	Ta_c	$\triangle Z_T$
2 mm	0.9846	1721	5.01 mm
8 mm	0.9412	1760	20.1 mm
48 mm	0.7246	1981	117.25 mm

Table D.1: Critical Laminar Taylor Numbers and Wavelengths

Re	2 mm	8 mm	48 mm
5×10^3	80	87	92
1×10^4	87	92	95
5×10^4	96	97	98

Table D.2: Comparison of the percentage of turbulent core

Grid Dimensions	CV	Shear Stress
16x16	256	5.30e-03
32x32	1024	4.79e-03
64x64	4096	4.82e-03
128x128	16384	4.83e-03

Table D.3: C_M for the 8 mm case, $Re = 8 \times 10^3$

Grid Dimensions	CV	Shear Stress
16x16	256	4.26e-03
32x32	1024	3.87e-03
64x64	4096	3.70e-03
128x128	16384	3.73e-03

Table D.4: C_M for the 8 mm case, $Re = 1.6 \times 10^4$

Test Case	Re	Emprical	CFD	%
2 mm	5,000	0.0042	0.0045	8
2 mm	8,000	0.0033	0.0039	15
2 mm	10,000	0.0030	0.0036	19
2 mm	20,000	0.0026	0.0031	16
8 mm	5,000	0.0063	0.013	52
8 mm	8,000	0.0050	0.0048	-4
8 mm	16,000	0.0041	0.0037	-9
8 mm	20,000	0.0039	0.0042	7
48 mm	8,000	0.0084	0.0067	-25
Square 48 mm	8,000	0.0084	0.0084	1
Square 48 mm	20,000	0.0065	0.0046	41

Table D.5: Comparison of C_M values between the Empirical equations of Bilgen et al. and the current CFD calculations.

Test Case	Before Transition	After Transition
2 mm	$Re = 5.00 \times 10^3$ $Ta/Ta_c = 224$ see figure D.5	$Re = 8.00 \times 10^3$ $Ta/Ta_c = 573$ see figure D.6
8 mm	$Re = 8.00 \times 10^3$ $Ta/Ta_c = 2140$ see figure D.7	$Re = 1.60 \times 10^4$ $Ta/Ta_c = 8550$ see figure D.8
48 mm	$Re = 8.00 \times 10^3$ $Ta/Ta_c = 8900$ see figure D.9 and figure D.10	$Re = 2.00 \times 10^4$ $Ta/Ta_c = 55600$ see figure D.11

Table D.6: List of Re, Ta/Ta_c and figure numbers for the test cases before and after transition.

§D.7 Figures

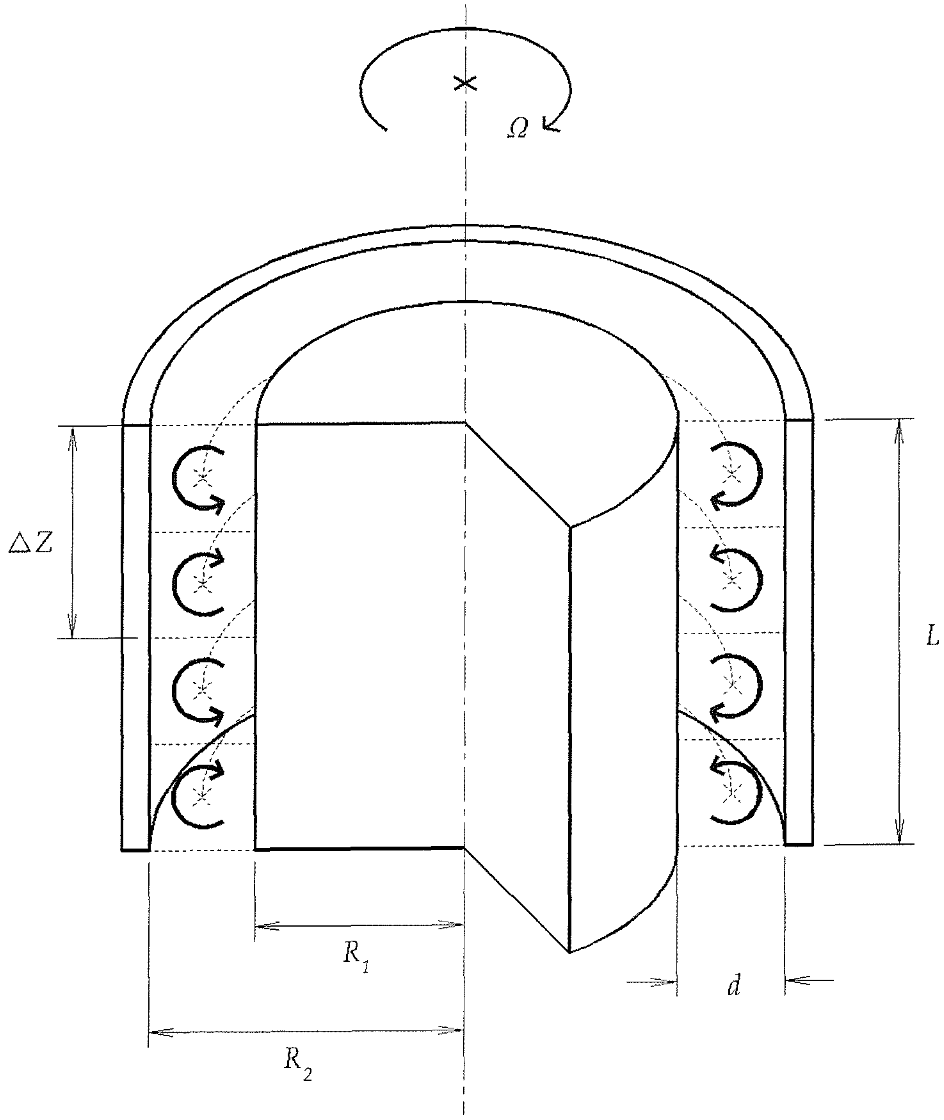

Figure D.1: Schematic Section of the Geometry

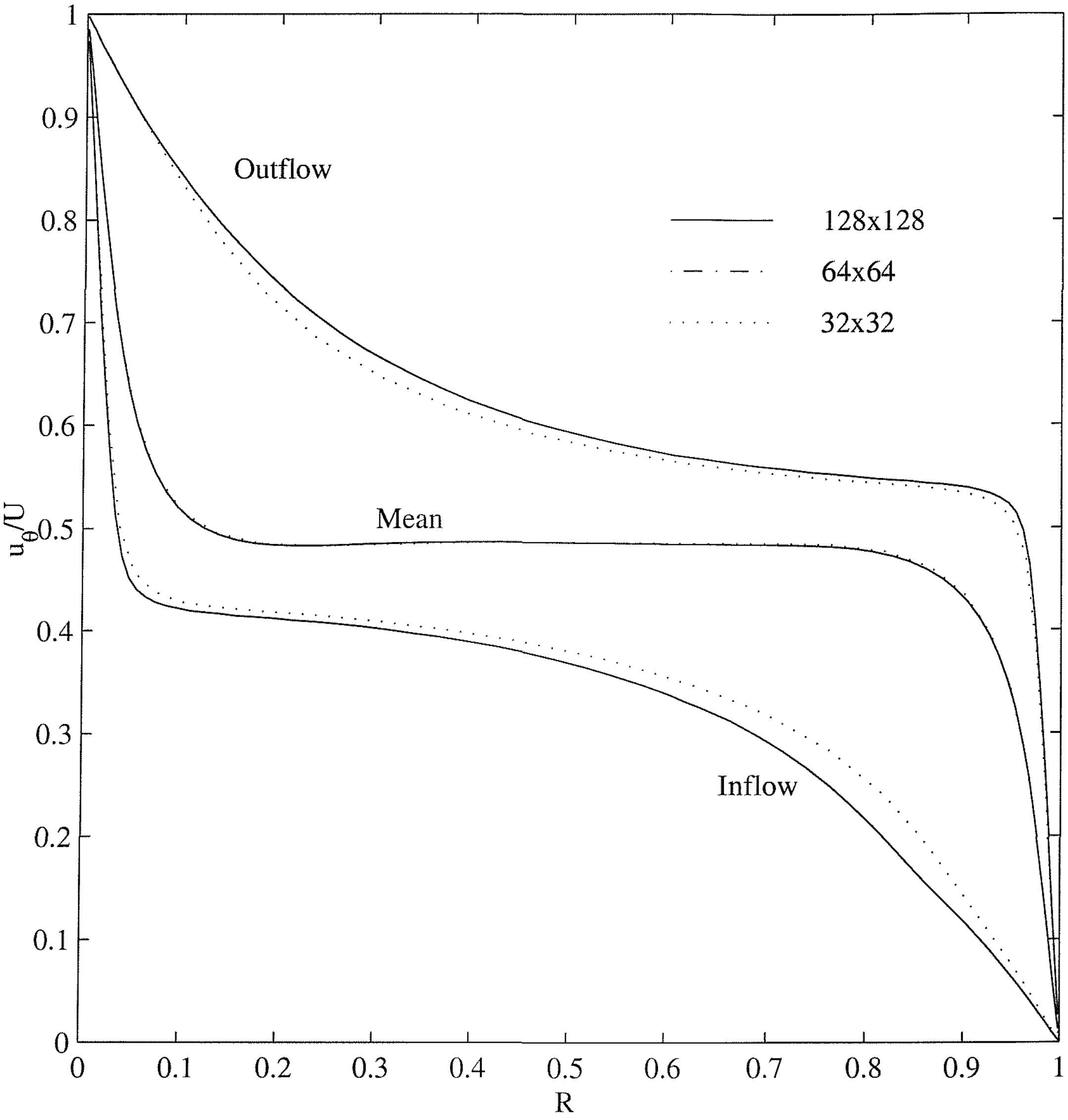

Figure D.2: Profile Plot for the 8 mm case, $Re = 8 \times 10^3$

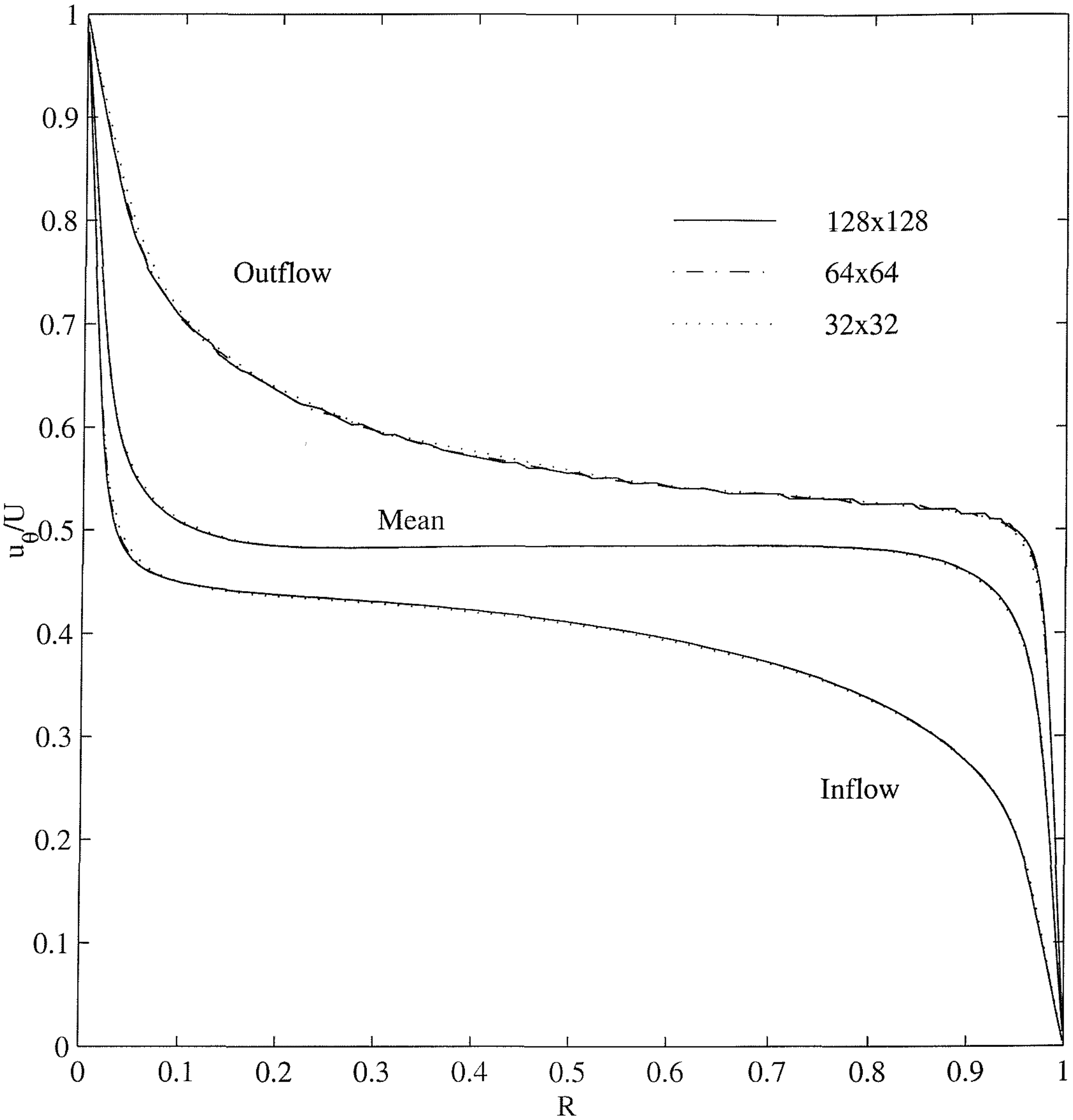

Figure D.3: Profile Plot for the 8 mm case, $Re = 1.6 \times 10^4$

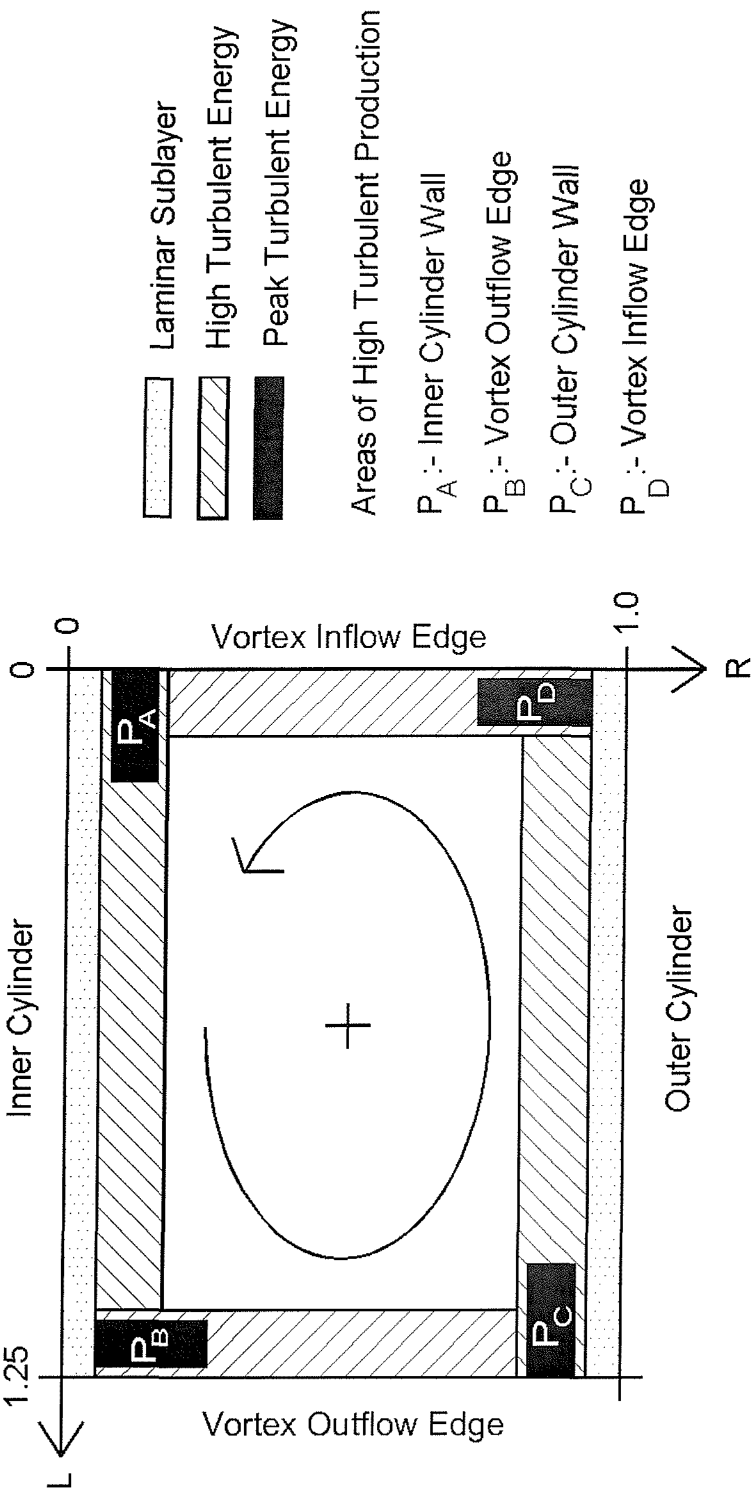

Figure D.4: Schematic Drawing of a Taylor Vortex indicating areas of high turbulent energy.

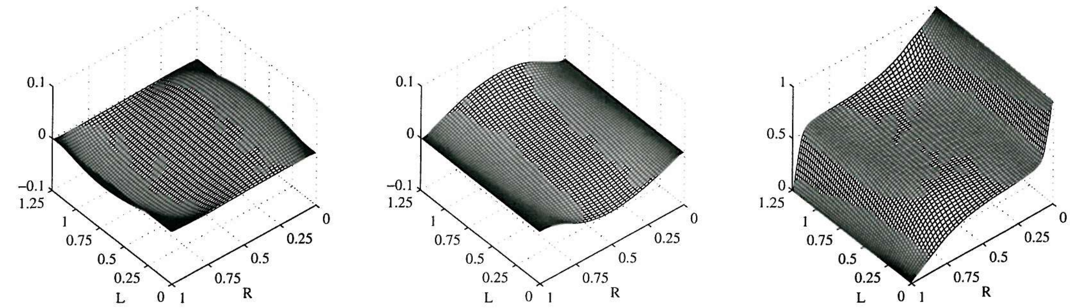

i: Axial Velocity, $\frac{u_x}{U}$ **ii:** Radial Velocity, $\frac{u_r}{U}$ **iii:** Azimuthal Velocity, $\frac{u_\theta}{U}$

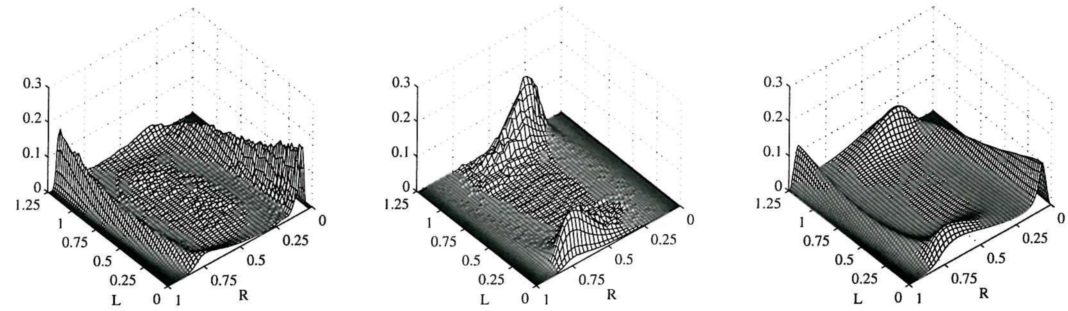

iv: Axial Turbulence Production, $\frac{\nu\mu_T(du_\theta/du_x)^2}{\rho {u_\tau}^4}$ **v:** Radial Turbulence Production, $\frac{\nu\mu_T(du_\theta/du_r)^2}{\rho {u_\tau}^4}$ **vi:** Turbulent Dissipation, $\rho\omega k \cdot \frac{\nu}{u_\tau \rho}$

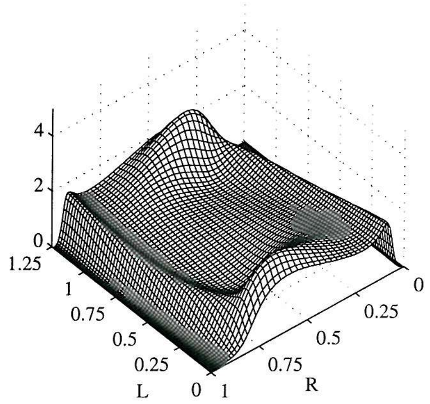

vii: Turbulent Energy, $\frac{k}{{u_\tau}^2}$

Figure D.5: Components for 2mm case $Re = 5 \times 10^3$

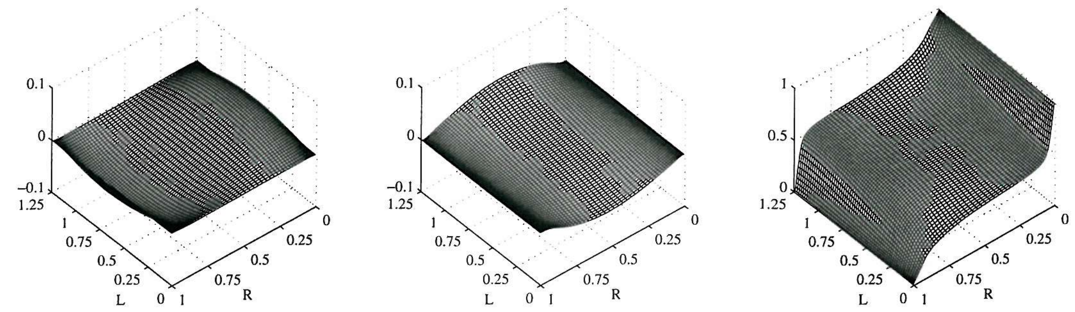

i: Axial Velocity, $\frac{u_x}{U}$ **ii:** Radial Velocity, $\frac{u_r}{U}$ **iii:** Azimuthal Velocity, $\frac{u_\theta}{U}$

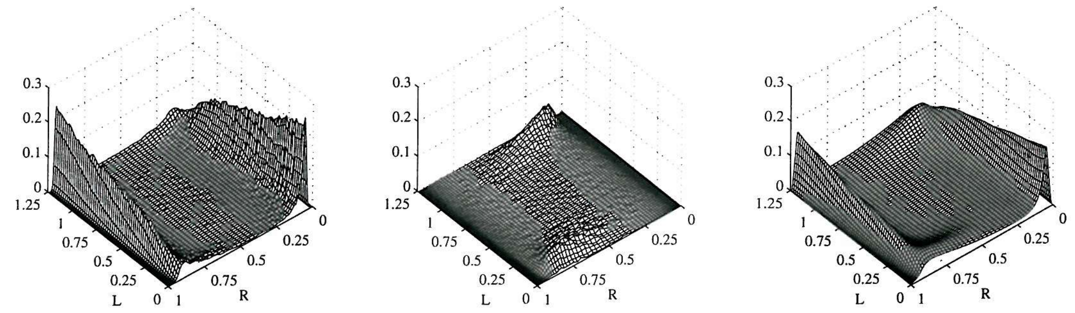

iv: Axial Turbulence Production, $\frac{\nu \mu_T (du_\theta/du_x)^2}{\rho {u_\tau}^4}$ **v:** Radial Turbulence Production, $\frac{\nu \mu_T (du_\theta/du_r)^2}{\rho {u_\tau}^4}$ **vi:** Turbulent Dissipation, $\rho \omega k \cdot \frac{\nu}{u_\tau \rho}$

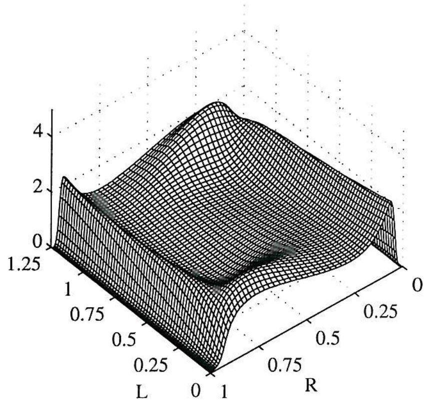

vii: Turbulent Energy, $\frac{k}{{u_\tau}^2}$

Figure D.6: Components for 2mm case $Re = 8 \times 10^3$

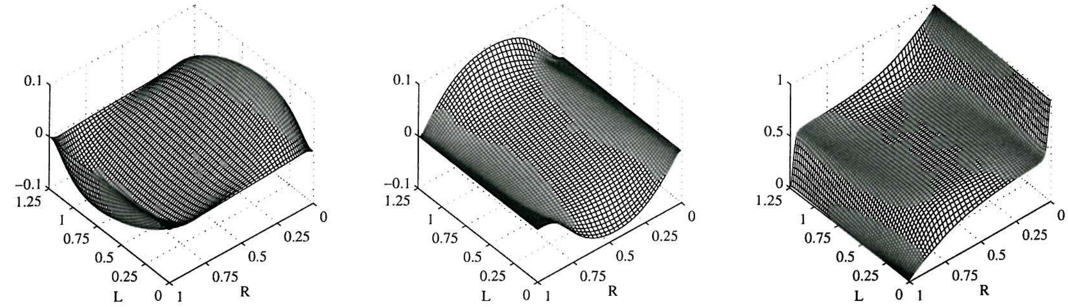

i: Axial Velocity, $\frac{u_x}{U}$

ii: Radial Velocity, $\frac{u_r}{U}$

iii: Azimuthal Velocity, $\frac{u_\theta}{U}$

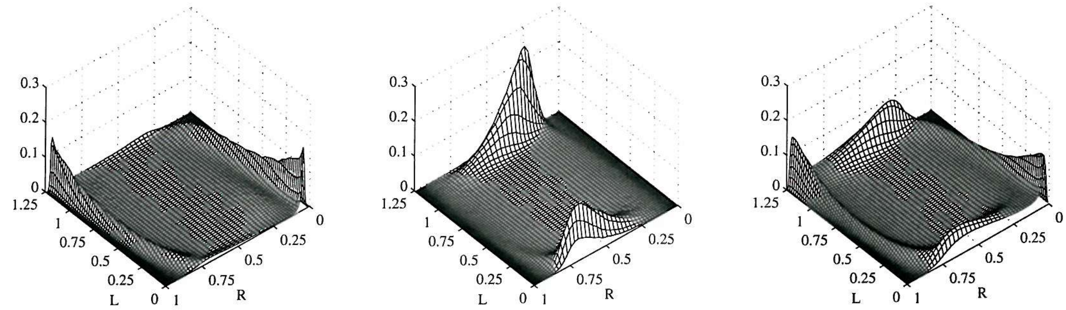

iv: Axial Turbulence Production, $\frac{\nu\mu_T(du_\theta/du_x)^2}{\rho {u_\tau}^4}$

v: Radial Turbulence Production, $\frac{\nu\mu_T(du_\theta/du_r)^2}{\rho {u_\tau}^4}$

vi: Turbulent Dissipation, $\rho\omega k\cdot\frac{\nu}{u_\tau\rho}$

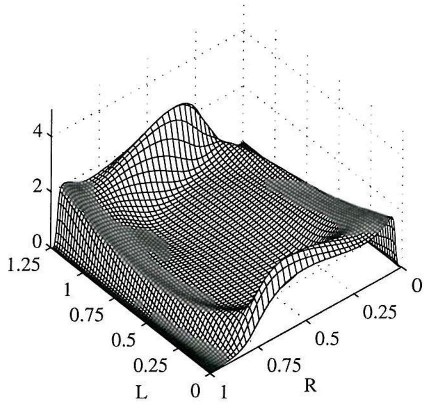

vii: Turbulent Energy, $\frac{k}{{u_\tau}^2}$

Figure D.7: Components for 8mm case $Re = 8 \times 10^3$

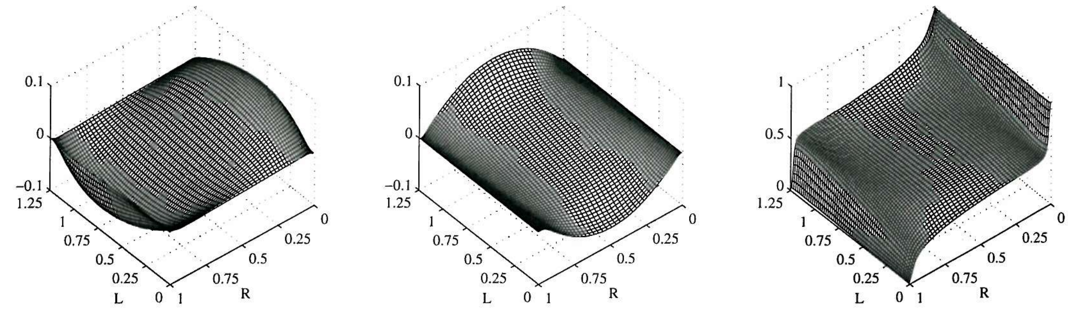

i: Axial Velocity, $\frac{u_x}{U}$ **ii:** Radial Velocity, $\frac{u_r}{U}$ **iii:** Azimuthal Velocity, $\frac{u_\theta}{U}$

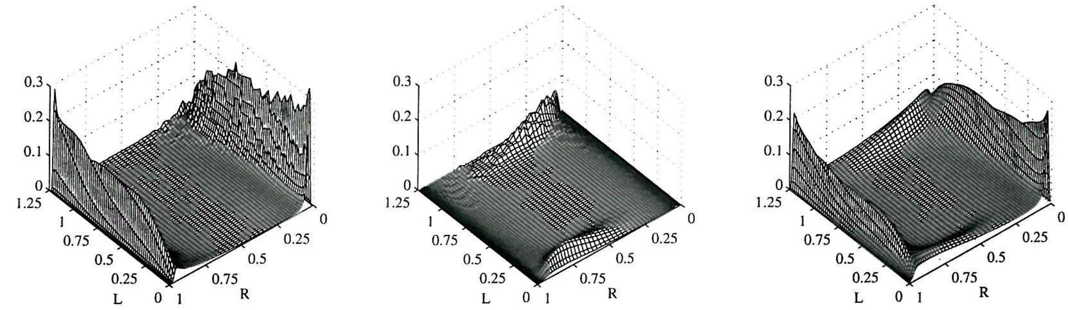

iv: Axial Turbulence Production, $\frac{\nu\mu_T(du_\theta/du_x)^2}{\rho u_\tau{}^4}$ **v:** Radial Turbulence Production, $\frac{\nu\mu_T(du_\theta/du_r)^2}{\rho u_\tau{}^4}$ **vi:** Turbulent Dissipation, $\rho\omega k \cdot \frac{\nu}{u_\tau \rho}$

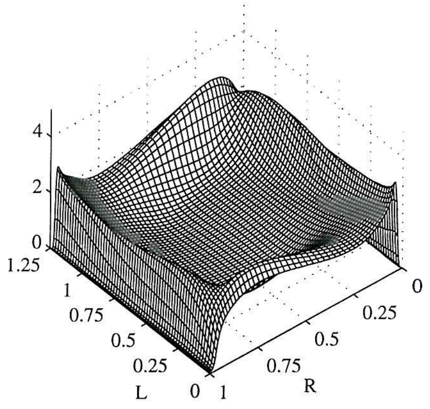

vii: Turbulent Energy, $\frac{k}{u_\tau{}^2}$

Figure D.8: Components for 8mm case $Re = 1.6 \times 10^4$

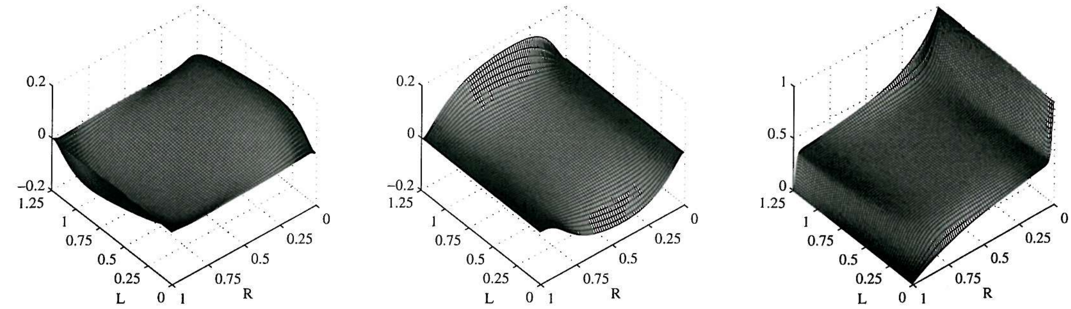

i: Axial Velocity, $\frac{u_x}{U}$

ii: Radial Velocity, $\frac{u_r}{U}$

iii: Azimuthal Velocity, $\frac{u_\theta}{U}$

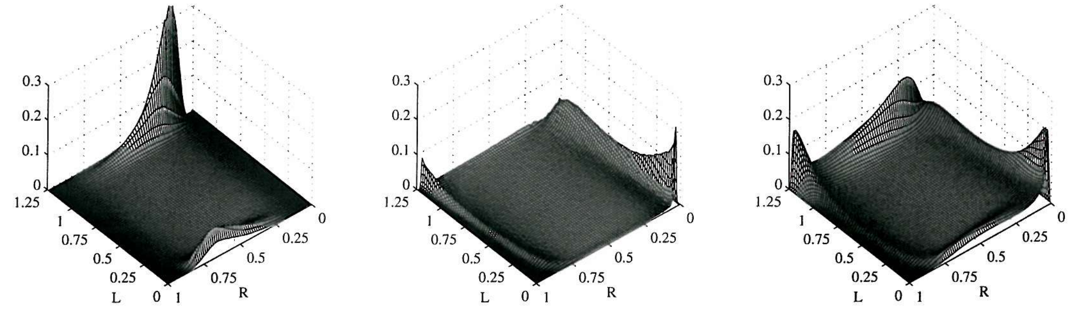

iv: Axial Turbulence Production, $\frac{\nu\mu_T(du_\theta/du_x)^2}{\rho u_\tau{}^4}$

v: Radial Turbulence Production, $\frac{\nu\mu_T(du_\theta/du_r)^2}{\rho u_\tau{}^4}$

vi: Turbulent Dissipation, $\rho\omega k\cdot\frac{\nu}{u_\tau\rho}$

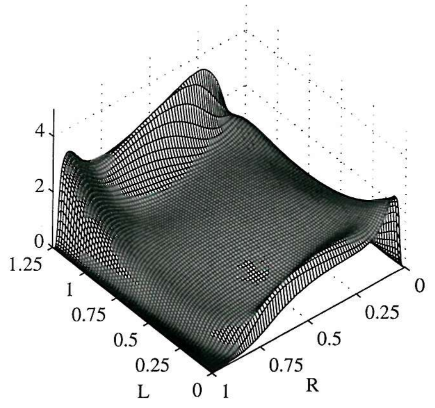

vii: Turbulent Energy, $\frac{k}{u_\tau{}^2}$

Figure D.9: Components for 48mm case $Re = 8 \times 10^3$

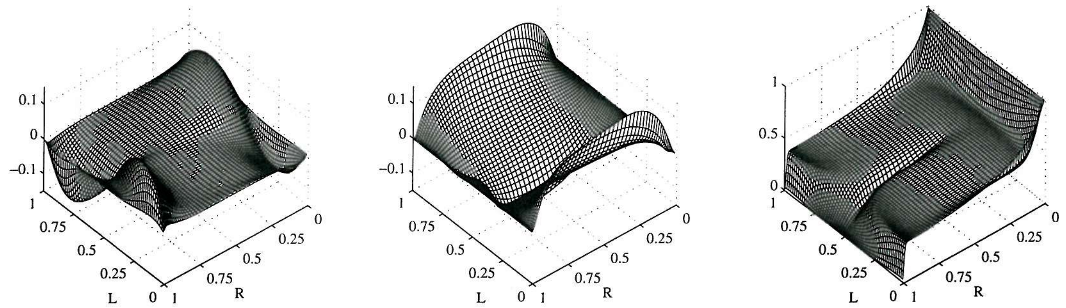

i: Axial Velocity, $\frac{u_x}{U}$

ii: Radial Velocity, $\frac{u_r}{U}$

iii: Azimuthal Velocity, $\frac{u_\theta}{U}$

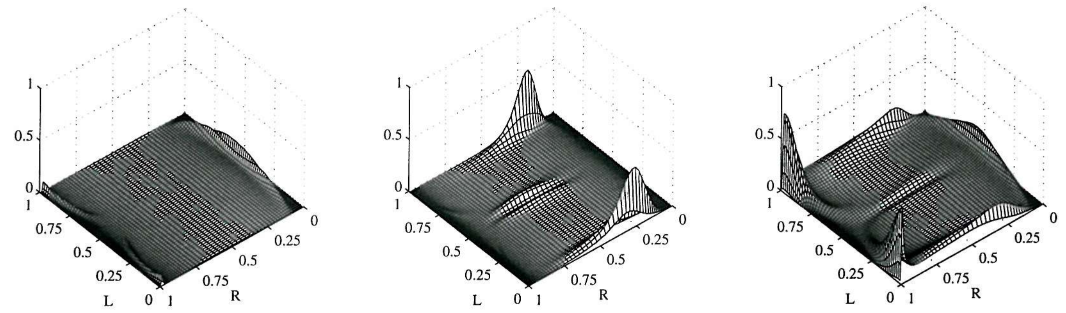

iv: Axial Turbulence Production, $\frac{\nu\mu_T(du_\theta/du_x)^2}{\rho {u_\tau}^4}$

v: Radial Turbulence Production, $\frac{\nu\mu_T(du_\theta/du_r)^2}{\rho {u_\tau}^4}$

vi: Turbulent Dissipation, $\rho\omega k \cdot \frac{\nu}{u_\tau \rho}$

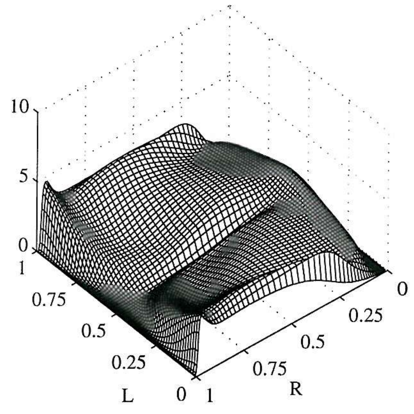

vii: Turbulent Energy, $\frac{k}{{u_\tau}^2}$

Figure D.10: Components for square 48mm case $Re = 8 \times 10^3$

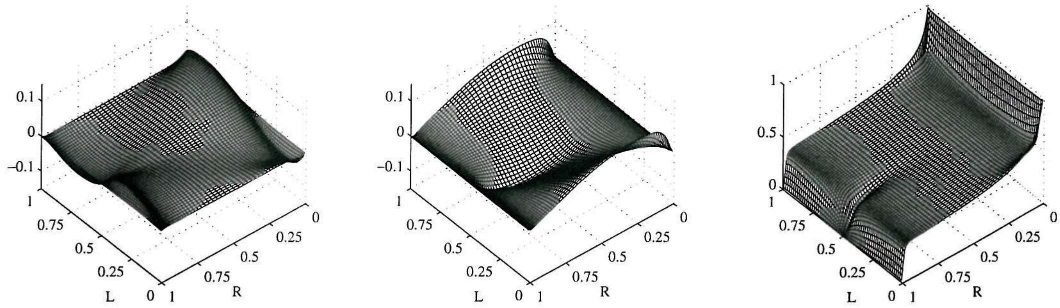

i: Axial Velocity, $\frac{u_x}{U}$ **ii:** Radial Velocity, $\frac{u_r}{U}$ **iii:** Azimuthal Velocity, $\frac{u_\theta}{U}$

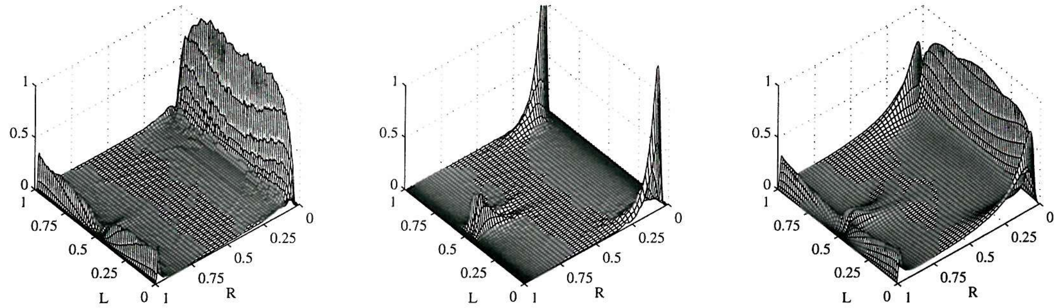

iv: Axial Turbulence Production, $\frac{\nu\mu_T(du_\theta/du_x)^2}{\rho {u_\tau}^4}$

v: Radial Turbulence Production, $\frac{\nu\mu_T(du_\theta/du_r)^2}{\rho {u_\tau}^4}$

vi: Turbulent Dissipation, $\rho\omega k \cdot \frac{\nu}{u_\tau \rho}$

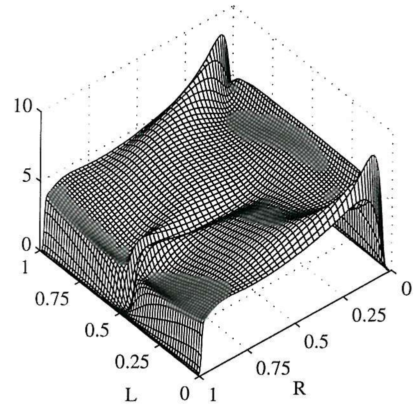

vii: Turbulent Energy, $\frac{k}{{u_\tau}^2}$

Figure D.11: Components for square 48mm case $Re = 2 \times 10^4$

APPENDIX

E

2D Start-up Results for $Re = 8 \times 10^3$

As stated in the main text the P-DNS test at $Re = 8 \times 10^3$ is presented in this appendix.

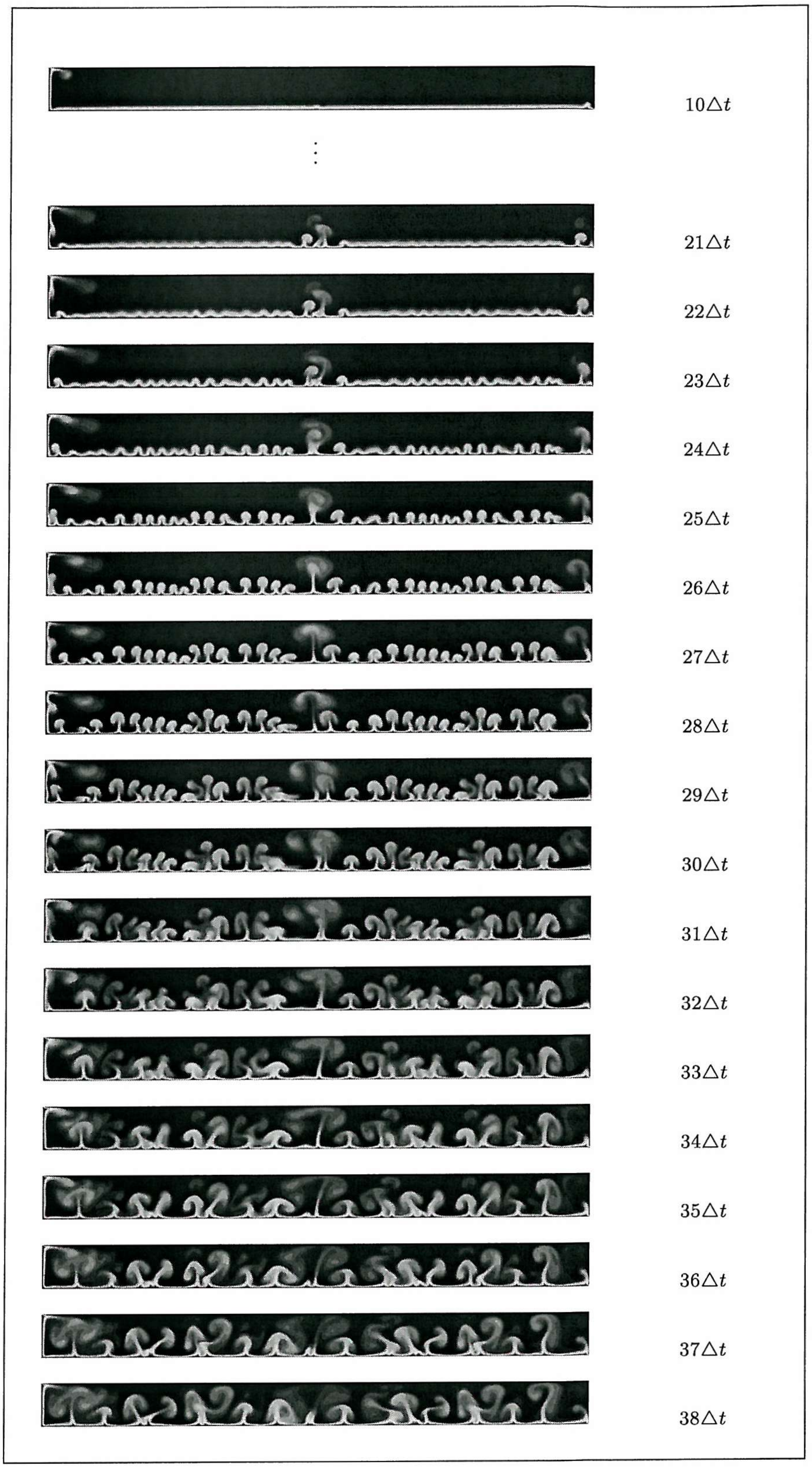

Figure E.1: Part I: Initial formation of Görtler vortices, $Re = 8 \times 10^3$

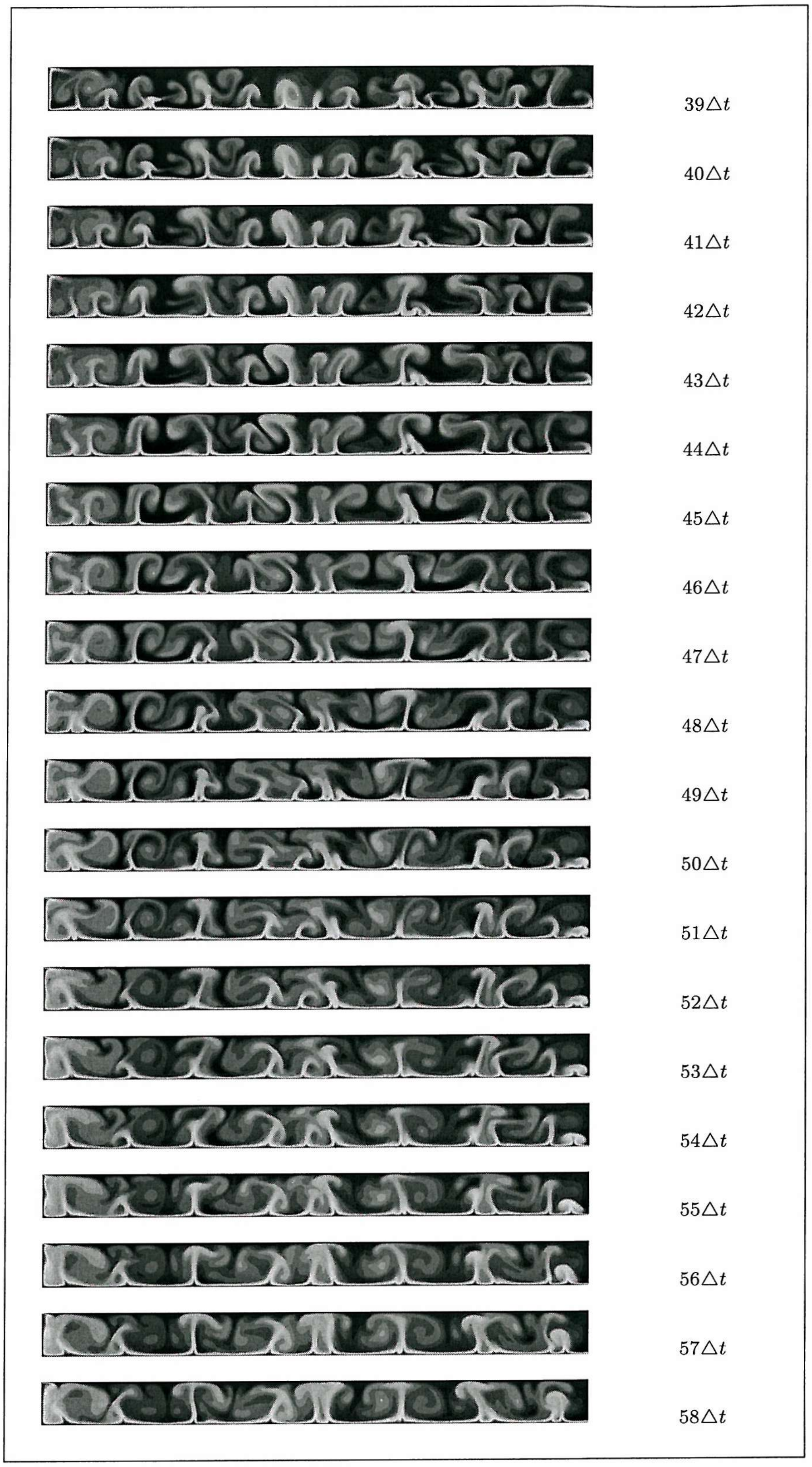

Figure E.2: Part II: Mixing of Görtler vortices phase, $Re = 8 \times 10^3$

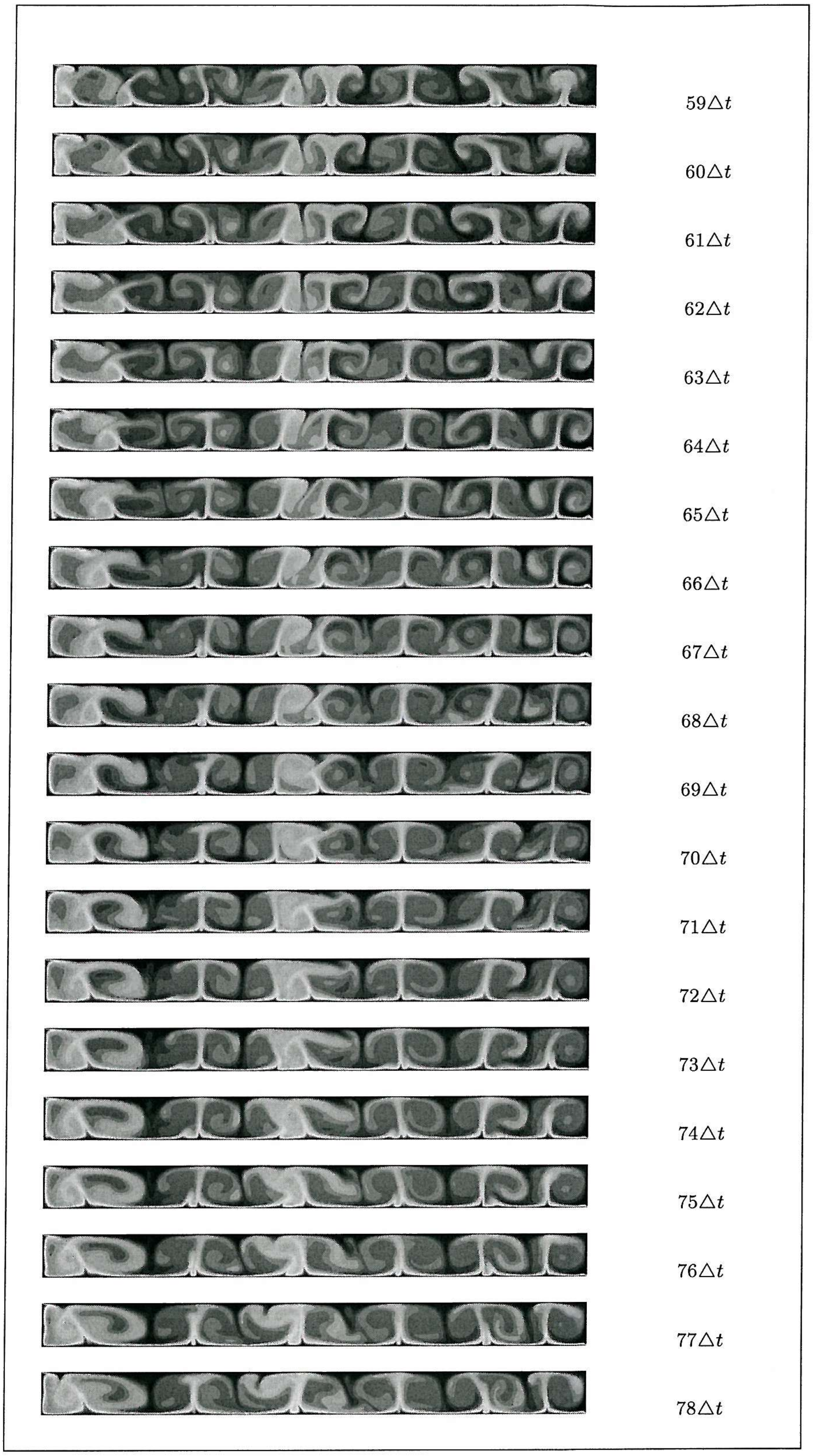

Figure E.3: PART III: Chaotic Görtler/Taylor vortex mixing phase, $Re = 8 \times 10^3$

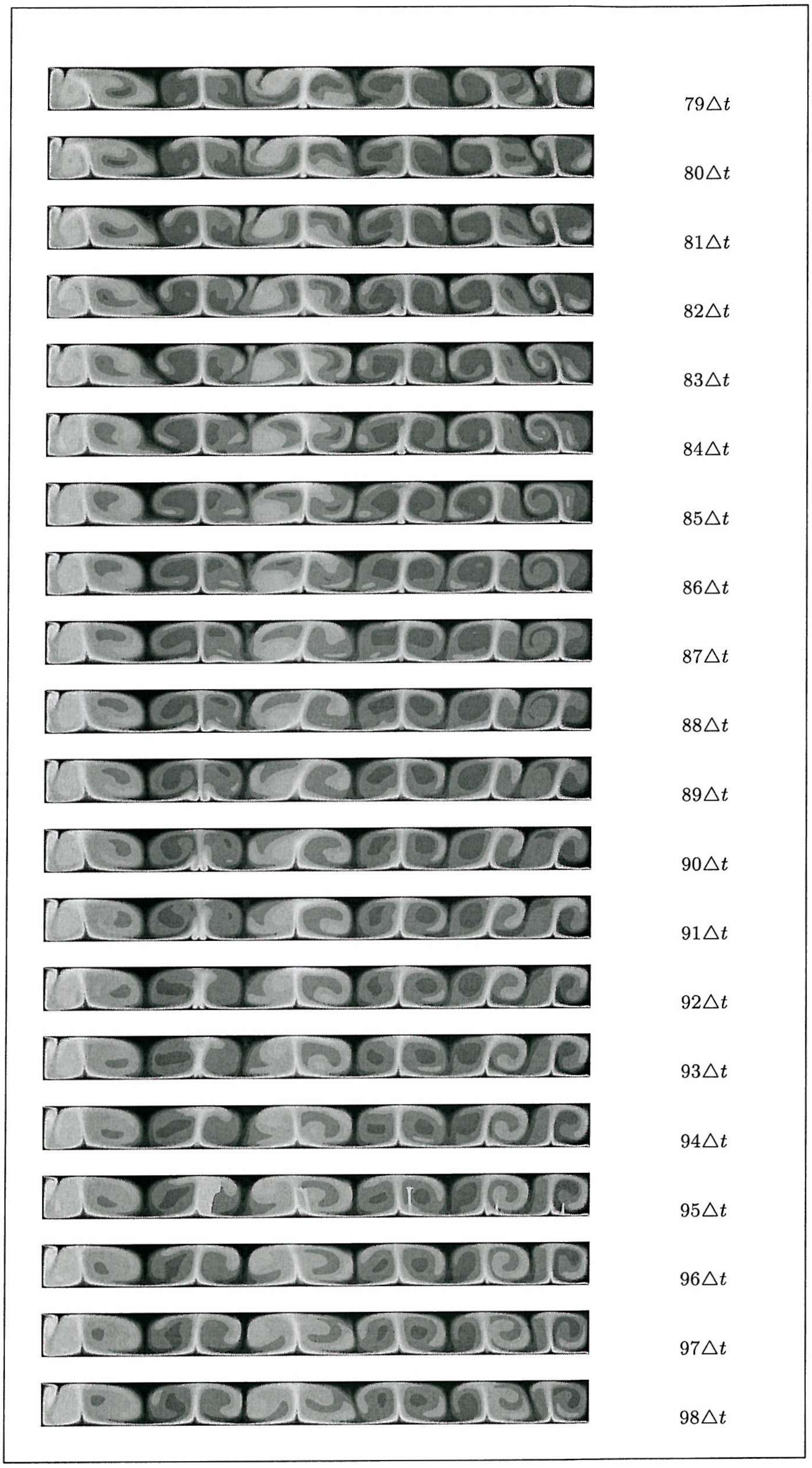

Figure E.4: Part IV: Stabilization of the Taylor vortices, $Re = 8 \times 10^3$

BIBLIOGRAPHY

[1] A. W. Hughes, *Investigation of Tip-Driven Thruster and Waterjet Propulsion Systems.* PhD thesis, School of Engineering Sciences, University of Southampton, 2000.

[2] A. W. Hughes, S. M. Abu-Sharkh, and S. R. Turnock, "Design and testing of a novel electromagnetic tip driven thruster for underwater vehicles," in *Tenth International Offshore and Polar Engineering Conference*, (Seattle), ISOPE, May 2000.

[3] A. W. Hughes, S. R. Turnock, and S. Abu-Sharkh, "CFD modelling of a novel electromagnetic tip driven thruster for underwater vehicles," in *Tenth International Offshore and Polar Engineeing Conference*, (Seattle), ISOPE, May 2000.

[4] G. I. Taylor, "Stability of a viscous liquid contained between two rotating cylinders," *Trans. Royal Soc. London, A*, vol. 233, pp. 289–343, 1923.

[5] W. Versteeg, H K amd Malalasekera, *An introduction to computational fluid dynamics.* Addison Weseley Longman Limited, 2 ed., 1995.

[6] S. B. Pope, *Turbulent Flows.* Cambridge university press, 1 ed., 2000.

[7] I. Stwart and M. Golubitsky, *Fearful symmetry: Is God a geometer?* Penguin books, 1 ed., 1993.

[8] A. Mallock, "Determination of the viscosity of water," *Proc. Royal Soc. London*, vol. A, no. 45, pp. 126–137, 1888.

[9] R. C. Di Prima and H. L. Swinney, "Instabilities and transition in flow between concentric rotating cylinders," in *Hydrodynamics Instabilities and the Transion to Turbulence* (H. L. Swinney and J. P. Gollub, eds.), pp. 139–180, New York, Springer, 2 ed., 1981.

[10] C. D. Andereck, S. S. Liu, and H. L. Swinney, "Flow regimes in a circular Couette system with independently rotating cylinders," *J. Fluid Mech.*, vol. 164, pp. 155–183, 1986.

[11] A. Barcilon and J. Brindley, "Marginal instability in Taylor-Couette flows at very high Taylor number," *J. Fluid Mech.*, vol. 94, pp. 453–463, 1979.

[12] G. P. Smith and Townsend, "Turbulent Couette flow between two concentric cylinders at large Taylor numbers," *J. Fluid Mech.*, vol. 143, pp. 429–459, 1982.

[13] J. Parker and P. Merati, "An investigation of turbulent Taylor-Couette flow using laser doppler velocimetry in a refractive index matched facility," *Trans. ASME, J. Fluids Eng.*, vol. 118, pp. 810–818, 1996.

[14] S. Chandrasekhar, *Hydrodynamic and Hydromagnetic Stability.* Oxford Clarendon Press, 1961.

[15] E. L. Koschmieder, *Bénard Cells and Taylor Vortices.* Cambridge University Press, 1 ed., 1993.

[16] P. Chossat and G. Iooss, *The Couette Taylor Problem.* Berlin, Springer, 1992.

[17] J. E. Burkhalter and E. L. Koschmidieder, "Steady supercritical Taylor vortices after sudden starts," *Phys. Fluids*, vol. 17, no. 11, pp. 1929–1935, 1974.

[18] P. H. Roberts, "The solution of the characteristic value problem," *Proc. Royal Soc. London*, vol. A, no. 283, pp. 547–553, 1965.

[19] A. Davey, "The growth of Taylor vortices in flow between rotating cylinders," *J. Fluid Mech.*, no. 14, pp. 336–368, 1962.

[20] R. D. Moser and P. Moin, "The effects of curvature in wall-bounded turbulent flows," *J. Fluid. Mech.*, vol. 175, pp. 479–510, 1987.

[21] M. Kobayahi and H. Maekawa, "Turbulent flow accompanied by Taylor-Görter vortices in a two-dimensional curved channel," *Flow Meas. Instrum.*, vol. 6, no. 2, pp. 93–100, 1995.

[22] D. P. Lathrop, J. Fineberg, and H. L. Swinney, "Transition to shear-driven turbulence in Couette-Taylor flow," *Phys. Rev. A*, vol. 46, no. 10, pp. 6390–6405, 1992.

[23] E. Bilgen and E. Bilgous, "Functional dependence of torque coefficient of coaxial cylinders on gap width and Reynolds numbers," *Trans. ASME, J. Fluids Eng.*, vol. 95, pp. 122–126, 1973.

[24] G. I. Taylor, "Fluid friction between rotating cylinders,1–torque measurments," *Proc. Royal Soc. London, A*, vol. 157, p. 546, 1936.

[25] R. J. Donnelly and N. J. Simon, "An empirical torque relation for supercritical flow between rotating cylinders," *J. Fluid Mech.*, vol. 7, p. 401, 1959.

[26] Y. Yamada, "Torque reistance of a flow between rotating co-axial cylinders having axial flow," *Bulletin of JSME*, pp. 634–642, 1961.

[27] L. A. Dorfman, *Hydrodynamic reistance and heat loss of rotating solids.* Oliver and Boyd, 1st english ed., 1963.

[28] S. T. Wereley and R. M. Lueptow, "Spatio-temporal character of non-wavy and wavy Taylor-Couette flow," *J. Fluid Mech.*, vol. 364, pp. 59–80, 1998.

[29] M. Rudolph, T. Shinbrot, and R. M. Lueptow, "A model of mixing and transport in wavy Taylor-Couette flow," *Physica D*, no. 121, pp. 163–174, 1998.

[30] J. A. Vastano and R. D. Moser, "Short-time Lyapunov exponet analysis and the transition to chaos in Taylor-Couette flow," *J. Fluid Mech.*, vol. 233, pp. 83–118, 1991.

[31] D. Coles, "Transition in circular Couette flow," *J. Fluid Mech.*, no. 93, pp. 385–425, 1965.

[32] T. Brooke Benjamin and T. Mullin, "Notes on the multiplicity of flows in the Taylor experiment," *J. Fluid Mech.*, vol. 121, pp. 219–230, 1982.

[33] E. L. Koschmieder, "Turbulent Taylor vortex flow," *J. Fluid Mech.*, vol. 93, pp. 515–527, 1979.

[34] S. T. Wereley and R. M. Lueptow, "Azimuthal velocity in supercritical cirular couette flow," *Exp. Fluilds*, vol. 18, pp. 1–9, 1994.

[35] Y. Takeda, "Quasi-periodic state and the transition to turbulence in a arotating Couette system," *J. Fluid Mech.*, vol. 389, pp. 81–99, 1999.

[36] W. Y. Tam and H. L. Swinney, "Mass transport in turbulent Couette-Taylor flow," *Phys. Rev. A*, vol. 36, no. 3, pp. 1374–1381, 1987.

[37] P. M. Wild, N. Djilali, and G. W. Vickers, "Experimental and compuational assessment of windage losses in roatating machinery," *Trans. ASME, J. Fluids Eng.*, vol. 118, pp. 116–122, 1996.

[38] B. E. Launder and D. B. Spalding, "The numerical computations of turbulent flow," *Comp. Meth. Applied Mec. Eng.*, vol. 13, pp. 269–289, 1974.

[39] V. Yakhot and S. Orszag, "Renormalization group analysis of turbulence," *J. Sci. Comp.*, vol. 1, no. 1, pp. 3–57, 1986.

[40] B. E. Launder, G. J. Reece, and W. Rodi, "Progress in the development of a Reynolds-stress turbulent closure," *J. Fluid Mech.*, vol. 63, pp. 537–566, 1975.

[41] D. C. Wilcox, *Turbulence Modeling for CFD.* DCW Industries, 2 ed., 1998.

[42] K. Atkhen, J. Fontaine, and J. E. Westfreid, "Highly turbulent Couette-Taylor bubbly flow patterns," *J. Fluid Mech.*, vol. 422, pp. 55–68, 2000.

[43] H. Djéridi, J.-V. Favé, J.-Y. Billard, and D. Fruman, "Bubble capture and migration in Couette-Taylor flow," *Exp. Fluids*, vol. 26, pp. 233–239, 1999.

[44] T. Wei, E. M. Kline, S. H. K. Lee, and S. Woodruff, "Goïtler vortex formation at the inner cylinder in Taylor-Couette flow," *J. Fluid Mech.*, vol. 243, pp. 47–68, 1992.

[45] S. Abu Sharkh, W. Batten, M. El-Hami, and A. Hughes, "Technical note ITM02, Preliminary design of the first 2 kW prototype," tech. rep., Department of Electical engineering and ship science, University of Southampton, May 1998.

[46] S. Abu Sharkh, W. Batten, M. El-Hami, and A. Hughes, "Technical note ITM01, Preliminary design of the first 2 kW prototype," tech. rep., Department of Electical engineering and ship science, University of Southampton, February 1998.

[47] S. Abu Sharkh, W. Batten, M. El-Hami, and A. Hughes, "Technical note ITM03, Preliminary design of the first 2 kW prototype," tech. rep., Department of Electical engineering and ship science, University of Southampton, March 1999.

[48] E. L. Koschmieder, "Taylor vortices between eccentric cylinders," *Phys. Fluids*, vol. 19, pp. 1–4, 1976.

[49] R. R. Lessard and S. A. Zieminski, "Bubble coalescence and gas transfer in electrololitic aqueous solutions," *Ind. Eng. Chem. Fundam.*, vol. 20, pp. 260–269, 1976.

[50] R. Zenit, D. L. Koch, and A. S. Sangani, "Measurements of the average properties of a suspension of bubbles rising in a vertical channnel," *J. Fluid Mech.*, vol. 429, 2001.

[51] N. W. Bressloff, "Three-dimensional pulsatile flow through asymmetrically and symmetrically constricted vessels," *ASME, Bioengineering Conference*, vol. 50, pp. 525–526, 2001.

[52] J. P. Van Doormal and G. D. Raithby, "Enhancements of the simple method for prediciting incompressible fluid flows," *Numer. Heat Transfer*, vol. 7, pp. 147–163, 1984.

[53] S. V. Patankar and D. B. Spalding, "A calculation procedure for heat, mass and momentum transfer in three-dimensional parabolic flows," *Int. J. Heat Mass Transfer*, vol. 15, pp. 1787–1792, 1972.

[54] R. I. Issa, "Solution of implicitly discretised fluid flow equations by operator splitting," *J. Comput. Phys.*, vol. 62, pp. 40–65, 1986.

[55] D. S. Jang, R. Jetli, and S. Acharya, "Comparison of the piso, simpler and simplec algorithms for the treatment of the pressure-velocity coupling in steady flow problems," *Num. J. Heat Transfer*, vol. 10, pp. 209–228, 1986.

[56] N. W. Bressloff, "A parallel pressure implicit splitting of operators algorithm applied to flow at all speeds," *Int. J. Numer. Meth. in Fluids*, vol. 36, pp. 497–518, 2001.

[57] B. Van Leer, "Towards the ultimate conservative difference scheme," *J. Comp. Phys.*, vol. 14, pp. 361–370, 1977.

[58] AEA Technology plc, *CFX-4.2: Solver*, 1997.

[59] B. E. Launder and B. T. Shara, "Application of the energy dissipation model of turbulence to the calculation of flow near a spinning disc," *Lett. Heat and Mass Transfer*, vol. 11, pp. 131–138, 1974.

[60] G. E. Moore, "Cramming more components onto intergrated circuits," *Electronics*, vol. 38, no. 8, 1965.

[61] R. A. Law and S. R. Turnock, "Utilising existing computational resources to create a commodity PC network suitable for fast CFD computation," in *Parallel Computational Fluid Dynamics - Trends and Applications - Proceedings of the Parallel CFD 2000 Conference* (C. B. Jenssen, ed.), pp. 115–122, Elsevier Science B.V., 2001.

[62] J. H. Ferziger and P. M, *Computational methods for fluid dynamics.* Springer-Verlag, 2 ed., 1999.

[63] P. R. Spalart, "Strategies for turbuence modelling and simulations," *Int. J. Heat and Fluid Flow*, vol. 21, pp. 252–263, 2000.

[64] L. Davidson, "Hybrid LES-RANS: a combination of a one equation SGS model and a k-ω model for predicting recirculating flows," in *Computational Fluid Dynamics Conference*, (Swansea, Wales), ECCOMAS, September 2001.

[65] T. B. Gatski, M. Y. Hussaini, and L. J. L, *Simulation and Modeling of Tubulent flows.* Oxford University Press, 1 ed., 1996.

[66] J. Gullbrand, "An evaluation of conservative fourth order DNS code in turbulent channel flow," *Center for Turbulence Research, Annual Research Briefs*, pp. 211–218, 2000.

[67] P. M. Eagles, J. T. Stuart, and R. C. DiPrima, "The effects of eccentricity on torque and load in taylor vortex flow," *J. Fluids Mech.*, vol. 87, pp. 209–231, 1978.

[68] A. A. Townsend, "Axisymmetric couette flow at large Taylor numbers," *J. Fluid Mech.*, vol. 144, pp. 329–362, 1984.